

**THE DEVELOPMENT OF X-RAY EXCITED OPTICAL
LUMINESCENCE (XEOL) SPECTROSCOPIC TECHNIQUES
FOR MINERALOGICAL AND PETROLOGICAL
APPLICATIONS**

Richard Peter Taylor

**A Thesis Submitted for the Degree of PhD
at the
University of St Andrews**



2013

**Full metadata for this item is available in
Research@StAndrews:FullText
at:**

<http://research-repository.st-andrews.ac.uk/>

Please use this identifier to cite or link to this item:

<http://hdl.handle.net/10023/3739>

This item is protected by original copyright

The development of X-ray Excited Optical Luminescence (XEOL) spectroscopic techniques for mineralogical and petrological applications



University of
St Andrews

600
YEARS

Richard Peter Taylor

This thesis is submitted in partial fulfilment for the degree of

PhD

at the

University of St. Andrews

2013

Full metadata for this item is available in

Research@StAndrews:FullTextat:<http://research-repository.st-andrews.ac.uk/>

Please use this identifier to cite or link to this item:

The development of new XEOL and PL spectroscopic techniques for mineralogical and petrological applications

Submitted for the degree of Doctor of Philosophy

School of Geography & Geosciences

University of St Andrews

Richard Peter Taylor

January 2013

I, Richard Peter Taylor hereby certify that this thesis, which is approximately 56,000 words in length, has been written by me, that it is the record of work carried out by me and that it has not been submitted in any previous application for a higher degree.

I was admitted as a research student in September 2009 and as a candidate for the degree of Doctor of Philosophy in September 2009; the higher study for which this is a record was carried out in the University of St Andrews and The Diamond Light source between 2009 and 2013.

date

signature of candidate

I hereby certify that the candidate has fulfilled the conditions of the Resolution and Regulations appropriate for the degree of Doctor of Philosophy in the University of St Andrews and that the candidate is qualified to submit this thesis in application for that degree.

date

signature of supervisor

3. Permission for electronic publication:

In submitting this thesis to the University of St Andrews I understand that I am giving permission for it to be made available for use in accordance with the regulations of the University Library for the time being in force, subject to any copyright vested in the work not being affected thereby. I also understand that the title and the abstract will be published, and that a copy of the work may be made and supplied to any bona fide library or research worker, that my thesis will be electronically accessible for personal or research use unless exempt by award of an embargo as requested below, and that the library has the right to migrate my thesis into new electronic forms as required to ensure continued access to the thesis. I have obtained any third-party copyright permissions that may be required in order to allow such access and migration, or have requested the appropriate embargo below.

The following is an agreed request by candidate and supervisor regarding the electronic publication of this thesis:

Access to printed copy and electronic publication of thesis through the University of St Andrews

date

signature of candidate

date

signature of supervisor

ABSTRACT

This thesis investigates the use of X-ray Excited Optical Luminescence (XEOL) and Time Resolved X-ray Excited Optical Luminescence (TR XEOL) within the Earth sciences. The project contains two primary objectives, the first of which is the design and building of a high-resolution luminescence spectroscopy facility. This includes the installation and commissioning of the facility on the I18 microfocus beamline at Diamond, the UK's national synchrotron facility. In describing the systems design and commissioning, I explore many implications of the technique.

The second objective is using this new facility to investigate a suite of minerals to develop new analytical techniques utilizing XEOL and TR XEOL spectroscopy for applications within the Earth sciences. An aspect of this investigation is to explore the potential of Time Resolved Optically Derived X-ray Absorption Spectroscopy (TR OD XAS) of substitute trace elements in minerals. To date CW OD XAS has been shown to have very limited application within the Earth sciences. (Soderholm et al., 1998-120) The thesis explores differences between photoluminescence (PL) and XEOL responses in mineral systems, and investigates how these differences can be exploited.

Luminescence, the phenomenon upon which the thesis is based, is a complex and poorly utilised phenomena within Earth sciences, it is however, orders of magnitude more sensitive, than many of the more accepted techniques used for the detection of trace elements, on this basis alone I would suggest it deserves further consideration.

Luminescence techniques have developed much further in other disciplines; I therefore have incorporated many descriptions, models, and interpretations from other disciplines

in order to identify methodologies and techniques that have the potential to be utilized in the study and interpretation of luminescence within the Earth sciences.

The thesis demonstrates that luminescence in minerals with measured lifetimes, as fast as ~ 20 ps exist. Previously the recorded luminescent lifetimes, for minerals, in the literature are measured in ns. This finding leads to the novel concept that the measurement of TR XEOL with ps resolution combined with the measurement of the intensity of a luminescent signal as a function of excitation can provide significant new insights into the nature of the emission and the luminescent processes. I explore and demonstrate the potential of using dose dependence techniques of continuous wave and TR XEOL as a new analytical technique.

I also demonstrate the use of a technique used extensively within Biology has an application with Earth sciences. The methodology incorporates the calculation of the natural lifetime of an emission through the relationship between the absorption and emission coefficients. (Strickler and Berg, 1962). I discuss how knowledge of the natural lifetime of an emission allows quantification of luminescence through measurement of a modified lifetime of emission. The quantification of a luminescent emission has significant potential within the geosciences one example being the identification of disputed emissions. I also consider the potential to use TR XEOL techniques in mapping complex heterogeneous rocks and minerals.

Contents

ABSTRACT	5
Contents	7
List of Equations	13
List of Tables	14
List of figures	16
Abbreviations Used	23
ACKNOWLEDGEMENTS	25
1 INTRODUCTION	27
2 LUMINESCENCE	31
2.1 Luminescence in a Historical Context	31
2.2 Defining Luminescence terminology	33
2.3 Clarifying the Use of the Terms Luminescence and Fluorescence	35
2.4 Contemporary Understanding of Luminescence	39
2.5 Energy Transformation	40
2.6 Lifetime	42
2.7 The Exciton	42
2.8 Quantification	43
	7

2.8.1 Mathematical Relationships	45
2.8.2 The Einstein Coefficients	46
2.8.3 General Relationship between the Coefficient of Absorption and Emission	48
2.8.4 The Relationship between Absorption and Emission Lifetimes for Molecules	48
2.8.5 Calculating Radiative Transition Rates from First Principles	50
2.8.6 Quenching	52
2.8.7 Spin Selection Rule	52
2.8.8 Laporte Selection Rule	54
2.8.9 Hund's Rule	55
2.8.10 Expanded Descriptions and Definitions of the Luminescent Processes	55
2.9 Intrinsic and Extrinsic Luminescence	57
2.10 Energy Transfer	58
2.10.1 Trivial Energy Transfer	60
2.10.2 Förster (Singlet) Transfer	60
2.10.3 Dexter (Triplet or Singlet) Energy Transfer	63
2.10.4 Tunnelling	65
2.10.5 Triplet-Triplet Annihilation	66
2.10.6 Implications for Energy Transfer Mechanisms	68
2.10.7 Implications of Phonons in Direct Transitions	68
2.11 Types of Transitions	69
2.11.1 Direct and Indirect Transitions and their Probabilities	70
2.11.2 The Implications for Extended Defects on Energy Transfer	71
2.11.3 Hole Transitions	72
2.11.4 Thermal Effects on Luminescence	73
2.11.5 Hot Luminescence	75
2.11.6 Quantum Efficiency	76

2.12 Comparisons of High-Energy Excitation	79
3 SAMPLE CHARACTERISATION	81
3.1 Why is Sample Characterisation Important?	81
3.2 Luminescence of a Localised Centre	82
3.3 Types of Defects	83
3.4 Interactions between the Matrix and Point Defect Lumiphores	85
3.5 Textural Information in Luminescent Signals	86
3.6 Feldspar	87
3.6.1 MISI Iron Rich Microcline	89
3.6.2 Cleavelandite	90
3.6.3 Moonstone	91
3.6.4 Copper Bearing Feldspar	92
3.7 Gem Quality Samples with Known Absorption Luminescent Centres	95
3.8 Zircon	98
3.9 Topaz	101
3.10 Chrome Tourmaline	102
3.11 RT1-1 Synthetic ruby	104
4 SYNCHROTRON RADIATION	107
4.1 X-ray Absorption Spectroscopy	107
4.2 X-ray Excited Optical Luminescence	111

4.3 TR XEOL	112
4.4 Optically Derived X-ray Absorption Spectroscopy	113
4.5 Soft X-ray and Vacuum Ultra Violet Excitation	116
4.6 Polarisation	118
4.7 Heterogeneity	119
4.8 The XEOL Detection System	119
4.8.1 System Requirements	121
4.8.2 Techniques for Collecting Time-Resolved Data	122
4.8.3 Initial Design Proposals	128
4.8.4 Design Modifications Following Commissioning	131
4.8.5 The Final System	133
4.8.6 Continuous Wave Measurements	134
4.8.7 Time-Resolved Measurements	135
4.9 Experimental Techniques	139
4.9.1 CW XEOL Spectroscopy	139
4.9.2 TR XEOL	141
4.9.3 XEOL Spatial Mapping	142
4.9.4 OD XAS	143
4.10 System Test Results	143
4.10.1 XEOL Dose and Dose Rate Dependence	144
4.10.2 TR XEOL Lifetime Measurement	150
4.10.3 Fibre Optic Transit Time	156
4.10.4 Investigation into Anomalous Second TR Peak	157
4.10.5 OD XAS	159

5 RESULTS FROM FELDSPAR MINERALS	162
5.1 MISI -Iron rich microcline alkali feldspar	163
5.1.1 TR energy dependence	165
5.1.2 Dose effects on TR	172
5.2 Cleavelandite Feldspar (CLBR)	174
5.2.1 Dose Dependence	181
5.2.2 Dose Rate	190
5.3 Moonstone	194
5.3.1 XEOL	194
5.3.2 Dose Dependence	195
5.3.3 Dose rate	202
5.4 Copper Bearing Feldspar	204
5.4.1 Characterisation	204
5.4.2 CW XEOL	213
5.4.3 TR XEOL	217
5.5 Chapter summary	226
5.5.1 Suggested further work	227
6 ADDITIONAL RESULTS	229
6.1 Zircon	230
6.1.1 CW XEOL	230
6.1.2 TR OD XAS	231
6.1.3 TR XEOL as a Function of Incident Energy	235
6.2 Topaz	237
6.2.1 Orientation	237
	11

6.2.2 Dose Dependent Anisotropy	242
6.1 Synthetic Ruby RT1-1	247
6.1.1 Strickler and Berg Calculation	249
6.2 Chrome Tourmaline	253
6.2.1 CW Dose Dependent XEOL	253
6.2.2 Temperature Dependence of TR XEOL	255
6.3 Summary of Chapter 6	258
7 CONCLUSIONS	259
7.1 Further Development	270
8 APPENDIX	271
Appendix 1. Hamamatsu MCP PMT R3809U-50	271
Appendix 2. Specification sheet time card	279
Appendix 3. Ortec 9327	281
Appendix 4. ORTEC 566	285
Appendix 5. Transmission curves optic fibres	287
Appendix 6. Fitting results from ZAF5 red zircon	288
9 REFERENCES	290

List of Equations

<i>Equation 1</i>	46
<i>Equation 2</i>	46
<i>Equation 3</i>	47
<i>Equation 4</i>	47
<i>Equation 5</i>	48
<i>Equation 6</i>	48
<i>Equation 7</i>	49
<i>Equation 8</i>	50
<i>Equation 9</i>	50
<i>Equation 10</i>	51
<i>Equation 11</i>	62
<i>Equation 12</i>	62
<i>Equation 13</i>	64
<i>Equation 14</i>	66
<i>Equation 15</i>	76
<i>Equation 16</i>	77
<i>Equation 17</i>	108
<i>Equation 18</i>	111
<i>Equation 19</i>	121
<i>Equation 20</i>	138
<i>Equation 21</i>	157
<i>Equation 22</i>	250

List of Tables

<i>Table 2-1 Chronological list of events</i>	32
<i>Table 2-2 - Classification of light emission as a function of the source of excitation</i>	37
<i>Table 2-3 – Popular analytical techniques used within the Earth sciences</i>	44
<i>Table 2-4 - Electric dipole selection rules for single electron atoms</i>	53
<i>Table 2-5 List of the features and requirements for trivial energy transfer</i>	60
<i>Table 2-6 Typical energy conversion/transfer times involved in the luminescent process. Source</i>	75
<i>Table 2-7 Factors that can affect the QE and lifetime of a luminescent emission</i>	78
<i>Table 3-1 - Localised luminescent centres</i>	83
<i>Table 3-2 - Chemistry and summary of the crystal structure of the feldspar group end members</i>	87
<i>Table 3-3 Feldspar samples used in Cu investigation section 5.4</i>	94
<i>Table 3-4 Gem quality Allochromatic minerals</i>	96
<i>Table 3-5 Gem quality of idiochromatic minerals</i>	97
<i>Table 3-6 - Comparative chemical analysis of RT1-1</i>	106
<i>Table 4-1 - Summary of samples used to test system</i>	139
<i>Table 4-2 - Summary of attenuation foil thicknesses and relative attenuation for 7 keV X-rays</i>	140
<i>Table 4-3 - Summary of CW XEOL spectral features compared with published data</i>	145
<i>Table 5-1- Summary of emission features for CW XEOL LT ~91K</i>	176
<i>Table 5-2 - Peak positions for CLBR low temperature XEOL experiment</i>	180
<i>Table 5-3 - Table showing luminescent emissions identified in XEOL collected from moonstone RT83 at 7keV at RT. Collected using 150 line grating centred at 550 nm (2.25 eV) compared to typical luminescent emissions from alkali feldspar (Garcia-Guinea et al., 1996)</i>	195

<i>Table 5-4 - Analysis of the measured edge energy of a number of natural and treated samples column 1 is edge energy of absorption edge for sample</i>	<i>210</i>
<i>Table 5-5 - Peak positions from XEOL collected from samples of treated and untreated labradorite and andesine.</i>	<i>217</i>
<i>Table 5-6 TR XEOL representative spectra collected from treated and untreated samples of feldspar detailed in</i>	<i>218</i>
<i>Table 5-7 - TR XEOL responses of RT52 colourless Andesine Collected using 7 keV excitation, 1 mm slits 150 line grating blazed at 500 nm 2.48 eV centred at 410 nm (3.02 eV).</i>	<i>220</i>
<i>Table 6-1 - Summary of CW XEOL spectral features collected from crystallographically orientated topaz RT63. Excited at 7 keV using 150 line grating blazed at 500 nm 2.48 eV centred at 550 nm 2.25 eV 0.5 mm slits.....</i>	<i>240</i>
<i>Table 6-2 - Summary of XEOL emission peaks for RT 1_1 synthetic ruby excited using 7 keV for 60 s.....</i>	<i>248</i>
<i>Table 6-3 - Results of curve fitting from Origin Pro ver. 8.5.1 of absorption spectra taken from RT1-1 Figure 6-22.....</i>	<i>250</i>

List of figures

<i>Figure 2-1: The phosphorescent relaxation route of an excited electron through the triplet state. Source: (Nassau, 2001).....</i>	<i>34</i>
<i>Figure 2-2 Three possible photon electron interactions.....</i>	<i>39</i>
<i>Figure 2-3 - Search of SciVerse®</i>	<i>50</i>
<i>Figure 2-4 Laporte states used to define allowed and disallowed transitions.....</i>	<i>54</i>
<i>Figure 2-5 - Allowed and disallowed spin distributions. (Fox, 2006).....</i>	<i>55</i>
<i>Figure 2-6 - Jablonski energy diagram.....</i>	<i>56</i>
<i>Figure 2-7 - Band gap energy diagram</i>	<i>57</i>
<i>Figure 2-8 Donor acceptor interaction.(Yen et al., 2007).....</i>	<i>61</i>
<i>Figure 2-9 The spectral response to the addition of an acceptor molecule to a polymer host.</i>	<i>63</i>
<i>Figure 2-10 Representation of singlet–singlet and triplet-triplet Dexter energy transfer</i>	<i>64</i>
<i>Figure 2-11 Triplet-triplet energy transfer</i>	<i>67</i>
<i>Figure 2-12 - Morse curves</i>	<i>69</i>
<i>Figure 2-13 - Stokes shift</i>	<i>74</i>
<i>Figure 3-1 (a) The image shows a growth pattern in a volcanic fluorite crystal from Chemnitz, Germany ..</i>	<i>86</i>
<i>Figure 3-2 - Ternary diagram showing chemical and compositional boundaries in the feldspar group.....</i>	<i>88</i>
<i>Figure 3-3 - Maximum microcline refinement.</i>	<i>89</i>
<i>Figure 3-4 - Albite cleavelandite refinement.</i>	<i>90</i>
<i>Figure 3-5 - Labradorite refinement.</i>	<i>92</i>
<i>Figure 3-6 - Zircon refinement.</i>	<i>99</i>
<i>Figure 3-7 - Topaz low OH refinement.....</i>	<i>101</i>
<i>Figure 3-8 - Chrome tourmaline (Dravite) refinement.....</i>	<i>103</i>

<i>Figure 3-9 Absorption spectra of chrome tourmaline.....</i>	<i>103</i>
<i>Figure 3-10 - Ruby refinement.....</i>	<i>104</i>
<i>Figure 3-11 - Absorption spectra ruby.....</i>	<i>105</i>
<i>Figure 3-12 - Emission spectra ruby.....</i>	<i>105</i>
<i>Figure 3-13 - TR ruby spectra ²E emission at 694.2nm single exponential decay 4.26 ms.</i>	<i>106</i>
<i>Figure 4-1 - Periodic table showing the XAS accessible elements for many third generation synchrotrons.</i>	<i>108</i>
<i>Figure 4-2 The effect of interference upon the ejected electron wave from the surrounding atoms.</i>	<i>109</i>
<i>Figure 4-3 - Section of the electromagnetic spectrum from hard X-rays to infrared and wavelength energy conversions.</i>	<i>117</i>
<i>Figure 4-4 - XEOL luminescence exhibited by synthetic ruby.....</i>	<i>120</i>
<i>Figure 4-5- The method for calculating the steradian in a sphere.</i>	<i>120</i>
<i>Figure 4-6 Phase modulation or frequency domain measurements.....</i>	<i>123</i>
<i>Figure 4-7 - Decay time measurements using gated detection in a pulse sampling mode.</i>	<i>124</i>
<i>Figure 4-8 - Typical laser based system configuration for streak plate TR analysis.</i>	<i>125</i>
<i>Figure 4-9 - Up conversion using non-linear crystal (BBO)</i>	<i>126</i>
<i>Figure 4-10 - Classic time-correlated single photon counting experiment.</i>	<i>127</i>
<i>Figure 4-11 - TCSPC system incorporated onto synchrotron.</i>	<i>127</i>
<i>Figure 4-12 The layout of the XEOL detection system for the I18 beamline. Inset shows the sample, beam, and optic fibre alignment.</i>	<i>133</i>
<i>Figure 4-13 Diamond synchrotron ring standard</i>	<i>136</i>
<i>Figure 4-14 - CW-XEOL spectra from cleavelandite (CLBR) excited using 7 keV X-rays.</i>	<i>144</i>
<i>Figure 4-15 - A sample set of CW-XEOL data taken from a data set collected from CLBR.</i>	<i>147</i>
<i>Figure 4-16 - CW XEOL spectra showing the dose rate dependence of CLBR to varying beam intensities. .</i>	<i>148</i>

<i>Figure 4-17 TR XEOL from RT1020 signal collected from a sample of thin film GaN on sapphire substrate</i>	<i>150</i>
<i>Figure 4-18 - TR XEOL from sample, ref MISI</i>	<i>152</i>
<i>Figure 4-19 - TR XEOL RT1011 pink kunzite</i>	<i>153</i>
<i>Figure 4-20 - Short lifetime luminescent emission (LH axis) plotted against wavelength for (MISI).</i>	<i>155</i>
<i>Figure 4-21 – Fibre transit time.</i>	<i>156</i>
<i>Figure 4-22 - Transit time per unit length.</i>	<i>157</i>
<i>Figure 4-23 - CLBR 7 keV excitation TR spectra collected at 460 nm (2.70 eV) centre</i>	<i>158</i>
<i>Figure 4-24 CW XEOL of Eu₂O₃.</i>	<i>159</i>
<i>Figure 4-25- Comparison of OD XAS collected from 608nm emissions</i>	<i>160</i>
<i>Figure 5-1 MISI dose rate responses.</i>	<i>164</i>
<i>Figure 5-2 – MISI normalised dose rate response.</i>	<i>164</i>
<i>Figure 5-3 - Sample of TR XEOL collected from MISI</i>	<i>165</i>
<i>Figure 5-4 - Sample of TR XEOL collected from MISI log intensity vs time</i>	<i>166</i>
<i>Figure 5-5 - Sample of TR XEOL collected from MISI</i>	<i>166</i>
<i>Figure 5-6 - Summary of TR XEOL spectra collected from MISI.</i>	<i>168</i>
<i>Figure 5-7 -Comparative summary of peak heights and lifetimes of TR XEOL emissions from MISI</i>	<i>171</i>
<i>Figure 5-8 - TR XEOL collected from the first integration from MISI.</i>	<i>173</i>
<i>Figure 5-9 - TR XEOL collected from MISI second data collection</i>	<i>174</i>
<i>Figure 5-10 – CLBR dose dependent XEOL</i>	<i>175</i>
<i>Figure 5-11 - CW XEOL dose dependence experiment from CLBR first spectra.</i>	<i>177</i>
<i>Figure 5-12 - CW XEOL dose dependence experiment from CLBR last spectra.</i>	<i>178</i>
<i>Figure 5-13 – Dose dependence fitted spectra collected after 510 s from CLBR at RT.</i>	<i>182</i>
<i>Figure 5-14 - Dose dependence fitted spectra collected after 30 s from CLBR at RT.</i>	<i>182</i>

<i>Figure 5-15 - Dose dependence peak height vs peak position ~729 nm (~1.7 eV) taken from the CLBR spectra Figure 5-17</i>	183
<i>Figure 5-16 - Dose dependence comparative peak height and peak position ~729 nm (~1.7 eV) from CLBR at RT.</i>	184
<i>Figure 5-17 - Dose dependence comparative peak height and peak position 564 nm (~2.2 eV) from CLBR at RT.</i>	185
<i>Figure 5-18 - Dose dependence peak height vs peak position collected at ~564nm (~2.2 eV) taken from CLBR spectra</i>	185
<i>Figure 5-19 - Dose dependence fitted spectra collected after 30 s from CLBR at RT.</i>	186
<i>Figure 5-20 TR XEOL from three spectra collected at different emission energies.</i>	186
<i>Figure 5-21 - Dose dependence comparative peak height and peak position</i>	188
<i>Figure 5-22 - Dose dependence comparative peak height and peak position</i>	188
<i>Figure 5-23 - Dose dependence comparative peak height and peak position</i>	189
<i>Figure 5-24 - Dose dependence comparative peak height and peak position</i>	189
<i>Figure 5-25 - Dose dependence comparative peak height and peak position</i>	190
<i>Figure 5-26 - CLBR TR dose rate experiment excited at 7 keV.</i>	191
<i>Figure 5-27 - CLBR TR dose rate experiment excited at 7 keV.</i>	192
<i>Figure 5-28 - CLBR TR dose rate experiment excited at 7 keV.</i>	192
<i>Figure 5-29 - XEOL from RT 83 Moonstone excited at 7 keV.</i>	194
<i>Figure 5-30 - RT83 Moonstone dose dependence spectra.</i>	196
<i>Figure 5-31 - Expanded section of the dose dependence response of RT83 moonstone. (Figure 5-30)</i>	197
<i>Figure 5-32 - Fitted dose dependence spectra after 2 seconds.</i>	197
<i>Figure 5-33 - Fitted dose dependence spectra after 4 seconds.</i>	198
<i>Figure 5-34 - Fitted dose dependence spectra after 95 seconds.</i>	198
<i>Figure 5-35 - First three spectra from RT83 Moonstone dose dependence spectra</i>	200

<i>Figure 5-36 - Peak heights taken from figure 5-31 and plotted as a function of time.....</i>	<i>202</i>
<i>Figure 5-37 - RT moonstone dose dependence using 7keV excitation corrected for system response.</i>	<i>203</i>
<i>Figure 5-38 - Dose dependence normalised peak height against beam intensity</i>	<i>203</i>
<i>Figure 5-39 - Natural Plush feldspar</i>	<i>205</i>
<i>Figure 5-40 - Treated feldspar</i>	<i>206</i>
<i>Figure 5-41 - Natural and treated plush feldspar samples.</i>	<i>207</i>
<i>Figure 5-42 - The standards measured for the three copper oxidation states.....</i>	<i>208</i>
<i>Figure 5-43 – First derivatives of XANES.....</i>	<i>209</i>
<i>Figure 5-44 - First derivatives of XANES.....</i>	<i>209</i>
<i>Figure 5-45 - - First derivatives of XANES.....</i>	<i>209</i>
<i>Figure 5-46 -Absorption spectra copper bearing natural ‘plush’ feldspar.</i>	<i>211</i>
<i>Figure 5-47 - Luminescence spectra copper bearing natural ‘plush’ feldspar</i>	<i>212</i>
<i>Figure 5-48- CW XEOL RT57 colourless Mongolian Andesine</i>	<i>212</i>
<i>Figure 5-49 - CW XEOL RT23 treated red Andesine excited 7 keV.</i>	<i>214</i>
<i>Figure 5-50 - CW XEOL RT30 treated green Andesine excited 7 keV.</i>	<i>214</i>
<i>Figure 5-51 CW XEOL RT43 natural green Labradorite excited 7 keV.....</i>	<i>215</i>
<i>Figure 5-52 CW XEOL RT28 natural colourless Labradorite excited 7 keV.....</i>	<i>215</i>
<i>Figure 5-53 CW XEOL RT35 treated andesine excited 6 keV.....</i>	<i>216</i>
<i>Figure 5-54CW XEOL RT45 natural red labradorite excited 6 keV</i>	<i>216</i>
<i>Figure 5-55 RT58 Albite TRPL emission scan showing before and after heat treatment spectra.</i>	<i>219</i>
<i>Figure 5-56 - Dose Dependent TR XEOL from RT52</i>	<i>221</i>
<i>Figure 5-57 - Dose Dependent TR XEOL from RT52</i>	<i>222</i>
<i>Figure 5-58 - Dose dependence TR XEOL data collected from RT52</i>	<i>223</i>

<i>Figure 5-59 - Absorption and energy transfer model to explain TR spectra of RT.</i>	225
<i>Figure 5-60 -RT57 labradorite Inner Mongolia dose rate TR XEOL. Normalised TR Peak height as a function of beam intensity.</i>	226
<i>Figure 6-1 - ZAF5 CW XEOL spectrum collected from red zircon.</i>	230
<i>Figure 6-2 - TR XEOL from red zircon (ZAF5) best fitted with a double exponential.</i>	231
<i>Figure 6-3 - ZAF5 red zircon TR XEOL energy scan from 6.95- 7.01 keV</i>	232
<i>Figure 6-4 - ZAF5 Red Zircon TR XEOL energy scan from 6.95- 7.01 keV.</i>	233
<i>Figure 6-5 - ZAF5 red zircon TR XEOL energy scan from 6.95- 7.01 keV.</i>	234
<i>Figure 6-6 - TR XEOL spectra collected from 4 - 10 keV.</i>	235
<i>Figure 6-7 - TR XEOL spectra collected from 4 - 10 keV</i>	235
<i>Figure 6-8 - XEOL spectra from topaz RT63 collected</i>	237
<i>Figure 6-9 - XEOL spectra collected from topaz RT63</i>	238
<i>Figure 6-10 -XEOL spectra collected from topaz RT63</i>	239
<i>Figure 6-11 - Absorption spectra from untreated topaz samples.</i>	241
<i>Figure 6-12 - Topaz RT63-13 'b' first dose dependence spectra shown with no data correction.</i>	242
<i>Figure 6-13 - Topaz RT63-13 'b' dose second dependence spectra shown with no data correction.</i>	243
<i>Figure 6-14 - Topaz RT63 dose rate analysed by peak for each crystallographic orientation.</i>	245
<i>Figure 6-15 - Topaz RT63 dose rate analysed by axis for each peak.</i>	246
<i>Figure 6-16 - XEOL spectra of RT 1_1 synthetic ruby excited using 7 keV for 60 s.</i>	247
<i>Figure 6-17 - Absorption spectra from RT1-1 synthetic ruby.</i>	249
<i>Figure 6-18 - Octahedral coordination and the CF splitting energy levels.</i>	252
<i>Figure 6-19 - TR XEOL spectra collected from RT1-1 7 keV excitation.</i>	252
<i>Figure 6-20 - RT1013 chrome tourmaline dose dependence.</i>	254

Figure 6-21 - CW XEOL from RT1013 chrome tourmaline..... 254

Figure 6-22 - TR XEOL Spectra collected at 336 nm for 180 s at ~91 K excited at 7 keV..... 257

Figure 6-23 - TR XEOL Spectra collected at 336 nm for 600 s at ~91 K excited at 7 keV..... 257

Figure 6-24 - TR XEOL Spectra collected at 340 nm for 300 s at RT excited at 7keV 257

Abbreviations Used

CCD	Charge Coupled Device
CFD	Constant Fraction Discrimination
CFT	Crystal Field Theory
CL	Cathodoluminescence
CW	Continuous Wave
EM	Electromagnetic
EPICS	Experimental Physics And Industrial Control Systems
EMP	Electron MicroProbe
EPR	Electron Paramagnetic Resonance
EXAFS	Extended X-Ray Absorption Fine Structure
FLIM	Fluorescence Lifetime Imaging Microscopy
FRET	Förster Resonance Energy Transfer
FWHM	Full Width Half Maximum
GDA	Generic Data Analysis
ICP MS	Inductively Coupled Mass Spectrometry
IVCT	Inter Valance Charge Transfer
KVM	Keyboard Video Mouse
LA ICP MS	Laser Ablation Inductively Coupled Mass Spectrometry
LFT	Ligand Field Theory
LIBS	Laser Induced Breakdown Spectroscopy
LOD	Limit of Detection
LT	Low Temperature
MCA	Multi Component Analysis
MCP PMT	Multi-Channel Plate PhotoMultiplier Tube
NMR	Nuclear Magnetic Resonance
OD XAS	Optically Derived X-Ray Absorption Spectroscopy
OPO	Optical Parametric Oscillator
OS	Operating System
OSL	Optically Stimulated Luminescence
PL	Photoluminescence
PP	Pump Probe
QE	Quantum Efficiency
QM	Quantum Mechanical
RET	Resonant Energy Transfer
RI	Refractive Index
ROI	Region Of Interest
RT	Room Temperature
SDK	Software Development Kit
SIMS	Secondary Ion Mass Spectroscopy
SNOM	Scanning Near-Field Optical Microscopy

STE	Self-Trapped Exciton
STJ	Superconducting Tunnel Junction
STM	Scanning Tunnelling Microscope
TCSPC	Time Correlated Single Photon Counting
TEM	Transmission Electron microscopy
TEY	Total Electron Yield
TIMS	Thermal Ionization Mass Spectroscopy
TL	Thermo Luminescence
TR	Time Resolved
TRPL	Time Resolved Photo Luminescence
XANES	X-Ray Absorption Near Edge Spectroscopy
XAS	X-Ray Absorption Spectroscopy
XEOL	X-Ray Excited Optical Luminescence
XRD	X-Ray Diffraction
XRF	X-Ray Fluorescence

Acknowledgements

This I consider the most difficult section of my thesis and possibly the most important as I owe so much to so many. I must start by thanking my two primary supervisors, Dr Adrian Finch and Professor Fred Mosselmans. They were a source of unreserved support and reassurance throughout my thesis, showing immense amounts of patience when I struggled and unreserved encouragement for my enthusiasm. I am enormously indebted to you both.

My wife, Annette, whose patience and perseverance was tested beyond what could normally be expected, thank you for your continued faith.

I am indebted to my colleagues at the Diamond Light Source for their help and support particularly Dr Paul Quinn, for not only the support but also the worthwhile discussions we had. I must include Tina Geraki, Steve Keylock, Pete Leicester and Loradana Brinza for their immensely valuable help and friendship. I must also mention Dr Stan Botchway and Dr Dave Clark at the Laser facility for all their help and assistance.

At The University of St Andrews Dr Colin Donaldson my second supervisor who was always on hand, thank you. More generally, I would like to thank **all** the academic staff, support staff, and students within the department, you each helped to make my period at St Andrews so worthwhile and rewarding. I must thank the technical staff within the department namely Angus Calder, Donald Herd, Colin Cameron and Andy Mackie, who each in their own individual ways added support and help along my journey.

My PhD was funded jointly by the University of St Andrews and the Diamond Light Source without whose generous support I would have been unable to complete my research. I also received the most amazing support from the following institutions and private individuals including financial support, the supply of materials and samples, and access to facilities. The Gemmological Association of GB, the Gemological Institute of America, the Mineralogical Association of GB through the mineral physics group, National museums Scotland, and Dr Brian Jackson, the IMA, the STFC for supporting beam time at both the Diamond Light Source and the Central Laser Facility, AGS, Dr Don Hoover, Dust Devil mining company, Richard W Hughes, Bear Stone laboratories.

Throughout my PhD, I have had the pleasure to work with the most wonderful and inspiring colleagues and organisations. It has been a joy to get up in the morning, even on those inevitable days when it seemed the challenges ahead were insurmountable. The support I received not only got me through but also helped me enjoy every single minute.

I extend a heartfelt thank you to all that have not been mentioned by name. The list is far too long to mention everybody, but that does not diminish the significance of your contribution, or the sincerity of my gratitude.

1 Introduction

Minerals, the building blocks of the Earth's mantle and crust, are naturally occurring inorganic solids, with a definite chemical composition and characteristic structure.

Minerals however, contain defects including trace element substitution whose creation primarily occurs during crystal growth (Klein and Dutrow, 2008), and their nature and abundance are sensitive to the local environmental temperature, pressure, and chemistry. Defect populations can therefore be used to reconstruct historical geological conditions. Defects include: chemical substitution, incorporation (interstitial atoms), and point defects such as vacancies; structural features, such as line defects; lattice defects and dislocations, including broken bonds and atomic dislocations; and more extended planar and lattice dislocations. Bulk defects can be considered as clusters of defects or voids. In addition, grain boundaries within heterogeneous crystals and multiphase rocks, for the purposes of this thesis are considered as a crystallographic discontinuity or defect.

The relationship between the conditions necessary for the creation of defects and their detection and interpretation in minerals underlies the rationale for this thesis. Defects are not static within a mineral; they are mobile over geological time and sensitive to environmental conditions within which the mineral is held. The investigation of defects in minerals is complicated by the fact that their nature is varied and transient over time, being susceptible to modification, addition, and destruction with populations derived and/or destroyed subsequent to genesis. Typically, a mineral will contain a diverse population of defects of multiple origins.

To interpret a defect population in a mineral, a number of challenges exist. Firstly, the positive identification, discrimination, and quantification of individual defect populations are required. The characterisation of individual defects is critical to allow interpretation. Characterisation not only includes, for example, the identification of a chemical substitution and its oxidation state, but also the site-specific relationship with the host matrix. An elemental substitution can frequently occur in more than one site effectively generating a different defect in each non-equivalent site. In addition, the inter-relationships between defects and their local environment must be considered as an additional factor of characterisation. The combination of these factors will help define the genesis of a particular mineral, the stability, and the relative mobility of the defect population, allowing the interpretation of the history, modification, and emplacement of a mineral.

There are many analytical techniques available for the identification and characterisation of defects but they tend to be either sensitive to the chemistry or the site-specific nature of the defect site as summarised in (Table 2.3); this creates an ambiguity in our understanding. Luminescence in contrast is sensitive to both; it is also a highly sensitive technique capable of detection at concentrations of a lumiphore as low as Parts Per Billion (ppb) (Lakowicz, 1999). Luminescence, therefore, is potentially the ideal mechanism to investigate defects in minerals. Luminescence involves the detection of light emitted following excitation from an incident energy. Commonly, the energy of excitation is visible light of a higher energy (shorter wavelength), this is known as photoluminescence (PL). This present study focuses on X-ray excited luminescence to differentiate, identify, and characterise defects in minerals. The excitation selected is

from the soft to hard X-ray regime in the range $\sim 2.5 - 12$ keV. The benefits of working in this region of the Electromagnetic Spectrum (EM) are manifold. Firstly, X-rays of this energy penetrate the majority of minerals sufficiently to allow the analysis to be considered a bulk analysis and not a surface-dominated technique. Within this energy range, the radiation is ionising and for the majority of elements of interest, is sufficiently energetic for core electron excitation, eliminating the constraints of resonant absorption inherent with Photo Luminescence (PL). The investigation utilises synchrotron energy generated on the i18 beamline of the diamond light source. The X-ray beam used can be both focused and tuned, which allows element sensitive analysis with a high degree of spatial resolution, which is ideal for working with heterogeneous minerals. Synchrotron radiation is, by its nature of production, pulsed and by using a special fill of the electrons within the ring, the collection of picosecond (ps) resolution Time Resolved (TR) X-Ray Excited Optical Luminescence (XEOL) spectra is facilitated. The lifetime of a luminescent emission is a measure of the probability of the spontaneous emission and has to date primarily found applications in characterisation and differentiation of lumiphores and in a limited number of circumstances the quantification. In this thesis, I explore applications combining the analysis of the lifetime of emissions with their intensity, and this approach has not been used previously. The probing of the different/common factors that control these two aspects of emission allows novel interpretations of the mechanism. I also explore the application of lifetime in the quantification of luminescent emissions within minerals adapting a methodology normally used within organic chemistry (Strickler and Berg, 1962).

The mechanisms controlling luminescence in minerals are manifold and complex. They are an interaction between the bulk and the local defect and the nature of the incident energy. In comparison to other luminescent systems, minerals show particularly complex luminescent responses. A simple word search of SciVerse/Scopus© (November 2012) using 'fluorescence' or 'luminescence' (fluorescence being a subset of luminescence limited to ElectroMagnetic (EM) excitation) for the last 10 years returns 604,761 hits, of which only ~1.7% are Earth science related. To date, luminescence as a mineral characterisation technique in Earth sciences has been limited due to difficulties in the deconvolution of the complex responses inherent in mineral luminescence due to the complex population of defects they normally contain. Nevertheless, defects within minerals undoubtedly encode information regarding the chemistry and conditions of both genesis and emplacement and so remain of significant interest. With the exception of dosimetry, applications are primarily qualitative and there is a challenge to find additional methods to quantify luminescence.

2 Luminescence

Luminescence is best modelled as a sequential three-stage process; excitation, followed by energy transformation and then finally emission. Luminescence responses as a first approximation can be described in terms of both the intensity and energy of emission. These variations can then also be expressed as a function of the excitation energy and/or intensity, orientation of the incident radiation to the sample, and sample temperature. If luminescence in minerals is sample dependent and experiments are devised to express responses as a function of sample chemistry or structure this could be problematic. The efficiency of individual processes within luminescence can be modelled mathematically, (Fox, 2006) pg. 36-80, which potentially could be used for the quantification of luminescence spectroscopy. The challenge is that luminescence in minerals is typically a complex convoluted signal, comprising of signals from a number of different sources that are frequently competitive within any or all aspects of the process.

The quantification of an individual luminescence signal requires the discrimination, identification and quantification of all competing radiative and non-radiative mechanisms because the quantum efficiency (QE) of the response can be moderated by these competitive processes.

2.1 Luminescence in a Historical Context

Although luminescence has been described since antiquity, our modern understanding has its foundations in the work completed by Stokes (1850) under the rather unfamiliar titles of '*the refrangibility of light*' and '*dispersive reflexion*'. The phenomenon of the

absorption and re-emission of light at a longer wavelength of light was named after Stokes and the magnitude of difference is known as 'Stokes shift'. Table 2-1 provides a few notable events recording the development of our understanding of luminescence.

<i>Date</i>	<i>Source</i>	<i>Phenomenon</i>
1500-1000 BC	Shih Ching	Description of bioluminescence in glow worms
200 BC	Mahabharata (Anon)	Description of bioluminescence in fire flies
384-322 BC	Aristotle in Meteorologia	Description aurora borealis
560-636	Etymologiae of St Isidore	Account of luminous stone 'exposed in the day time becomes impregnated with light'
1602-1604	Vincenzo Cascariolo	Bologna stone first recorded artificial phosphorescent lumiphore
1663	Robert Boyle	Thermoluminescence in diamond
1839	A.C. Becquerel	Described different radiations producing different luminescent responses the strongest in the UV
1852	G. G. Stokes	Stokes shift to longer wavelength luminescent emission
1888	Weidemann & Schmidt	The term 'Luminescenz' (<i>sic</i>) first used

Table 2-1 Chronological list of events illustrating the early development of ideas and concepts surrounding luminescent phenomena source: (Harvey, 1957)

Phosphorescence from the Greek word phosphor meaning 'morning star' has a contemporary colloquial use for describing the afterglow seen in some luminescent samples following the cessation of excitation. The scientific definition describes it as a luminescent emission with a lifetime in excess of $>10^{-8}$ s. The term luminescence was first introduced in 1888 by Wiedemann and Schmidt (1896), which they defined then as "the excess emission over and above the thermal emission background." Wiedemann

and Schmidt defined a number of luminescence sub-categories, firstly photoluminescence excited by visible light was subdivided into fluorescence being 'instantaneous' and phosphorescence being 'afterglow'. They also recognised other types of luminescence differentiated by the nature of excitation detailed in

Table 2-2

2.2 Defining Luminescence terminology

With the advent of instrumental measurement of emission decay, it became clear that all luminescence has a measurable rate of fading (Wien, 1919) also known as the 'lifetime' varying from fs to s in duration. The terms 'fluorescence', 'phosphorescence' and 'luminescence' have varying usage within the literature; for example Nassau (2001) (364-368) is consistent with the Weidemann definition for non-thermal or 'cold light' emissions which he generalises as luminescence. Nassau defines fluorescence as a subset with the property of the 'spontaneous' *sic.* emission of light following exposure to any type of radiation. In addition he describes mechanisms that delay fluorescence emissions from the natural $\sim 10^{-8}$ s, and '*very long periods*' are defined as phosphorescence, i.e. a delayed fluorescence. Phosphorescence is further defined as applying to disallowed emissions from a triplet system as illustrated in Figure 2.1

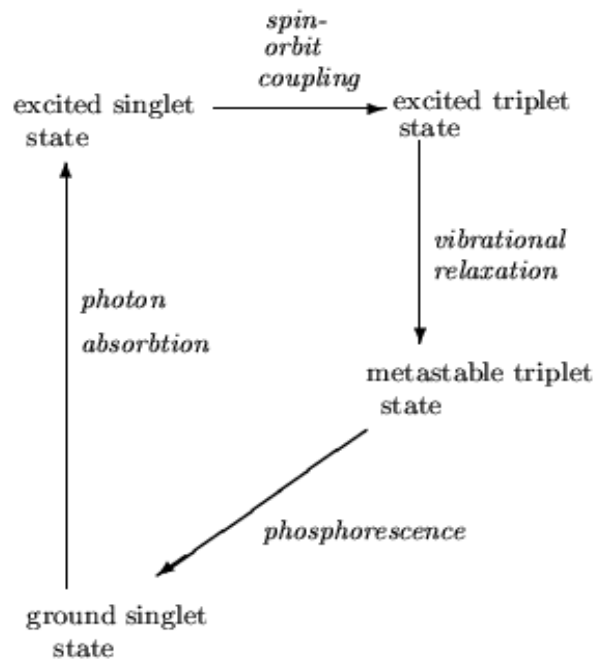


Figure 2-1: The phosphorescent relaxation route of an excited electron through the triplet state. Source: (Nassau, 2001)

Fox (2006) defines fluorescence as “an allowed electron transition” (allowed by electric dipole selection rules) and as being a ‘prompt’ process, whereby the emission occurs “within a few ns of the excitation of the atom”. He discriminates it from phosphorescence, which he defines as “a forbidden electron transition” with a “significant delay in the emission that shows a significant persistence following the ending of irradiation.” Fox does not quantify the time nor differentiate between luminescence and fluorescence. Marfunin (1979) (176-188) uses fluorescence to describe both long and short life emissions. Fluorescence is defined in Klein (2008) (26-28) as the emission of visible light during exposure to UV, X-rays, or electrons and delayed fluorescence (i.e. phosphorescence) is identified as a separate phenomenon. Yen et al. (2007) (26-30) defined luminescence firstly by differentiating luminescence

from organic molecules and inorganic materials. Within the organic environment, they describe the luminescent site as a distinct molecular unit, distinct from, for example, the substitutional ion in an inorganic sample. More importantly, they state that the organic lumiphore can luminesce in isolation from its host environment, whereas in inorganic samples the local atomic environment is an intrinsic aspect of the luminescent process. This means an inorganic luminescent system requires the combination of defect and matrix to luminesce, and separation or isolation from each other de-activates the inorganic lumiphore. Yen et al. defined phosphorescence in the organic environment as the triplet state with a disallowed relaxation transition; in inorganic phosphorescence, they define as emission from a metastable state - in Thermo Luminescence (TL) equivalent terminology is a trap. The definition of a metastable state is an energy level with a 'long lifetime' indicating the local relaxation pathway is forbidden. It is apparent from the above that variations in interpretation and use of the terms are prevalent.

2.3 Clarifying the Use of the Terms Luminescence and Fluorescence

I adopt the following definitions within this thesis:

Luminescence: is the emission of EM radiation (commonly, but incorrectly, considered to be limited to visible light) following many disparate forms of excitation, including, but not limited to, EM radiation that includes the visible and UV portion of the EM spectrum.

Fluorescence: is the emission of light typically, but not exclusively, from the visible range, following excitation only by EM radiation (again typically but not exclusively from the UV into the visible range), with a lifetime $< 10^{-8}$ s.

These definitions overlap, and consequently fluorescence is a subset of luminescence. It is quite permissible to use fluorescence or luminescence to describe fluorescence, the converse is however not true, as there are many luminescent processes that cannot be described as fluorescence, for example cathodoluminescence, the emission of light following irradiation by electrons.

A classification system for luminescence based upon the nature of excitation is summarised in table (2-2). I have included two terms: 'incandescence' and 'thermoluminescence' within the table for completeness, however both could be excluded for separate reasons. Incandescence is the emission of light due to temperature (black body radiation) and is therefore not a luminescent process, whilst in thermoluminescence, because the energy referred to (thermal) is just the mechanism through which the luminescence is released and not the primary source of excitation it is therefore a 'misnomer' in this context.

NAME	DESCRIPTION
Incandescence	Thermally produced blackbody or near black body radiation
Luminescence	All non-thermal light production
Fluorescence	Rapid luminescence
Phosphorescence	Persistent luminescence from a triplet state / metastable state
Photoluminescence (PL)	Fluorescence induced by UV or visible light
Resonance radiation	Emission of same wavelength, the simplest manifestation of PL
Cathodoluminescence	Light induced by electron interaction with matter
Radioluminescence	Light induced by radioactivity, i.e. energetic radiation or particles (ionoluminescence, X-rays measured during excitation
Thermoluminescence	Luminescence produced by raising temperature of a previously irradiated sample
Ionoluminescence	Luminescence following ion implantation excitation
Candoluminescence	Non blackbody radiation from a flame
Electroluminescence/Galvanoluminescence	Luminescence induced by an electric field or current
Triboluminescence	Luminescence induced by a mechanical disturbance
Crystalloluminescence	Luminescence induced by and during the crystallisation process
Sonoluminescence	Luminescence induced by sound waves passing through a liquid
Lyoluminescence	Luminescence induced by and during the dissolution of a solid
Chemiluminescence	Luminescence induced from released chemical energy
Bioluminescence	Chemiluminescence derived from a biological mechanism

Table 2-2 - Classification of light emission as a function of the source of excitation
Adapted from (Nassau, 2001)

The terms 'recombination' and 'recombination centre' find a mixed usage within the literature. Neither Lakowicz (1999) (1-698) or Gaft (2005) (1-353) make reference to a

recombination centre but instead make limited references to recombination but its use is limited to excitonic electron hole recombination. In contrast, Mckeever (1985) uses both concepts extensively and states '*all TL is a recombination process.*' I have only found a phenomenological description for a recombination centre, its use however appears limited to the TL and optically stimulated luminescence (OSL) communities. Other terms used extensively within the TL and OSL communities is the 'trap', which is used to describe the meta-stable state responsible for the storage of energy capable of activation to produce luminescence. Vij (1998) (272) describes them as:

'Causal impurities and activator atoms in the crystal leading to the appearance of localised energy levels in the bandgap. Some of them are deep i.e. they are located at a considerably distance (sic) from the top of the valance band or from the bottom of the conduction band. Such levels are metastable and play the role of traps for charge carriers.'

In considering a trap not only, the depth of the trap is significant but also its local environment. A trap has a local relaxation transition forbidden, that being either radiative or non-radiative, and is to a greater or lesser extent remote from any suitable energy level (recombination centre) to which the trapped electron/hole could escape. The term remote refers to a physical distance. The lifetime of the trap can therefore be considered a function of the physical distance between the trap and the closest recombination centre, and the depth of the trap is the energy difference between the trap and the bottom of the conduction band.

2.4 Contemporary Understanding of Luminescence

The first coherent modern description of luminescence was provided by Einstein (1916) and is illustrated in (Figure 2-2). In the first section of the cartoon a photon of light is absorbed by an electron promoting it to a higher energy level, and the energy difference between the two energy levels is equivalent to the energy of the incident photon. In the centre section, a photon of light is spontaneously emitted and the energy of the photon is again equivalent to the energy difference between the two energy levels. In the final section, the emission is a stimulated emission, whereby the excited electron is stimulated by the arrival of a second resonant photon to emit, thus producing two photons of identical energy and coherence. This third mechanism is the basis of laser emission that was predicted by Einstein nearly 50 years before the building of the first laser.

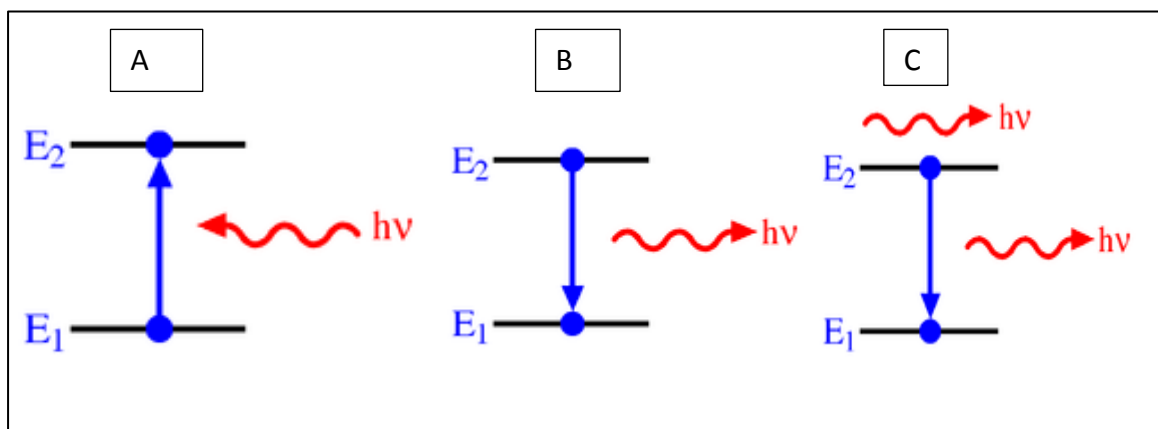


Figure 2-2 Three possible photon electron interactions
From left to right: **A absorption**, **B spontaneous emission**, and **C stimulated emission** The latter demonstrates how an incident photon stimulates the emission of a second coherent photon (the basis of lasing) (Einstein, 1916) illustration from (Commons, 2005).

Luminescence ordinarily involves a change in energy (Stokes shift) which takes place between excitation and emission, in classical terms an increase in wavelength. This is not

represented in the simple description of luminescence (Figure 2-2) as the process describes ground state, inter-band luminescence (demonstrating no frequency/wavelength shift between the absorbed and emitted photon). This type of luminescence is rare, only occurring in relatively very pure materials. It is also difficult to detect as apart from the change in direction of the light there is no change in the frequency to enable the discrimination of emitted photons from excitation photons. Additionally, scattered light (Raleigh scattering) could not be differentiated. Under these circumstances, lifetime theoretically offers a means of differentiation as scattering can be considered 'instantaneous' as it occurs within the time frame of one wavelength of light and retains temporal coherence (Becker et al., 2004). Luminescence emissions in comparison occur over a longer variable timeframe with a consequent loss of temporal coherence (Gaft et al., 2005) (10).

2.5 Energy Transformation

When considering luminescence in minerals, typically a change in energy is involved. The first phase is during the absorption of energy as this interaction takes place at the atomic quantum level with defined quanta of energy being absorbed by individual electrons, normally from the top of the valence band of the semiconductor/insulator mineral. Absorption is a resonant phenomenon that requires the energy absorbed to match the energy difference between the initial and excited state. This absorption of energy and promotion of an electron to an excited, higher energy state is in a normal experiment replicated ~'billions' of times per second. To understand and interpret the phenomena, we need to consider the behaviour of populations, rather than individual

electrons within the sample. If the excitation is monochromatic, i.e. all photons are at a single energy and within a range approaching the band gap, this will likely generate a single excited state population. The extent the energy of excitation exceeds the resonant absorption energy and or the band gap, it would follow the greater the probability for additional interactions that can generate a multiplicity of excited state populations.

Also (Condon, 1926), if the excitation energy is polychromatic (i.e. containing more than one wavelength/energy of photon), it is more likely that multiple resonant absorptions take place, and consequently the possibility for the creation of more than one excited state population increases.

The energy levels to which an electron is promoted is typically to one of the vibrational energy levels of the higher electronic state. From these higher vibrational levels, it will quickly lose energy through thermalisation. Thermalisation is the process of a particle reaching thermal equilibrium and when applied to an electron in an excited state, is the loss of its kinetic energy through interaction (inelastic collisions) with other particles and phonons resulting in the generation of heat (Rethfeld et al., 2002). This relaxation takes place typically in 10^{-12} s or less (Lakowicz, 1999). This 'lost' energy is represented within the 'Stokes shift.' (Vij, 1998)

A second aspect of energy transformation takes place during the spontaneous emission of light. This again is a resonant transition requiring the energy emitted to be equal to the energy difference between higher and lower energy levels. Transitions typically occur between the lowest vibrational energy level of the excited electronic state and higher vibrational states of the lower electronic energy level, or less likely, directly to the ground state (Frank Condon Principal). (Condon, 1926) The relative energy value

differences of the higher vibrational levels and the lower electronic energy level also contribute to the 'Stokes shift'. The consequence of energy transformation is the energy of the emitted luminescent photon normally has a lower energy than the absorbed excitation photon energy.

Another aspect of energy transformation is related to the concept of direct and indirect transitions, where indirect transitions being phonon assisted have an implication for the probability of the event occurring (McKeever et al., 1995) (1-19).

2.6 Lifetime

The natural lifetime of a luminescent emission is defined by the Einstein A coefficient, which is described in section 2.8.2. In an atomic transition, it has a finite value, but in a molecular environment the coefficient is a function of the transition energy, which in turn, is a function of the local electronic environment (Yen et al., 2007) (25-39).

2.7 The Exciton

The exciton is formed as a consequence of a photonic excitation of a semiconductor. Typically, excitons exhibit energy levels just below the band gap, which is the bound state of an electron and hole. The exciton is important as it facilitates energy transfer and the delocalisation of the electron. Excitons become more important in light emission processes at low temperatures.(Yen et al., 2007)(23-24,41-43)

2.8 Quantification

The quantification of luminescence is no trivial challenge and it is important to consider therefore if there are any benefits to be gained, and if any, are they worthwhile. It is also important to consider if any benefits are worthwhile, could they be achieved through alternative techniques. I therefore briefly consider the capabilities of alternative analytical techniques frequently used within the Earth sciences. These are listed in Table 2-3; this should not be considered an exhaustive list. Certain microanalysis techniques such as thermal ionisation mass spectroscopy (TIMS), Secondary Ion Mass Spectroscopy (SIMS), laser ablation inductively coupled mass spectrometry (LA ICPMS) and laser induced breakdown spectroscopy (LIBS) involve micro ablation/breakdown that can cause the loss of temporal/micro structural information.

Acronym	Technique	Sensitivity/ limitations
EPMA	Electron Probe Micro Analysis	Quantitative; elemental; limited low Z sensitivity macro/micro structural
SEM	Scanning electron microscope	Qualitative; elemental; and Macro/micro structure
LA ICPMS	Laser Ablation Inductively Coupled Plasma Mass Spectroscopy	Quantitative; elemental; macro/micro structure
SIMS	Secondary Ion Mass Spectrometry	Quantitative; elemental; macro/micro structure
TIMS	Thermal Ionisation Mass Spectroscopy	Quantitative; elemental; macro/micro structure
XRF	X-Ray Fluorescence	Quantitative; elemental
XRD	X-Ray Diffraction	Quantitative; elemental; average nano structure
UV Vis	Ultra Violet –visible Spectroscopy	Quantitative; elemental; micro structure can be sensitive qualitatively to nano structure
FTIR	Fourier Transform Infrared Spectroscopy	Quantitative; elemental; micro structure can be sensitive qualitatively to nano structure limited by symmetry
Raman	Raman Spectroscopy	Quantitative; elemental; micro structure can be sensitive qualitatively to nano structure limited by symmetry
EPR	Electron Paramagnetic Resonance	Quantitative; elemental; micro structure can be sensitive quantitatively to nano structure limited by electronic structure of outer electrons requires unpaired electron
NMR	Nuclear Magnetic Resonance	Quantitative; elemental; micro structure can be sensitive quantitatively to nano structure limited by magnetic moment of nucleus
CL	CathodoLuminescence	Qualitative; micro-structural but limited to surface detection
SXAS	Synchrotron X-ray Absorption Spectroscopy	Quantitative; micro-structural
STED	Stimulated emission depletion microscopy	High resolution beyond diffraction limits limited to single luminescent emission

Table 2-3 – Popular analytical techniques used within the Earth sciences

From Table 2-3 it is clear that there is no requirement for luminescence to provide an alternative quantitative chemical analysis, as there are many established techniques. However, luminescence has two potential strengths that are poorly represented in the table above; it is a powerful technique for qualitative mapping using Fluorescence Lifetime imaging Microscopy (FLIM) (Becker, 2008) Luminescence a highly sensitivity probe of the nano-structural environment, i.e. luminescence can be sensitive to structural variations and can be considered site selective in the crystalline environment. Many of the techniques above are insensitive to this. Luminescence can also be sensitive to extended defects such as planar dislocations and grain boundaries. (Vij, 1998) (173-178) Within the techniques listed there is only a limited capability to qualitatively or quantitatively analyse the nano-structure and luminescence is highly sensitive to both nano-scale structural defects and their associations. The potential for luminescence is therefore to provide insights into the combined aspects of chemical and associated structure defects. This creates the question: “are there any benefits to be gained from this knowledge?” Here a useful comparison can be made with elemental substitution whose characterisation has proven to be extremely valuable in the interpretation of mineral genesis and emplacement (Burns, 2005) (1-551). I hypothesise the same will be the case for structural defects, and their interrelationships with substitutional defects.

2.8.1 Mathematical Relationships

A prerequisite for the quantification of luminescence requires the mathematical modelling of the processes involved and how these relationships interact. Much work has been completed within many disciplines outside of the geosciences and I will explore how this existing work is applicable to luminescence in Earth science. These mathematic

relationships can be divided into two concepts; the quantum efficiency of the process, and the interrelationship of lifetime and intensity of luminescence.

2.8.2 The Einstein Coefficients

Einstein (Einstein, 1916) described three interactions between an electron within an atom and a photon. He defined each interaction as having a fundamental probability, known as the Einstein coefficients; these can be interpreted as rate functions that are interdependent. The process of absorption can be quantified by the following equation where an electron is excited from a lower energy level E_1 by the absorption of a quantum of energy (a photon) to a higher energy level E_2 :

$$(Fox, 2006)(48-51) \quad E_1 + h\nu \rightarrow E_2 \quad \text{Equation 1}$$

Where: h is Planks constant, ν is the frequency of light Hz, E_1 is the relaxed energy value of the electron in the valence band and E_2 is the lowest energy level of the excited state electron as shown in Figure 2-2 .

For the absorption of light the Einstein B_{12} coefficient is used to calculate the absorption cross section of a material which can then be used to calculate the concentration of a known absorber using the Beer Lambert formulae (Beer, 1852).

$$(Fox, 2006)(48-51) \quad \frac{dN_1}{dt} = B_{12}^\omega N_1 u(\omega) \quad \text{Equation 2}$$

**Where: N_1 is the number of atoms in level 1 at time t
 B_{12}^ω is the Einstein B coefficient $m^3srJ^{-1}s^{-2}$ for the transition for angular frequency of light ω $\omega = 2\pi\nu$ $u(\omega)$ is the spectral energy density in $Jm^{-3} (rad/s)^{-1}$.**

The Einstein coefficient for spontaneous emission, the A_{21} Coefficient, is defined as follows:

(Fox, 2006)(48-51)

$$\frac{dN_2}{dt} = -A_{21}N_2$$

Equation 3

**Where: N_2 is the population of excited state electrons at time t
 A_{21} is the Einstein coefficient for the transition $E_2 \rightarrow E_1 \text{ S}^{-1}$**

The Einstein A_{21} coefficient is the probability for luminescent emission due to the spontaneous relaxation of the excited state electron and the simultaneous emission of a quanta of light as shown in the central section of Figure 2-2 .

The **A** Einstein coefficient can be used to calculate the rate of luminescence or the 'half-life' of the excited state of the lumiphore following excitation. The probability of emission can be an essential aspect for calculating the quantum efficiency (QE) of a luminescent process.

If an electron in a pre-existing excited state is stimulated, emitting a photon due to the proximity of a second resonant photon, this is referred to as 'stimulated emission' and has the same probability as the Einstein B coefficient.

(Fox, 2006)(48-51)

$$\frac{dN_2}{dt} = -B_{21}^{\omega}N_2u(\omega)$$

Equation 4

The emission rate is expressed as a ratio of the B coefficient for the transition to the number of atoms in the excited state N_2 and as a function of time t . Stimulated emission is a coherent quantum mechanical effect in which the photon emitted is in phase with the photon that induced the transition. This type of emission is the basis of lasing.

2.8.3 General Relationship between the Coefficient of Absorption and Emission

Einstein derived a relationship between the Einstein A and B coefficients. This derivation was based upon a body reaching equilibrium in black body radiation, and Einstein deduced that at equilibrium the upward transition rates must exactly balance the downward emissions due to spontaneous and stimulated emission. Therefore from Equation 2, Equation 3 and Equation 4:

$$(Fox, 2006) (51-58) \quad B_{12}^{\omega} N_1 u(\omega) = A_{21} N_2 + B_{21}^{\omega} N_2 u(\omega) \quad \text{Equation 5}$$

Using Boltzmann's law of thermal equilibrium the population ratios of N_1 and N_2 can be derived leading to the relationship:

$$(Fox, 2006)(51-58) \quad A_{21} = \frac{\hbar\omega^3}{\pi^2 C^3} B_{21}^{\omega} \quad \text{Equation 6}$$

This relationship describes transitions in the atomic environment; it cannot be applied in this form to the molecular environment of a mineral.

2.8.4 The Relationship between Absorption and Emission Lifetimes for Molecules

Einstein's derived relationship between the absorption probability, Einstein 'B' coefficient, and the probability of spontaneous emission, Einstein A coefficient, is a relationship related to the 'natural lifetime' of emission (Einstein, 1917). This is strictly limited to atomic systems with sharp transmission lines. Luminescent emissions from the solid state are not discrete sharp emissions but in general broad bands of emission derived from the effects of non-radiative interactions with the matrix. Strickler and Berg (1962) investigated the Einstein relationship to see if a modified form could be derived

that could be applied to a lumiphore in a molecular environment. They derived the following Equation 7 shown below in its most frequently used form.

(Strickler and Berg, 1962)
$$\frac{1}{\tau_0} = A_{u_0 \rightarrow l} = 2.880 * 10^{-9} n^2 \langle \tilde{\nu}_f^{-3} \rangle_{Av}^{-1} \left(\frac{g_l}{g_u} \right) \int \epsilon(\nu) \delta \ln \tilde{\nu} \quad \text{Equation 7}$$

Where $A_{u_0 \rightarrow l}$ is the transition probability coefficient for spontaneous emission from an upper state u to the lower state l, $\langle \tilde{\nu}_f^{-3} \rangle_{Av}^{-1} = \nu_f^{-3}$ is the fluorescence maximum in cm^{-1} , n is Avogadro's number, g_l and g_u are the degeneracies of the lower and upper states, ϵ is the molar extinction coefficient.

Their work showed a good correlation between the measured and calculated fluorescent probability for a number of molecular lumiphore samples, and is widely referenced in fluorescent literature, particularly within the biological sciences, however there has been no similar usage within the geosciences. To explore this discrepancy further I undertook a search of SciVerse Scopus© for all citations between 1934 and 2011 using 'fluorescence lifetime' as the key words and compared this to the associated search using both 'fluorescence lifetime' 'lifetime measurement' within the category of 'Earth sciences'. The results are recorded in. I have only been able to find one example of the Strickler and Berg paper being cited in a earth and planetary science publication. The Strickler and Berg paper was included in 'citation classics' published by Current Contents, and currently has recorded on Web of Science 1605 citations. This clearly demonstrates the comparative lack of use of lifetime within the category Earth and planetary sciences in comparison to other disciplines.

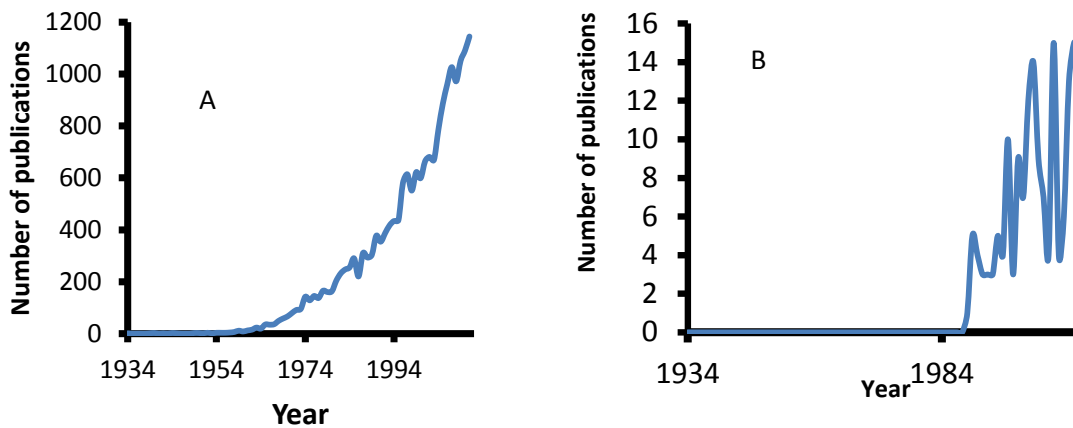


Figure 2-3 - Search of SciVerse©

(A) The frequency of publications including fluorescence lifetime.

(B) Publications within the category of Earth and planetary science combining containing either the words fluorescence lifetime or lifetime measurement. The highest number of citations including geoscience is two orders of magnitude smaller than the total.

2.8.5 Calculating Radiative Transition Rates from First Principles

If the wave functions of the initial and final states can be calculated, the matrix elements of the transition can be evaluated. Then using 'Fermi's golden rule' the transition rate for an individual atom can be calculated.

$$(Fox, 2006)(51-58) \quad B_{12}^{\omega} = \frac{\pi}{3\epsilon_0 \hbar^2} |\mu_{12}|^2 \quad \text{Equation 8}$$

$$(Fox, 2006)(51-58) \quad A_{21} = \frac{\omega^3}{3\epsilon_0 \hbar C^3} |\mu_{12}|^2 \quad \text{Equation 9}$$

A factor to be considered in relation to the analysis above is that the equations would require modification if the levels are degenerate, which for non-hybridised d and p transitions would be the situation, commonly found in minerals.

An alternative version of Equation 9 in a semi-classical format is:

$$A_{21} = \frac{8\pi h}{\lambda^3} B_{12} = \frac{1}{\tau_n}$$

Where τ_n is the natural lifetime of the emission, i.e. in the absence of any quenching process, λ nm the wavelength of the absorption emission, h Planks constant, A_{21} and B_{12} the Einstein coefficients of fluorescence and absorption respectively, with units of s^{-1} .

The most significant concept to note from this equation is that the probability of fluorescence is proportional to the third power of the transition wavelength. This illustrates a first order approximation that the greater the energy of emission the shorter the lifetime of the emission. This semi-classical equation also illustrates the potential that from a measured absorption coefficient the probability of emission can be derived.

2.8.6 Quenching

Quenching is seen frequently to affect luminescence in minerals and the effect in some cases is to eliminate luminescence altogether. Quenching is also described as non-radiative relaxation.

2.8.7 Spin Selection Rule

Within a model of luminescence, an important quantum effect that requires consideration is the 'selection rules'. Absorption or emission in its simplest form can be considered as the interaction of the oscillating field of EM radiation with a transition dipole of an optically active centre. The dipole has a magnetic orientation in three dimensional space described by quantum number m , then depending on the polarisation and direction of the incident EM radiation the fields are capable or not of interaction. This capability, m , to interact is represented in Table 2-1 and mathematically represents the description above. If a dipole has zero ' m ' value in a particular orientation ' z ', the probability of an interaction with EM radiation oscillating in the ' z ' orientation is zero. The rules apply to the quantum numbers of the initial and final states and apply equally to both absorption and emission transitions. The ' s ' quantum number describes the spin of an electron; as EM radiation does not interact with an electron's spin a change in the ' s ' value is a forbidden transition as detailed in the table (Yen et al., 2007). (10,13,28) The selection rule relating to the ' l ' quantum number is described in the next section as the Laporte rule, the m_s relates to the transition rules between higher order transitions for example between a magnetic dipole and electric quadrupole. These additional rules are detailed in Table 2-4

<i>Quantum Number</i>	<i>Selection Rule Changes</i>	<i>Polarisation</i>
L	$\Delta l = \pm 1$	
M	$\Delta m = +1$	Circular: σ^+
	$\Delta m = -1$	Circular: σ^-
	$\Delta m = 0$	Linear: z
	$\Delta m = \pm 1$	Linear: (x,y)
S	$\Delta s = 0$	
M_s	$\Delta m_s = 0$	

Table 2-4 - Electric dipole selection rules for single electron atoms
Source: (Fox, 2006) (54).

The z-axis is usually defined by the direction of the applied magnetic or electric field. The rule Δm for circular polarisation applies to absorption and the sign is reversed for emission. The rule for Δl derives from the spherical harmonic functions. It is consistent with the parity rule because the wave functions have parity $(-1)^l$. The Δm rule is derived from the knowledge that σ^+ and σ^- circularly polarised photons carry angular momenta of \hbar^+ and \hbar^- respectively along the z axis, and hence m must change by one unit to conserve angular momenta. For linearly polarised light along the z axis the photons carry no z component of momentum implying $\Delta m=0$, while x or y polarised light can be considered an equal combination of σ^+ and σ^- photons giving $\Delta m=\pm 1$. The spin selection rule deriving Δs follows from the fact that the photon does not interact with the electrons spin (Fox, 2006).

2.8.8 Laporte Selection Rule

There must be a change in the parity (symmetry) of the complex defined through the terms: **g** - gerade-even-orbital has a centre of inversion, **g** lumiphore transition with a centre of symmetry **u**- ungerade-odd-orbital has no centre of inversion, **u** lumiphore transition without a centre of symmetry electric dipole transition can occur only between states of opposite parity. (Fox, 2006)

Laporte-allowed transitions are $g \rightarrow u$ or $u \rightarrow g$

Laporte-forbidden transitions: $g \rightarrow g$ or $u \rightarrow u$



Figure 2-4 Laporte states used to define allowed and disallowed transitions.

A simple application of the Laporte rule would be the transitions between p and d orbitals that are disallowed because of the Laporte rule. Atoms in a molecular environment apply the principle of the centre of symmetry to the molecule. The rule can be weakened through 'disruption' of the centre of symmetry through the Jahn Teller effect or asymmetric vibrations of the crystal matrix (Jahn and Teller, 1937).

2.8.9 Hund's Rule

Allowed transitions: singlet \rightarrow singlet or triplet \rightarrow triplet

Forbidden transitions: singlet \rightarrow triplet or triplet \rightarrow singlet

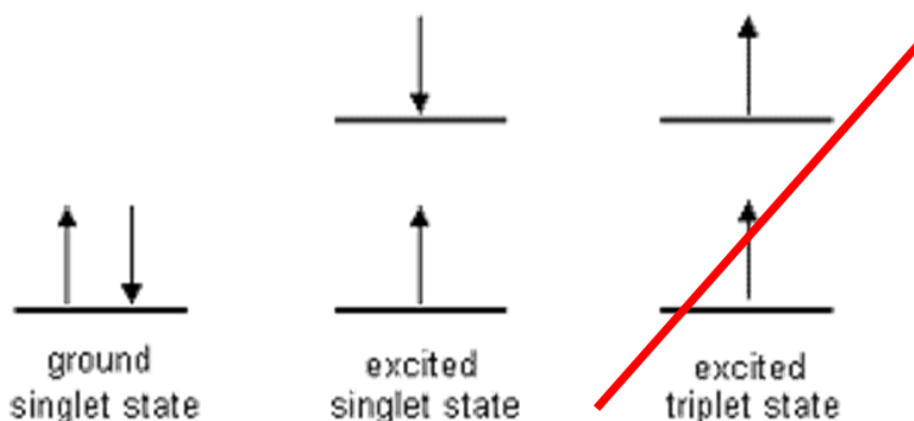


Figure 2-5 - Allowed and disallowed spin distributions. (Fox, 2006)

The application of Hund's rules, also known as the rule of maximum multiplicity, is relevant for allowed transitions. It relates to the distribution of electrons according to their spin angular momentum (S). There are also two further rules, one relating to orbital angular momentum (L), and another relating to total angular momentum (J). (Fox, 2006) (54-56) All the rules are involved in determining the lowest energy configuration.

2.8.10 Expanded Descriptions and Definitions of the Luminescent Processes

A diagram used to describe luminescence in the molecular environment that better fits the complexity of many luminescent transitions is shown in Figure 2-6 which incorporates the intervening energy transfer mechanisms in terms of vibrational relaxation, internal conversion, and intersystem crossing. In this cartoon the wavelength of emission can be seen as a function of the band gap energy, E_g , shown on the

illustration as the energy difference between S_0 and S_1 , the energy difference between the valence and conduction band in a semi-conductor, and the extent of vibrational relaxation in the excited state known as the Stokes shift. These relaxation processes not only affect the peak wavelength of emission but also the line width or 'broadening' of the emission. This relaxation is a measure of the interaction between the lumiphore and the host matrix. The relationship is demonstrated using the example of REE emissions, which tend to display narrow emission bands displaying only limited broadening due to the shielding of the excited electrons by surrounding orbitals.

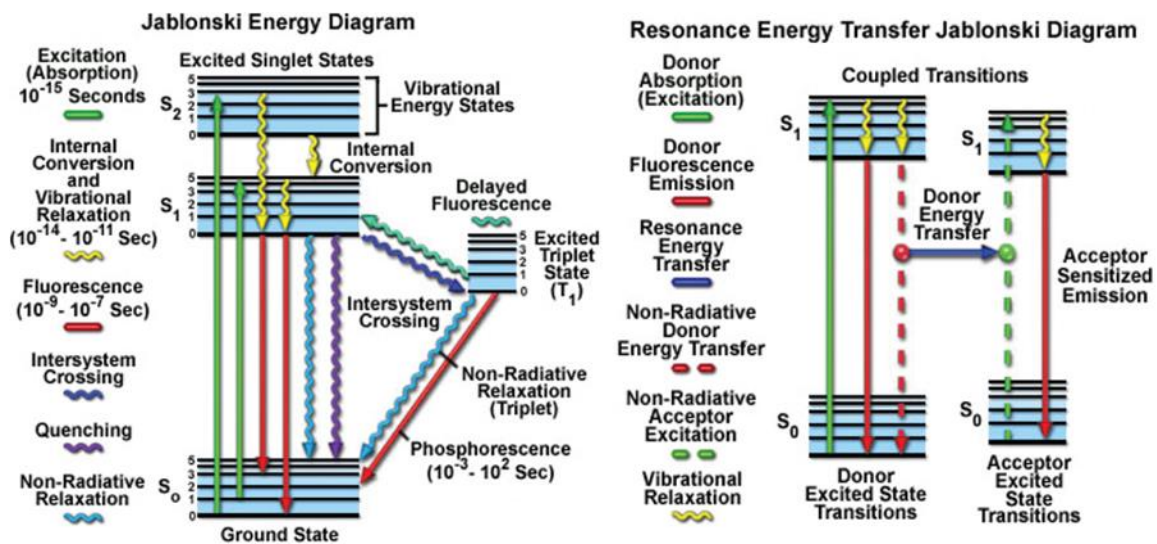


Figure 2-6 - Jablonski energy diagram showing the different energy exchange mechanisms involved in luminescent processes.

Source: (Johnson, 2012)

This fuller explanation is however still inadequate to describe the typical luminescence seen in minerals. Minerals in general have a large band gap with values frequently >5 eV, which exceeds the energy range of visible light and yet visible light fluorescence is frequently seen. It must therefore be that for fluorescence detected in the UV to near IR range, energy levels must exist within the forbidden zone allowing energy gaps smaller

than the intrinsic band gap and of a magnitude equivalent to visible light $\sim 750\text{-}400\text{ nm}$ ($\sim 1.65\text{-}3.1\text{ eV}$). Therefore, a more accurate description of fluorescence in minerals would be as illustrated by the relationships and interactions with the energy levels in the band gap as seen in Figure 2-7. The splitting of energy levels is an important aspect of both the energy of emission and the lifetime of the emission. The influence of local environment and coordination is intrinsic.

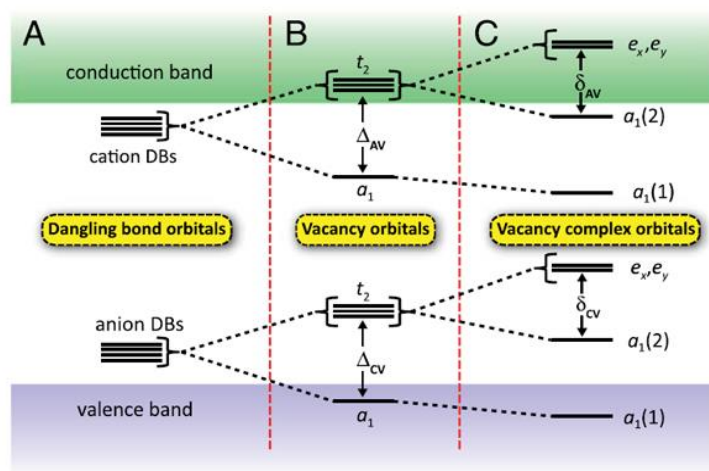


Figure 2-7 - Band gap energy diagram showing the behaviour of different defect types with energy levels in the forbidden zone and the energy splitting effects of the lattice coordination. This shows the mechanism by which energy differences lower than the intrinsic band gap energy are generated diagram, energy splitting and defect types (Awschalom, 2012, Becker, 2005, Weber et al., 2010).

2.9 Intrinsic and Extrinsic Luminescence

A further way to define luminescence is through the classification or description of the lumiphore. Intrinsic luminescence and extrinsic luminescence are two terms used to define the source of luminescence in a material. Intrinsic luminescence is defined as a luminescence signal derived from the matrix material, but a question of whether this definition includes inherent structural defects such as Schottky, Frenkel and dislocation

defects is ambiguous within the literature. Extrinsic luminescence involves the incorporation of additional/replacement atoms/ions into the matrix material and possibly includes defects from absent or displaced matrix atoms. A comprehensive description and discussion of the implications is provided in Vij (1998).

2.10 Energy Transfer

Processes involved in luminescence following excitation can be modelled in many ways but to consider the system following excitation as being in non-equilibrium is helpful in understanding the range of subsequent transactions. Non-equilibrium free energy carriers (electrons and holes) are generated in bulk semiconductor materials by the absorption of electromagnetic radiation and irradiation with high-energy particles. After the generation of the carriers has ceased, the system returns to equilibrium through a number of processes including the annihilation of the electron-hole pairs by recombination, a major source of luminescence. In the case of X-ray excitation following the generation of a core hole and the production of either a localised or de-localised excited electron, the core hole relaxes rapidly ($\sim 10^{-15}$ s)(Bunker, 2010) (33) either emitting a high energy X-ray photon or with a greater probability the release of an Auger electron. The released Auger electrons then typically proceed through a series of inelastic scattering events generating secondary electrons and holes in the outer electrons. These processes in turn generate energy cascades that populate any luminescent defects present in the structure that then emit optical photons through their subsequent spontaneous emission. (Bunker, 2010) (1-36)

Another concept to be considered is that the promotion of an electron to an excited state creates an electron hole in the valence band. In large band gap semiconductor

minerals (the majority), this hole and electron will have a strong tendency to associate to form an exciton. The exciton is the coulombic coupling of an electron with a hole, which acts as a neutrally charged particle and shows great mobility within the crystal lattice. The exciton is classified into two types: the Wannier-Mott (Wannier, 1937) and the Frenkel, which can be differentiated by the extent of delocalisation. The Frenkel exciton is typically found in materials with a low dielectric constant where the coulombic attraction between the two particles is strong and dominates. (Frenkel, 1931) It therefore has a small radius and can be considered localised and with a binding energy of between 0.1-1.0 eV. The Wannier-Mott exciton occurs in semiconductors with a larger dielectric constant, which reduces the effect of the coulombic attraction through electric field screening. This tends to allow the Wannier-Mott exciton to have a much larger radius and behave as a delocalised particle with a much lower binding energy, typically ~ 0.01 eV. Minerals typically have Wannier-Mott excitons, whilst charge transfer excitons primarily occur in ionic crystals and can be considered similar to the Frenkel exciton but with a slightly larger radius (Gaft et al., 2005). This can be of particular importance when considering energy transfer mechanisms in a donor/acceptor luminescence mechanism. It is worth noting that excitons can also exist on surfaces and interfaces where the hole is contained within the matrix and the electron exists above the surface (Lagois and Fischer, 1976). The behaviour of the exciton and the energy transfer it allows is different and needs to be differentiated from three other energy transfer mechanisms, which are discussed below, namely Trivial, Förster, and Dexter.

2.10.1 Trivial Energy Transfer

Trivial energy transfer is a two-step process involving the emission of a photon followed by the re-absorption of the photon at a different site. Trivial energy transfer is also known as radiative energy transfer and is defined Table 2-5

<i>It is normally limited to a radius $R > 10$ nm</i>
It is a two-step process
$D^* \rightarrow D + h\nu$
$h\nu + A \rightarrow A^*$
Requirements
Quantum efficiency of D donor is high
High density of A acceptor molecules in emission path
High absorption coefficient of A
Spectral overlap between emission of D and absorption of A
Implications
No variation in lifetime τ of D^*

Table 2-5 List of the features and requirements for trivial energy transfer where D is a donor site facilitating the initial absorption and A is an acceptor site absorbing the emission from the Donor site facilitating the luminescent emission from the acceptor. The * symbol indicates the excited state.

2.10.2 Förster (Singlet) Transfer

There is a radiationless version of the trivial energy transfer mechanism where $(D^* + A) \rightarrow (D + A^*)$, where D^* exhibits radiationless relaxation and A^* exhibits excitation without absorption. D and D^* , A and A^* are relaxed and excited states of electrons with the * denoting the excited state with the energy levels being contained within the forbidden zone as described by Cleave (1999). This radiationless energy transfer mechanism does not involve the emission of light from the donor and the mechanism of energy transfer is

the Coulombic interaction of the dipoles of the two centres. The dipole movement in the donor creates an oscillating dipole, which in turn induces an alternating electric field, and this oscillating electric field in turn induces a dipole in the acceptor molecule. This mechanism requires resonance between the two dipole moments. This creates coupling via a dipole – dipole interaction thereby creating the route for energy transfer.

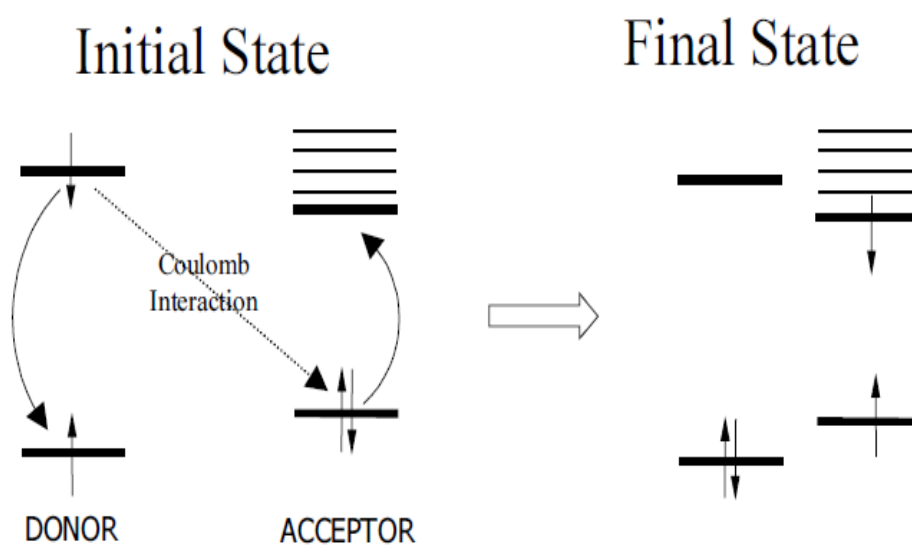


Figure 2-8 Donor acceptor interaction.(Yen et al., 2007)

Unlike trivial transfer, Förster transfer is effectively a competitive relaxation to spontaneous emission for the donor site, and therefore modifies not only the QE of a donor, but also the measured lifetime τ of the donor emission. This has implications for the measurement of both intensity and lifetime, as these values would vary if the donor site has a competitive non-radiative relaxation channel or not. If it only had a single radiative relaxation channel, then it is rate dependent and the non-radiative channel is bypassed for example by a much faster Förster transfer rate.(Förster, 1948) Förster identified that the resonance conditions for energy transfer are related to the overlap of

the emission and absorption spectra, even though the energy transfer mechanism involves neither emission nor absorption. Förster also determined the relationship between the probability of energy transfer and the distance between the donor and acceptor sites.(Förster and Hoffmann, 1971)

(Vij, 1998)

$$k_{ET} = \frac{1}{\tau_D} \left(\frac{R_0}{R} \right)^6$$

Equation 11

Where k_{ET} is the rate constant for the resonance energy transfer, τ_D is the lifetime of the excited state of the donor, and R is the mean distance between the centres of the donor and acceptor dipoles. R_0 is a constant called the critical separation for a given donor acceptor pair corresponding to the mean distance between the donor and acceptor dipoles for which energy transfer from donor to acceptor and luminescence from donor are equally likely. R_0 is related to the acceptor through the following equation:

(Vij, 1998)

$$R_0 = \frac{3000}{4\tau n[A]_{1/2}}$$

Equation 12

Where n is Avogadro's number and $[A]_{1/2}$ is the concentration of the acceptor for which the quantum yield of Luminescence becomes half of its measured value in the absence of the acceptor (Sharma and Schulman, 1999).

Spectra from a biological system showing the spectral responses following the addition of increasing concentrations of acceptor in a solid-state polymer system are shown in Figure 2-9.

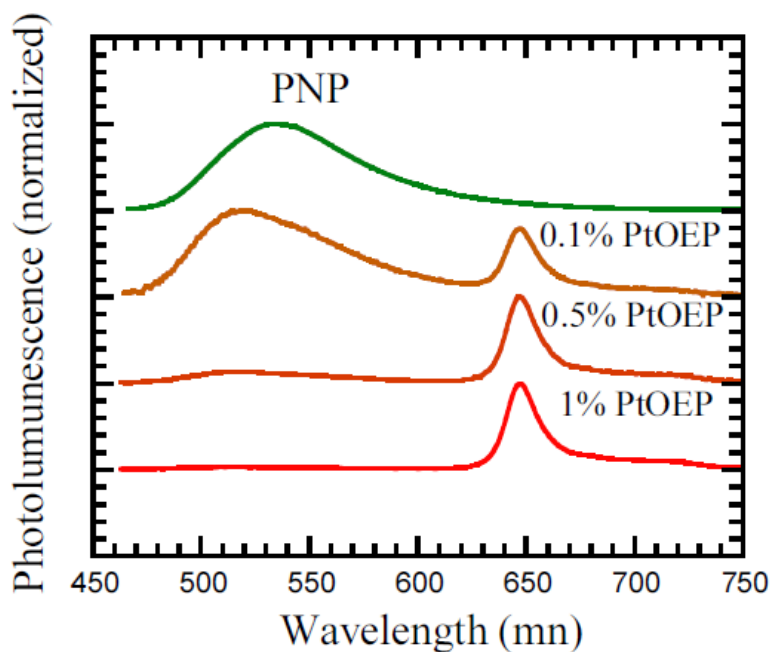


Figure 2-9 The spectral response to the addition of an acceptor molecule to a polymer host.

PNPs are plant natriuretic peptides and a green-emitting lumiphore , and pt-OEP are Pt-octaethyl porphyrin, a red-emitting acceptor Lumiphore (Cleave, 1999).

2.10.3 Dexter (Triplet or Singlet) Energy Transfer

This third energy transfer system is a tunnelling mechanism and requires a spatial overlap between the electronic wave function in donor and acceptor (Dexter, 1953). The mechanism is an electron exchange process where the excited state electron from the donor molecule/atom is exchanged for a ground state electron from the acceptor molecule atom. It can occur simultaneously or in a stepwise fashion (Figure 2-10).

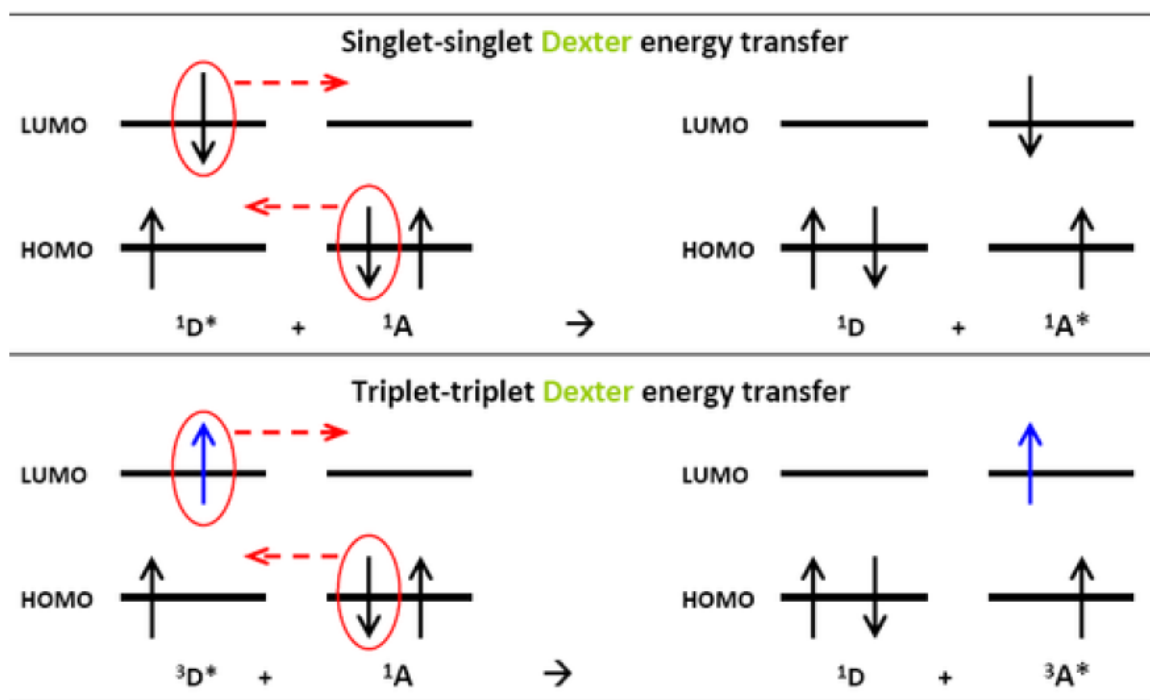


Figure 2-10 Representation of singlet–singlet and triplet-triplet Dexter energy transfer (Vij, 1998) cartoon (Cleave, 1999)

Dexter energy transfer is exponentially dependent on the distance between the donor and acceptor molecules, because the mechanism involves the overlap of the electron's wave function, the electron spin is of no consequence and so the mechanism can also operate in formally spin forbidden transfers between triplet states (Cleave, 1999). The rate constant for Dexter transfer is shown in Equation 13: (Yen et al., 2007)

$$K_D = KJ \exp\left(-2\frac{R_{DA}}{L}\right) \quad \text{Equation 13}$$

(Vij, 1998)

where K_D is the Dexter energy transfer rate, K is an experimentally measured factor related to specific orbital interactions, J is the normalised spectral overlap, integral R_{DA} is the donor acceptor and separation Å, L is the sum of the van der Waals or Bohr Radii (system dependent) (Lucarez, 2003).

2.10.4 Tunnelling

Tunnelling as a mechanism for an electron to escape a trap was first suggested as a phenomenon in minerals by Hoogenstraaten(1958) with a Quantum Mechanical (QM) description. It has its classical counterpart in the evanescent wave. The probability for tunnelling is controlled in the frequently used two-dimensional QM 'particle in a box' description utilising two factors, namely the energy of the trapped electron and the trap depth. This picture defines the trap whereby the walls of the trap are a function of the energy barrier and the physicality of the trap are not considered. In modelling a 'real' scenario, for example the junction tunnelling through a thin film as in a superconducting tunnel junction (STJ) or in the case of a scanning tunnelling microscope (STM), the 'thickness' of the trap walls becomes a physically 'measurable' entity. In the case of the STJ this is the thickness of the insulating material separating the two superconductors or in the case of the STM is the gap between the probe and the sample being measured (Tersoff and Hamann, 1985). Tersoff and Hamann describe tunnelling as being exponentially dependent on distance, whereas Golubov et al. (1995) describe the tunnelling function for STJ to be dependent on not only the distance, but also the 'transparency' of the intermediate film. For the description of tunnelling in minerals neither model is appropriate. For minerals the trap wall thickness is the distance between the trap (donor in these circumstances, the terms donor and trap can be considered equivalent and interchangeable) and acceptor site. This is illustrated in (McKeever, 1985) where he describes the tunnelling relationship between trap and acceptor as being exponentially dependent on distance and that for an energy difference of 3.5 eV between trap and acceptor, the lifetime varies between 10^{-4} seconds for $r = 20\text{\AA}$ to greater than 1 million years for $r = 50\text{\AA}$, where $r =$ distance

between trap and acceptor site. The energy and trap depth remain as factors, but their relative importance reduces as distance increases. The following equation describes the probability of tunnelling as a function of distance between donor and acceptor:

$$(Yen \text{ et al., 2007}) \quad P_{ex}(R) = \left(\frac{2\pi}{\hbar}\right) K^2 \exp\left(-\frac{2R}{L}\right) \int f_D(E) F_A(E) dE \quad \text{Equation 14}$$

Where $P_{ex}(R)$ is the transfer probability as a function of distance, K^2 is a constant with a dimension of energy squared, and L is an effective Bohr radius \AA , an average of D (donor) in the excited state and A (acceptor) in the ground state. $f_D(E)$, $F_A(E)$ represent the D emission spectra and A absorption spectra, respectively.

This relationship could be used for mineralogical research by the application of modelling of the distribution of defect centres. For the purposes of tunnelling in minerals the energy of the electron is simply considered as a function of the sample temperature added to the ground state of the trap; the trap depth is simply the energy difference between the trap and the conduction band, or lowest energy localised band tail. It is also worth commenting that the concept of tunnelling also applies to trapped holes.

2.10.5 Triplet-Triplet Annihilation

Another mechanism for energy transfer is known as triplet-triplet annihilation described by Staroske et al. (2007). This mechanism allows energy transfer between triplet state excited atoms in which atom 1 is excited into a singlet state and through inter-system crossing relaxes into a triplet state if an acceptor atom 2 is in an excited triplet state and is in reasonably close proximity ($\sim <10 \text{ \AA}$) using a Dexter or Förster style energy transfer. Both triplet states are then annihilated producing an excited singlet state and another in its ground singlet state. This usually generates a singlet emission of a higher energy than

the absorption (Figure 2-11, Zhao et al. (2011)). The apparent process of energy transfer is described as ‘ultra-fast’ although the measured lifetime will be controlled by the distance between the two excited states through the Dexter and Förster distance factors (Cheng et al., 2010).

Triplet-triplet annihilation

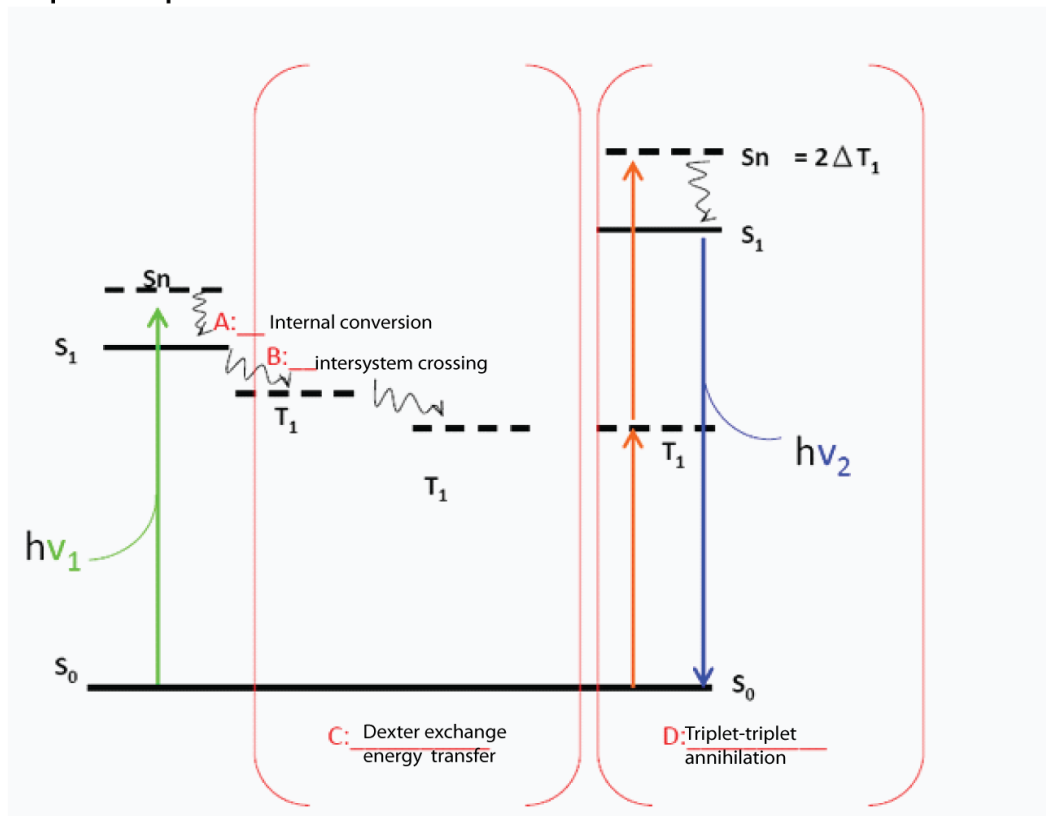


Figure 2-11 Triplet-triplet energy transfer illustrating the two stage process of excitation. - adapted from (Vij, 1998).

From the first stage to a singlet state that relaxes to a triplet state, the second stage is the energy transfer mechanism that promotes an already excited triplet state to a higher energy singlet state that can then emit a higher energy photon through radiative relaxation

2.10.6 Implications for Energy Transfer Mechanisms

The distance between a donor and acceptor site is of critical importance in determining both the QE and lifetime of an emission involving a resonant energy transfer (RET). The QE of the emission will also be dependent on the concentration and spatial distribution of the donor and acceptor sites, and if there is more than one energy transfer mechanism possible, the relative proportions of each mechanism.

2.10.7 Implications of Phonons in Direct Transitions

In luminescent emissions that can be described as 'direct', $\Delta R = 0$ as displayed in Figure 2-12A. Where R is defined as the quantum of change in the momentum of an electron. This is where the primary electronic transition does not require a change in momentum of the electron. In addition to this primary emission, the emission can be coupled with vibronic sidebands. The primary emission is known as the zero phonon line and does not involve the energy of a phonon. The other linked vibronic emissions typically can be described as the energy of excitation less the energy of a phonon. Within this thesis, for the purposes of lifetime measurement, I consider vibronic sidebands where present as discreet, although frequently overlapping in wavelength, with the primary emission ; Wall et al. (1971) described the variation of lifetimes from different vibronic emissions from a common primary electronic emission. Vibronic emissions change the momentum of the relaxed electron.

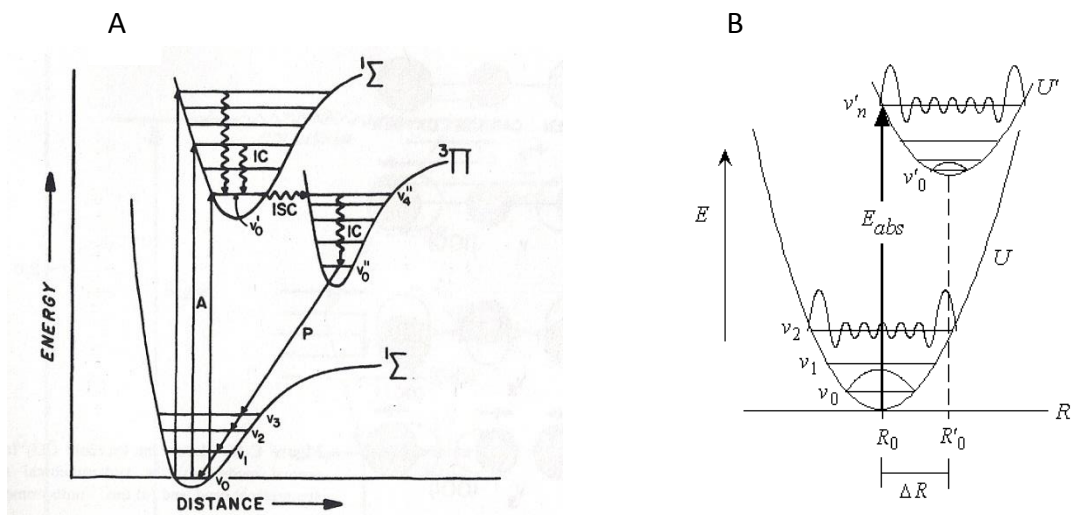


Figure 2-12 - Morse curves

(a) Morse curves with vibrational states showing A- Absorptions IC,- internal conversions, ISC Inter system crossings, P- phosphorescence (adapted from (Beran and Libowitzky, 2004)) Pi π and sigma Σ shown in the diagram differentiate the typical bonds involved in the energy level and are linked to degeneracy.

(b) Morse curves showing the 'R' relationship Implications of phonons in direct transitions.

2.11 Types of Transitions

To understand luminescence I consider it is necessary to classify the nature of the emissive relaxation. I will describe transitions involved in the emission of light, and show how they can be classified in different ways, understanding these classifications helps to interpret both the nature of the emission, and its QE. Many classifications used are derived from luminescence in liquids and gases; although many definitions are also applicable to solids, they can in some cases require modification. For example, the description of Förster resonance in Lacowicz (1999) is based upon molecules in motion within a solution, whereas within a mineral the positions of the lumiphores are considered static.

2.11.1 Direct and Indirect Transitions and their Probabilities

Electrons in a crystalline solid are delocalised in the energy bands, and they therefore have a poorly defined position but a well-defined momentum due to the uncertainty principle. It is therefore more convenient to consider replacing the XYZ spatial axes with momentum axes when considering electrons. This new 'space' is known as 'k' space or reciprocal space. The electron $E(k)$ value when represented in k space produces an energy surface represented by k_x, k_y, k_z . In optical absorptions in crystals, the k value of the electron making a transition does not change because the k value of a photon in the optical region is of many orders of magnitude less than that of an electron. This means that optical absorptions can only take place between states with the same k value. This rule is known as the crystal momentum selection rule or the 'k' selection rule. A transition obeying the crystal momentum rule is a 'direct' transition (Fox, 2006) (Pahaju, 2005). However, in many crystals the top of the valence band and the bottom of the conduction band do not coincide in k space. In this kind of band structure the direct transition to the bottom of the conduction band from the top of the valence band is forbidden due to the k selection rule. The transition can be 'partly allowed' with the assistance of a phonon, i.e. the transition is facilitated by the simultaneous absorption or emission of not only a photon but also an additional phonon. The phonon provides the momentum for the vector change of the electron. This type of transition is known as an 'indirect' transition and has a probability in the range of 3 to 4 orders of magnitude lower than a direct allowed transition. Band to band luminescence only occurs in very pure samples as the probability of transitions involving defects in the forbidden zone is much greater than direct or indirect band to band transitions (Pankove, 1971).

Luminescence in minerals is typically neither direct nor indirect inter band relaxation, as the cross sections, which is the effective area which governs the probability of a scattering or absorption event with larger cross sections having greater probability of occurrence, for such transitions are typically 10^{-21}cm^2 in comparison to the much larger cross sections of defect transitions of 10^{-15}cm^2 . To put these values in context, the typical concentration cross section of defects in an un-doped crystal is 10^{-15}cm^2 to 10^{16}cm^2 . An additional factor to consider is that band-to-band transitions produce emissions outside of the visible and extending through the UV into the VUV. In minerals, the emission is typically from substitutional and structural defects that create energy levels within the forbidden zone. In minerals, substitutional ions from the transition elements and the rare Earth elements (REEs) are commonly involved in substitutional luminescence (Burns, 2005).

2.11.2 The Implications for Extended Defects on Energy Transfer

Surfaces or grain boundaries are regions of unsatisfied or broken valence bonds. These generate energy levels that are unrepresentative of the bulk and thus create an additional source of energy levels within the forbidden band. This feature of surfaces facilitates radiative and non-radiative relaxations. This has implications for the spatial distribution of luminescence in a solid, and has implications for the type of excitation energy. An excitation with a low transmission in a sample would tend to have luminescence dominated by surface emission. The affect is also significantly influenced by the nature of the energy transfer mechanisms; if energy transfer is excitonic then the nature of the exciton, i.e. localised or de-localised, becomes important. Another

important factor would be the probability ratio for radiative and non-radiative relaxation at the surface, which is highly sample dependent (Vij, 1998).

2.11.3 Hole Transitions

The perception of light emission from a mineral is that it is limited to the relaxation of an electron from an excited state to a lower energy level with the energy difference being emitted as a photon. Vij (1998) describes an alternative mechanism involving a trapped hole and a process that involves the thermal release of the hole from a trap that then relaxes from the valance band up to the lowest vibrational energy level of a recombination defect situated in the forbidden band. The energy difference between the top of the valance band and the lowest vibrational energy level of the recombination defect is the energy of the emitted photon. The fact that the hole is relaxing to an apparently higher energy level is counterintuitive, but is explained by considering the simultaneous relaxation of an electron. Alder et al. (1998) reported measuring the time resolved photo luminescence (TRPL) signal of a hole relaxation in a InAs/GaAs quantum dot system, where the measured lifetime of the hole relaxation was 400 ps compared to the electron relaxation of ≤ 50 ps. This process has implications for the quantification of luminescence, in a simple photon event accounting system, if the excited electron emits through a luminescent site then the concept of 'single photon in-single photon out' is affected. Another area for consideration is within the application of dosimetry and dating using TL and the possibility if the wavelengths of a hole and electron emissions were close enough to be measured/counted together. The process of core hole relaxation and emission, particularly through the Auger electron, is well documented but the relaxation of valance holes as an aspect of XEOL has to date not attracted interest.

2.11.4 Thermal Effects on Luminescence

In modelling the effects of temperature on luminescence, firstly a clear differentiation must be made between TL and other thermal effects. TL is a stimulated emission similar to OSL that is modelled as a two-stage excitation; one to populate a 'trap' and the second to allow release from the 'trap' and subsequent emissive relaxation. The effects of temperature on luminescence involve a fundamentally different mechanism that includes the influence of the vibrational energy of the lattice on the transition as displayed in Figure 2-13 (McKeever, 1985, McKeever et al., 1995). It must be remembered that the quantification of quenching requires that this one-dimensional model must be converted into a multi-dimensional model. Reflecting the more complex three-dimensional interaction of the luminescent centre with the lattice and with the incident light. However, from the diagram quenching can easily be explained. In addition, the converse increasing luminescence due to reductions in temperature can be explained using the same mechanism. Reductions in luminescence as the temperature drops beyond a particular threshold can also occur. This can be modelled as in indirect semiconductors, regardless of temperature as there is a momentum difference between the valence and conduction band electrons. This means for a transition to occur there must be a transfer of momentum between the electron and the lattice. The reduction of temperature in a sample beyond a certain threshold reduces the probability of transition due to the limitation of vibrational energy available to facilitate a luminescent transition

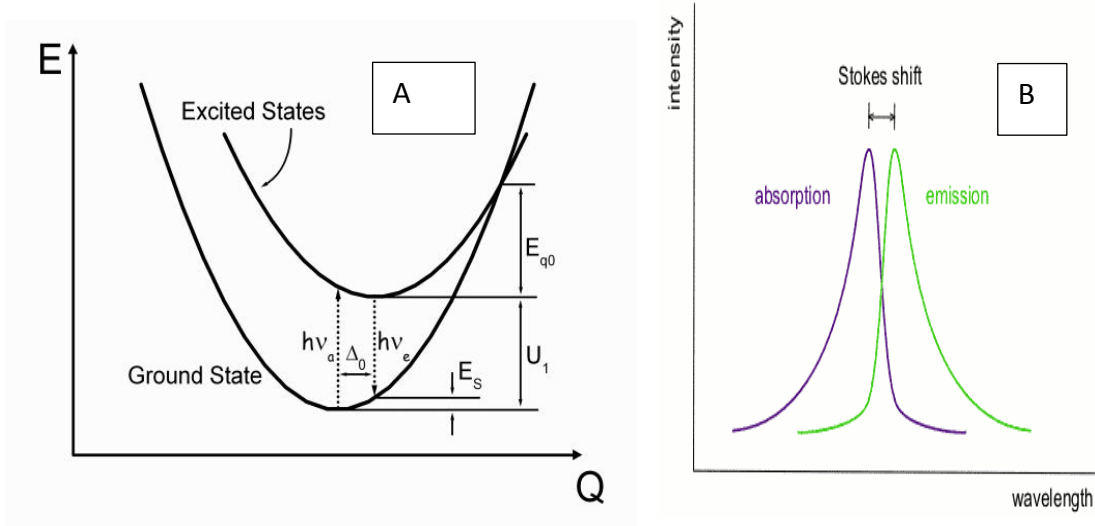


Figure 2-13 - Stokes shift

Left A: Schematic configuration coordinate diagram where Δ_0 is the relative displacement of the excited state potential well with respect to the ground state $h\nu_e$ is the PL emission energy $h\nu_a$ is the energy of absorption. U_1 is the electronic energy difference between the minimum points of the excited and ground states. Stokes shift is $(h\nu_a - h\nu_e)$, the quenching energy E_{q0} is the energy barrier for the electron to cross non-radiatively from the equilibrium of the excited potential well to the ground states allowing non-radiative relaxation.

Right B: the spectral effect of Stokes shift (Yen et al., 2007)

Typically, temperature quenching occurs at higher temperatures because of the increased probability of non-radiative transition from the luminescence centre and low temperature generates an increase in intensity due to a reduced probability of non-radiative transition. It is possible to model the temperature sensitivity in luminescence using the effects of crystal field coordination coupled with vibronic influences. This model allows for great flexibility and for this reason some commentators question the veracity of the interpretations (Leverenz, 1968). Typically, peaks shapes are narrower at lower temperatures; they also show a tendency to display a shift in energy as a function of temperature (Lakowicz, 1999). The luminescence decay lifetime can also alter at low temperatures, for example, in calcite the Mn^{2-} peak has measurably shorter decay times at lower temperatures (Macrae and Wilson, 2008, Mason et al., 2005). Alternatively,

Canzanelli (1999) found that below a certain low temperature threshold, the QE of luminescence reduces significantly as a function of even lower temperatures

2.11.5 Hot Luminescence

Hot luminescence is the relaxation of a 'hot electron', an electron that has not fully thermalised following absorption, to a vibrational level of the electronic level. Table 2-6 lists typical transition times for energy conversion transfer mechanisms involved in the luminescent process.

<i>Transition</i>	<i>Process</i>	<i>Rate constant</i>	<i>Timescale (seconds)</i>
S(0)→S(1) or S(n)	Absorption (excitation)	Instantaneous	10^{-15}
S(n) →S(n)	Internal conversion (ic)	K(ic)	10^{-14} to 10^{-10}
S(1) →S(1)	Vibrational relaxation (vr)	K(vr)	10^{-12} to 10^{-10}
S(1) →S(0)	Luminescence (f)	K(f)	10^{-9} to 10^{-7}
S(1) → T(1)	Intersystem crossing (pT)	K(pT)	10^{-10} to 10^{-8}
S(1) →S(0)	Non radiative Relaxation Quenching (Knr) (Kq)	K(nr) or K(q)	10^{-7} to 10^{-5}
T(1) →S(0)	Phosphorescence (Kp)	K(p)	10^{-6} to 100
T(1) →S(0)	Non radiative relaxation Quenching (Knr) (KqT)	K(nr) or K(qT)	10^{-6} to 100

Table 2-6 Typical energy conversion/transfer times involved in the luminescent process. Source (Vij, 1998)

It can be seen from Table 2-6 that 'hot luminescence' must take place in the very short period following excitation, between $\sim 10^{-12}$ to 10^{-10} s. This raises a question as to whether 'hot luminescence' is more likely when using X-ray excitation in comparison to PL, because X-ray energy generates large populations of 'hot electrons' unlike laser induced PL which generally uses excitation energies close to the band gap energy. Hot

luminescence would display shorter wavelength emissions than the comparable lowest energy level emissions. These shorter wavelength emissions would also be limited to the time window immediately after the excitation pulse and will aid identification.

2.11.6 Quantum Efficiency

Inherent in the study of luminescence is the concept of QE. In the simplest scenario, a simple photon absorbed and then re-emitted could be described as having a QE of 100% but this would be ignoring the Stokes shift energy absorbed. Measuring the QE of luminescence is complex and can be achieved using a number of different techniques and metrics. An alternative to the photon-in photon-out 'scenario' could be the measure of total energy in compared to total energy out, however this measure ignores multiple photon events and due to Stokes shift would mean that 100% efficiency could never be measured. This measure also reduces in meaning as the energy of excitation exceeds the band gap as the probability of multiple events increases. The other factor that makes all measures of efficiency in luminescence complex to measure is the intrinsic temporal dimension of the phenomenon. These issues are reviewed in Vij (1998). Among the many factors, affecting the QE of luminescence is quenching, which is a competitive non-radiative relaxation. A simple equation to describe the relationship between radiative and non-radiative transitions between two energy levels d_{ji} and d_{ij} is:

$$(Vij, 1998) \qquad d_{ji} = d_{ij} \exp(-E_{ij} / kT) \qquad \text{Equation 15}$$

Where the product of the Boltzmann constant is k, T is time and $-E_{ij}$ is the energy difference between the i and j energy levels.

In an alternative approach in considering the QE of the transition, Φ_f representing the fraction of lumiphores that luminesce given conditions of temperature and environment as a fixed physical constant, the following semi-classical equation can be used:

(Sharma and Schulman, 1999)

$$\Phi_f = \frac{k_f}{k_f + \sum k_d}$$

Equation 16

Where k_f is the probability that an excited state electron will fluoresce, and $\sum k_d$ is the sum of the rate constants for deactivation of the lowest excited singlet state by all the competitive non-radiative relaxation processes

No	Description
1	The frequency of excitation (Wavenumber)
2	The intensity of excitation (Flux)
3	The concentration of absorber/s (absorption cross section) and volume excited
4	The spectral range measured
5	Optical indicatrix in anisotropic medium in relation to excitation
6	The identification and concentration and cross section of quenchers
7*	Sample heterogeneity (defect clustering)
8*	In donor-acceptor systems relative concentrations and spatial distributions
9*	The optical indicatrix in relation to the measurement of the emission
10	The quantum of self-absorption (absorption of luminescent emission by matrix)
11	The extent of secondary and tertiary emissions following self-absorption
12	Phonon distribution (temperature)
13	Negative luminescence (reduction in emission in respect to black body emission) (Stepanov, 1961)
14	Excitation in excess of bandgap (Hot luminescence the emission from an electron still in an higher vibrational state) (Rebane, 1976)
15	Stimulated emission from generation of inverse population due to self-absorption (super luminescence) (Gribkovskii, 1975)
16	Scattering
17	Number and identification of lumiphores contained within medium
18	Non-linear interactions (e.g. multi photon excitation)(Sharma and Schulman, 1999)
19	Total internal reflection
20	Core /Valance Hole relaxation emission (Adler et al., 1998)

Table 2-7 Factors that can affect the QE and lifetime of a luminescent emission.

The QE of luminescence from a more holistic viewpoint is simply defined as the amount of radiant luminescent energy emitted per unit time. However, all the following factors as shown in Table 2-7 would need to be considered for full quantification, and the starred items are unique for crystalline materials.

The temperature dependence of luminescent QE is well documented and can usually be explained by one or more of the other factors influencing the QE of luminescence.

Quenching efficiency is a major factor in temperature dependence, and this concept again emphasises the importance of having a full understanding of the luminescent

process as a prerequisite for quantification. When the TL of feldspar is measured for dating purposes anomalous-fading tests are normally now conducted. The consequence is that if not accounted for in luminescent dating then the age calculation is significantly overstated. For optically stimulated luminescence (Spooner, 1994) in a study of museum feldspar specimens showed that anomalous fading occurred in most. Recently new protocols have been introduced for the dating of Kspar including Multi Elevated Temperature Post IR –IRSL (MET-pIRIR) (Li and Li, 2011, Thomsen, 2012). Regardless not all-fading behaviour has been modelled this issue if explained and modelled robustly could further enhance the use of feldspars in the field of geochronology.

2.12 Comparisons of High-Energy Excitation

Two forms of high-energy excitation (significantly greater energy than the band gap energy) are frequently used within luminescence applications in mineralogy. X-ray excited optical luminescence XEOL and electron excitation cathodoluminescence (CL). CL is best interpreted as a surface phenomenon when used in the typical energies used in cathodoluminescence imaging ~1-30 kV since electron penetration into the sample is only shallow (e.g. nm), whereas X-radiation is generally more penetrative (e.g. mm) and is therefore more representative of the bulk sample, although both techniques have the potential for sample modification. CL requires both a hard vacuum environment and greater sample preparation including conductive coatings for non-conductive samples.

The nature of excitation is significant because for excitation that significantly exceeds the band gap in a semiconductor there is less reliance on resonant absorption, which allows the bypassing of disallowed absorption transitions. High-energy excitation also

allows the probing of emissions not available using traditional PL excitation probing of the hard UV portion of the spectrum.

PL excitation relies upon resonant absorption and the selection of the appropriate excitation energies to excite particular emissions is a significant factor of PL excitation. to induce sample modification, a significant issue for higher energy excitation.

3 Sample Characterisation

The relevance for understanding the chemistry and structure of the samples used to study luminescence has not been discussed directly in the previous chapter. In this chapter, the nature of sample characterisation and its application to luminescence is discussed in this chapter. I discuss and characterise the nature of defects within a crystalline material and also the implications for luminescence. I characterise the samples studied by providing from the literature general mineralogical characterisation, and where appropriate give sample specific detail.

3.1 Why is Sample Characterisation Important?

It is possible to divide the analytical techniques currently used in the geosciences into three aspects, those that are sensitive to the chemistry of the material, those sensitive to the bulk structure and crystallography, and thirdly techniques sensitive to sample heterogeneity and texture, extending from the macro to nano scale. These divisions are not discreet in for example the effects of the chemistry of a sample will affect the crystallography but are created to explore the type of information various techniques can provide. The division implicitly incorporates the effects of both chemistry and structure and their interrelationships. Investigation is through techniques including thin section microscopy, nuclear magnetic resonance (NMR), EPR, TEM, and extended X-ray absorption fine structure (EXAFS described in section 4.1) and various analytical mapping techniques including luminescence.

Luminescence is sensitive to all three of the above divisions, so it could be argued that detailed characterisation for every sample should be completed including all aspects,

however this would be impractical. This apparent conflict must be balanced against the specific requirements in characterising and quantifying a particular luminescent response. It is important to constrain the potential sources of emission and competitive quenching and this is particularly important when trying to identify previously unattributed emissions.

Luminescence centres are described by Barbin and Schvoerer (1997) as most commonly being point defects in a crystal lattice of two types; trace element impurities, and ion gaps (vacancies). They further state that: *'impurities fall into two main type-, transition metals, whose 3d electron configuration is partly filled, and rare Earth elements ions with a 4fⁿ configuration.'* Many centres are difficult to ascribe and , blue luminescence in feldspar for example is the subject of continued debate. The luminescent centre has been attributed to many different causes including Ti⁴⁺ (Geake, 1977, Lee et al., 2007a, Parsons et al., 2008), and defect related (Finch, 1999, Correcher et al., 2007b). Finch and Klein (1999) and Correcher et al (2007a). proposed an oxygen related defect linked to the Lowenstein bridge as the mechanism for the blue luminescence. The UV luminescence has been attributed to mobile alkali ions (Garcia-Guinea et al., 1999).

3.2 Luminescence of a Localised Centre

Many luminescent materials have localised PL luminescent centres that (Parsons et al., 2008) and defect related (Correcher et al., 2007b) can be characterised by their typical electronic transitions. Yen et al. (2007) described a number of typical localised electronic transitions as shown in Table 3.1.

<i>Transition type</i>	<i>Type of centre</i>	<i>Ion type</i>
$1s \rightleftharpoons 2p$	F centre	
$ns^2 \rightleftharpoons nsnp$	Tl ⁺ type ions	Ga ⁺ In ⁺ Tl ⁺ Ge ²⁺ Sn ²⁺ Pb ²⁺ Sb ³⁺ Bi ³⁺ Cu ⁻ Ag ⁻ Au ⁻
$3d^{10} \rightleftharpoons 3d^9 4s$		Ag ⁺ Cu ⁺ Au ⁺
$3d^n \rightleftharpoons 3d^n 4d^n \rightleftharpoons 4d^n$	First and second row transition metal ions	
$4f^n \rightleftharpoons 4f^n 5f^n \rightleftharpoons 5f^n$	Rare Earth and actinide ions	
$4f^n \rightleftharpoons 4f^{n-1} 5d$		Ce ⁺ Pr ⁺ Sm ²⁺ Eu ²⁺ Tm ²⁺ Yb ²⁺ and absorption only for Tb ³⁺
Charge transfer transition	Anion p electron and an empty cation orbital	VO ₄ ³⁻ WO ₄ ²⁻ MoO ₄ ²⁻

Table 3-1 - Localised luminescent centres.

Source: (Yen et al., 2007)

The concept of localisation is of particular importance when considering the potential of OD XAS.

3.3 Types of Defects

Luminescent centres based on defects are of two main types; element substitution and structural defects that can be categorised as described below.

Substitutional defects can be either isovalent and have the same oxidation state as the atom it is replacing or aliovalent where the substitutional atom has a different oxidation state to the atom it is substituting and there is an associated charge compensation mechanism to maintain electronic neutrality. (Klein and Dutrow, 2008) Defect clustering and defect complexes can form that do not directly involve substitution; as illustrated by defect clustering in diamond (Bangert et al., 2009) nevertheless, this can be an

important factor in the behaviour of substitutional atoms. Isovalent substitution is frequently associated with the creation of recombination centres

Luminescent centres can include point structural defects, including site position defects (antisite). An example of this would be a lattice of alternating atoms (A,B) where the local orientation is reversed and A is in the B position and B is in the A position. Another example can be described as a topological defect, as displayed by the Stone Wales effect (Partovi-Azar and Namiranian, 2010). This describes the joining mechanism for two different types of carbon nano tubes that involves the local variations of the unit cell structure, where instead of the six-carbon ring the join utilises a seven and five carbon ring. Vacancies and the associated 'F centre' and interstitial defects, Schottky defects and Frenkel defects are other examples of structural defects.

Luminescence can be the effect of longer-range line defects known as edge dislocations, where a lattice plane terminates inside the lattice creating a line of dislocation, as the lattice restructures around the defect. Another type of extended point defect is a helical dislocation defect, described as a screw defect. Extended defects in crystals generates strain expressed in terms of the Burgess factor (Callister, 2005).

Planar defects include dislocations where a crystal plane has slipped in relation to its adjacent plane leaving a plane of misalignment. Grain boundaries can also be considered as an expression of a planar defect. Antiphase boundaries are a plane with typically a mirror inversion of the ordering, such as in twin plane. Finally, a repeating version of this is the stacking defect that can include a one or two layer-repeating defect. (Klein and Dutrow, 2008)

Examples from all of these categories either individually or in combinations are capable of being instrumental or a significant influence on luminescent responses.

3.4 Interactions between the Matrix and Point Defect Lumiphores

Many defects involve a size mismatch with the substitutional atom's environment thereby changing the surrounding site symmetry and introducing localised strain into the matrix. In addition, aliovalent substitution creates a local redistribution of the electronic structure. These effects can be modelled using techniques like crystal field theory (CFT) (Bethe, 1929) and ligand field theory (LFT) (Schlafer and Gliemann, 1969). Burns (2005) using both CFT and LFT explored the energy implications of the interaction between the symmetry of the atom and the surrounding crystal. CFT is normally used to interpret absorption spectra; however, the changes in energy levels change the dipole moment of luminescence as the same transitions involved in the absorption of light are involved in the emission of luminescence. This leads to the interpretation that not only does crystal field influence the wavelength of luminescent emissions but also the lifetime, generating a new natural lifetime for each new energy level. Another aspect is that crystal field directly affects the absorption cross section of the site, although Burns (2005) discussed the effects of crystal field on the energy of transition and not directly to intensity through changes in the Einstein 'B' coefficient.

The influence of the site of a particular defect within a crystalline structure on both the intensity and lifetime of an emission can be inferred from the above discussion. This has important implications on the potential uses and interpretation of both CW and TR

luminescence spectroscopy in mineralogy. To date, these aspects have not been fully exploited.

3.5 Textural Information in Luminescent Signals

Texture can incorporate both chemical and structural information. Luminescence is an ideal tool to explore this phenomenon.

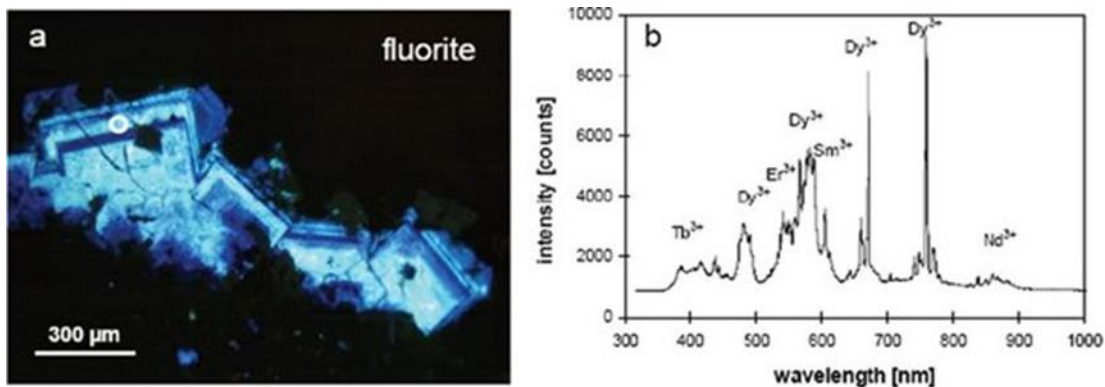


Figure 3-1 (a) The image shows a growth pattern in a volcanic fluorite crystal from Chemnitz, Germany Displays strong oscillatory growth zoning that is only visible under CL. The CL image of crystals of fluorite that can be interpreted as encoding the chemical and temperature history of the genesis of the crystals. (b) The CL spectrum of a distinct green blue zone (as shown by the circle in a) reveals the dominant activation of the luminescence by Sm³⁺ and Dy³⁺ ions source (Götze, 2009).

The interpretation of such phenomena present intriguing potential into magma evolution and element enrichment processes with applications for prospecting. The restraining factor is the complexity of luminescence, and the problem of deconvolution and positive identification, characterisation and interpretation of individual luminescence centres. This is inherently difficult due to the reliance on the correlation between the concentration of the potential lumiphore and the intensity of luminescence that has been implicit in much work completed to date (Dalby et al., 2009).

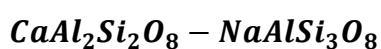
3.6 Feldspar

Feldspar $[(Ca,Na,K)_1(Fe,Al,Si)_4O_8]$ is a framework silicate similar to quartz (SiO_2) which can be considered as an infinite network of SiO_4 tetrahedra combined with AlO_4 .

<i>Name</i>	<i>End member composition</i>	<i>Space group</i>	<i>Tetrahedral order</i>
Sanidine	$KAlSi_3O_8$	$C2/M$	Disordered
Microcline	$KAlSi_3O_8$	$C\bar{1}$	Ordered
High Albite	$NaAlSi_3O_8$	$C\bar{1}$	Disordered
Low Albite	$NaAlSi_3O_8$	$C\bar{1}$	Ordered
p- Anorthite	$CaAl_2Si_2O_8$	$P\bar{1}$	Ordered

Table 3-2 - Chemistry and summary of the crystal structure of the feldspar group end members. (Smith and Brown, 1987)

The substitution of Si^{4+} by Al^{3+} requires a charge balancing coupled substitution that is accomplished using three elements; K^+ , Na^+ , or Ca^{2+} , and these ions reside in the interstitial spaces in the framework. This chemistry determines the creation of a solid solution with three primary end members as illustrated in Figure 3-2. Within the alkali feldspars, the substitution can be considered as a simple solid solution between Na and K, whereas in the plagioclase series the substitution is better modelled as a coupled substitution as described in the formulae below.



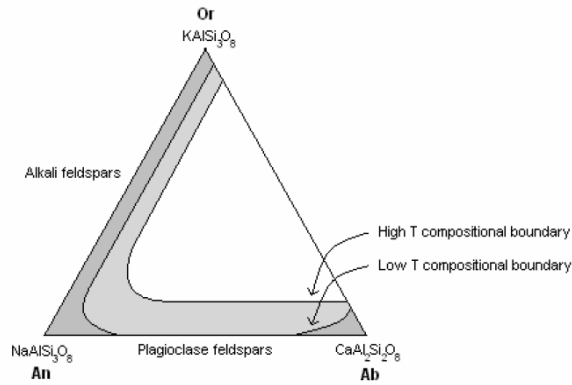


Figure 3-2 - Ternary diagram showing chemical and compositional boundaries in the feldspar group.
Source: (Evans and Grove, 2004).

Figure 3-2 illustrates the chemical differentiation that takes place within the solid solution and the further differentiation that takes place in feldspar according to the temperature of formation. This illustrates that to characterise feldspar correctly, more information than simply chemical composition is required, and an understanding of the internal atomic arrangement is necessary. Many feldspars also comprise of intergrowths of more than one composition, sometimes on such a small scale as to make them undetectable even with a high power optical microscope e.g. cryptoperthite.

Feldspars are defined by both chemistry and structure; feldspars grown at high temperature can be of compositions unstable at lower temperatures and exsolution occurs. Hence, feldspars are frequently intergrowths of two or more feldspar types. The process, which governs the chemistry and structural state of the feldspar formed, are a function of the genesis and geological history of the mineral.

3.6.1 MISI Iron Rich Microcline

The sample MISI is iron rich alkali feldspar that has no provenance, apart from a verbal description that it originated from the USSR. It has the generic formula of $KAlSi_3O_8$ with common trace element impurities of Fe, Ca, Na, Li, Cs, Rb, H₂, O, Pb is triclinic, a non-standard unit cell but by convention classified as $C\bar{1}$, space group ($P\bar{1}$).

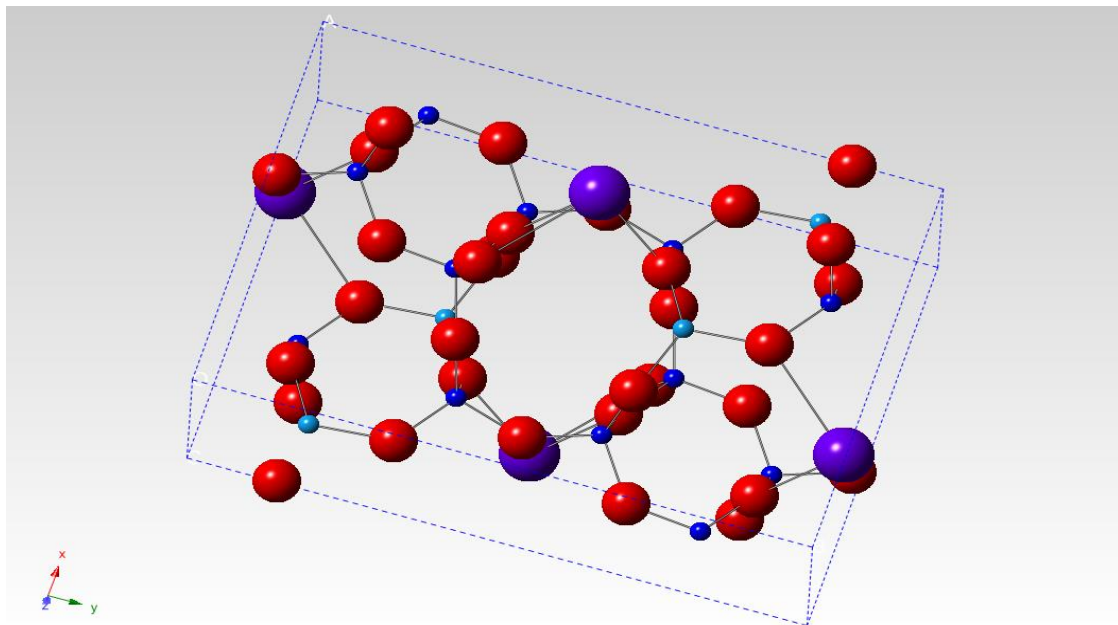


Figure 3-3 - Maximum microcline refinement.

**Pale blue – Al , Red – O, Large Blue –O, Small dark blue - Si
CrystalMaker © data (Brown and Bailey, 1964)**

3.6.2 Cleavelandite

Is a variety of albite with a chemical formula of $\text{NaAlSi}_3\text{O}_8$. It is triclinic ($\bar{1}$) with space group ($C\bar{1}$) and is described as a low albite with warped plates parallel to (010). It should be noted that most albite is low albite.

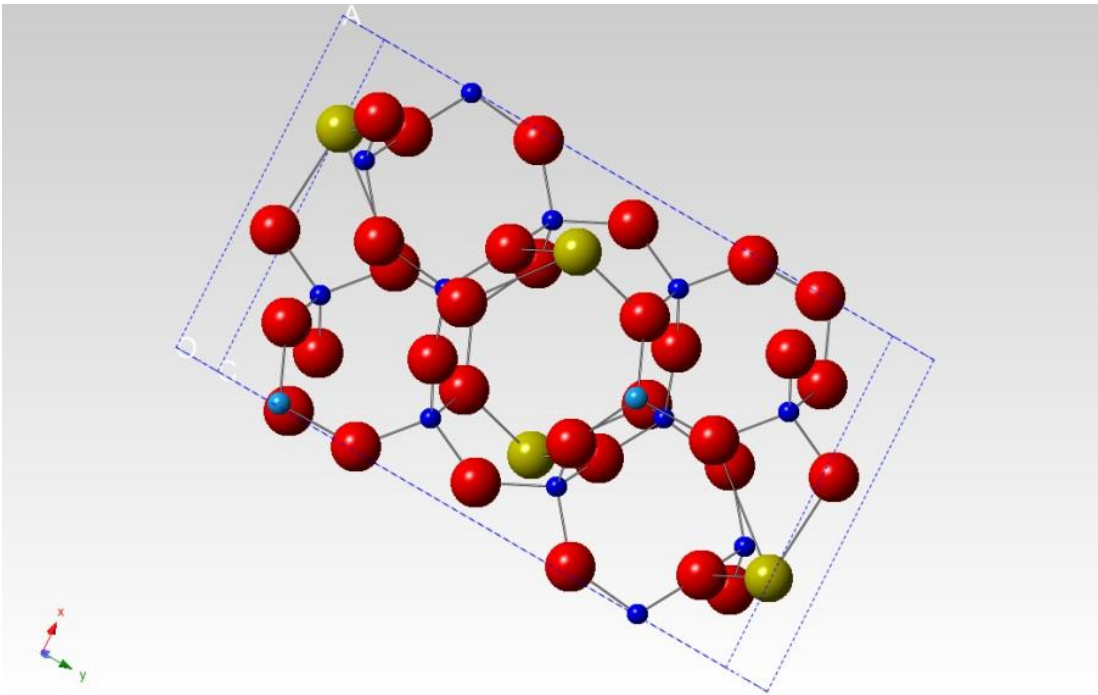


Figure 3-4 - Albite cleavelandite refinement.

Yellow – Na, Red – O Dark blue – Si, Light Blue - Al
CrystalMaker© data (Ribbe et al., 1969)

3.6.3 Moonstone

Moonstone is an alkali feldspar $(\text{NaK})\text{AlSi}_3\text{O}_8$ best described as a microcline, which has a typical composition $\text{Or}_{25}\text{-Or}_{35}$. It is a cryptoperthite with the perthite lamellar comparable in thickness to the wavelengths of light as shown by (Fleet and Ribbe, 1963) and Bollmann and Nissen (1968) using an electron microscope. They also showed the typical adularescence (blue sheen) seen in moonstone is due to the irregular nature of the alternating sheets of orthoclase and low albite that were approximately parallel to $(\bar{6}01)$ to $(\bar{8}01)$. The subsequent interference effects occurred because of reflections from the irregular planes. Further descriptions are contained in (Bollmann and Nissen, 1968, Akizuki and Sugawara, 1970, BACHINSKI and MÜLLER, 1971). Moonstone was selected as a sample to explore if the cryptoperthite lamellar structure of moonstone would be a significant influence on XEOL and TR XEOL emissions.

3.6.4 Copper Bearing Feldspar

Plush Oregon sunstone is plagioclase feldspar, compositionally a labradorite in the range of An₅₀₋₇₀. It shows a moderate to high order and is found in a highly fractionated porphyritic basaltic flow as large phenocrysts where green, red, and yellow to colourless varieties are found, some displaying a 'schiller' (from the German 'twinkle', an iridescence from within the body of the stone) .

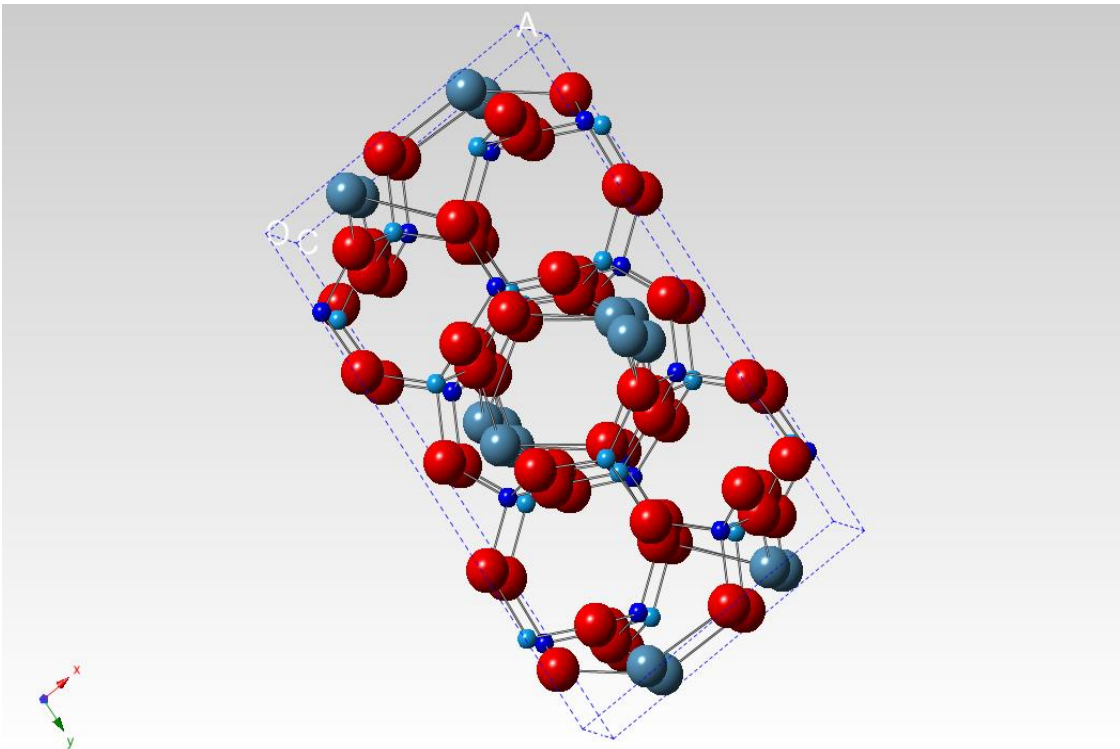


Figure 3-5 - Labradorite refinement.

**Small dark blue –Si, Small light blue - Al, Large light blue – Ca, Red - O
CrystalMaker © data (Angel et al., 1990)**

This copper bearing feldspar is a relatively rare gemstone, found in the Plush region of the state of Oregon in the USA. This gem quality feldspar (commonly known as 'Plush' feldspar) has a copper content in the range 50-500 ppm and is found in a number of varieties including colourless, red, green, and an included material displaying a schiller

from metallic platelets (Hofmeister and Rossman, 1985). In the last decade, significant amounts of copper diffused andesine have entered the commercial gem market imitating the natural 'Plush' material and there is an urgent need to discriminate between the natural and treated material. The commercial treatment/diffusion process used has not been disclosed. The samples investigated include known commercially treated samples and known natural material. I also tested samples I prepared in the laboratories at St Andrews these treated samples included samples of both plagioclase and alkali feldspars. I replicated the treatment process described by Emmett et al (2009) that they considered likely to be comparable to the commercial technique. The process is completed at relatively high temperatures $\sim 1000^{\circ}\text{C}$ with the samples to be treated packed into a refractory medium of powdered ZnO doped with between 1-5 weight % CuO for periods of 24 -168 hours heating taking place in an oxidising atmosphere.

The first description of the natural material was probably Aitkens (1931) who noted the occurrence of a gem quality labradorite, with a similar description to the material currently recovered, the original description was from an 'unspecified locality' in southern Oregon. The geology of the areas currently exploited for 'Plush feldspar' was described by Peterson (1972) that drew upon work completed by Fuller (1917).

Hofmeister and Rossman (1985) produced a comprehensive characterisation of the natural gem material. They concluded that the colouration of the red material was due to the presence of copper, but they were less convinced regarding the source of the green colour, although one suggestion considered was that copper was responsible for both colours and the size of nano inclusions of copper metal determined the colour. A description of the treated material and its entry into the market is included in Hughes

(2010). The current accepted cause of colour in the red plush feldspar is that it is due to either copper substitution or the inclusion of metal nano particles (Hofmeister and Rossman, (1985). The origin of the green colour has not been satisfactorily determined. My research explores both natural copper bearing samples ‘plush feldspar’, and compares them with samples with samples having an artificially induced copper content following diffusion by heat treatment. I completed heat treatment experiments on a suite of feldspar samples representing both alkali and plagioclase members included in

Table 3-3.

<i>Sample ref</i>	<i>Description</i>
RT 1-5, 21, 22, 23, 54, 55, 56, 58, 29, 30, 35, 36 45	Commercially treated Andesine
RT 6,7,15,16,40,42,43,44	Natural occurring Plush Feldspar
RT46	Albite natural colourless
RT47	Bytownite natural colourless
RT48	Microcline natural colourless
RT49	Andesine natural colourless
RT50	Labradorite natural colourless
RT51	Anorthite natural colourless
RT52	Oligoclase natural colourless
RT53	Andesine natural colourless
RT57	Andesine natural colourless
AF1	Cleavelandite natural colourless

Table 3-3 Feldspar samples used in Cu investigation section 5.4

3.7 Gem Quality Samples with Known Absorption Luminescent Centres

A selection of gem quality minerals was determined with known common absorption/emission centres. I postulated that in attempting to prove the system capable of collecting OD XAS, the most likely minerals to display this behaviour in trace element concentrations would be systems where known absorption and emission is through the same defect centre.

<i>Allochromatic minerals</i>	<i>Chromophore element</i>	<i>Chemical composition</i>	<i>Spectroscopic features (nm)</i>
Jade	Cr	Na(AlFe)Si ₂ O ₆	676,686,698,708,718 (ZPL plus phonon bands)
Emerald	Cr	Be ₃ Al ₂ Si ₆ O ₁₈	683,730, 696, 717,728, 738
Grossular garnet	Cr	Ca ₃ Al ₂ (SiO ₄) ₃	611, 489, 713, 690, 694, 698, 707,
Grossular garnet	V	Ca ₃ Al ₂ (SiO ₄) ₃	717
Grossular garnet	Mn	Ca ₃ Al ₂ (SiO ₄) ₃	590
Hiddenite Green spodumene	Cr	LiAlSi ₂ O ₆	'R' lines ~690
Hiddenite Green spodumene	Mn	LiAlSi ₂ O ₆	?
Ruby	Cr	Al ₂ O ₃	'R' lines doublet 693,694
Kornerupine	Cr	(MgFe)4Al ₆ (SiO ₄ BO ₄)5(O,OH) ₂	Yellow /green ?
Alexandrite	Cr	BeAl ₂ O ₄	Polarised (Cr1) 680,694 Cr(2) 678,680 663, 707, 701, 720
Alexandrite	Mn	BeAl ₂ O ₄	664, 689, 720
Sphalerite (green)	Co	(ZnFe)S	?
Sphalerite (green)	Mn	(ZnFe)S	595
Sphalerite (green)	V	(ZnFe)S	450,460,470
Sphalerite (green)	Cu	(ZnFe)S	640
Spinel	Co	MgAl ₂ O ₄	?
Pyrope Garnet	Fe	Mg ₃ Al ₂ (SiO ₄) ₃	?
Pyrope Garnet	Mn	Mg ₃ Al ₂ (SiO ₄) ₃	635

Pyrope Garnet	Cr	$Mg_3Al_2(SiO_4)_3$	694
Chrysoberyl yellow	Fe	$BeAl_2O_4$?
Chrysoberyl yellow	Cr	$BeAl_2O_4$?
Chrysoberyl yellow	Ti	$BeAl_2O_4$?
Chrysoberyl yellow	O*	$BeAl_2O_4$?
Citrine	Fe	SiO_2	Non Observed
Aquamarine	Fe	$Be_3Al_2Si_6O_{18}$?
Jadeite	Fe	$Na(AlFe)Si_2O_6$	739, 796
Jadeite	Ti	$Na(AlFe)Si_2O_6$	439
Peridot	Fe	$(MgFe)2SiO_4$	Non Observed
Tourmaline(green)	Fe	$Na(LiAl)3Al_6(BO_3)3Si_6O_{18}(OH)_4$	700-750
Tourmaline (green)	Cr	$Na(LiAl)3Al_6(BO_3)3Si_6O_{18}(OH)_4$	691, 697, 707
Tourmaline (green)	Mn	$Na(LiAl)3Al_6(BO_3)3Si_6O_{18}(OH)_4$	560-570
Spodumene (pink)	Mn	$LiAlSi_2O_6$	596
Spodumene (pink)	Cr	$LiAlSi_2O_6$	690
Tourmaline green	Mn	$Na(LiAl)3Al_6(BO_3)3Si_6O_{18}(OH)_4$	560,570
Andalusite	Mn	$Al_6Al_5OSiO_4$	Green/yellow
Spinel	Mn	$MgAl_2O_4$	550-612
Emerald	V	$Be_3Al_2Si_6O_{18}$?
Grossular Garnet	V	$Ca_3Al_2(SiO_4)_3$	717
Tsavorite Garnet	V	$Ca_3Al_2(SiO_4)_3$?
Blue sapphire	Fe Ti	Al_2O_3 (charge transfer)	

Table 3-4 Gem quality Allochromatic minerals.

with known emission/absorption centres that are common to both processes, chemistry, and known UV excited emission bands. Chemical formulae from (Webster and Anderson, 1983) spectral assignments (Gorobets and Rogojine, 2002)

<i>Idiochromatic minerals</i>	<i>Chemical composition</i>	<i>Chromophore</i>	<i>Luminescence emission nm</i>
Uvarovite garnet	$\text{Ca}_3\text{Cr}_2\text{Si}_3\text{O}_{12}$	Cr	697,702 Cr 'R' lines
Rhodochrosite	MnCO_3	Mn	Red
Rhodonite	MnSiO_3	Mn	(Mn 625)
Spessartine garnet	$\text{Mn}_3\text{Al}_2\text{Si}_3\text{O}_{12}$	Mn	(Mn) 650 (Cr) 627,606,707,694
Almandine Garnet	$\text{Fe}_3\text{Al}_2(\text{SiO}_4)_3$	Fe	Non observed
Malachite	$\text{Cu}_2(\text{CO}_3)(\text{OH})_2$	Cu	Non observed
Azurite	$\text{Cu}_3(\text{SiO}_4)(\text{OH})_2$	Cu	Non observed

Table 3-5 Gem quality of idiochromatic minerals. with known emission/absorption centres that are common to both processes, chemistry, and known UV excited emission bands. (Gorobets and Rogojine, 2002)

3.8 Zircon

The mineral zircon is classified as a neosilicate with a chemical formula of $ZrSiO_4$; however, the zirconium atom is commonly substituted with a wide range of REEs. These are often described with the following empirical formula to best represent this substitution:



This chemical formula is the empirical formula describing the nature of substitution in Zircon. Zircon is an important mineral in geoscience as it the most popular mineral for radiometric dating, holding the record as having the oldest recorded date of any mineral (Wilde, 2001). Its use for dating comes from a number of reasons; it is 'fairly hard' and resistant to physical wear and abrasion. Its hardness on Moh's scale of hardness varies between 6.5 and 7.5 a function of the degree of metamictisation.

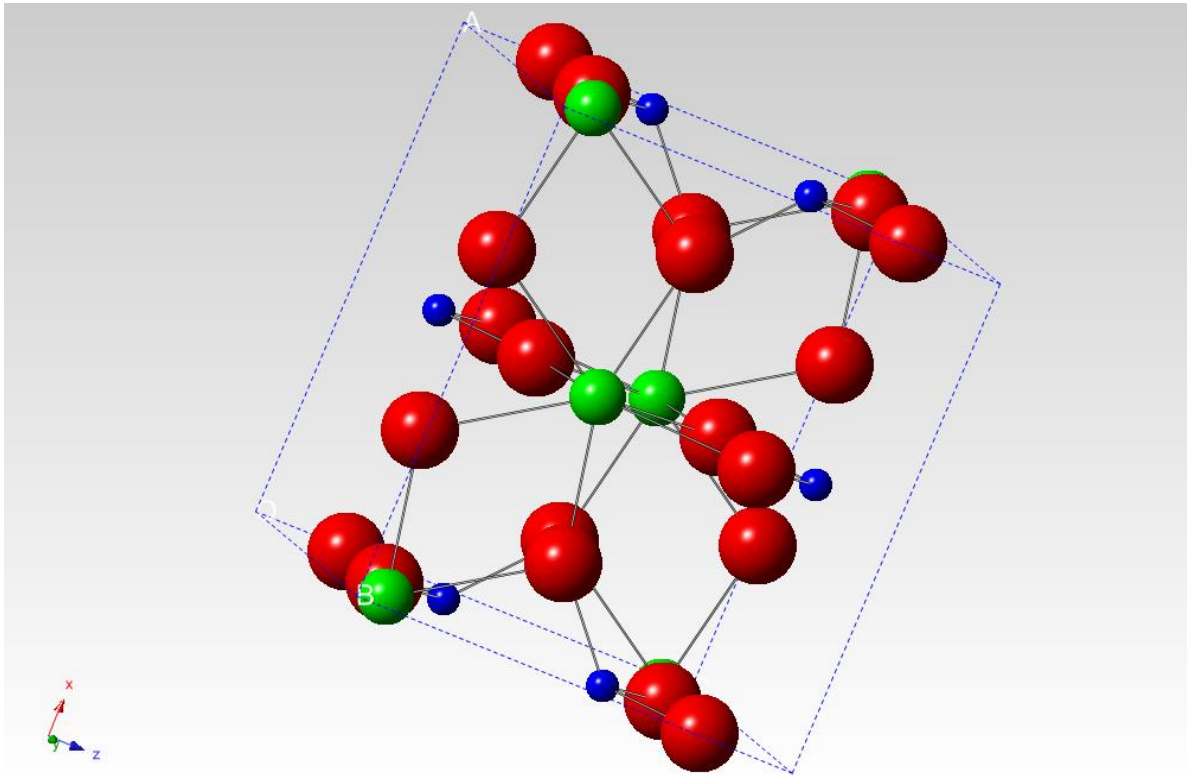


Figure 3-6 - Zircon refinement.
Green – Zr, Red – O, Blue - Si
CrystalMaker © data (Rios et al., 2000)

The mineral is considered chemically inert, and so zircon tends to persist where other minerals are destroyed. It is a common accessory mineral that tends to form in silicate melts rich in incompatible elements; this relationship with incompatible elements has the benefit of facilitating source interpretation. Most importantly from the aspect of dating, uranium readily substitutes into the zircon crystal structure where Pb is highly incompatible, making zircon an ideal mineral for isotopic dating as the 'radiometric clock' starts at zero. In addition, zircon is stable up to $\sim 900^{\circ}\text{C}$ that means in most instances the mineral is in its original form resisting even moderate metamorphic conditions. For accurate dating the maintenance of all the conditions listed above is a prerequisite, this however is not always the case. The need to differentiate suitable from unsuitable zircon specimens is important when applying the dating technique. Currently,

CL is the most used technique to investigate the texture and zoning of zircons. The consequence of using CL is that the zircon needs special preparation, typically a polished cross-section in an acrylic mount. CL imaging techniques have very limited penetration, on the \sim nm scale and must therefore be considered a surface technique only. Electron excitations at low accelerating voltages display no luminescence and this is known as the 'dead voltage'. This phenomenon can be explained by the concentration of broken bonds at the surface allowing a much higher degree of non-radiative relaxation. Dead voltage is known to decrease with conductivity, and so must also be a function of charge build up. In comparison, XEOL with significantly greater penetration, does not show significant surface effects and therefore represents a more reliable technique.

The presence of a radioactive element emitting high-energy particles in zircon affects the crystal structure, creating point defects such as Schottky and Frenkel. For this reason zircon is an ideal mineral with which to investigate a technique sensitive to localised point defects that has the also has the facility for deconvolution of overlapping emissions. An application of this type of investigation is for sample characterisation within the zircon dating community.

3.9 Topaz

Topaz is a fluorosilicate $\text{Al}_2\text{SiO}_4(\text{F},\text{OH})_2$ forming a complete solid substitution between the F and OH cations. Although in nature a maximum of ~30% of the F site is found occupied by OH cations, a synthetic fully hydrated analogue has been synthesised (Wunder et al., 1993). Pure F topaz is orthorhombic as Oh is substituted and the symmetry is lowered to triclinic. Non-orthorhombic $2/m2/m/m2$ topaz shows Piezoelectric and Pyroelectric properties. Topaz in the literature is described as mainly inert to UV excitation. Topaz with higher concentrations of OH is more likely to display luminescence. (Gatta et al., 2006).

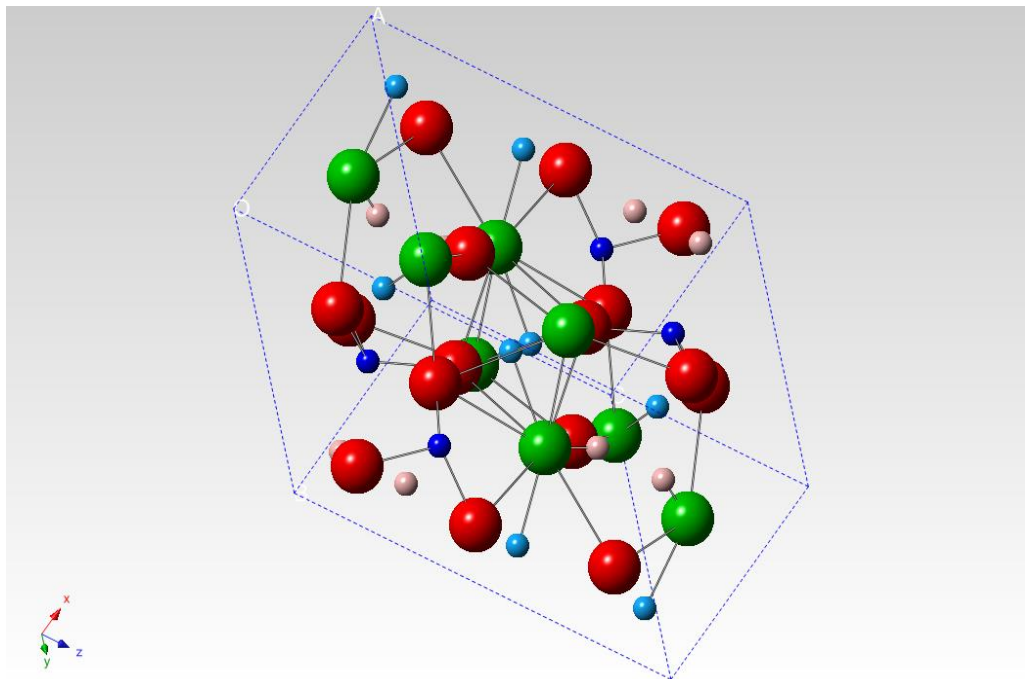


Figure 3-7 - Topaz low OH refinement.
Pale Blue –Al, Red – O, Green –F, Dark Blue – Si Pink - H
CrystalMaker © data (Gatta et al., 2006)

Samples collected by Dr Don Hoover from the Ouro Preto topaz mining area in Brazil where used for this experiment. The samples were divided into two groups: one

showing unusually strong UV luminescence and the second group representing 'run of the mill' material with limited to no-observable UV luminescent responses. Typical examples from each group were then cut and polished to generate three sample blocks, each with three polished faces orientated to be perpendicular to the a, b, c crystallographic axes.

Recently, work completed by Gatta et al. (2006) following the testing of a topaz sample from the Oro Preto region, concluded that the symmetry is always consistent with Pbnm and that the reflections previously reported that violated this could be attributed to the Renninger effect (Renninger, 1937). The authors did not comment on the peizo and pyro phenomena that have previously been linked to the lowering of symmetry.

3.10 Chrome Tourmaline

Tourmaline is a specific variety of the tourmaline group known as chrome dravite and has a generalised chemical formula of $\text{NaMg}_3\text{Cr}_6(\text{BO}_3)_3\text{Si}_6\text{O}_{18}(\text{OH})_4$. It is a trigonal crystal 3M, space group R 3m, typically with Al in a disordered replacement with the Mg.

Described as a cyclosilicate six membered ring with borate, the characteristic green colour is attributed to the presence of Cr and V. Typical substitutional elements found in topaz include F, Ti, Cr, Fe, Mg, Ca, V and Mn, as reported by Schott et al. (2003b). The order state of the F substitution is considered to be of importance by a number of authors. High temperature annealing $\sim 900^\circ\text{C}$ will result in complete disordering (Manning, 1969).

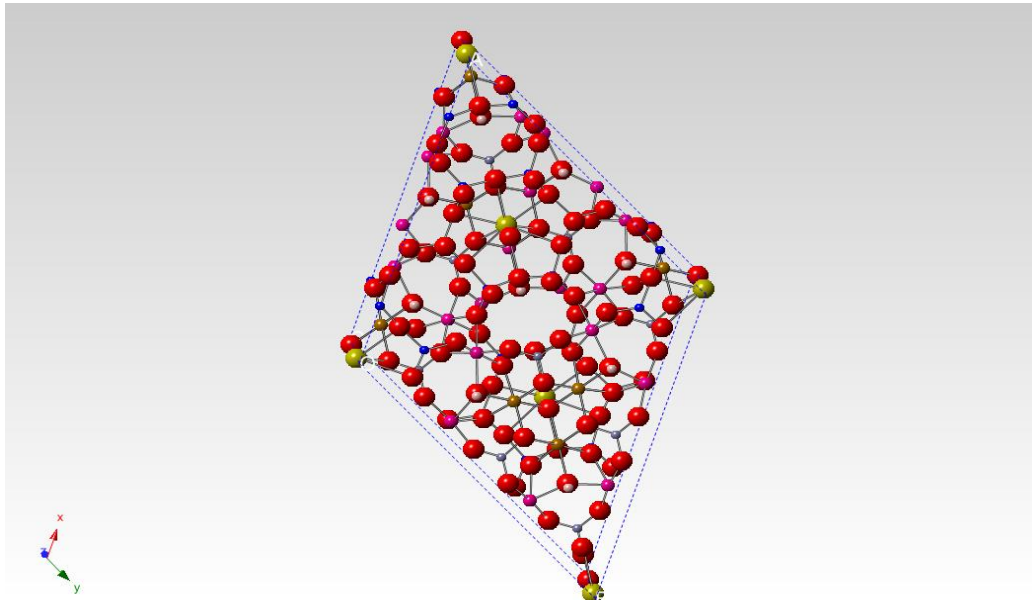


Figure 3-8 - Chrome tourmaline (Dravite) refinement
 Red – O, Yellow - Na, small plum – small brown – Fe, Small blue – Si, small pink – Cr, small silver – H, small Grey - B . CrystalMaker © data (Bosi et al., 2004)

Figure 3-8 shows the two main absorption band features of chrome tourmaline. In most tourmalines, absorption and emission are from inter valance charge transfer

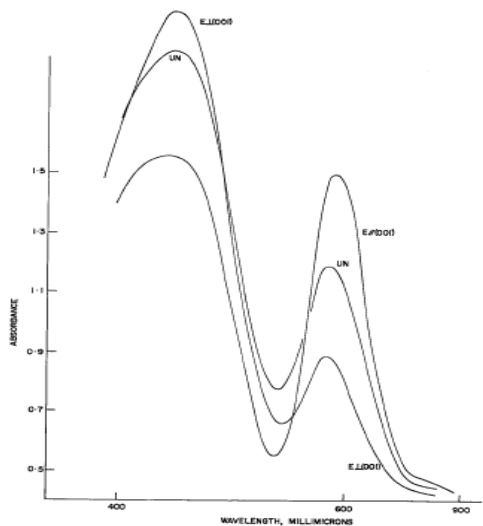


Figure 3-9 Absorption spectra of chrome tourmaline.
 with $E_{\perp}(001)$ and $E_{\parallel}(000)$ unpolarised $u \setminus N$ (Manning, 1969)

(IVCT) between $Mn^{2+} - Ti^{4+}$,and $Fe^{2+} - Ti^{4+}$. Chrome tourmaline is different with centres involving Cr^{3+} and V^{3+} being responsible.

3.11 RT1-1 Synthetic ruby

Ruby is a red coloured chromium bearing variety of the mineral sapphire. It crystallises in the trigonal crystal system ($\bar{3} 2/m$) in space group $R\bar{3}c$. To manufacture synthetic ruby Al_2O_3 (corundum) is doped with Cr_2O_3 . The sample RT1-1 is a synthetic ruby sample supplied by Industrie de Pierres scientifiques, Hrand Djevahirdjian S.A., Monthey, Switzerland. It was manufactured using the Verneuil process which involves an inverted oxy-hydrogen flame fusion process (Read, 1999).

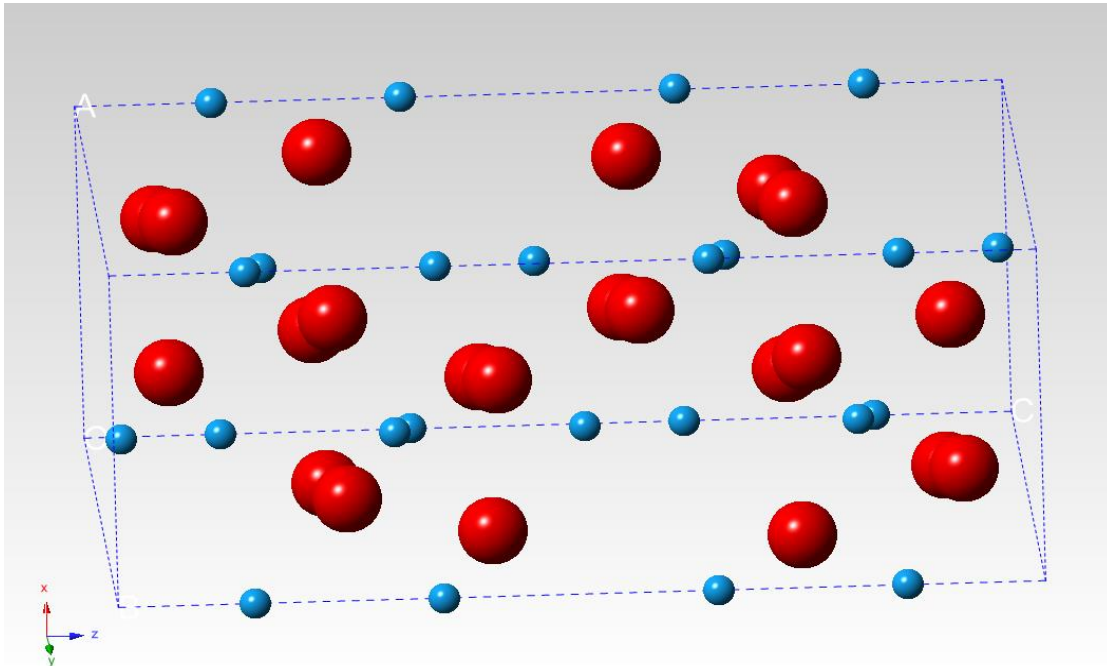
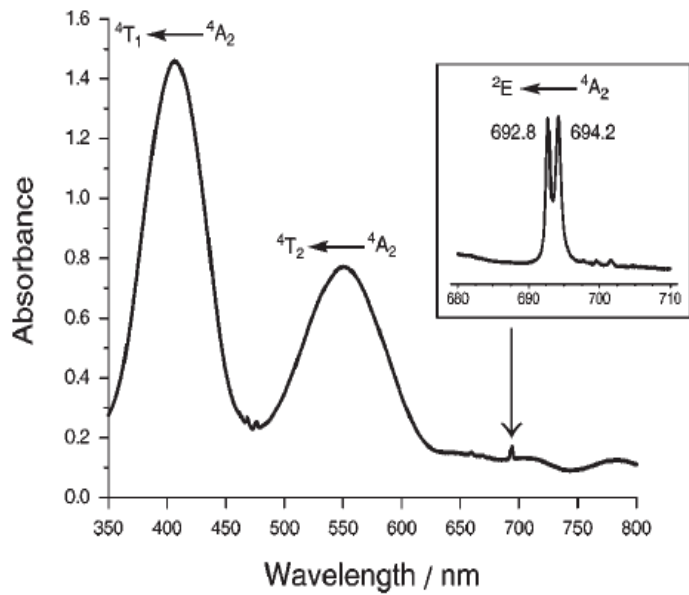


Figure 3-10 - Ruby refinement.
Red –O , Blue - Al
CrystalMaker © data (Oetzel and Heger, 1999)

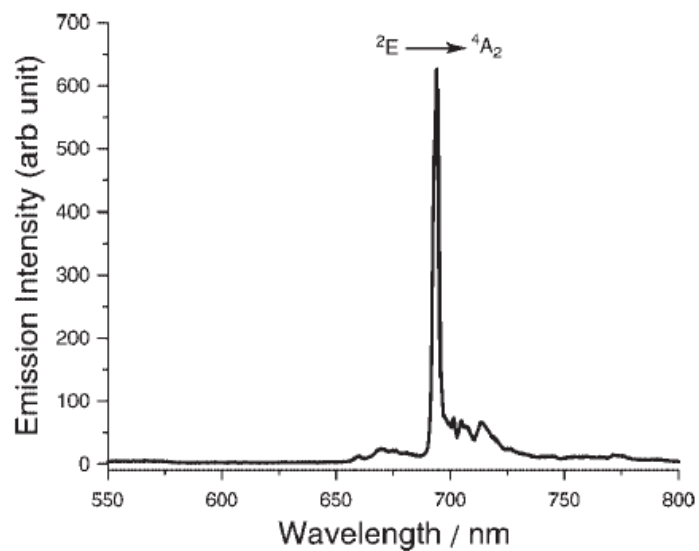
Cr substitutes in the Al site as a Cr^{3+} , which is an isovalent substitution. Cr^{3+} has three d electrons and the site symmetry in corundum is described as distorted octahedral. This gives rise to splitting of the energy levels of the d orbitals between the e_g and t_{2g} orbitals. The ruby luminescent spectra is well characterised and includes the two 'R' lines at

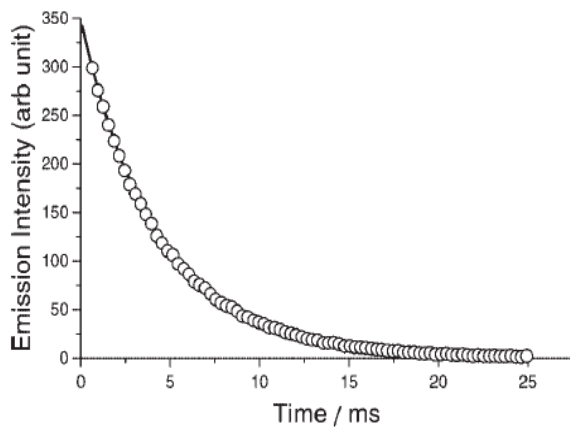
1.788 and 1.791eV that is produced from the zero phonon line of the 2E level splitting. At RT, there is a broad side band emission, to the lower energy side of the zero phonon line' this is produced by lower energy vibronic transitions. This is described for ruby in (Nassau, 2001) and a comparison of the Cr luminescence in a glass by (1985).



**Figure 3-11 -
Absorption spectra
ruby.
Source: (Esposti and
Bizzocchi, 2007)**

**Figure 3-12 -
Emission spectra
ruby.
Source: (Esposti
and Bizzocchi,
2007)**





<i>ICP MS Cr</i>	$\pm 2\sigma$	<i>EMP Cr</i>	$\pm 2\sigma$
834.3	6.3	818.8	

Table 3-6 - Comparative chemical analysis of RT1-1. from Electron MicroProbe (EMP) and Inductively Coupled Plasma Mass Spectrometer (ICP MS) reported in PPM to 2σ

Figure 3-13 - TR ruby spectra 2E emission at 694.2nm single exponential decay 4.26 ms.

Source: (Esposti and Bizzocchi, 2007)

4 Synchrotron Radiation

A synchrotron light source is a particle accelerator designed to produce high intensity EM radiation over a wide range of energies. The diamond light source generates light from 0.6 meV to 150 keV. The synchrotron in this study is used as the source of high intensity tuneable X-rays. Experiments were carried out on the I18 beamline at the Diamond Synchrotron, Didcot, Oxfordshire, UK. The design and capabilities of the synchrotron and the I18 microfocus beamline were reviewed in Thomas et al. (2006) and Thomas et al (2008), Mosselmans (2009) and Mosselmans et al. (2009). The X-ray energy available on I18 ranges from 2-20keV.

4.1 X-ray Absorption Spectroscopy

When X-rays interact with solids, responses can be divided into three main interactions: i) elastic scattering (Rayleigh) (Strutt, 1899); ii) inelastic scattering (Compton) (Bunker, 2010; and iii) absorption through the photoelectric effect (Bubb, 1924). Samples can be investigated by monitoring sample responses to X-rays using techniques including X-ray diffraction (XRD), X-ray fluorescence (XRF) and X-ray absorption spectroscopy (XAS). For the typical energies used for XAS (1-100 keV), the probability of absorption is between 100 and 1000 times greater than scattering (Bunker, 2010). XAS can be subdivided into a number of techniques including Extended X-ray Absorption Fine Structure (EXAFS) and X-ray absorption near edge spectroscopy (XANES). These closely related techniques use monochromated X-rays to measure the absorption coefficient as a function of the X-ray energy as it is scanned over the resonant absorption edge of the element of interest. As the energy reaches and then exceeds the resonant absorption, the Fermi energy, the absorption coefficient increases significantly (the absorption edge). The absorption

coefficient then oscillates for energies up to 1000 eV above the absorption edge. The XANES region is from 20eV below the edge to 50eV above and between 50 – 1000eV above the edge is the EXAFS region. XANES is sensitive to electronic information including oxidation state, local symmetry, and density of states, whilst EXAFS is sensitive to structural information such as bond distances and coordination spheres. The absorption coefficient in a transmission experiment is derived from the Beer-Lambert law:

(Bunker, 2010) *Equation 17*

$$i_1 = i_0 \exp(-\mu x)$$

Where i_0 is incident intensity, i_1 is the exiting intensity, x is the distance travelled through the material, and μ is the x-ray absorption coefficient of the material. cm^2g^{-1}

element detection **XANES only**; **EXAFS (challenging)**; **K-edge EXAFS**; **L3-edge EXAFS**; **L3/K-edge EXAFS**

H																			He
Li	Be										B	C	N	O	F	Ne			
Na	Mg										Al	Si	P	S	Cl	Ar			
K	Ca	Sc	Ti	V	Cr	Mn	Fe	Co	Ni	Cu	Zn	Ga	Ge	As	Se	Br	Kr		
Rb	Sr	Y	Zr	Nb	Mo	Tc	Ru	Rh	Pd	Ag	Cd	In	Sn	Sb	Te	I	Xe		
Cs	Ba	* Lu	Hf	Ta	W	Re	Os	Ir	Pt	Au	Hg	Tl	Pb	Bi	Po	At	Rn		
Fr	Ra	* Lr	Rf	Db	Sg	Bh	Hs	Mt	Ds	Rg									
		* La	Ce	Pr	Nd	Pm	Sm	Eu	Gd	Tb	Dy	Ho	Er	Tm	Yb				
		* Ac	Th	Pa	U	Np	Pu	Am	Cm	Bk	Cf	Es	Fm	Md	No				
		*																	

Figure 4-1 - Periodic table showing the XAS accessible elements for many third generation synchrotrons. Source: (Mosselmans, 2009)

Most XAS collected in this study utilises X-ray fluorescence rather than the transmission mode that is primarily used for standards. Fluorescence mode uses the intensity of the

X-ray fluorescence to calculate the absorption coefficient. EXAFS can be described as the oscillatory portion of the absorption spectrum superimposed on top of the uniformly decaying absorption coefficient μ_0 . The absorption coefficient is dependent on the energy (E) of the incident radiation. The absorption edges are generated as the incident X-ray becomes energetic enough to eject one of the core electrons (1s, 2s, 2p etc.) to the continuum. (Bunker, 2010) The edge is dependent on the shell from which the electron was ejected for example 1s = K edge (Figure 4-1).

In solids, the ejected photoelectron (wave) will be scattered by neighbouring atoms.

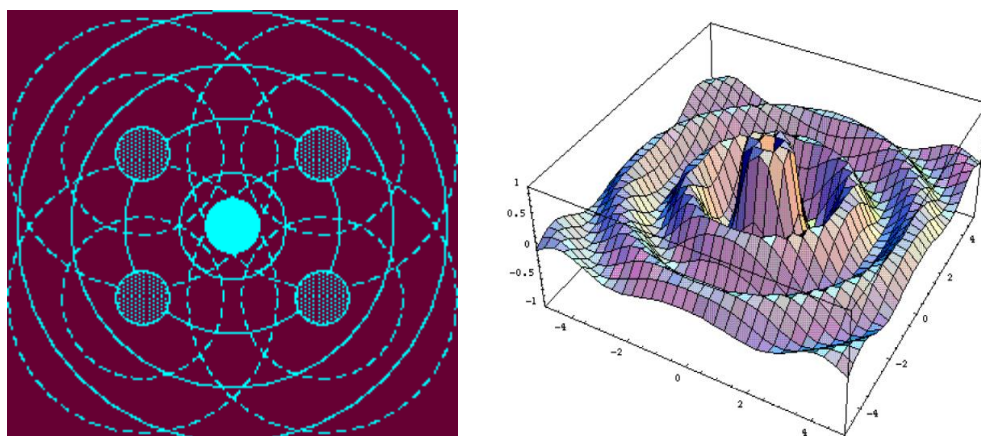


Figure 4-2 The effect of interference upon the ejected electron wave from the surrounding atoms.
Source (Mosselmanns, 2009).

Figure 4-2 depicts the interference of the electron wave following the ejection of a core electron. It is the interference between the outgoing electron wave and back-scattered ones, which leads to oscillations in the absorption spectrum above the edge, (i.e. EXAFS).

The process of extracting and analysing EXAFS data involves three steps:

- 1) Converting the raw data into an absorption spectrum

- 2) Extracting the EXAFS signal from the absorption spectrum
- 3) Fitting the EXAFS spectrum with a model environment

Software is available to aid the process, and the conversion of the raw data is completed using a software package called Athena, part of the IFEFFIT package (Ravel and Newville, 2005). For transmission data, the natural log of the I_0/I_1 ratio is used, where I_0 is the X-ray flux measured using a gas ionisation chamber prior to interaction upstream of the sample and I_1 is the measured transmitted signal downstream from the sample measured in the same way. Edge energy is calibrated using the beamline standards. The alternative technique used for measuring EXAFS is detecting X-ray fluorescence through a solid-state multi-element detector. The sum of the useful individual luminescence channels collected is divided by I_0 to calculate the absorption coefficient. The techniques and methods are detailed in full in the following publications (Stern, 1974, Stern et al., 1975, Koningsberger, Lytle et al., 1975)

The background signal is removed, the pre-edge background is removed, and the spectra normalised to the edge step using a first order polynomial. A number of smoothly joined linked polynomials subtract the post edge background to complete post edge subtraction and the process is completed in Pyspline (Tenderholt et al., 2007). The final part of the process is the fitting or data simulation. Traditionally in the UK, this is achieved with the program EXCURVE (Binsted, 1998). To create a simulated EXAFS spectrum the model is defined in terms of shells of the same atom type at the same distance from the central atom. The first to be defined is the type of central atom, and from this, potentials are calculated using the 'muffin tin' approximation; the muffin tin approximation is where the atomic potentials are approximated as spherically

symmetrical out to a finite radius and the interstitial potential between the atomic sphere is approximated as a constant. (Bunker, 2010) The potential outside the 'muffin tin' is then equalised. Using the core-hole width, the phase shifts are calculated for each of the atom types in the model. Phase shifts are calculated from the atomic potentials of each atom using the Hedin-Lundqvist ground states and Von Barth exchange potentials (Bunker, 2010).

In each shell, there are four principal parameters:

- 1) The distance from the central atom r ,
- 2) The type of atom in the shell ; f_i and δ_i ,
- 3) The number of atoms in the shell, and
- 4) The Debye-Waller factor for the shell.

The mathematical equation that forms the basis of the methodology is explained as:

$$\chi^k = \langle S_0^2 \sum_i \frac{3 \cos^2(\theta_i)}{kr_i^2} |f_i(\mathbf{k}; r)| e^{-\frac{2r_i}{\lambda(k)}} \sin(2kr_i + \delta_i(\mathbf{k}; r)) \rangle \quad \text{Equation 18}$$

(Mosselmans et al., 2009)

Where r_i is the distance to the i_{th} neighbour; $\langle \dots \rangle$ represents an average over all sites in the sample; λ is the electron mean free path, and S_0^2 is a loss factor; f_i and δ_i are the scattering amplitude and phase shift of atom i , θ_i is the angle between the electric polarisation vector of the x-ray beam e and \hat{r}_i from the centre atom to neighbouring atom i .

4.2 X-ray Excited Optical Luminescence

XEOL is the emission of visible light following excitation by X-rays and can be considered as a concurrent side effect of XAS. XEOL is generated from energy absorbed from the incident X-rays and is one of a number of alternative mechanisms for energy dissipation.

The only mechanisms that provide energy for XEOL are absorption and inelastic

scattering. During irradiation, absorbed energy generates a population of electrons and holes in excited states, and during their subsequent relaxation, the excess energy over the ground state is dissipated. Where energy is lost through the emission of visible light it is termed XEOL. The initial process of excitation is common between XEOL and XAS, as XEOL is generated as part of the energy release process of XAS. The site-specific nature of XEOL emissions is a feature that this current study intends to explore. The potential to use XEOL responses to monitor sample modification will also be explored. The probing of energy transfer mechanisms will be tested using dose rates. XEOL spectroscopy extending into the deep ultra violet (DUV) 200-300 nm will be investigated as this is a portion of the EM spectrum that is difficult to access through traditional luminescence spectroscopies.

4.3 TR XEOL

TR XEOL techniques are explored to extend the applications for XEOL. TR XEOL is the measurement of XEOL as a function of time. The technique can determine the spontaneous emission probability of luminesce by measuring the decay profile of the intensity of luminescence following excitation. The probability is a coefficient originally defined by Einstein (1916) (section 2.8.5). The probability of fluorescence as shown by Einstein is inversely proportional to the third power of the transition wavelength, meaning the shorter the wavelength the greater the probability of emission. However, this relates to the natural lifetime of a luminescent transition and in practice, this is rarely observed in minerals due to the effects of quenching and competitive energy transfer sections (2.8.6, and 2.10). TR XEOL allows the deconvolution of overlapping emissions, and its application to facilitate better modelling and quantification of

luminescence will be explored. The technique of collecting XEOL concurrently with either XRF or XAS will also be explored.

4.4 Optically Derived X-ray Absorption Spectroscopy

If the intensity of XEOL is linear with the XAS signal, 'optically derived' (OD) XAS is obtained if XEOL is measured as a function of incident X-ray energy. By analysis of specific light emissions linked to metals on particular substitutional sites, OD XAS is considered to be site-selective (Soderholm et al., 1998). XEOL has indeed been shown to carry XAS information and Bianconi and Jackson (1977) first reported XEOL in inverse correspondence with EXAFS collected from a sample of CaF_2 . The concept of using XEOL to access XAS was investigated by Goulon et al. (1983) who successfully showed site specificity by comparing pure ZnO with a mixture ZnO and ZnTPP (zinc mesotetraphenylporphyrin). The aim was to develop OD XAS to facilitate site selectivity into XANES and EXAFS data. The relationship between XEOL yield and its change in sign (the reduction of the intensity of luminescence correlating with the absorption edge the inverse of the intensity increase in the absorption taking place) as a function of sample preparation was explored by Emura et al. (1993), who proposed a model to explain the anti-correlation sometimes observed between X-ray absorption and XEOL. They modelled the results by varying the specimen thickness, and taking into account transitions from other lower energy edges of the absorber atom and K shell transitions of the lighter scattering atom that can create photoelectrons. The optical absorption coefficient of the sample material and the X-ray absorption coefficient are also factors incorporated into the model. However, work of Soderholm et al. (1998) using powdered

REE crystals found occasions when site selectivity was compromised through energy transfer, a mechanism they described as inter-ion XEOL. Soderholm et al. (1998) presented a pessimistic assessment of the potential for OD XAS as a useful technique. They acknowledged the potential of luminescence wavelength and time resolved analysis, however they were not confident that many limiting issues would be overcome. Poolton et al. (2004) described the successful use of spectrally resolved OD XAS data to discriminate between single-phase materials with different recombination pathways and secondly materials with invariant recombination pathways but having chemical phase separation. In more recent work, Poolton et al. (2006), working in the soft X-rays and VUV energy range, reported successful mapping using OD XAS. Poolton et al. (2007) reported on Pump Probe (PP) ODXAS and OD EXAFS as successful in micro mapping, and the methodology proved capable of discriminating radiative and non-radiative centres in heterogeneous silica. Hayakawa et al. (1999) reported the successful collection of OD EXAFS for ZnS and ZnO to obtain a reliable spectral match to conventional EXAFS data. Daldosso et al. (2000) completed work with simultaneous Total Electron Yield (TEY) and XEOL experiments that provided evidence of the sensitivity of the XEOL technique to the local structure of quantum confined luminescent sites. The OD XAS technique deserves further work as it retains unexplored potential, and if the apparent obstacles can be overcome, it has the potential to become a valuable extension to XAS. Another objective is to test the simultaneous collection of XEOL and XAS or XRF. If XEOL is to be used to derive OD XAFS, it will be essential to know in what circumstances the data will provide reliable coordination information. It will also identify areas where our understanding of the decay mechanism is inadequate to enable a

robust model. XEOL collected simultaneously with XRF or XAS and processed in tandem creates a powerful alternative analytical technique.

4.5 Soft X-ray and Vacuum Ultra Violet Excitation

Most interest and developments of XEOL have been in the soft X-ray and vacuum ultra violet (VUV) portion of the EM spectrum; although strict interpretation of XEOL would exclude VUV excitation as it is not excitation from X-rays. Recent work using TR-XEOL (Sham and Rosenberg, 2007, Sham et al., 2006, Murphy et al., 2007) are examples of this interest. The reason for the use of lower energy excitation revolves around the energy of emission being between $\sim 1-4$ eV and the energy of soft X-ray excitation is up to 124 eV for VUV. This energy difference is between one and three orders of magnitude smaller than the energy difference between the emission energies of hard X-ray excitation (>6195 eV) (Figure 4-3). To collect OD XAS, the luminescent emission must be excited primarily, if not exclusively, from energy from a local absorber. To achieve this, absorber and emitter must be one and the same, or the absorber must be intimately associated with the emission centre; in addition, energy derived from alternative remote absorption is negligible in comparison to the local. It is likely the greater the energy of excitation, the less likely this will occur for two reasons. firstly is that as well as energy absorption from the target element a large percentage of non-resonant absorption takes place, which increases as a function of excitation energy. This non-resonant absorption in turn affects the population of delocalised electrons, holes and excitons. The subsequent process of equilibration of the excited state, the delocalised population, is subject to a sequence of thermalisation events. These include radiative and non-radiative transitions that inevitably include any available luminescent pathways. The luminescence generated is unrelated to the local target absorber and could be relaxing via the emission pathway of interest, thereby 'polluting' the local OD XAS. The

luminescence generated would be expected to follow an energy dependent response, gradually increasing through the absorption edge, although this may not always be the case. Secondly, increasing the difference in energy increases the number of interactions required to 'lose' the excess energy, thereby increasing the potential for delocalised luminescence.

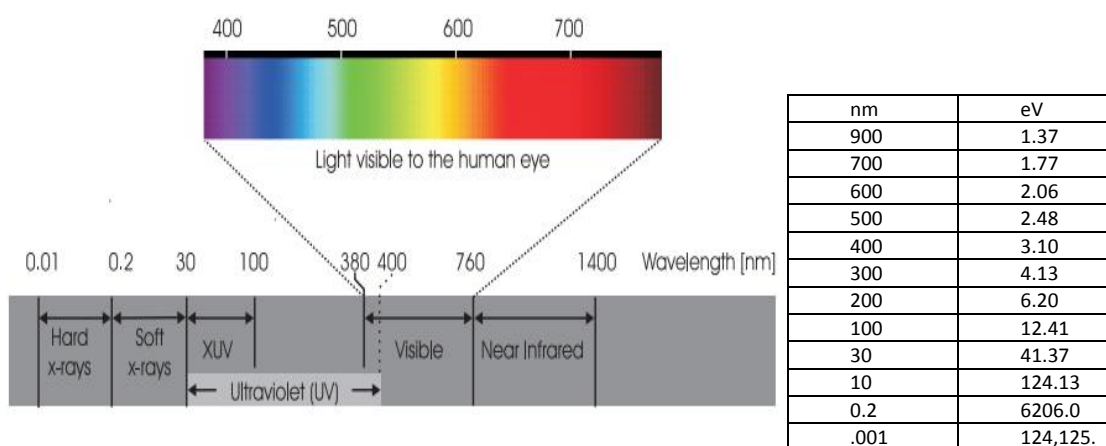


Figure 4-3 - Section of the electromagnetic spectrum from hard X-rays to infrared and wavelength energy conversions.

Source: (Elton, 1990)

Wavelength selectivity of emission can remove many known delocalised emissions; however, this methodology has the limitation that most emissions from transition elements, common lumiphores in minerals, tend to have broad overlapping emissions. The natural lifetime for a single luminescent emission is a fixed coefficient, if locally excited emissions have different natural lifetimes to emissions from delocalised excitation, this could allow the differentiation of a spectrally overlapped OD XAS signal. The testing of this hypothesis is a goal of this study. XEOL therefore has an important potential in improving our comprehension of minerals. It has an advantage over PL in

that it does not depend on resonant absorption X-rays generate a population of delocalised excited state electrons that subsequently relaxes through a complex energy cascade with the potential to excite all available luminescent centres within the material examined. The technique is therefore capable of probing both normal allowed PL and luminescent centres normally inaccessible. It therefore provides a more comprehensive overview of the defect structures present. Lankinen et al. (2008) used XEOL to investigate Mg-doped GaN, noting the activation of Mg luminescent defects not seen with low temperature PL. The nature of the energy cascade excites a broad range of energies including emissions approaching the VUV. Luminescent emissions approaching the VUV (200 nm 250 nm) are normally only accessible when VUV excitation is utilised thus XEOL significantly extends the observable luminescent spectrum. There is also a potential for using a modified system to explore VUV and soft X-ray excitation. This would facilitate access to the K edges of lighter elements. Due to the technical requirements of VUV, it is an aspect of mineral luminescence that has received very little attention. A Scopus© word search of 'VUV' records 3842 hits over the last 10 years, up to 2012 and when the search is repeated combining 'VUV' with 'mineral', only 46 hits are recorded, of which only 4 are within Earth Sciences.

4.6 Polarisation

The X-ray beam on the I18 beamline is linearly polarised with the electrical vector of the photons aligned within the horizontal plane. This enables the isomorphic nature of the absorption of the sample to be explored, measuring XEOL as a function of sample orientation. The technique probes the structure and orientation of the absorber. In addition, the technique can be further refined by exploring the polarisation of emission,

as luminescent emissions are polarised at the quantum level, so polarisation probes the orientation and structural order of the lumiphore (Bunker, 2010).

4.7 Heterogeneity

The beam size on the I18 beamline has a spot size typically of 1.5-3 x 2-5 μm , facilitating micron-scale spatial analysis of inhomogeneous samples (Mosselmans et al., 2009) . The simultaneous collection of spatially resolved XEOL maps and XAS or XRF data will be very useful in resolving contentious assignments of particular luminescent emissions to trace element.

4.8 The XEOL Detection System

The system design has two objectives the first is the collection of Continuous Wave (CW) XEOL, the second the collection of TR XEOL. Some aspects of the design project overlap between CW and TR. For both aspects, there is a shared requirement for the exclusion of all extraneous light from the sample area and also a mechanism to collect a 'significant' proportion of the spherical radiation, i.e. collecting the largest solid angle of emission. The factors affecting this are a combination of distance from source and the surface area of radiating sphere collected which can be calculated using the Equation 19.

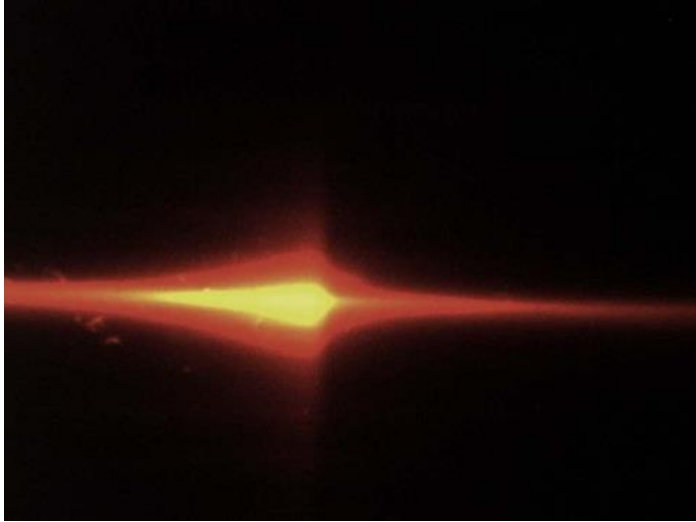


Figure 4-4 - XEOL luminescence exhibited by synthetic ruby using a 7keV $3/3\mu\text{m}$ beam incident on the polished face of the sample at an angle of 45° Image collected through the sample microscope camera with a view of the sample chamber as positioned inside the experimental hutch.

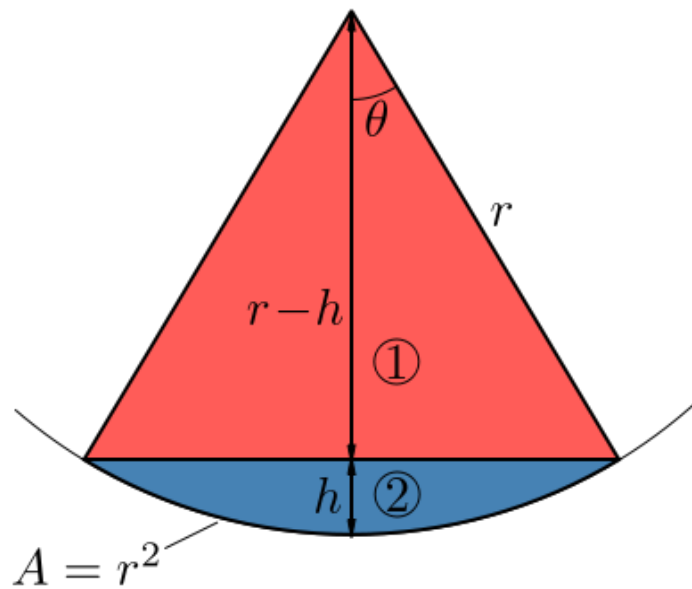


Figure 4-5- The method for calculating the steradian in a sphere. As applied to the calculation of the subtended surface area of the sphere. (Held, 2009)

$$\Omega = 2\pi(1 - \cos\theta)$$

Where θ is as displayed in Figure 4-5, and Ω is the surface area of a sphere subtended by the solid angle. It follows that the relationship between the solid angle and the subtended surface area is a simple application of the cosine rule. This relationship controls the design for maximisation of light collection.

4.8.1 System Requirements

The XEOL facility to be built around a JY Horiba Triax 190 spectrometer.

- 1) The system is to fit in and work primarily on the I18 microfocus beamline but portable for use on other beamlines.
- 2) The spectrometer and data collection is capable of remote control.
- 3) The system is compatible with all the existing control and detection systems on the beamline and capable of being operated in varying system configurations.
- 4) The system is capable of collecting both CW and TR XEOL data.
- 5) The system control and data acquisition is integrated with existing beamline software control systems operating on a Linux platform, namely the Experimental Physics and Industrial Control Systems (EPICS) and Generic Data Analysis (GDA) software. (EPICS) is used to control automated systems and detectors, whilst GDA software provides the user interface and data processing functionality.
- 6) The system is efficient from 200nm to 900nm, extending beyond the visible spectrum of ~400-700 nm and collects sufficient signal from the spherical emission for the efficient collection of data with optimal signal to noise ratio. The system be capable of ps time resolution

- 7) The design constraints include that the system works within, and not interferes with, the confines of the sample area, including existing detectors, video microscope, and sample stage with multiple degrees of freedom of movement.
- 8) An initial concept was to use standard microscope optics to focus the signal from the sample into a fibre optic probe. This was discounted, as the use of lenses would limit the spectral range.
- 9) The signal collection device is capable of mounting on a moveable stage that would give remote control and allow optimisation of collected signal.

4.8.2 Techniques for Collecting Time-Resolved Data

Five alternative methodologies for the collection of TR luminescence data were identified. The design process therefore included an evaluation of the alternative techniques to enable selection of the most appropriate methodology.

The five alternatives are:

- Phase modulation
- Gated detection/pulse sampling
- Streak camera
- Up conversion
- Time correlated single photon counting (TCSPC)

Frequency Domain or Phase Modulation

This is a technique that uses an intensity-modulated excitation, whereby the intensity of the excitation is varied (typically, a sine wave modulation is applied) at a frequency comparable to the reciprocal of the time decay τ of the sample. When a sample is excited with a modulated signal, the emission is forced to respond at the same

modulation frequency. The lifetime of the sample delays the emission in time relative to the excitation. This delay is measured as a phase shift as shown in Figure 4-6. The theory of frequency modulation is discussed in Lakowicz (1999). Frequency domain was discounted, as it required the modulation of the X-ray beam that is not possible.

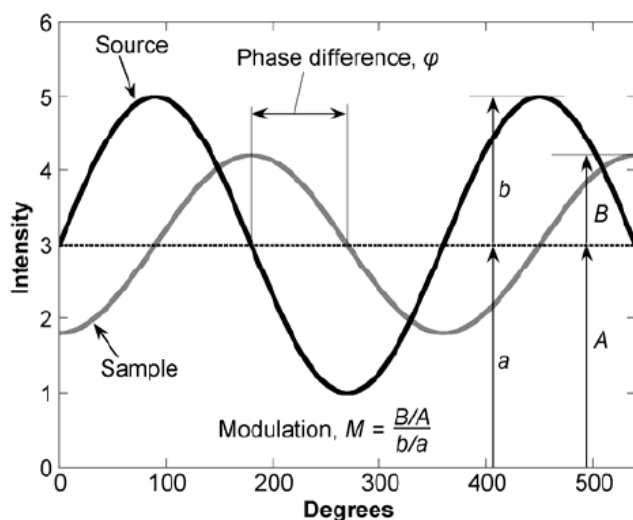


Figure 4-6 Phase modulation or frequency domain measurements. The ratios B/A and b/a represent the modulation of the emission and of the excitation, respectively, and the delay is measured as a phase shift ϕ (Lakowicz, 1999).

Gated Detection/Pulse Sampling

This technique predates TCSPC and uses either stroboscopic or pulse sampling techniques as illustrated in Figure 4-7. The technique can be accomplished by gating the detector, or alternatively, the detector can be on all the time, and the signal sampled through an oscilloscope. The technique is limited to ns temporal resolution and gated detection is discussed in Lakowicz (1999pp 116-121). The specifications for the system required ps temporal resolution and as this was beyond the techniques capabilities, it was discounted.

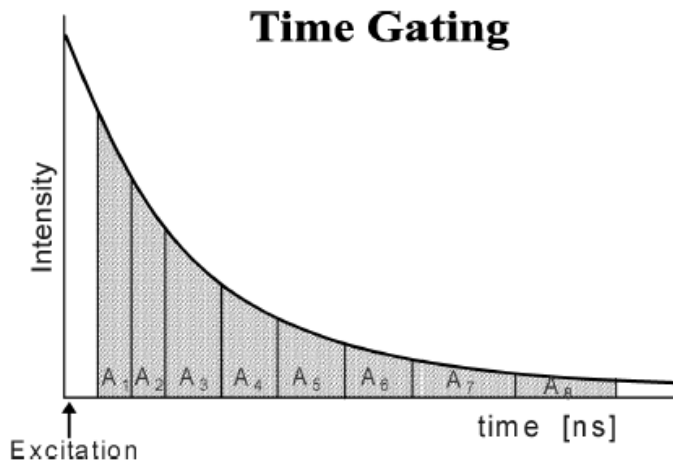


Figure 4-7 - Decay time measurements using gated detection in a pulse sampling mode.

At $t=0$ the specimen is excited with a short excitation pulse (ns/ps) and the detection gate is then opened after a short delay with respect to the excitation pulse (Gerritsen et al., 2004).

Streak Camera

A streak camera offers excellent time resolution capabilities and is capable of single digit ps resolution (Lakowicz, 1999). Jaanimagi (2004) announced an X-ray streak camera working with 100 fs temporal resolution. The technique disperses the photoelectrons over an imaging screen (Figure 4-8). This is accomplished at high speed through the use of deflection plates. The light can be dispersed as a function of wavelength across the photocathode detector enabling simultaneous measurements of wavelength and the decay time.

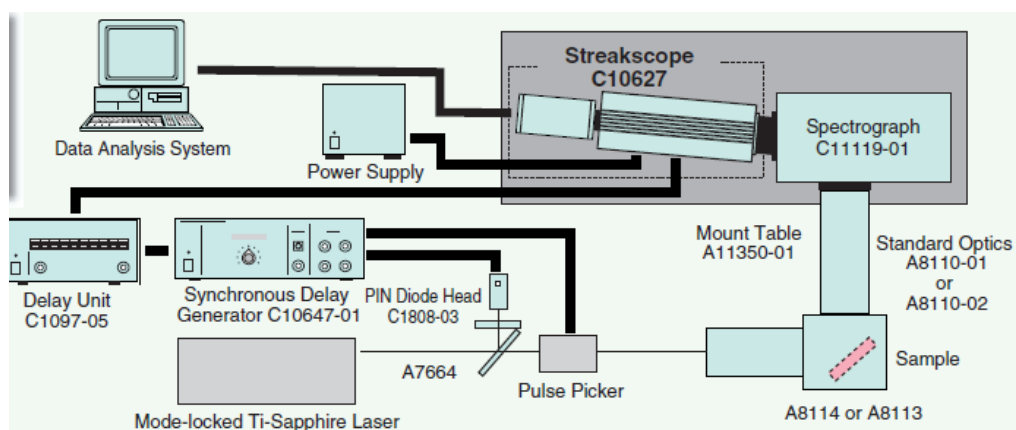


Figure 4-8 - Typical laser based system configuration for streak plate TR analysis.

Source: (Photonics., 2012)

The streak camera offered many advantages but issues regarding compatibility with the existing spectrometer and the significant costs involved excluded this alternative for the initial design. It could however be considered as a possible upgrade in the future. The technique is discussed in the publication by Hamamatsu (Photonics., 2012).

Up Conversion Methods

This technique provides the ultimate in time resolution bypassing the limitation of the time resolution of detectors and is limited only by the pulse widths of modern lasers that extend from ps and fs to as. The technique passes the luminescence signal through an up conversion crystal that is gated with a second laser pulse. The data observed are the shorter wavelength harmonic of the combined laser signal. The intensity decay is sampled by sweeping the gating pulse with a time delay as shown in Figure 4-9. This technique is a laser technique with no apparent application for synchrotron excitation, and was therefore discounted. (Lakowicz, 2006)

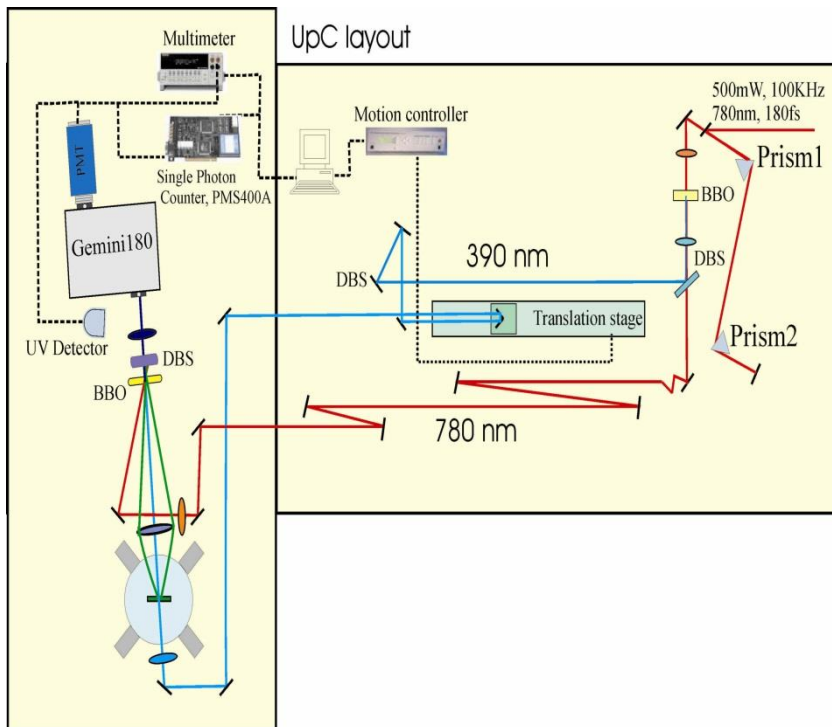


Figure 4-9 - Up conversion using non-linear crystal (BBO)

The optical layout is shown. The femtosecond laser source is a Coherent RegA 9000, it provides ~500mW pulses @ 180 fs & 100KHz and 780 nm. The setup is composed of a pulse pre-compensation unit with a pair of prisms, frequency doubling unit with a non linear BBO crystal, time delay translation stage, sample unit (4 K Cryostat), SFG unit with a BBO crystal, and PMT detection amplification unit by single photon counting technique (PMS_400A). The time resolution of this system is 200 fs
 Source: (Lakowicz, 2006)

TCSPC

This methodology operates by measuring the time delay between the excitation pulse and the first detected photon following excitation. The technique has a very good signal to noise ratio with every positive photon count significant (Becker, 2008, Becker et al., 2007, Becker et al., 2004, Becker et al., 2008). Additionally, the counting system requires a low flux to remove the possibility of data distortion due to double counting. This was particularly appropriate for the XEOL environment as the photon flux in comparison to

modern high power lasers is low, although the incident energy is much higher. The typical design for a TCSPC system is shown in Figure 4-10, and Figure 4-11 TCSPC was the methodology selected for the system.

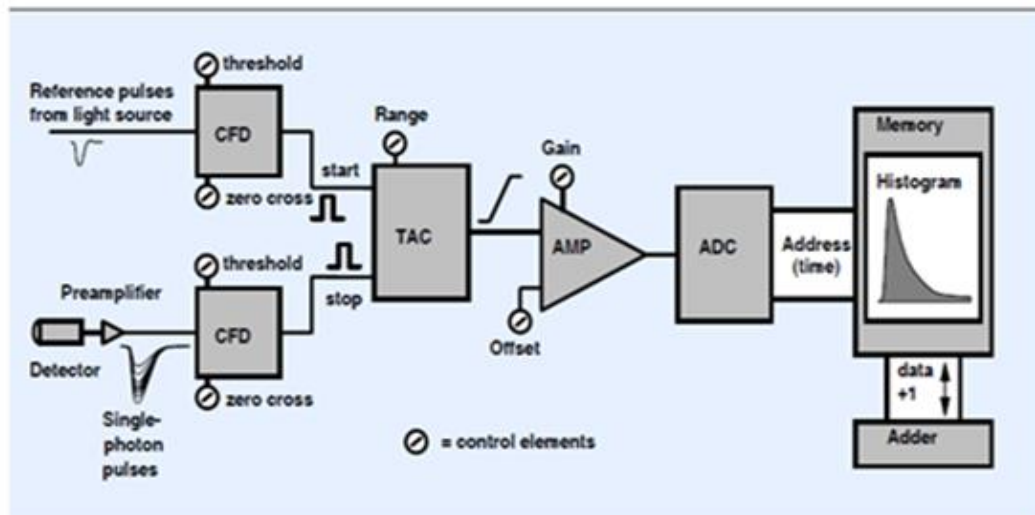


Figure 4-10 - Classic time-correlated single photon counting experiment. Classic design for a TCSPC system Continuous frequency discriminator (CFD) Time to amplitude converter (TAC) amplifier (AMP) analogue to digital converter (ADC) (Becker, 2008)

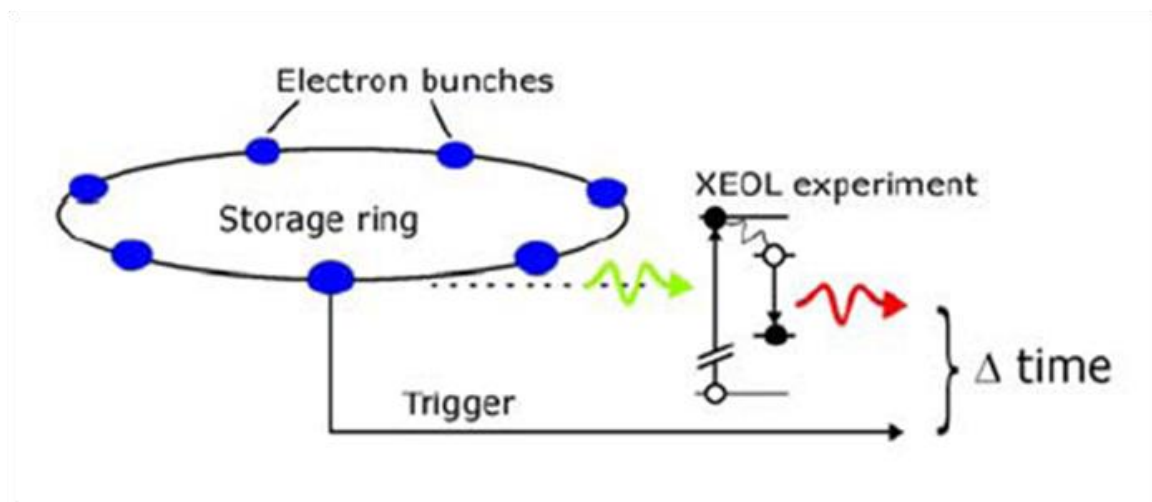


Figure 4-11 - TCSPC system incorporated onto synchrotron. Source: (Sham and Rosenberg, 2007)

4.8.3 Initial Design Proposals

The system was designed to use two 'off axis' parabolic mirrors when manoeuvred close enough to the sample collect a large enough solid angle to capture a significant proportion of the emission., then focusing the collected signal into the fibre optic cable. The losses due to inefficiency of the mirrors were calculated to be significantly less than the increase in primary beam collected. The alternative back-up solution was the direct collection into the fibre optic patch cable.

The fibre optic is a bespoke manufacture that included an even mix of two optic fibres; one optimised for visible into the near infrared transmission, the other optimised for transmission of the visible into the UV. The technical specifications of fibres are given in (appendix 5).The fibre optic was manufactured with a termination at the collection end with a circular core and the termination at the delivery end with a rectangular core profile, in order to optimise the amount of light entering the spectrometer through the entrance slits.

The spectrometer contains an automated rotating turret fitted with three diffraction gratings. Modification of the spectrometer included replacing one of the gratings with a lower resolution grating allowing collection of the entire spectral range, 200-900nm, in one integration onto the Synapse charge coupled device (CCD) detector.

The monochromator was capable of control through a serial (RS232) connection that could be directly connected through the Linux operating system (OS) and controlled by EPICS, and these software commands were developed in advance of the present study.

The monochromator was factory fitted with a synapse Peltier cooled charge coupled device (CCD) which was used for CW collection. The detector was controlled through a

type 2 USB connection. The Linux OS does not directly support any USB functionality, although emulators are available. However, the software developers of Diamond have a policy of not supporting Microsoft Windows USB devices due to stability concerns. This created the major issue that there was no mechanism by which to control data collection and retrieval from the synapse detector and retrieval collection directly from existing software systems.

The solution devised was the building of a Windows socket server, a software device that resides in the Windows system on the computer connected to the spectrometer. The socket server is programmed to listen for commands received on a defined port through the Transmission Control Protocol/Internet Protocol (TCP/IP) that can communicate across the different OS platforms. The socket server was developed using a software development kit (SDK) available from the manufacturers of the spectrometer. The SDK allowed access to the functionality of the spectrometer and remote control of the spectrometer through the socket server and the spectrometer could then be controlled with EPICS commands through the socket server system. The socket server was developed as part of the present study in Visual basic (VB).

The modified side exit of the spectrometer is fitted with a R3809U-50 Multi-Channel Plate PhotoMultiplier Tube (MCP PMT) with good sensitivity from 200nm to ~820nm, with a rapid reduction in sensitivity for longer wavelengths. The technical specification is included in Appendix 1.

The collection of TR data is accomplished by using a special fill of the storage ring called the 'hybrid mode' (see 4.8.7) and the use of a pulsed timing signal known as the 'clock

signal'. The clock signal is a single pulse coincident with one complete revolution of the storage ring. To receive and process the timing signal on the beamline an event receiver card was installed. It was originally designed for the Swiss light source and the modified design was subsequently supplied to Diamond. Technical specifications are included in Appendix 2. The card synchronises the clock signal with the arrival of the X-ray pulse at the sample. The XEOL signal generated by the MCP PMT is processed using an Ortec 9327 1GHz amplifier and timing discriminator technical specifications (see Appendix 3) that passes the signal to an Ortec 566 time to amplitude converter that incorporates a Constant Fraction Discrimination (CFD) facility (for technical specifications see Appendix 4). The signal is then passed via a specially installed low loss cable into the existing multi component analysis (MCA) data processing system in the control room of the beamline.

Positioning of the MCP PMT is critical to maximise the signal collected from the divergent beam exiting the side slit of the spectrometer. The beam size must coincide with the maximum available surface of the detector plate. The optimum position was first calculated and then tested using a light signal passed through the spectrometer with the output of the MCP PMT attached to an oscilloscope. Using this I could complete fine adjustment of position. The MCP PMT and mounting on the spectrometer were then marked to allow re-alignment.

The alignment of the optics and calibration of the side slit spectral range for each of the gratings was achieved using three laser sources; 405, 532 and 650 nm (3.06, 2.33 and 1.91 eV). By combining the adjustment of the centre of the grating and adjusting the side slit width, I could measure the spectral range measurable for different width settings of the side slits.

4.8.4 Design Modifications Following Commissioning

The mirror system was found to be difficult to align and the signal was disappointing when compared to direct collection into the fibre. I identified a flaw in the original design that was that the parabolic mirrors used are designed for the collection of parallel light. The closer the mirror is positioned to the sample to increase the solid angle collected, the less efficient the mirror becomes, as a reducing percentage of the collected rays are collected due to the increasing divergent nature of the emission incident on the first mirror. It was found that even though the solid angle collected was significantly larger through the mirror than direct collection with the fibre optic, the fibre optic was more efficient in total signal collection. It was also found that alignment and the optimisation of the signal was much easier to achieve using a collection configuration direct into the fibre optic.

The software control of the spectrometer through the RS232 and USB through EPICS commands issued to the socket server, respectively, had long response times $\sim >30$ s that made the use of the software as an integrated process with the GDA software control unviable due to the excessive dead time. This necessitated a re-evaluation of how the spectrometer was controlled. The solution was to control the laptop remotely from the control room using a keyboard video mouse (KVM) switch via the proprietary software. This facilitated the operation and collection of both CW and TR data. TR data is collected only using the MCP PMT and hence simply requires the position of the grating, slit widths, and opening the shutter. The remainder of the data collection and processing is controlled through GDA software. CW is collected entirely through remote control of the spectrometer. These alterations to the design introduced two major drawbacks. Firstly,

integration with the GDA software and EPICS control system was lost preventing the fully automated collection of data and all commands to the spectrometer are operator initiated. The data collection, storage and processing are separate to the beamline software for all CW data.

The power supply within the experimental hutch is on a separate circuit to the data collection computer rack within the control hutch. I identified that this configuration had the potential for a ground loop to affect the timing system. The Earth wiring of the Diamond installation had been completed with the aim of removing this issue. Initially the system was operated utilising the separate circuits but it was quickly found that a ground loop artefact could be detected in the data as regular peaks along the time axis. To resolve this problem an additional power feed was run from the data processing computer rack in the control hutch into the experimental hutch. This feed is used to supply power to all the TR electronics inside the experimental hutch and this resolved the ground loop issue.

Clock signal synchronisation was adjusted within the control room using GDA software and EPICS controls. If the offset value selected is an odd number, it introduces a time delayed artefact into the TR data whereas, the artefact disappeared if an even number offset was selected. The source of the artefact is obviously within the software, so a pragmatic approach to the problem was adopted, limiting the selection of offset values to even numbers; this approach did not have any detrimental effects on the experiments.

4.8.5 The Final System

For all XEOL experiments, the experimental hutch was in darkness apart from the LEDs on the electronics and limited safety lighting. To remove all extraneous light from the sample table the experimental area was covered with a thick blackout sheet, which was tightly secured around the base of the experimental platform. A light blank was completed before every analytical session. A schematic of the system is shown in (Figure 4-12). All experiments described in this chapter were carried out at room temperature (RT) and the X-rays were typically delivered as a $3 \mu\text{m}^2$ 7 keV beam with an intensity at the sample of $\sim 3 \times 10^{12}$ photons/s (Mosselmans et al., 2009).

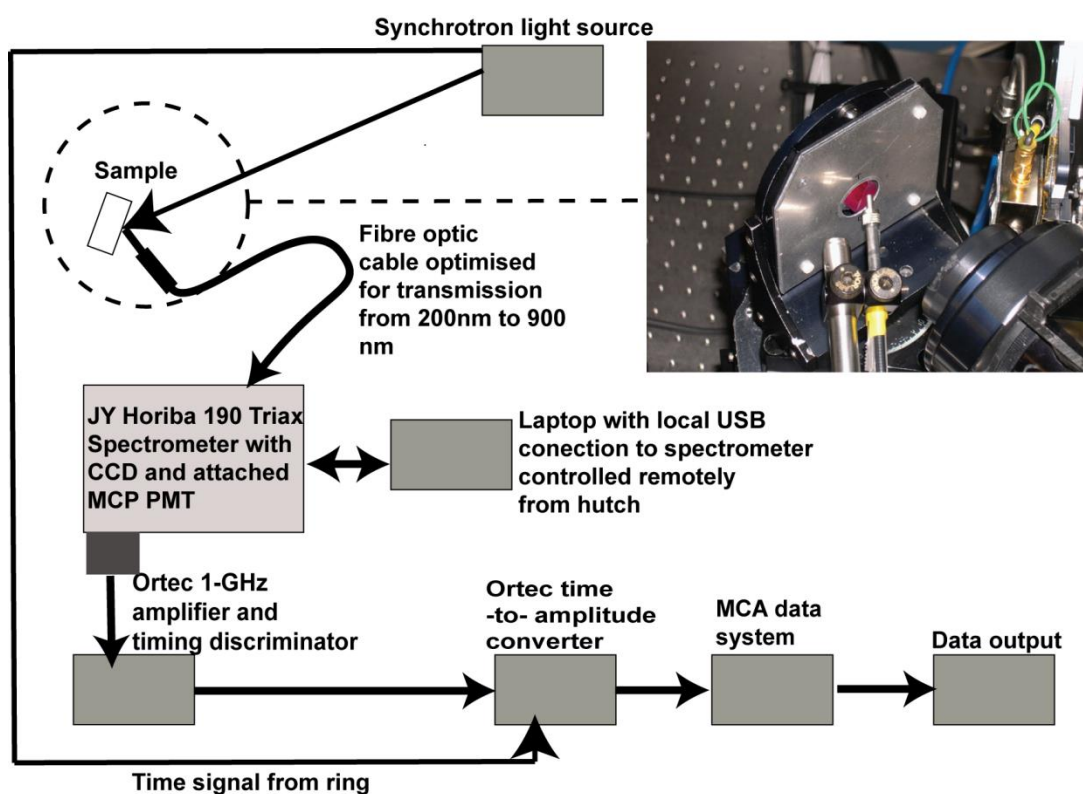


Figure 4-12 The layout of the XEOL detection system for the I18 beamline. Inset shows the sample, beam, and optic fibre alignment. Source (Taylor et al., 2013)

Samples are placed with their surfaces at ca. 45° angle to the incident X-ray and the fibre optic is positioned between 2-4 mm from the sample surface and at 90° angle to the

incident beam (Figure 4.12 inset). Light from the sample is delivered to the spectrometer using a bespoke fibre optic. The spectrometer is a Triax 190 monochromator /spectrograph (Horiba Jobin-Yvon), with corrected cross Czerny Turner layout (Gil et al., 1988), fitted with three gratings (150 lines blazed at 500 nm) (1200 lines blazed at 500 nm) (1200 lines blazed at 900 nm) on an automated three-sided turret. The signal was optimised for each experiment by monitoring the signal in the continuous collection mode of the spectrometer.

4.8.6 Continuous Wave Measurements

The main exit port to the spectrometer is fitted with a Synapse 81100 Peltier-cooled CCD with 1024x256 pixels and the CCD is used to collect CW XEOL. The intensity of the incident light is controlled by motorised entrance slits. The typical dark current is ~1150 cps compared with 30,000-50,000 cps from the albite sample CLBR. The typical integration times used are ~ 5-30 s using the 150 grating, a spectral range of ~700 nm can be collected in a single integration with a resolution of ~0.5 nm. The 1200 grating gives greater wavelength resolution as ~90 nm of light is delivered in each frame, with each pixel having ~0.1 nm resolution. A MCP PMT is attached to the side exit of the Triax and is operated using a 3 kV HV supply, and this has greater sensitivity than the CCD. Light intensity measurements for a particular part of the spectrum (the width controlled by the grating chosen and the slit widths) can be made on low luminescing samples. The maximum wavelength ranges (i.e. with the slits fully open) integrated by the MCP PMT are 100 nm for the 1200 grating and 500 nm for the 150 grating. By combining the movement of the grating with sequential measurement of the signal from the MCP PMT, the system can in principal create high sensitivity wavelength spectra for poorly

luminescent samples. However, all of the samples analysed were sufficiently bright that the charge-coupled device (CCD) provided faster spectral acquisition. The primary use of the MCP PMT is for TR experiments (see below). All spectroscopic data were corrected for system response offline using correction files created using standard light sources and operated through software written in house by Adrian Finch.

4.8.7 Time-Resolved Measurements

The lifetimes of the XEOL, i.e. TR XEOL can be measured by studying the response of the MCP PMT in different operating modes. The normal operation of the synchrotron is where 900 of the 936 possible buckets of electrons of the storage ring are filled with electrons and there are approximately 4.3 billion electrons (~ 0.7 nC) in each bucket (Walker, 2009). In hybrid mode, the main fill consists of 685 buckets filled with electrons, leaving a gap of 251 buckets; the central bucket in this gap is also filled with up to 37.5 billion electrons (6 nC). This gives a pseudo "single-bunch" which has a FWHM of 50 ps with a time gap of ~ 0.24 μ s before and after the adjacent bursts of X-rays ([Figure 4-13](#)). The X-ray peak shape is Gaussian and repeats every 1.8 μ s. I also experimented with TR XEOL in "low alpha-mode", where the general profile is similar but the pulse width is exceptionally short (~ 1 -5 ps) and the charge carried in the bunch limited to tens of μ A (Martin et al., 2011). The low alpha mode might provide lifetime data approaching the response time of the MCP PMT (i.e. <10 ps), but the commensurate loss of X-ray intensity and the binning of data over smaller timeframes means that the decay times of the resulting data are unresolvable due to insufficient

counts. Thus the hybrid mode proved the most successful fill pattern for TR XEOL and was used to collect all the TR data reported here.

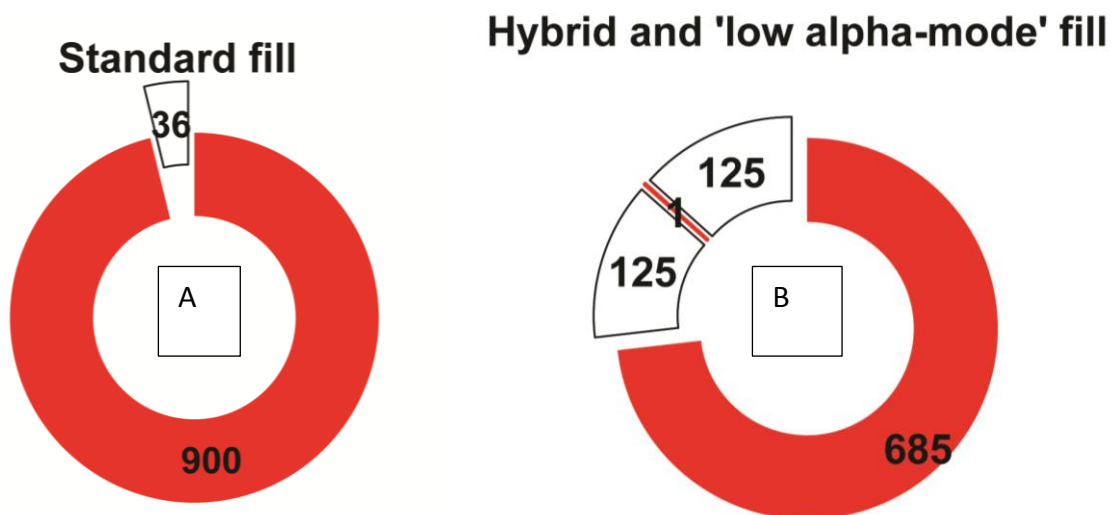


Figure 4-13 Diamond synchrotron ring standard

A with the solid red area indicating 900 buckets filled with bunches of electrons and the remaining (white) 36 buckets remain empty.

In the hybrid and low alpha modes,

B the main bunch consists of 685 buckets (red solid area) filled with electrons and in the remaining part, one bucket (red line) is filled with electrons preceded and followed by 125 empty buckets (white). Produced from data included in (Walker, 2009, Martin et al., 2011)

. Source (Taylor et al., 2013)

The analysis of emitted light produced by the X-rays in the pseudo "single bunch" is used for TR experiments. The MCP PMT has a typical event rise time of 150 ps and a transit time spread of ≤ 25 ps FWHM, allowing the measure of the arrival times of individual photons to an accuracy of 10's of ps. To facilitate TR experiments the ring produces a timing signal from the synchrotron that can be synchronised with the hybrid pulse at the sample. The time difference between the hybrid pulse arriving and the first

luminescence signal being detected is converted to a voltage pulse by the Time to amplitude converter (TAC), the size of pulse being proportional to the time difference. These pulses are then processed through a fast multi component analysis (MCA). The layout is shown in Figure 4-12 and this design is capable of modelling lifetimes from ~ 25 ps (half the width of the pulse) to ~ 400 ns (i.e. twice the width of the window after the bunch).

Data collection and analysis are through the technique of single photon counting, measuring the elapsed time for the first photon to be detected following the excitation timing pulse, whilst the timing comes from the TAC timing card. The timer starts when the X-ray pulse arrives (every $1.8 \mu\text{s}$) and stops when a photon is detected. If it reaches the 50, 100 or 200 ns user defined time limit it stops until the next start signal resets the card and how many starts occur is recorded. At $1.8 \mu\text{s}$, the maximum that can be recorded is 550 kcps. A detected photon within the time limit is called a valid conversion and flux is limited so that only 5% of the possible 550,000 starts are valid conversions, i.e. in 95% of cases no photon is detected in the 50-200ns time limit. The goal being that this ensures all photon events are recorded, as the probability of two photon events in the measured test period is negligible. The photon is detected by the MCP PMT, which is detecting all the time. The TAC differentiates pulses and times their arrival after the excitation pulse. To test the effectiveness, data collected within the range of 1% to 10% of the valid conversion rates are compared, and this showed no significant variation in measured lifetimes both for short and long life emissions, nor are any non-linear responses as a function of the intensity detected. This ratio is an established technique used in TCSPC to prevent 'pile up' (the arrival of a second photon) in the experimental

period (Becker, 2008). The intensity of the count rates is moderated by closing the entrance slits so that the dead time on the detectors is <5% in order to avoid non-linear responses as a function of data intensity. The events are binned into time bins with respect to the synchrotron time pulse and via repeat measurements; the data build to a distribution histogram that reflects the decay signals. The integration times were typically 20 minutes per profile. These data are de-convoluted using least squares fitting. The data fitting was completed initially for a single exponential decay and then for a double exponential decay; the final fit used representing the better fit. The TR data fitting is completed using Igor Pro 6.2.2. graphing software and the formula:

$$Y = y_0 + \sum_1^n A_n \exp\left\{\frac{-(x - x_0)}{\tau_n}\right\} \quad \text{Equation 20}$$

Where Y is the observed amplitude at time x , A_n is amplitude, τ_n is the fitted lifetime and y_0 is the background. x_0 represents the time offset for the beginning of the exponential decay and the process is repeated for n components. The fitting methodology used is least squares utilising the Levenberg–Marquardt algorithm to generate iteratively the de-convoluted fit (Marquardt, 1963)

4.9 Experimental Techniques

	Sample list			
<i>Ref.</i>	<i>Name /description</i>	<i>Details</i>	<i>References</i>	<i>Element of interest</i>
RT1020	one quarter of a 2" wafer with a nominally un-doped GaN epilayer of 4.4 micrometres thickness on a 430 micrometres thick sapphire substrate	density of threading dislocations measured at 3e8 cm ⁻² as determined by AFM	(Kappers M.J., 2011)	
RT1013	single crystal chrome rich tourmaline	Gem specimen		Cr
MISI	single crystal alkali feldspar	Microcline		Fe
R1-11a	Rapakivi Granite suite of South Greenland it is from the Prins Christians Sund granite		(Harrison et al., 1990, Finch and Klein, 1999)	Fe
RT1001	Pyrope garnet	Gem specimen		Fe
RT1002	Andalusite	Gem specimen		Mn
RT1003	Tsavorite garnet	Gem specimen		V
RT1004	Grossular garnet	Gem specimen		V
RT1005	Yellow chrysoberyl	Gem specimen		Cr
RT1006	Ceylon sapphire	Gem specimen		Ti
RT1007	Yellow chrysoberyl displaying chatoyancy	Gem specimen		Ti
RT1008	Kashmir sapphire	Gem specimen		Ti
RT1010	Jadeite	Gem specimen		Ti
RT1011	Kunzite	Gem specimen		Cr
RT1012	Rhodolite garnet	Gem specimen		Cr
RT1013	Chrome tourmaline	Gem specimen		Cr

Table 4-1 - Summary of samples used to test system.

4.9.1 CW XEOL Spectroscopy

Collection of a CW XEOL spectrum is achieved using the synapse CCD detector with the 150 grating, and with this configuration, the entire spectrum from 200 to 900 nm is collected in a single integration with a wavelength resolution of ~0.9 nm. For the majority of minerals the integration times are a few seconds.

Dose dependence of a sample is determined through a sequence of CW XEOL spectra collected from the same spot. The CW XEOL spectrum is collected and repeated multiple (e.g. 1000) times the experiment explores how the luminescence changes with time. The doses experienced by the sample can be estimated as the product of time and X-ray flux. Beamline I18 has a range of attenuators upstream of the final focussing mirrors (Mosselmans et al., 2009), principally aluminium foils of different thicknesses. CW XEOL was also explored as a function of dose rate by inserting combinations of these foils into the X-ray beam upstream of the experiment (Table 4-2). The estimated attenuation of the X-rays for a particular energy was calculated using the X-ray transmission data available at [http://henke. lbl. gov/optical_constants/](http://henke.lbl.gov/optical_constants/). All of the CW experiments in this section were completed on a Na rich feldspar called cleavelandite (CLBR).

Al foil thickness (μm)	Attenuation (%)
250	99
150	94
100	84
50	61
30	45
15	25
0	0

Table 4-2 - Summary of attenuation foil thicknesses and relative attenuation for 7 keV X-rays.

Source: [http://henke. lbl. gov/optical_constants/](http://henke.lbl.gov/optical_constants/)

4.9.2 TR XEOL

Using the hybrid mode of the synchrotron and examining the timing of photon arrival events following excitation, the decay profile of the XEOL is determined Figure 4-17. A prerequisite in TCSPC is to model the system response to enable its subtraction from the data collected. Most systems have some inherent distortion to the decay profile, which can be determined and therefore corrected. In TR PL, the primary laser profile is measured directly using a medium that scatters the primary beam and has no significant lifetime. For our TR XEOL system, analysis of the primary beam profile using scattering is not possible since the X-rays used for excitation are not detected by the CCD or MCP PMT. I therefore sought a material which has an ultrafast (e.g. fs) luminescence decay during X-irradiation as a substitute for a scattering medium. I obtained a sample of a GaN thin film RT1020 that from pulsed PL measurements is known to have a lifetime less than 10 ps. Personal communication (Kappers M.J., 2011) data is also collected from a Fe-rich microcline (ordered potassium feldspar) MISI.

As an experimental procedure, it proved valuable to collect CW XEOL spectrum using the CCD before each TR XEOL experiment so that the lifetime component could be understood within the context of the overall spectrum. The time window between the single bunch and the main bunch in hybrid and alpha modes is ~ 200 ns, (Thomas et al., 2006) and hence lifetimes longer than ~ 400 ns cannot be resolved. However, the presence of longer lifetimes can be inferred from the intensity of the 'background' signal.

Each electronic transition has a natural lifetime τ_n . I used TR XEOL on MISI to scan a range of emission wavelengths to probe the extent and shape of individual TR emission

profiles. The experiment was completed using 4.5 keV excitation, an entrance slit width of 2 mm and the 150 groove 500 blazed grating centred at 300, 350, 375, 400, 425, 450 and 500 nm on 2 mm side exit slits to MCP PMT with 60 s integration.

4.9.3 XEOL Spatial Mapping

This experimental methodology explores the capabilities of TR XEOL in heterogeneous samples. The beamline has an existing micron resolution XRF mapping facility that can be utilised with this system. To test the viability spectra were collected from different points in a multi-phase sample R1-11a using 4.02 keV X-rays, with an entrance slit width of 1 mm using the 1200 groove 500 blazed grating centred at 500 nm on 2 mm side exit slits giving a spectral width of ~ 200 nm onto the MCP PMT. If developed this is a valuable technique to investigate texture and can reveal concealed and overlapping emissions on a micron scale spatial resolution. Larcheri et al. (2008) have investigated scanning near-field optical microscopy (SNOM) to detect CW XEOL with success at high spatial resolutions but the technique is primarily a surface technique. Rosenberg et al. (2012) has reported on CW XEOL imaging using a conventional microscope to collect the signal, achieving resolutions in μm . Sham et al. (2010) have reported on the combined collection of XEOL and XANES for imaging but this is primarily a CW technique. Reiger et al. (2010) describe a new system at the Canadian Light Source (CLS) incorporating a streak camera capable of single collection combined TR and wavelength resolved data. A XEOL /XANES mapping system has been developed at the ESRF described in (Martinez-Criado et al., 2007)

4.9.4 OD XAS

Beamline I18 delivers X-rays from 2-20 keV and I have completed experiments to measure OD XAS in this harder X-ray regime. TR XEOL spectra were collected from a suite of mineral samples (Figure 4-17); RT1003, RT1004, RT1002, RT1001, RT1005, RT1006, RT1008, RT1007, RT1011, RT1010, RT1012, and RT1013, with reported inter-ion absorption-relaxation centres with known PL characteristics. Spectra were collected from above and below the K (or L₃) absorption edge of interest to identify samples showing a TR-OD-XAS response.

4.10 System Test Results

CW XEOL Spectroscopy

The sample of albite (CLBR) was excited using 7 keV X-rays and the spectra collected used an integration time of 2 s with an entrance slit width of 1 mm. In Figure 4-14 four peaks are identified and labelled in the XEOL spectrum, which correlate with Table 4-3 (Gaft et al., 2005). The system to provide high spatial resolution for investigating heterogeneous samples

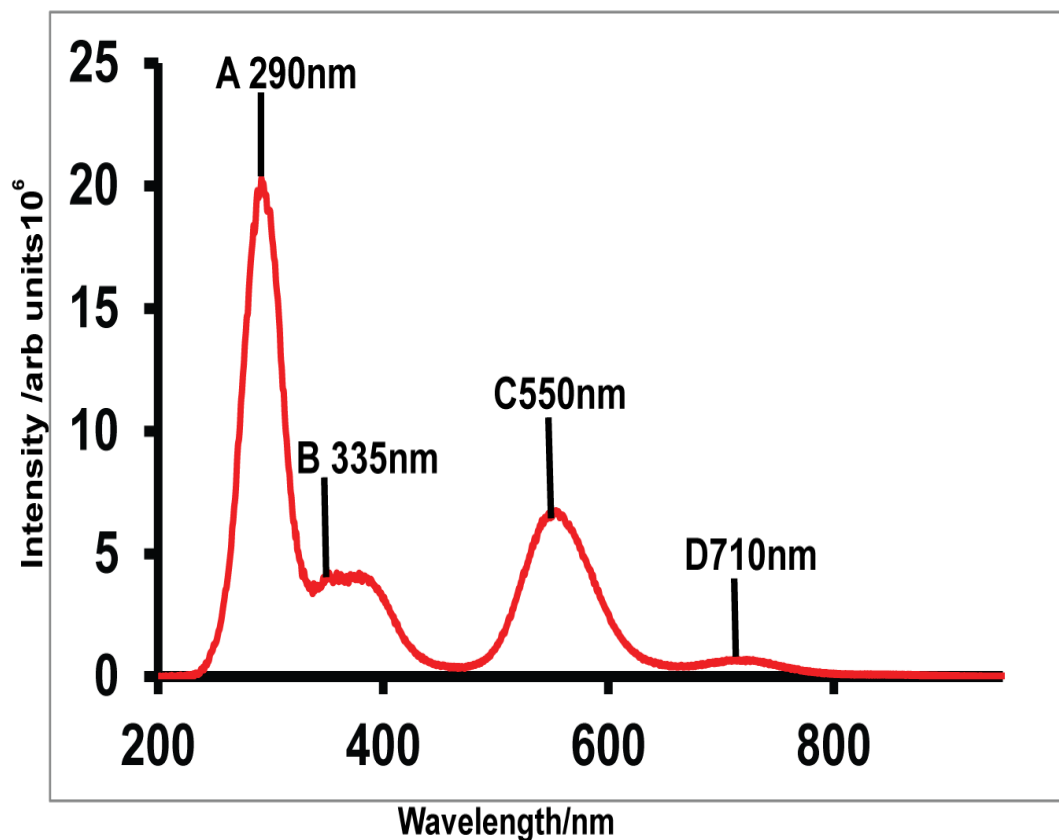


Figure 4-14 - CW-XEOL spectra from cleavelandite (CLBR) excited using 7 keV X-rays.

The sample displays 4 distinct emission peaks labelled A-D on the spectrum with peak maxima at 290, 335, 550, 710 nm. Source (Taylor et al., 2013)

4.10.1 XEOL Dose and Dose Rate Dependence

This type of experiment explores the stability of the luminescent centres in samples to X-irradiation. The experiment on CLBR shows a dose dependent response with peak 'C' at 557 nm showing a reduction in signal as a function of dose rate dependence of different luminescent peaks in the same sample.

Identified Peak	Wavelength measured (nm)	eV	±	Literature wavelength (nm)*	eV	Attribution
A	290	4.28	.02	296	4.19	Pb ²⁺ / Na phase or interface
B	335	3.71	.02	335	3.71	Ce ³⁺
C	550	2.26	.02	555	2.23	Mn ²⁺
D	710	1.75	.02	716	1.72	Fe ³⁺

Table 4-3 - Summary of CW XEOL spectral features compared with published data.

Source: (Gaft et al., 2005)

Dose dependence experiments probe the behaviour of a sample as it interacts with the incident radiation. X-ray excitation interacts with sample typically changing the charge state of defects leading to the disappearance /creation of luminescent emission features these transactions are encoded within the luminescence response. Although dose dependence responses are complex, dose dependence studies can be used to test the veracity of suggested causes for the luminophores within systems in which there is prior characterisation. Variations in responses and recovery as a function of temperature can also explore the energy levels of trap defects and their susceptibility to modification. It is also conceivable that the modification could be orientation sensitive, for example if modification can only occur from a resonant incident photon and none of the subsequent elastic or inelastic scattering events or lower energy secondary X-ray photons. This orientation sensitive signal could then be used to infer site-specific information regarding the absorber. Such experiments are analogous to ion implantation experiments where the luminescence behaviour of materials during irradiation by ion beams is studied (King et al., 2011b, King et al., 2011a, Friis et al., 2011, Finch et al.,

2003). For example, the X-ray dose dependence studies of CLBR shown in Figure 4-16 show rate dependence of different luminescence peaks in the same sample. This allows peaks resulting from different defect types to be identified since different emissions from the same centre type should have similar dose rate dependences. For example, the dose rate dependence of blue, yellow and red luminescence bands in the albite CLBR are different. This reinforces the view that these emissions are from different centre types the spectra shown in figure 4-16 show similar responses to ion beam dose dependence studies on the same sample (Garcia-Guinea et al., 2007a), in that certain emissions are affected and other emissions are not. I have also explored the potential for dose dependence using varying incident photon energies. However, X-ray flux also changes as a function of X-ray energy providing responses that are the product of both dose rate and energy. Because of the non-linear response of the ion chambers that are used to measure incident photon flux, varying photon energy simple by normalising the data to I_0 is insufficient. Dose rate experiments are illustrated by the analysis of the albite CLBR at 7 keV using the attenuators listed in Table 4-2 to provide beam intensities ranging from 1-100% of the maximum. To avoid dose dependence compounding with dose rate dependence behaviour, the sample was exposed to the least intense beam first, the dose rate increased gradually, and the sample was moved to a fresh position for each measurement. The synapse CCD detector was used using the same parameters as the CW XEOL spectrum as shown in Figure 4-14.

Quantification of dose rate behaviour provides insights into the nature of lumiphores and such experiments are similar to the comparison of luminescence from ions and molecules (Correcher et al., 2007a). In a single excitation from ground state, the

intensity of luminescence would be in principle linearly dependent on the incident X-ray flux. However, where the luminescence derives from excitation of a previously excited (e.g. triplet) state, the probability of luminescence is dependent upon the square of the flux rate dependence of different luminescence peaks in the same sample.

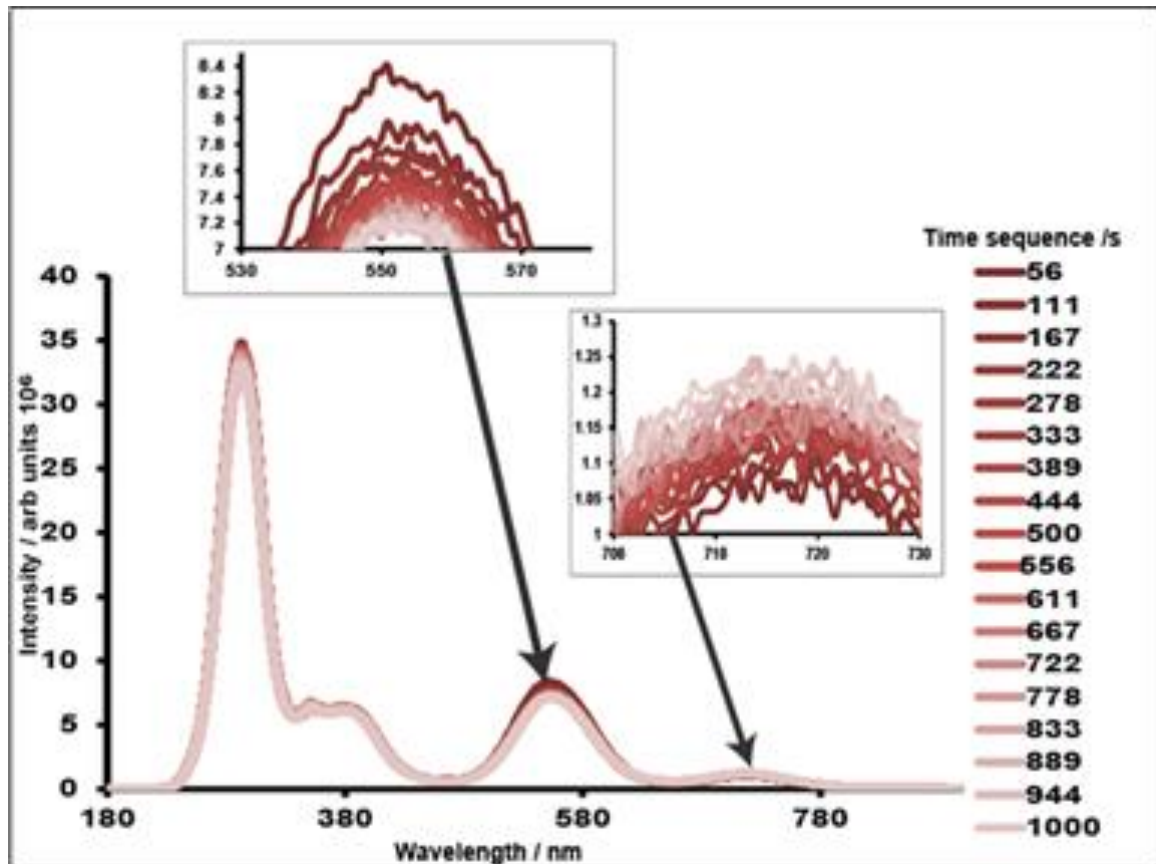
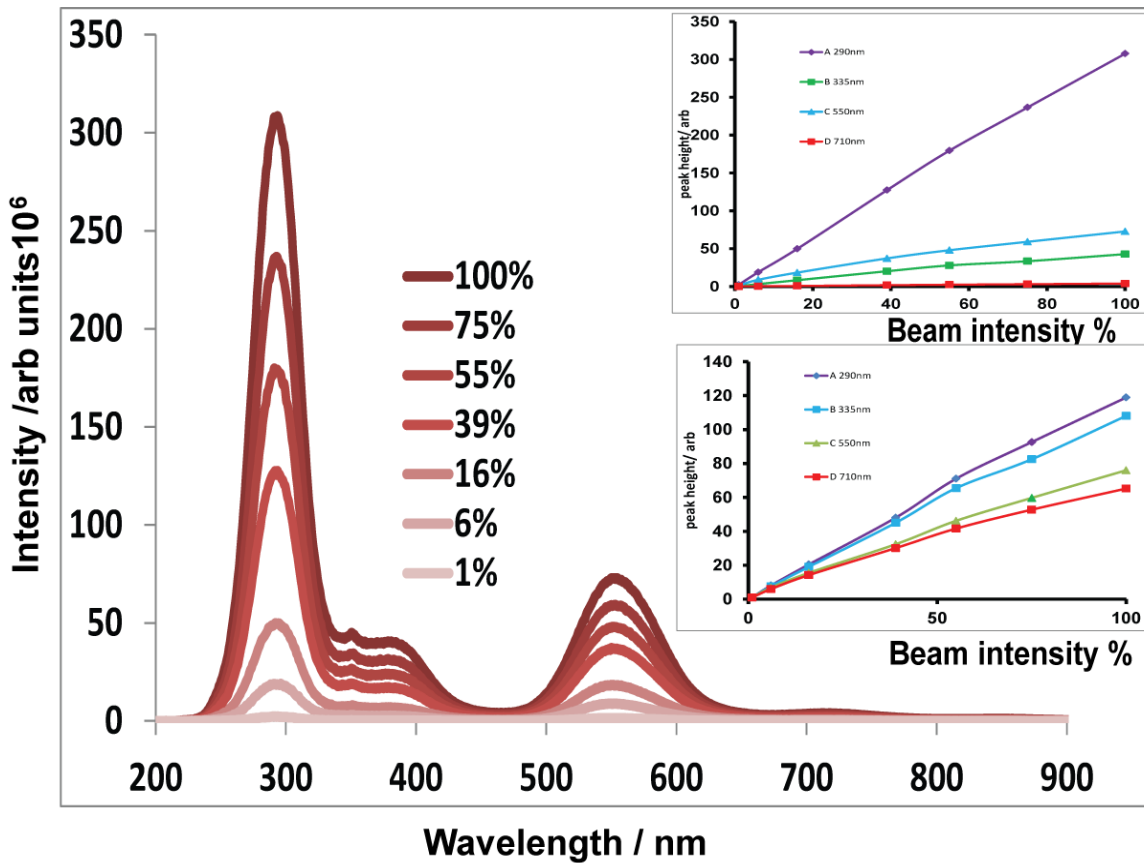


Figure 4-15 - A sample set of CW-XEOL data taken from a data set collected from CLBR.

The data collection consisted of 1000×1 -second integrations. The figure illustrates the dose dependent response of the sample, which was collected at 7 keV from the same spot. From the insets, it can be seen the C peak (as labelled in Figure 4.15) shows a significant reduction in signal while the D peak shows an increase in signal over the same period of irradiation. Source (Taylor et al., 2013)



Peak	Orientation 1 top Y=	Orientation 2 bottom Y=
A 290nm	$3E+06x + 2E+06$	$1.2041x + 1.2233$
B 335nm	$432208x + 1E+06$	$1.0855x + 1.6818$
C 550nm	$711862x + 1E+06$	$0.756x + 2.3945$
D 710nm	$39193x + 128372$	$0.653x + 2.8852$

Figure 4-16 - CW XEOL spectra showing the dose rate dependence of CLBR to varying beam intensities. inset graphs show the peak heights (A-D), measured from two different crystallographic orientations (sample rotated through 90^0), and plotted as a function of beam intensity. The responses are seen to vary between the two orientations. The polynomial fit results for each curve are summarised in a table at the base. Source (Taylor et al., 2013)

Quantitative comparisons of the dose rate dependence of different emission bands in a single spectrum provide insights into whether luminescence derives from singly or multiple excited states. Dose dependence experiments utilising exposure time with fixed incident energy flux have a number of applications. Firstly, they are important as a validation of other experiments to eliminate sample modification as an explanation for

experimental results. Dose dependence can be used to investigate the nature of radiation damage and more specifically, the stability and energy environment of particular defects. Dose rate experiments probe the behaviour of electrons while in the excited state, which is a poorly constrained aspect of the solid state (Bloch, 1929, Muhlhausen and Gordon, 1981) . The technique also has applications to explore the excitation of the excited state and trap defects, non-linear responses and the variation between different emissions, and forms an important technique for quantitative analysis. The experimental results also allow us to probe decay routes at varying excited state populations. The dose and dose rate dependence of minerals is currently of particular interest in TL and OSL dating (Chen and Leung, 2001, Chen and Pagonis, 2011). This illustrates how excitation and consequent differences in the nature of the excited state population can significantly influence relaxation/emission pathways. CLBR is an anisotropic mineral and to explore the effect of the polarised nature of the incident X-ray beam on the XEOL signal, I collected the dose response at two orientations, with the sample being rotated $\sim 90^\circ$ between measurements. The signal being transmitted through a fibre bundle loses coherence and polarisation during transit and I therefore ruled out polarisation effects within the spectrometer (Burgess et al., 2010). A summary of the results is shown in the inset of Figure 4-16. The intensities are orientation sensitive and vary for individual emissions. There are two possible interpretations for these variations, the variations in the absorber QE as a function of excitation photon polarisation are being measured, or alternatively the variations in the absorption cross section of the luminescent signal are being measured in an anisotropic sample. It is possible to differentiate between the two alternatives by including a polarising filter with adjustable orientation positioned immediately in front of the entrance to the fibre

optic. In some anisotropic samples differences in the measured emissions were determined dependant on the orientation of the polarising filter.

4.10.2 TR XEOL Lifetime Measurement

The results from RT1020, a GaN thin film on a sapphire substrate, display much longer lifetimes than recorded by PL excitation at a slightly shifted wavelength of 330 nm. The lifetimes recorded were $\tau_1=1.39 (\pm 0.07)$ ns and $\tau_2= 53 (\pm 1)$ ns by TR XEOL (Figure 4-17) in comparison to lifetimes of between 5-10 ps recorded from PL. The inset shows the CW emission spectra for the sample displaying two peaks. The peaks identified were individually analysed using the TR data and exponential curve fitting that calculates the

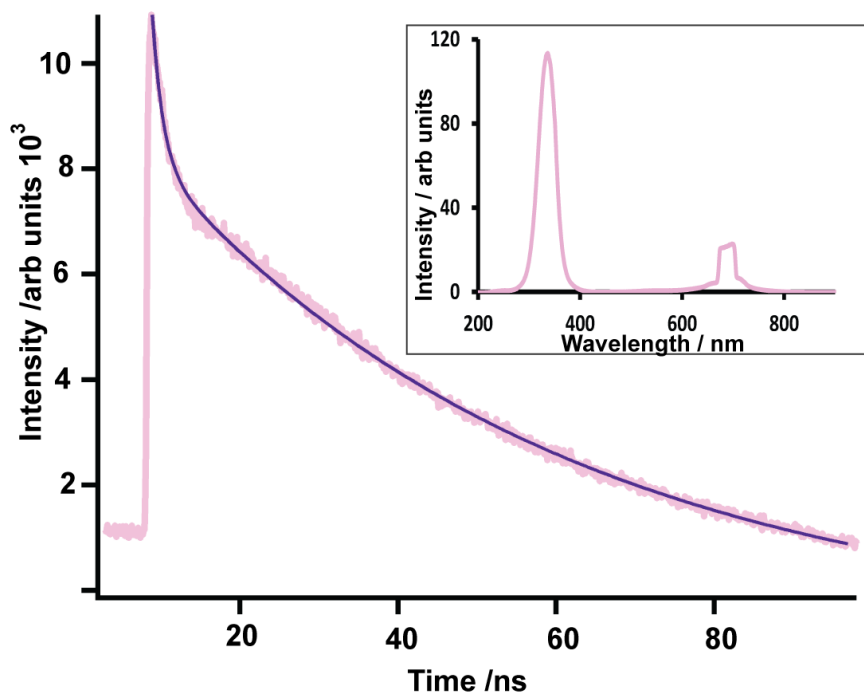


Figure 4-17 TR XEOL from RT1020 signal collected from a sample of thin film GaN on sapphire substrate

Excited at 7000eV centre 335nm The data fits to a double exponential with $\tau_1=1.39 \pm 0.07$ ns, $\tau_2= 53 \pm 1$ ns. Inset shows the CW-XEOL spectrum from the same sample (Taylor et al., 2013) .

lifetime (τ) values for the individual emission decays and their relative amplitudes. The main body of Figure 4-17 shows the fit for the 335nm emission. The emission at $\sim 700\text{nm}$ was not identified but had a lifetime that was longer than the system was capable of measuring ($>200\text{ ns}$). I hypothesise that the difference in measured lifetime to that previously communicated to me from PL analysis is due to the localisation of the absorption /emission of the excitation that does not occur with X-ray excitation. In contrast, a Fe-rich microcline (ordered potassium feldspar, MISI), showed a fast luminescence component ($\tau_1 \sim 0.13\text{ ns}$) centred on $\sim 450\text{ nm}$ using an incident energy of 4.5 keV Figure 4-18. This was modelled as a symmetrical Gaussian profile (Figure 4-18) inset) and a good fit was obtained; therefore, I consider this profile to approximate to the profile of the X-ray pulse with a FWHM of $\sim 50\text{ ps}$. These data indicate that system artefacts in the processing of pulse events are negligible and in these experiments, I have never observed the X-ray pulse morphology deviate from this model.

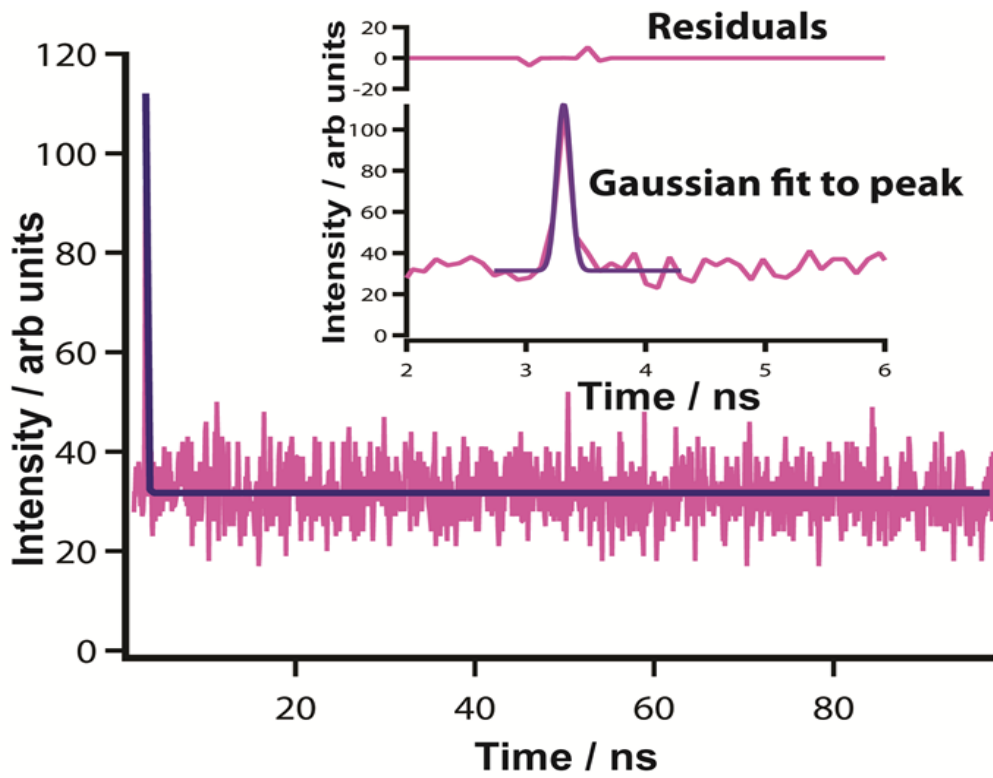


Figure 4-18 - TR XEOL from sample, ref MISI best fitted with multiple luminescent decays with the shortest lifetime (21 ps). Inset shows the Gaussian fitted TR peak with residuals Source (Taylor et al., 2013)

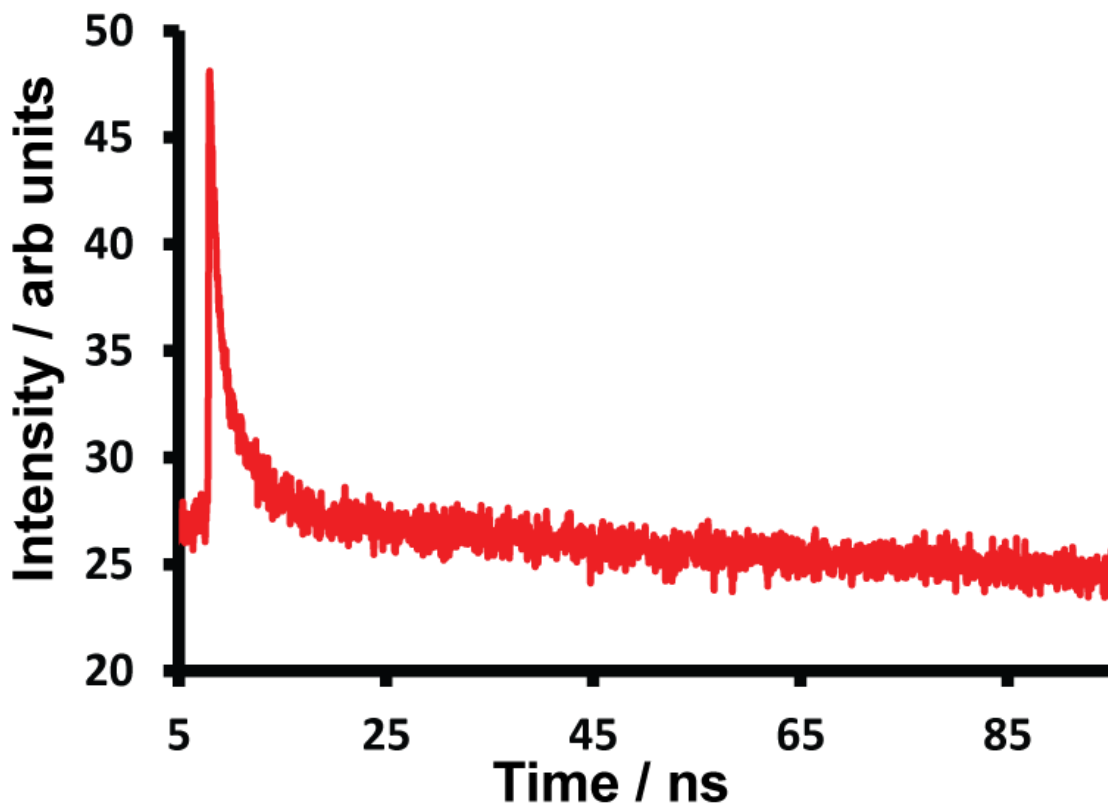


Figure 4-19 - TR XEOL RT1011 pink kunzite illustrating the response from a relatively short life component with a longer life component with a lifetime ≥ 200 ns Source (Taylor et al., 2013).

Comparisons of TR PL and TR XEOL are informative. For example, TR PL on CLBR showed lifetimes ranging from a few ns to a few ms. TR XEOL similarly shows a range of luminescence lifetimes from those measured in ps to responses that are slower (>100 's of ns) than the resolution capability of the system. A long lifetime in the range of 0.2 – 1 μ s is reflected as an increase in intensity from that of the level reached at the end of the exponential decay and that displayed in the period immediately prior to the hybrid pulse. This increase in intensity reflects the response of the sample to the main pulse in the ring (Figure 4.19). The effect is not seen with luminescent responses that consist only of short (<200 ns) lifetime responses that decay within the preceding empty window. Lifetimes longer than 400 ns are seen as high background counts. Modelling of

the decay profile has been possible in some cases as a single exponential, but the majority of profiles can only be modelled satisfactorily as multiple exponentials indicating that in many cases, there are multiple, overlapped emissions.

The sample MISI, shows a much shorter lifetime emission than RT1020 and that provided a good profile of the TR machine response. The lifetimes recorded for luminescence/spontaneous emission is over two orders of magnitude shorter than that normally recorded in the literature for bulk material luminescent lifetimes. These results have been replicated for examples of the featured samples using other instrumentation and utilising ps laser excitation. The TR results from MISI display a short lifetime emission convoluted with a long lifetime emission that is outside the system's ability to resolve. The τ value for the short life signal tends to lower values as it approaches 450 nm from a high of 0.5 ns at 400 nm Figure 4-20 then between 450 nm and 500 nm the signal disappears. An example is described within the TR experiment exploring the profile of an individual TR emission in the sample MISI. The short lifetime reaches a maximum at 400 nm of 260 ps and then rapidly reduces until it reaches a minimum at 450 nm of 65 ps; beyond 450 nm, the signal rapidly disappears, and at 500 nm, it is not detectable.

The TR XEOL consistently provides resolutions in the ps domain. The results provide an overview of a range of experiments of which the system is capable. TR XEOL as a technique offers great potential. In particular, the system has the potential for the development of TR XEOL micron-scale spatial mapping. Collecting a broad range of the XEOL spectra (300-500 nm) allows the analysis of overlapping emissions that can be combined with the spatial capabilities of the microfocus beamline to investigate the

fabric of heterogeneous material. The system can limit the spectral range examined to < 5 nm width allowing the probing of individual emissions.

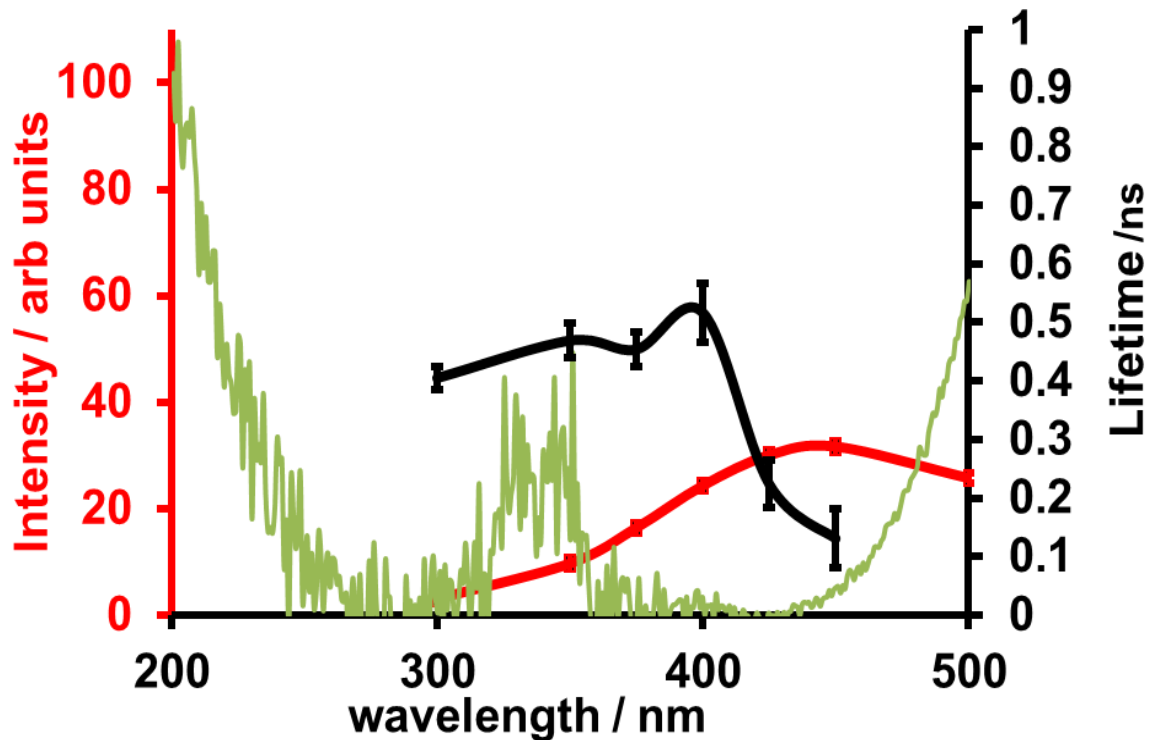


Figure 4-20 - Short lifetime luminescent emission (LH axis) plotted against wavelength for (MISI).

The intensity of the longer lifetime luminescent emission (RH axis) displayed as high background in spectra. The lifetime (ns) of the short life emission when measured at different wavelengths shows an inverse relationship with the intensity of the long lifetime (2σ error bars). Excitation energy 4.5keV Source. Green curve CW XEOL spectrum (Taylor et al., 2013) .

4.10.3 Fibre Optic Transit Time

To explore the implications of transit time in the fibre optic, the temporal position of the TR peak is analysed as a function of emission wavelength. Figure 4-21 displays transit time for the fibre optic plotted as a function of wavelength calculated from the arrival time of the time resolved pulse of MISI, whilst Figure 4-22 displays the exponential relationship described by Cochrane et al. (2001). Fibre optic transit time has no impact on the measurement of lifetime. Transit time simply changes the value of X_0 , but it will be shown in section 5.2 that this has other implications.

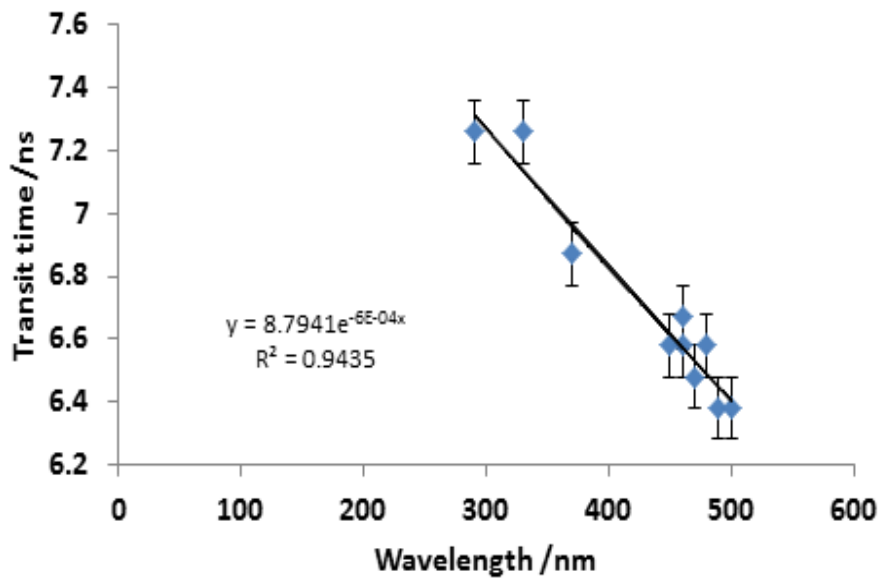


Figure 4-21 – Fibre transit time.
Showing the measured transit time of the TR pulse through the fibre optic cable as a function of wavelength the trend is as expected.

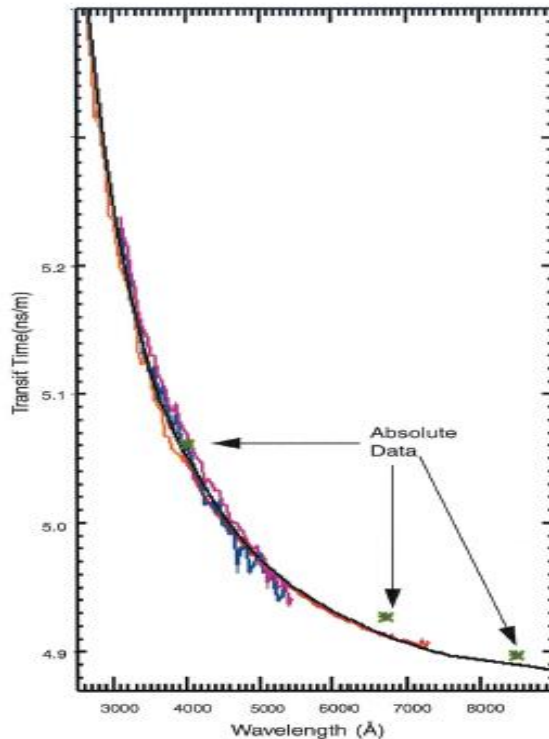


Figure 4-22 - Transit time per unit length.
Graph from (Cochrane et al., 2001). The asterisks represent measured data and the coloured curves are measured whilst the black line is derived.

(Cochrane et al., 2001)

$$\tau = \frac{L}{c} \left(n - \lambda \frac{dn}{d\lambda} \right)$$

Equation 21

Where the transit time τ for a single mode to travel distance L , c is the speed of light in vacuum λ is the wavelength of the light n is the refractive index of the glass fibre.

4.10.4 Investigation into Anomalous Second TR Peak

CLBR recorded an unexplained second TR peak response and this anomaly was also detected in a number of other unrelated mineral samples. My hypothesis was that the second peak was the detection from a harmonic of a strong high-energy UV signal. Due to the extended path length that a short wavelength signal has in a fibre optic, its arrival at the detector had a \sim ns delay from the original pulse. The delayed (artefact) signal was measured through the wavelength selecting exit slits as a harmonic generated on the

grating. The nature of the artefact was explored by placing a UV opaque filter (silica glass slide) into the emission signal beam between the sample and the diffraction grating. This completely removed the delayed peak as can be seen in Figure 4-23. Hence, in this case I infer the second peak is caused by the detection of a harmonic of a strong UV emission.

The design of the system includes dual fibre optics. The fibres are made of glasses with different refractive indices (RI), and as can be seen from Equation 21, the transit time is a function of the RI of the glass, which has the potential to be an additional factor to the wavelength dependent artefact.

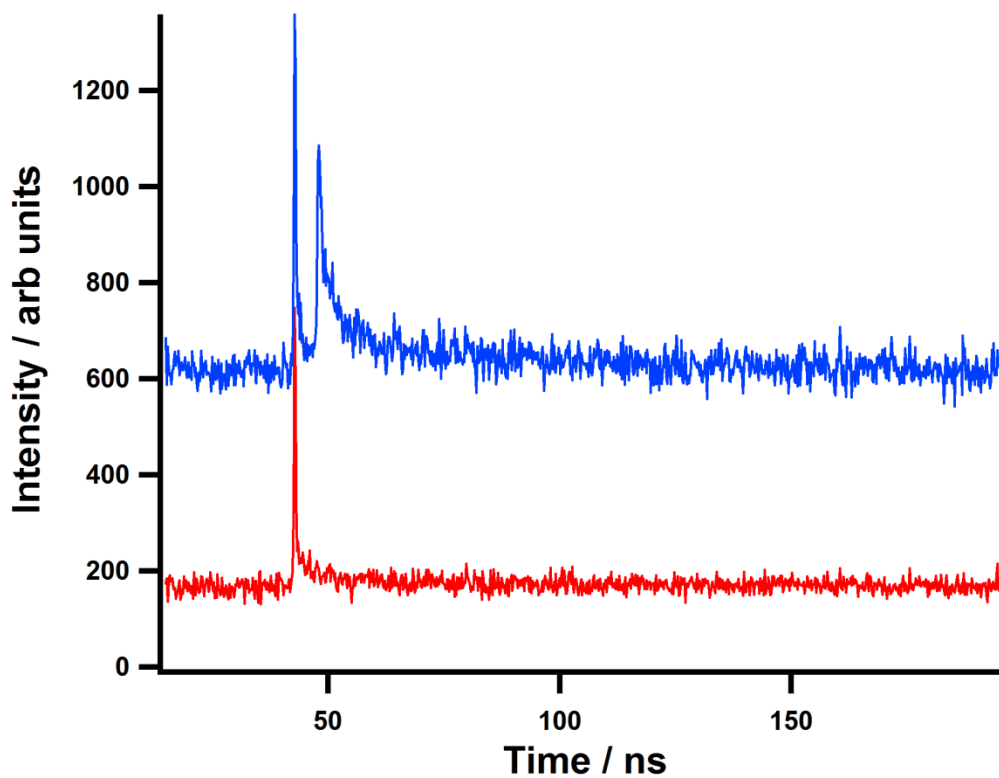


Figure 4-23 - CLBR 7 keV excitation TR spectra collected at 460 nm (2.70 eV) centre 1 mm exit slits. Red curve with silica glass UV filter inserted into emission beam path blue curve with no filter (an offset value has been set for the blue curve y-axis intensity).

One of the hypotheses, I originally proposed, was that shorter wavelength emissions would have shorter measured lifetimes. From Figure 4-23 it can be seen that the longer wavelength left hand peak has a noticeably shorter lifetime τ than the shorter wavelength right hand peak of the blue curve. This is consistent with the original hypothesis, as the measured lifetime is unlikely to be the natural lifetime, but is more likely to be a modified lifetime shortened by a quenching or an energy transfer mechanism.

4.10.5 OD XAS

Looking at a range of Fe-bearing feldspars, I see no evidence of the Fe K-absorption edge in the luminescent intensities. To test the system I repeated the Soderholm et al. (1988) OD XAS experiment using a 10% Eu_2O_3 prepared sample I collected OD XAS with an energy scan over the Eu L_3 edge.

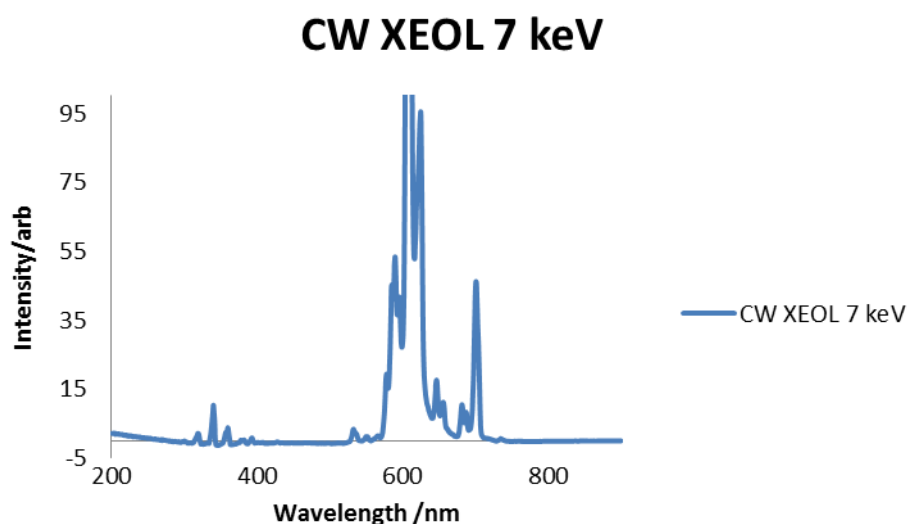


Figure 4-24 CW XEOL of Eu_2O_3 collected using 7 keV excitation prepared as a diluted ground powder suspended in ethanol and spread onto Al sample plate.

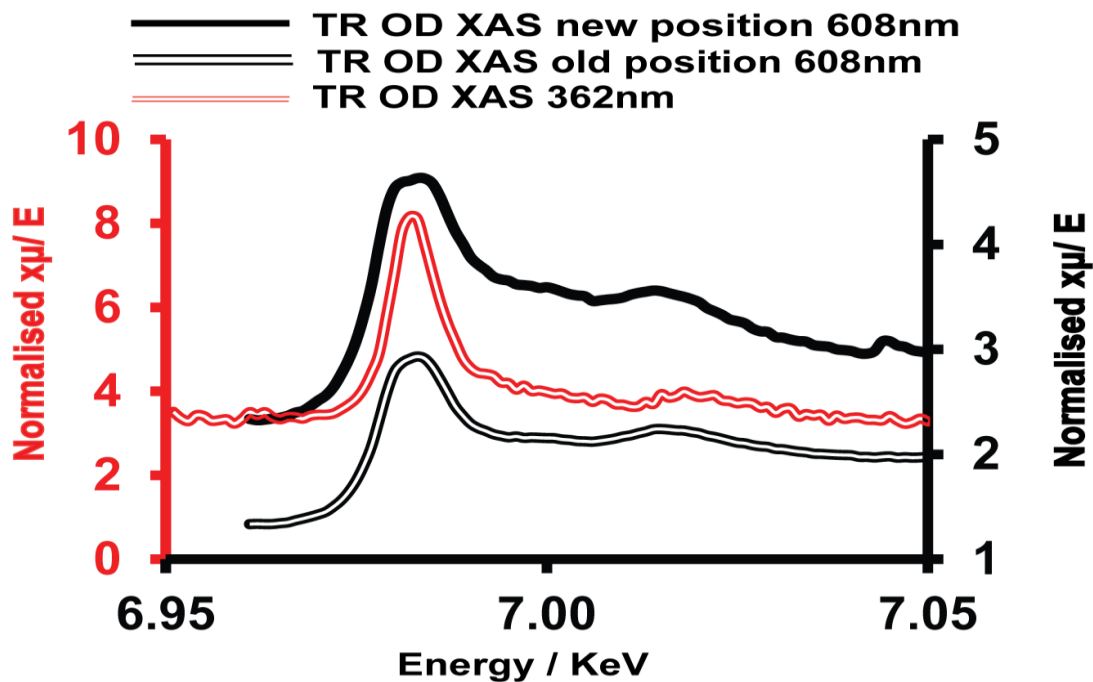


Figure 4-25- Comparison of OD XAS collected from 608nm emissions (RH axis solid single lines) and OD XAS collected from 362nm emissions (LH axis double line) from a 10% sample of Eu_2O_3 Source (Taylor et al., 2013)

The results compare TR OD XAS data collected at 608nm that had no detectable short life TR component with data collected at the 362nm emission that displayed a significant short life TR component (Figure 4-25). The long lifetime emission for the 608nm emission was collected direct from the PMT; the short lifetime TR OD XAS spectrum was collected using the 362 nm emission from the unfitted raw signal from the timing discriminator that samples signal from the 200ns window following excitation. The white line (Historical term describing peak at top of edge) of the peak from the TR XEOL signal labelled TR OD XAS shows a more significant response than either of the TR OD XAS spectra collected. The two CW spectra also show a drop in signal between them that I attribute to a dose dependence effect.

The results confirm the systems capability of detecting OD XAS and that where an OD XAS signal is not detected; it is as has been previously found not a system failure but the effects of concentration. In mineral systems, the concentration of trace elements is several orders of magnitude less than the sample of Eu_2O_3 which was prepared at 10%. The lack of sensitivity at trace element concentration ranging from 10^{-3} to 10^{-6} is most likely due to the effects of multiple overlapping emissions and multiple competitive energy relaxation routes. Meaning that without the deconvolution/ selectivity of the TR signal the OD XAS signal is lost beneath the inherent noise in the system. The TR system is capable of further refinement in its use by collecting a TR spectrum for each energy step, with each individual spectrum then being fitted to determine lifetimes and relative intensities. The intensity of the individual lifetimes could then be plotted to investigate if any isolated emission component carries an OD XAS signal. However, a typical EXAFS spectrum contains >300 data points and with a minimum data collection time for each individual point of 300 s, this would mean a single experiment could last in excess of 24 hours. Therefore, TR OD XAS is possible in principal but such long irradiation can generate substantial sample modification, limiting the viability even if the beamtime were available.

5 Results from feldspar minerals

This chapter investigates inter-relationships between lifetime and the QE of luminescence in both CW and TR modes in feldspar. This novel approach exploits the fact that the lifetime and QE of luminescence have both common and discreet factors affecting their responses. Through a range of experiments that measure responses as a function of these varying factors, the potential for insights into the luminescent process to be inferred from variations between the two measures is investigated. The primary objective of the work is to establish the concept that this type of comparative analysis generates useful additional insights into the luminescent mechanisms investigated. In addition, for the individual samples investigated interesting results are presented that generate a number of interesting avenues for future work. Results from a diverse range of samples are investigated to illustrate the technique is not limited and has potential for application in a wide range of materials and luminescent mechanisms. The X-ray excitation used is a powerfully ionising radiation adding the additional aspect to the analysis of sample alteration. This aspect is of particular interest to the Earth sciences as it is an important factor in the interpretation of mineral age and history. Sample change does however have a limiting aspect in respect of TR analysis; to collect a significant TR spectrum requires a period of excitation that would typically encompass any sample alteration generated. This means that sample change must always be considered when interpreting any spectra collected with this methodology.

Experiments are completed to explore sample responses as a function of dose and dose-rate; these techniques are particularly useful in exploring the extent and influence of sample change. The results presented are sample specific and I have limited the analysis

on occasions to the behaviour of individual emissions. Unless conceptually necessary I have not attempted to identify and allocate individual emissions as that is beyond the scope of this thesis. Many of the emissions are compared to previously identified emissions reported in the literature. In section 5.4, I have included the results of an investigation into the gem feldspar known as 'Plush feldspar' to illustrate how the TR and CW XEOL techniques are complimentary with the more conventional experimental techniques application such as XANES, EXAFS, LA ICP MS, and EMP .

5.1 MISI -Iron rich microcline alkali feldspar

Additional results for this sample are included in the previous chapter where they are used to illustrate the utility of the XEOL system. The results presented in this section are directed at sample investigation.

Dose rate dependence XEOL

Figure 5-1 shows a CW dose dependence XEOL experiment with a Fe peak centred at 691 nm (1.89 eV) and a shoulder centred at ~450nm (2.76 eV) that is not discernible at this resolution. These emissions are investigated in the time domain and the peak heights of the emission at 691 nm (1.80 eV) are plotted as a function of dose rate where they display a linear relationship (Figure 5-2)

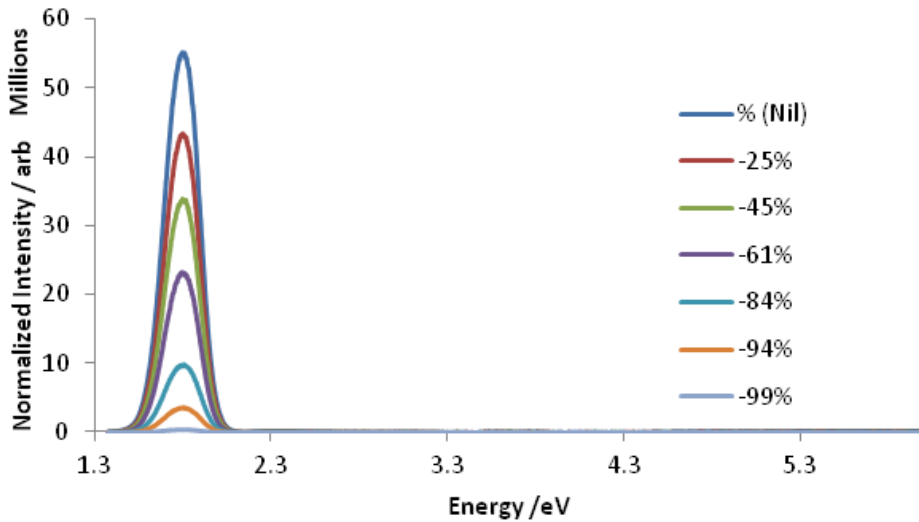


Figure 5-1 MISI dose rate responses.
 Responses to a 7 keV excitation beam with decreasing attenuation.
 Collection centred on 550 nm (2.26 eV) with 1mm slits and 150 line grating
 blazed at 500 nm 60 s integrations.

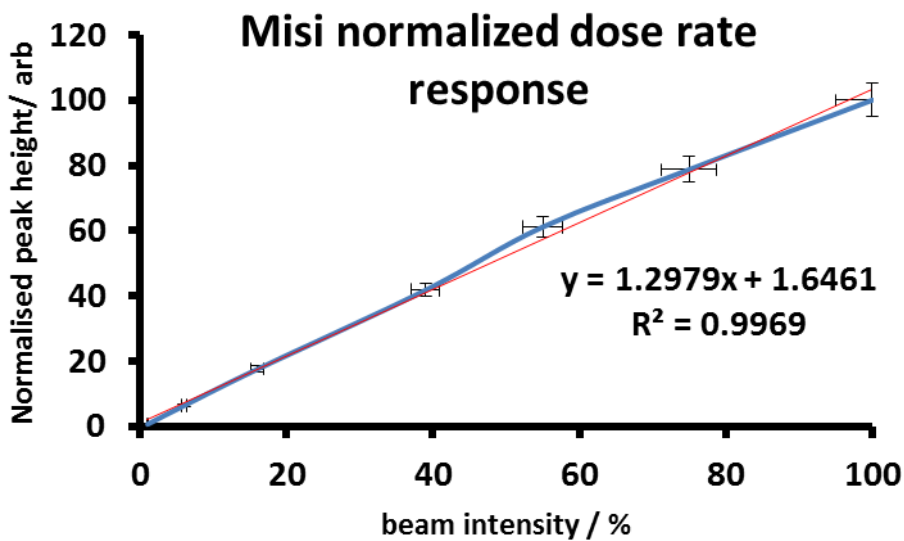


Figure 5-2 – MISI normalised dose rate response.
 Normalised peak height responses 60 s integrations 691 nm-1.80 eV with
 1mm slits and 150 line grating blazed at 500 nm. Peak heights taken from
 dose rate experiment (Figure 5-1). Data plotted complies with a linear fit
 illustrating the QE is unaffected by dose rate. Error bars 2σ .

5.1.1 TR energy dependence

The emission at 450 nm (2.76 eV) is investigated using two different excitation energies 7 keV and 4.5 keV and the results are shown in Figure 5-3 and Figure 5-5. Unless otherwise stated, every experiment is preceded by a 5 μ m move of the sample to prevent the introduction of dose effects.

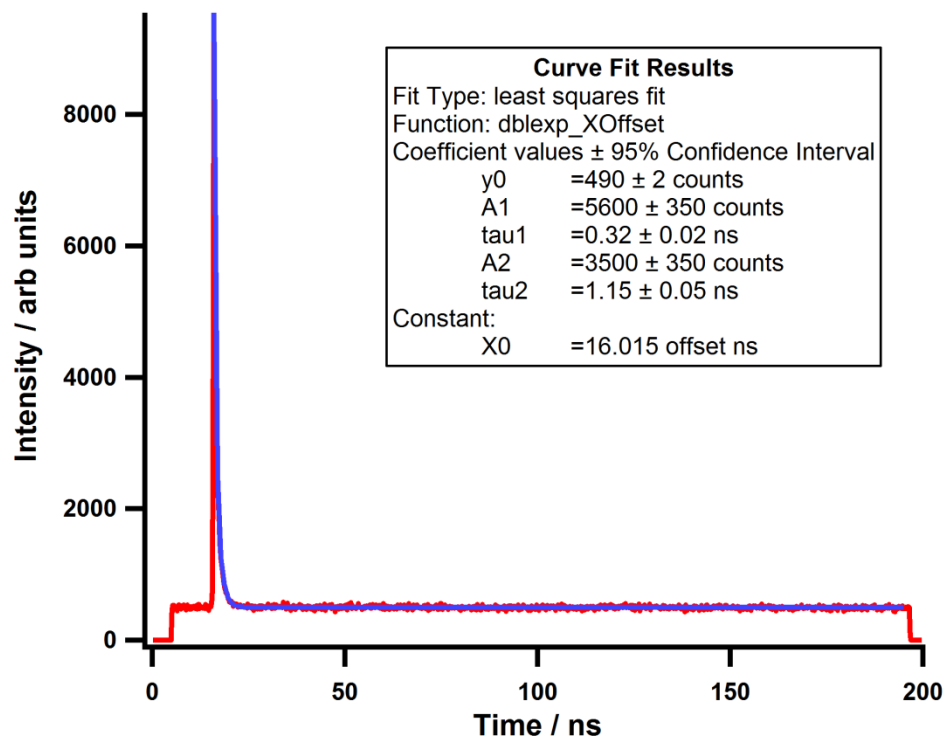


Figure 5-3 - Sample of TR XEOL collected from MISI response to 7 keV for 1200 second integration. Collected using the 150 line grating blazed at 500 nm (2.48 eV) centred at 375 nm (3.31 eV) Hybrid bunch 1.2 micro coulomb.

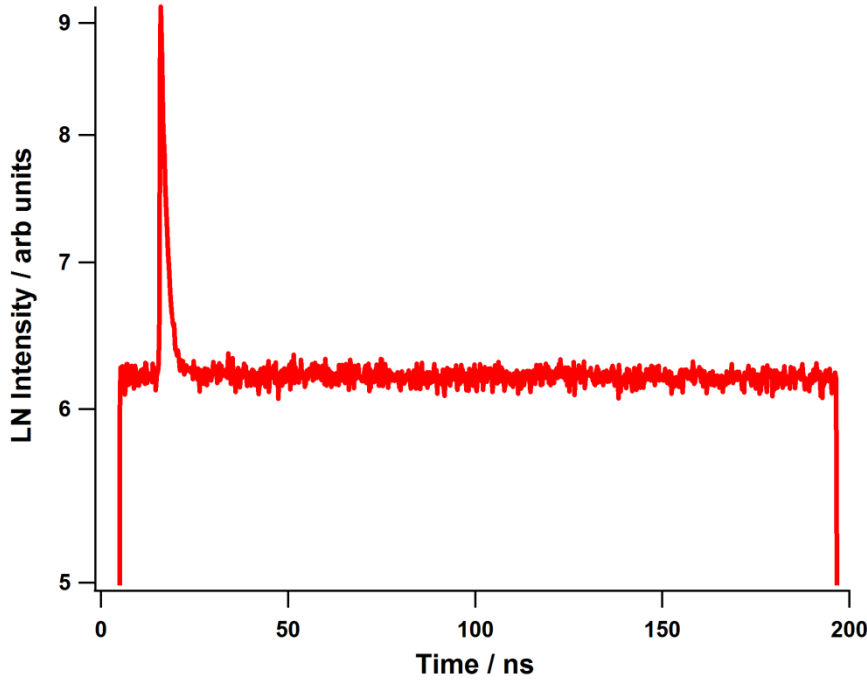


Figure 5-4 - Sample of TR XEOL collected from MISI log intensity vs time response of 7 keV for 1200 second integration. Collected using the 150 line grating blazed at 500 nm (2.48 eV) centred at 375 nm (3.31 eV) with the hybrid bunch 1.2 micro coulomb.

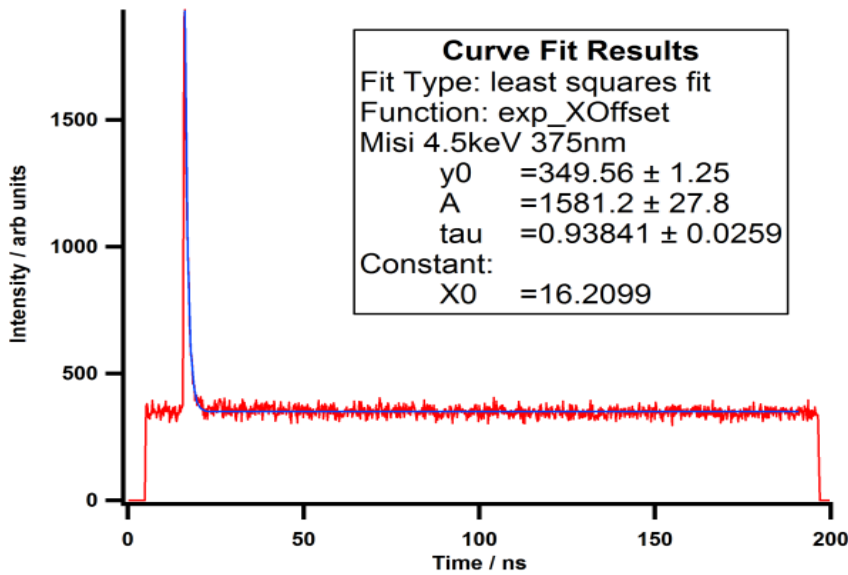


Figure 5-5 - Sample of TR XEOL collected from MISI
 Collected at 4.5 keV 1200 second integration. Collected using the 150 line grating blazed at 500 nm (2.48 eV) centred at 375 nm (3.31 eV) Hybrid bunch 2.5 micro coulomb.

The results from TR XEOL energy scans collected using two different energies of excitation (4.5 and 7.0 keV) are shown in Figure 5-3 ,Figure 5-5 and Figure 5-6 shows the data is plotted for comparison as a function of excitation energy. In considering just the intensity / QE of emission, the following factors are known to affect the intensity of a XEOL emission:-

- 1) Increases in X-ray energy increases the luminescence intensity because of increasing penetration depth of the more energetic radiation: at 7 keV the penetration depth will be $\sim 50 \mu\text{m}$, at 4.5 keV $\sim 20 \mu\text{m}$, thereby increasing the probability of interaction.
- 2) For a constant photon flux, increases in X-ray energy increases the total energy absorption and thereby the supply of energy available to luminescent sites, tending to increase the intensity of luminescence.
- 3) Increases in photon flux will increase luminescence as between the two experiments the size of the hybrid bunch was increased by just over a factor of two, increasing the incident flux by approximately the same ratio.

Comparative TR Lifetime

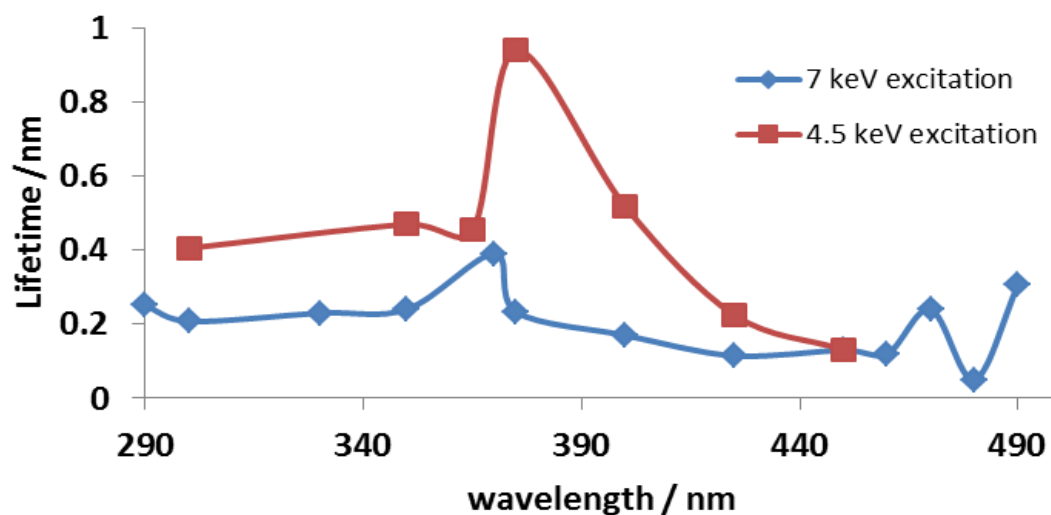


Figure 5-6 - Summary of TR XEOL spectra collected from MISI.

Using two energies of excitation; 4.5 and 7.0 keV. The responses diverge at $\sim 375\text{nm}$ (3.31 eV) emission. The majority of the spectral range collected from the lower excitation energy has the longer τ lifetime. Error bars 2σ .

When considering TR XEOL spectra three criteria should be considered, firstly the gross luminescent signal intensity is determined for the particular measured range of wavelengths of emission from the intensity of the fitted peak height. Secondly, the intensity of overlapping emissions with lifetimes exceeding 200 ns can be estimated from the value of Y_0 . Thirdly, from the fitted spectra the lifetimes and their relative intensity of emission for lifetimes less than 200 ns are estimated through the τ_n and A_n values respectively.

A significant increase in intensity is anticipated from the combination of the factors described above. From Figure 5-4 and Figure 5-5 the 4.5 keV excitation generates a peak height of ~ 1900 counts; in comparison, the peak height is ~ 9500 counts with 7 keV excitation and the peak height for the 7 keV experiment therefore displays an increase of $\sim 520\%$ to the 4.5 keV peak. From the same spectra, Y_0 (the measure for the quanta of luminescent emissions with a lifetime >200 ns (τ)), is 349.56 ± 1.25 , for the 4.5 keV excitation the Y_0 value and at 7 keV the Y_0 value increases to 497.61 ± 1.79 an increase in intensity of $\sim 42\%$. The significantly lower ratio of increase for Y_0 between the 4.5 keV and the 7 keV excitation therefore requires explanation. It is known from the analysis of beam intensity at constant energy that doubling flux doubles response. (Figure 5.2) Hence, the increase in Y_0 between the 4.5 and 7 keV experiments is significantly less than the doubling expected from doubling the flux. Therefore, if this aspect is accounted for, the intensity of Y_0 shows an inverse response to the increase in energy of the X-rays. This could however be explained in part if the emission responsible for the Y_0 signal has a lifetime approaching μs . It would then primarily be excited by the main fill and show a

much smaller response to changes in the hybrid bunch. Regardless of this factor, the difference in the ratios of change is still significant.

From Figure 5-7 it is seen that the lifetimes being measured for both excitation energies are <1 ns, therefore they are 'modified natural lifetimes' (see 2.10), i.e. the luminescent centre is subject to competitive relaxation that is reducing the measured lifetime. The differences in measured lifetimes between the two excitation energies illustrates that the relationship of intensity of response to incident energy varies between different XEOL emission sites, as lifetime is site sensitive. Lifetimes show insignificant sensitivity to flux as seen later in CLBR (section 5.2.3). On the basis that this emission is behaving similarly, the difference between the lifetimes of the 4.5 and 7 keV excitations is due to the change in excitation energy and not from variations in flux. This is intuitively correct, but the mechanism requires scrutiny. Firstly, if the intensity of XEOL were a simple function of incident energy then the response from the long and short lifetime responses should be of the same ratio. The variation in the luminescence intensity as a function of energy is compared to the lifetimes of the short lifetime emission as a function of excitation energies in Figure 5-7. The 4.5 keV data displays to a limited extent, an inverse relationship between the intensity and lifetime data. This can be explained if the decrease in lifetime is due to a reduction in energy transfer, as this would account for both the increase in intensity of emission and the lengthening of lifetime.

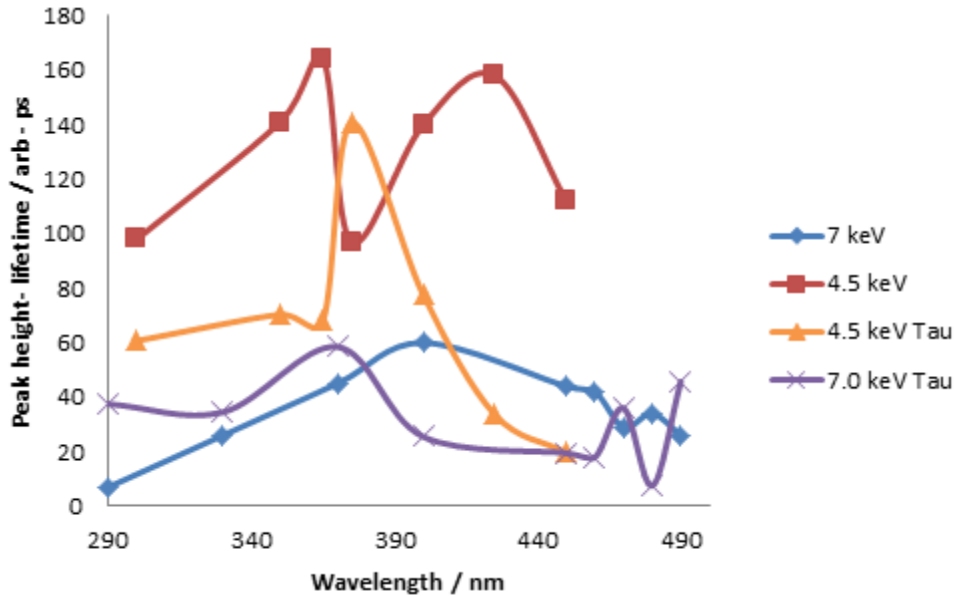


Figure 5-7 -Comparative summary of peak heights and lifetimes of TR XEOL emissions from MISI collected using 4.5 keV and 7 keV excitation.. 1200 s integrations and 1mm slits with the 150 grating blazed at 500nm.

The XEOL spectrum as shown in Figure 4-20 shows two weak overlapping features at ~330-350 nm (3.76 – 3.54 eV) with a broad emission peak starting from 250 nm (4.96 eV) extending into the VUV and a broad emission starting at 450 nm (2.76 eV) extending into the green. The data presented are not adequate to substantiate this explanation and require additional experimental work for confirmation. The mechanism through which a change in excitation energy could generate these effects requires further investigation but these results probe the absorption and relaxation mechanisms between primary excitation and XEOL emission. When interpreting the results, as lifetime is site specific, variations in lifetime reflect changes to the luminescent site or its local environment. Peak height is not site specific as it is a convolution of all the XEOL signal in the particular wavelength range measured; however, an 'A₀' value of a deconvoluted lifetime can in general be considered site specific. These results show the

energy of excitation differentiates between emissions in terms of the effect on intensity of emission. This can either be interpreted as a localised effect between the absorber and emitter site, which interestingly is also the most likely to carry XAS information. The alternative is that preferential relaxation mechanisms exist that are energy dependent upon the incident X-ray energy, thereby differentially affecting the intensity of different sites of emission. In mineral systems, the mechanisms between the initial absorption and the subsequent XEOL emission are poorly constrained and these results show this technique can explore this aspect. If the same emission is being measured between the two excitation energies, the lifetime should remain constant unless other factors are changing, for example the rate of quenching or energy transfer. As the experimental conditions are consistent here, there is no reason to suspect this. The difference in lifetimes measured in MISI is displayed in figure 5-6. It can be seen that at 375 nm (3.31 eV) the lifetime of the emission diverges significantly. This behaviour supports the hypothesis that the effect is due to variations in preferential absorption associated with preferential energy transfer mechanisms. An alternative hypothesis for this behaviour is the effect of hot luminescence, (see 2.11.5). Hot luminescence involves increases in the energy of emission but in the energy range of typical phonon energies <1 eV.

5.1.2 Dose effects on TR

To exploring dose effects on lifetime, the results from two 1200 s TR experiments are shown in Figure 5-8 and Figure 5-9. The data are collected from the same position on the sample with the second experiment immediately commencing on completion of the first. The lifetime of the short lifetime emission is unaffected by dose, however the QE/intensity increases as a function of dose with peak height above 'background'

increasing from ~1500 to ~3100 counts. This is accompanied by a pronounced decrease in the QE/intensity of the longer lifetime emission seen between the first and second experiments showing a decrease in the value of Y_0 by approximately an order of magnitude. I interpret this as sample alteration, reducing the population of the existing long life emission.

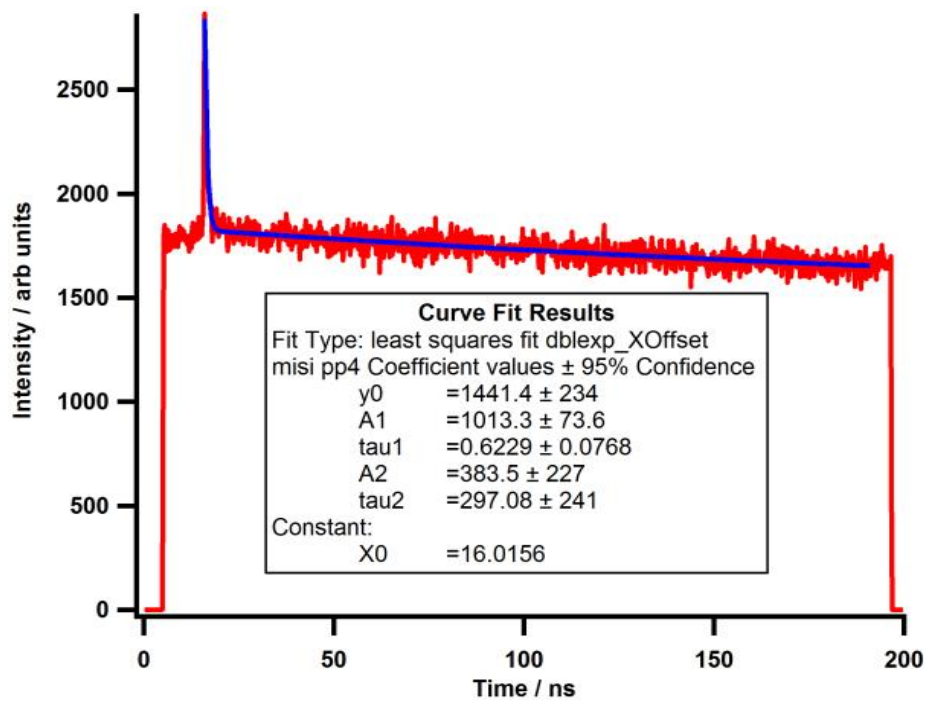


Figure 5-8 - TR XEOL collected from the first integration from MISI. Excited with 7keV spectra collection centred at 375 nm (3.31 eV) 1200 s integrations using the 150-line grating blazed at 500 nm 1mm slits.

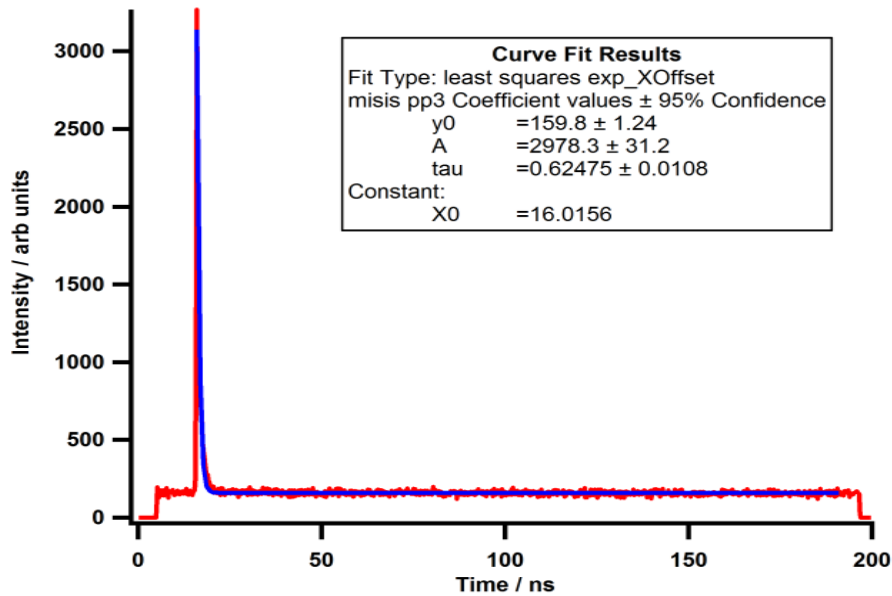


Figure 5-9 - TR XEOL collected from MISI second data collection run consecutively from the same sample position as Figure 5-8. Excited with 7 keV spectra collection centred at 375 nm (3.31 eV) 1200 s integrations.

One explanation for the change in the QE/ intensity of the short lifetime emission could involve a variation/change in the efficiency of either Dexter or Förster energy transfer; however, both are competitive so should be detected as a shorter lifetime in the second data set that is absent. An alternative mechanism for the decrease in QE/intensity is that a proportion of the long life luminescent defects are altered to create short lifetime defects, or that a new population of defects are created or activated by the incident radiation.

5.2 Cleavelandite Feldspar (CLBR)

Additional results for CLBR are included in Chapter 4, where they are used to illustrate the utility of the XEOL system. The results presented in this section are sample specific. Low temperature (LT) ~90 K Low Temperature Dose Dependence. A dose dependence experiment on CLBR at RT (see 4.10.1) was repeated at LT. The results are in Figure

5-10. In comparison of the LT spectra to the RT spectra Figure 4-16 This was achieved by with the addition of the cryo stream unit that is available on the beamline

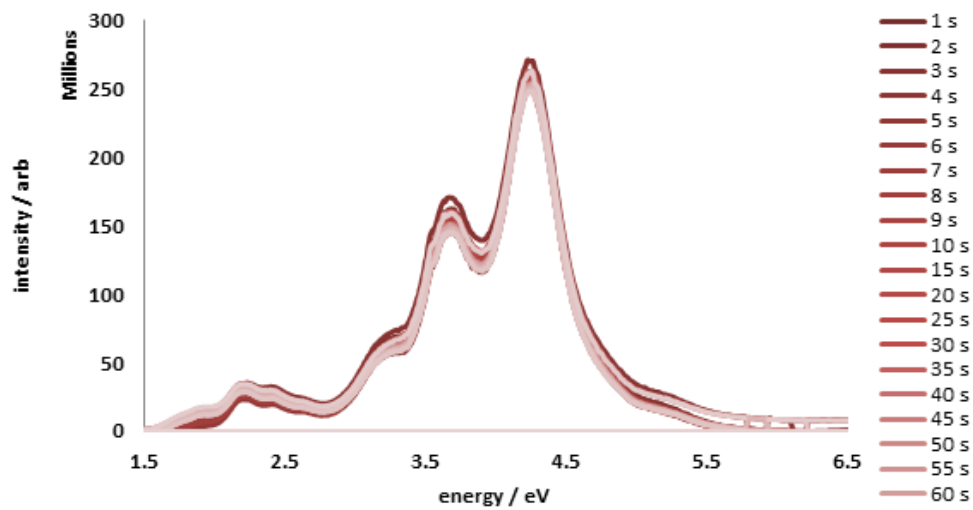


Figure 5-10 – CLBR dose dependent XEOL dose dependence spectra collected from CLBR at ~90 K, with system-corrected emissions. The low energy emission centred at 688 nm (~1.8 eV) shows the QE/intensity increases as a function of dose, whereas the higher energy emissions display a decrease in QE as a function of dose

The features as expected show a good correlation although displaying a narrowing of the features and the spectra display additional fine structure at LT. These effects are frequently seen with other forms of excitation at LT. System corrected data taken from individual spectra are fitted using Magic Plot Pro 3.2 and a comparison of the fitted luminescent responses from the corrected LT and the RT XEOL spectra are summarised in Table 5-1.

Wavelength/nm at 4.5 keV ~91 K	eV		RT XEOL peaks /nm at 7 keV excitation	Comments	Reference
307.7± 2 δ 0.3	4.03				
291.7 ± 2 δ 0.3	4.25	Pb ²⁺	290	Tentative	(Gaft et al., 2005)
340.6 ±2 δ 0.3	3.64		335	Not previously seen	
391.1±2 δ 0.3	3.17	Tb ³⁺		Identified	(Gaft et al., 2005))
568.7±2 δ 0.3	2.18			Not previously seen	
534.4 ± 2 δ 0.3	2.32			Not previously seen	
	2.73	Mn ²⁺	555	Identified	(Gaft et al., 2005, Gorobets and Rogojine, 2002)
681.2± 2δ 0.3	1.82	Fe ³⁺ ?	710	Broad Fe peak centred ~720-750nm	(Kayama et al., 2010) (Garcia-Guinea et al., 2007b)

Table 5-1- Summary of emission features for CW XEOL LT ~91K collected using 4.5 keV for dose dependence experiment of CLBR. Comparison with spectra from the same sample collected using 7 keV at RT. Each integration for 0.5 s is centred at 550 nm (2.25 eV), collected through 1mm slits.

To explore the nature of the sample change generating these differences in the intensity/QE response experienced as a function of dose, the first and last system corrected integrations are fitted using Magic Plot Pro ver. 3.2 to complete least squares fitting; the results are displayed in Figure 5-11 and Figure 5-12. The reduction in the higher energy luminescence $\lambda > 496 < 276$ nm ($> 2.5 < 4.5$ eV) and the intensity/QE is primarily due to the loss of the broad emission centred at 324 nm (3.82 eV). The increase in QE intensity at low energy 826 - 496 nm (1.5-2.5 eV) is due to the creation of

two new emissions centred at 682 nm and 569 nm (1.82 and 2.18 eV), respectively. No references or assignments for these new LT emissions are found in the literature. The behaviour of the dose dependent signal between 263 and 225 nm (4.7 and 5.5 eV) is unusual, as it appears to diverge into two separate responses. This could reflect the introduction of a second luminescent emission and this would be supported by the comparison of the spectra in Figure 5-11 and Figure 5-12.

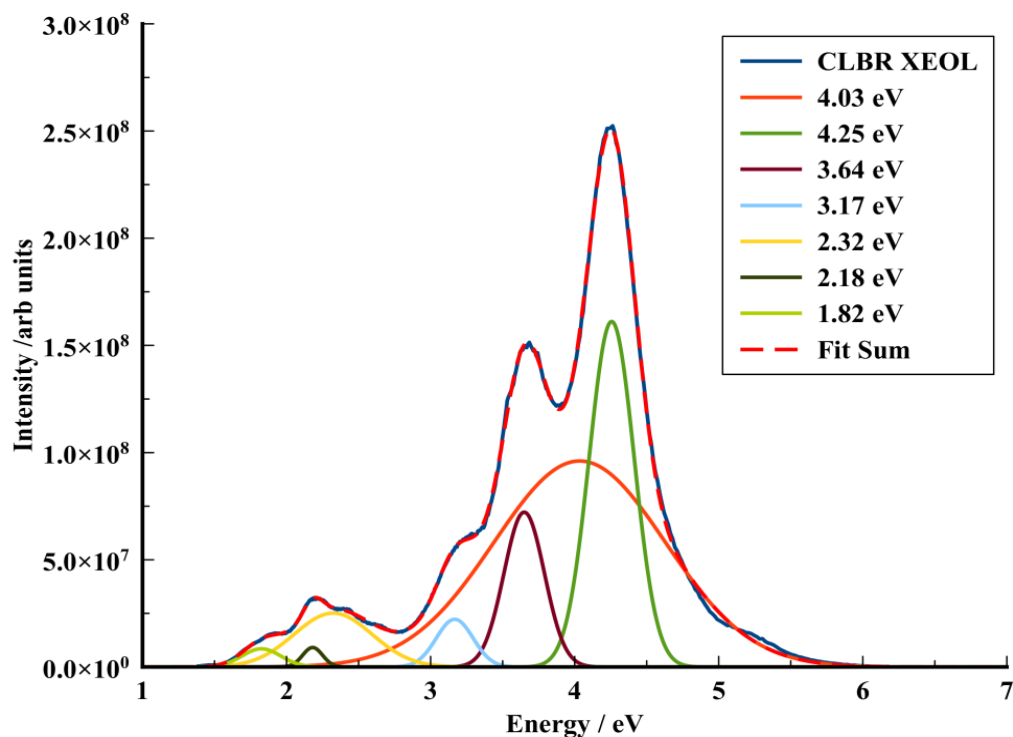


Figure 5-11 - CW XEOL dose dependence experiment from CLBR first spectra.

Collected from a hundred 1 s integrations using 150 line grating blazed at 500nm (2.48 eV) centred at 550nm (2.25 eV), 1mm slits 4.5 keV excitation. Fitted using Magic Plot Pro 3.2 to complete least squares fitting

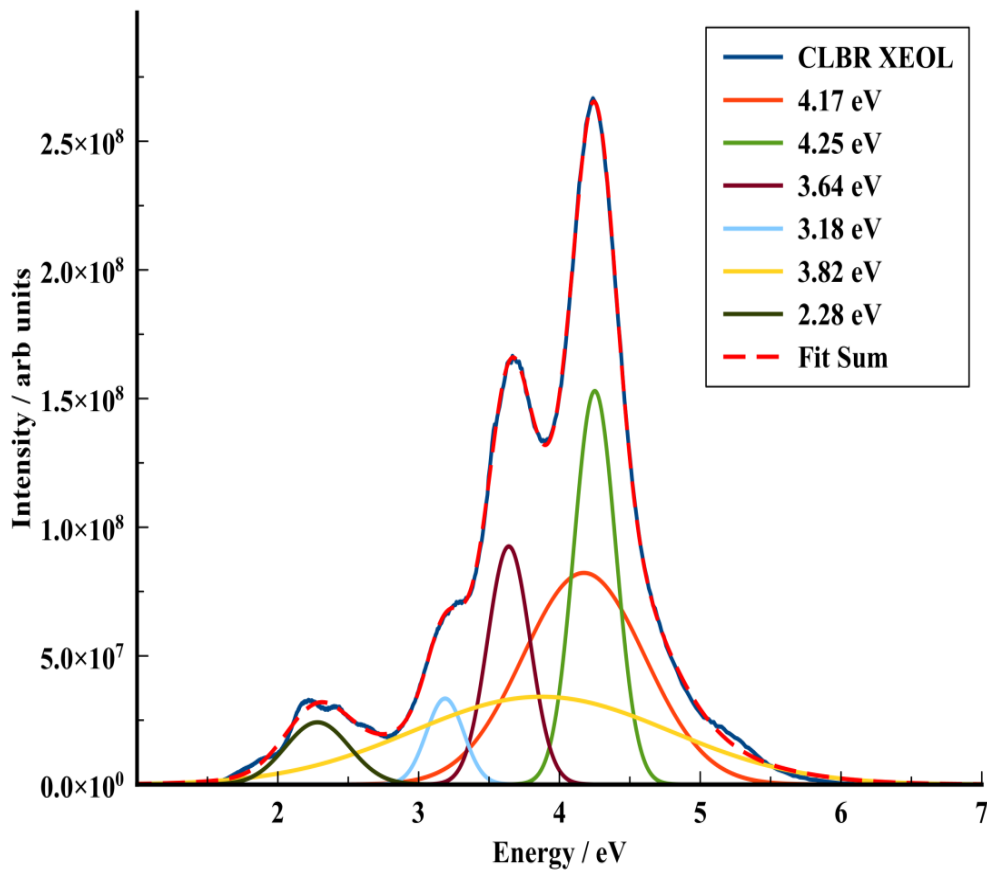


Figure 5-12 - CW XEOL dose dependence experiment from CLBR last spectra.

Collected from a hundred 1 s integrations using 150 line grating blazed at 500 nm (2.48 eV) centred at 550 nm (2.25 eV) 1mm slits 4.5 keV excitation. Fitted using Magic Plot Pro 3.2

X-ray excitation can populate energy levels normally inaccessible with PL excitation, including triplet states that have disallowed excitation transitions from the valence band. These same rules disallowing transitions apply equally to relaxation. Therefore, the population of a 'new' energy level is not necessarily sufficient to generate a previously unseen emission, as there is a requirement for an allowed emissive relaxation. Peak fitting with complex spectra has reliability issues and it is generally accepted by changing fit parameters it is possible to achieve different results, the following discussion is therefore an example of how such data could be interpreted bearing in mind further experimental data would be required before acceptance. The

'new emissions' detected could however be explained through triplet-triplet annihilation (see 2.10.5). Triplet-triplet annihilation requires high populations of populated triplet states due to the ~10 nm diameter limitation of Förster energy transfer the generation of large populations of populated triplet states is favoured by the conditions generated by X-ray excitation, namely the production of large populations of de-localised electrons. If the hypothesis of triplet-triplet annihilation is correct and transitions to and from this energy level and the valance band are disallowed through the selection rules (see 2.8.7, 2.8.8, 2.8.9), the energy level would be described as 'meta-stable', and could act as a 'trap' as defined in TL and OSL dosimetry. The identification of a 'traps' is by their nature challenging; traps do not normally luminesce or absorb light by excitation/relaxation direct from the valance band, (Van den Eeckhout et al., 2010) the standard mechanisms used to identify defects. The potential for these techniques within XEOL spectroscopy to identify and characterise this type of defect would be of significant benefit to the OSL dating community. The fitted peak positions recorded in

Table 5-2 shows peak position shifts, removal or modification of existing peaks, and the addition of new peaks over the period of the integration.

<i>2.5 seconds</i>	<i>47.5 seconds</i>
Energy / eV	Energy / eV
4.25±2δ 0.01	4.25 ±2δ 0.01
	4.03±2δ 0.01
4.17±2δ 0.01	
3.82±2δ 0.01	
3.64±2δ 0.01	3.64±2δ -0.01
3.18±2δ 0.01	3.17±2δ 0.01
2.32±2δ 0.01	2.29±2δ 0.01
	2.18±2δ 0.01
	1.82±2δ 0.01

Table 5-2 - Peak positions for CLBR low temperature XEOL experiment. Consisting of 100 1 s integrations data taken from the 5, and 90 integration, excitation 7 keV using spectra collected using 150 line grating blazed at 500nm using 1mm slits. The collection is centred at 550 nm, 2.26 eV, the data show several peaks with energies constant within error.

These results have a number of implications they illustrate in the sample examined that dose dependence is a result of changes to the luminescent centres. By using this combination of techniques new emissions are accessed that can then potentially be identified. The results show that the emissions with unaffected intensity also have no spectral shift as a response to dose. This I interpret as indicating that dose does not alter the luminescent centre or its local electronic structure in a cumulative or stepwise fashion. Changes to the active luminescent centre population are most likely a single step process with no intermediate luminescent steps. The comparisons in Table 5-1 show three common peaks between RT and LT spectra, in which two display a small red shift at lower temperatures that could be explained by reduced phonon interaction. This

behaviour has been described previously, for example (Perna et al., 1998). The peak positions show no sensitivity to the energy of excitation.

5.2.1 Dose Dependence

Analysis of RT dose dependence data Figure 5-14 and Figure 5-13 from CLBR excited at 7 keV, indicate that the high-energy peak at 292 nm (4.24 eV) is best fitted with a convolution of three emissions whose ratios vary between fits that makes the dose dependent response interpretation difficult. The five peaks below 335 nm (3.7 eV) are less complex

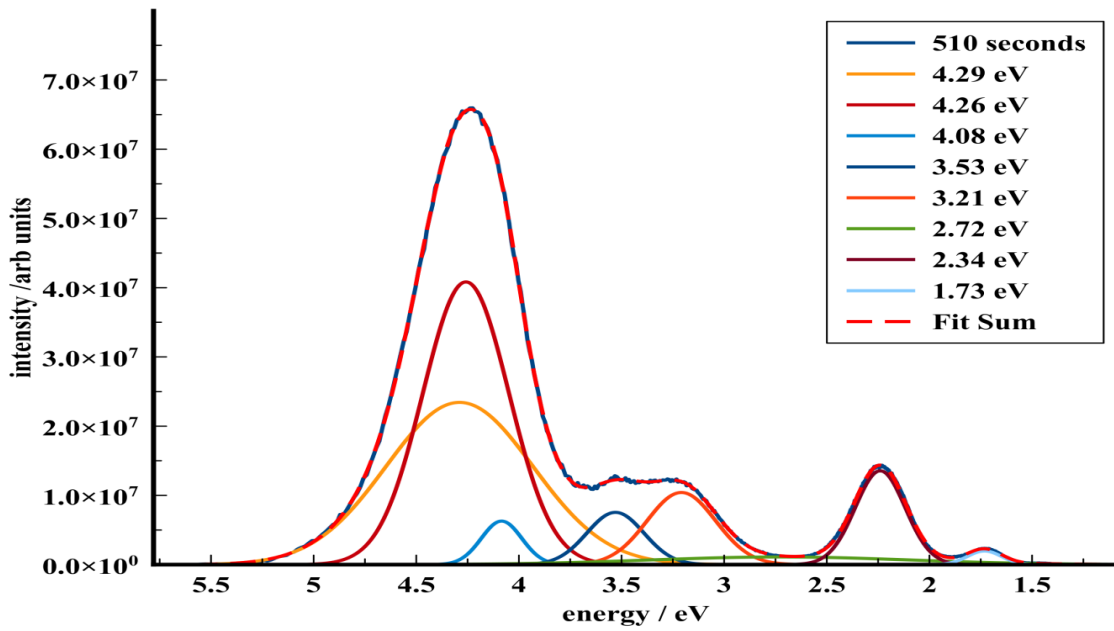


Figure 5-13 – Dose dependence fitted spectra collected after 510 s from CLBR at RT.
 Collected using 0.5 s integrations centred at 550 nm (2.25 eV), 7keV excitation, 1mm slits. Magic Plot Pro 3.2

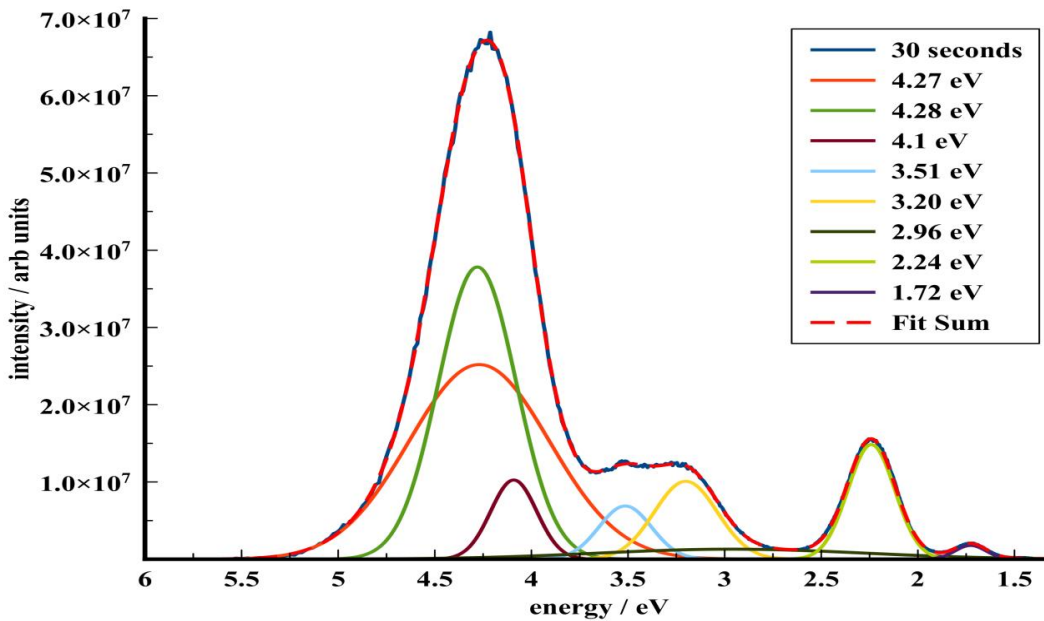
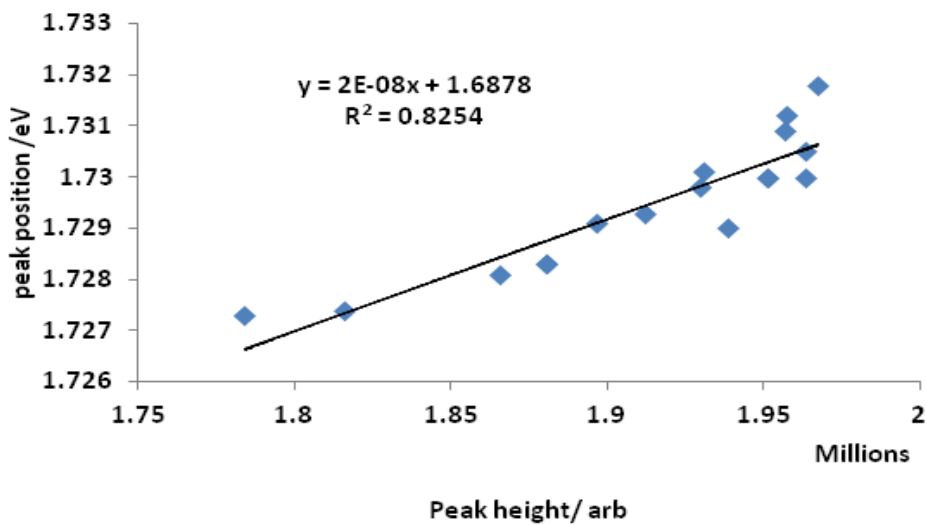


Figure 5-14 - Dose dependence fitted spectra collected after 30 s from CLBR at RT.
 Integration for 0.5 s centred at 550 nm (2,25 eV), 150 line grating blazed 500 nm (2.48 eV), 7keV excitation, 1mm slits. Fitted using Magic Plot Pro 3.2

The lowest energy peak at 713 nm (1.74 eV) displays no convolution at either 30 or 510 seconds after commencement of the experiment (Figure 5-13, and Figure 5-14). In Figure 5-17 and Figure 5-18 the increase in QE and the shift in energy of the peak at ~729 nm (~1.7 eV) displays a linear correlation. A mechanism consistent with the energy shift associated with an increase in intensity is sample alteration, which if it generated lattice changes surrounding the luminescent centre that in turn affect the energy levels of the site and thereby the energy of emission and that would in doing so affect the probability of transition and thereby the QE of the emission. This hypothesis can be tested by measuring the lifetime of this emission, as it would require the original emission to be a forbidden transition with a lifetime in ~ms.



**Figure 5-15 - Dose dependence peak height vs peak position ~729 nm (~1.7 eV) taken from the CLBR spectra Figure 5-17
Collected at RT each integration for 0.5 s centred at 550 nm (2.25eV), 7 keV excitation, 1 mm slits**

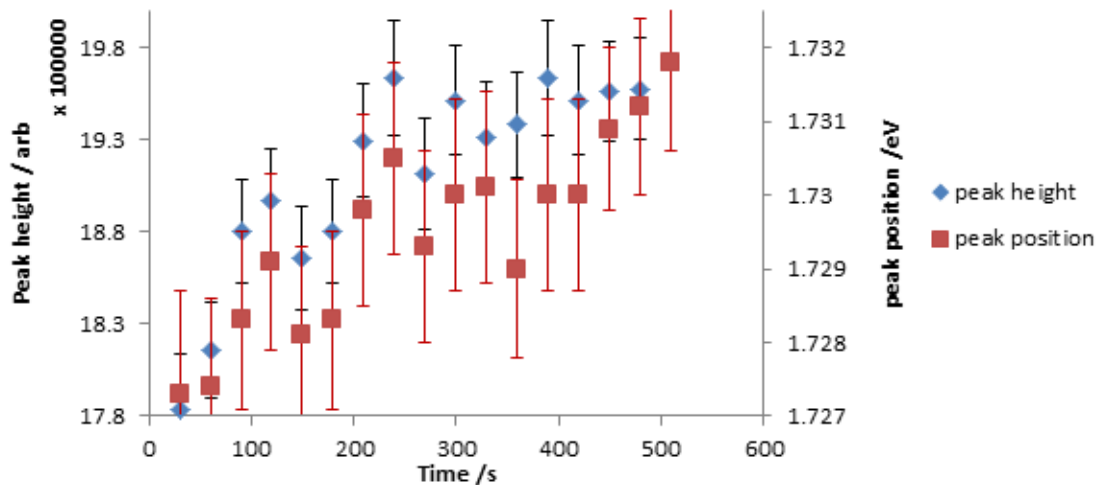


Figure 5-16 - Dose dependence comparative peak height and peak position ~729 nm (~1.7 eV) from CLBR at RT. Each integration for 0.5 s centred at 550 nm, 7 keV excitation, 1 mm slits. Peak position in eV in red squares peak height in blue diamond's error bars 2σ .

In comparison the 564 nm (2.2 eV) emissions shows a decrease in QE/intensity as a function of dose that also shows a linear correlation with a red shift in energy position (Figure 5-17 and Figure 5-18). This can be explained by the reverse process of changes in matrix reducing the 'relaxation' of the rule forbidding the transition and this again could be tested by measuring the lifetime of the emission. In Figure 5-19, the TR XEOL emission spectra is best fitted with two lifetime components with the higher energy emission reducing in QE/intensity with a simultaneous red shift in the convoluted peak..

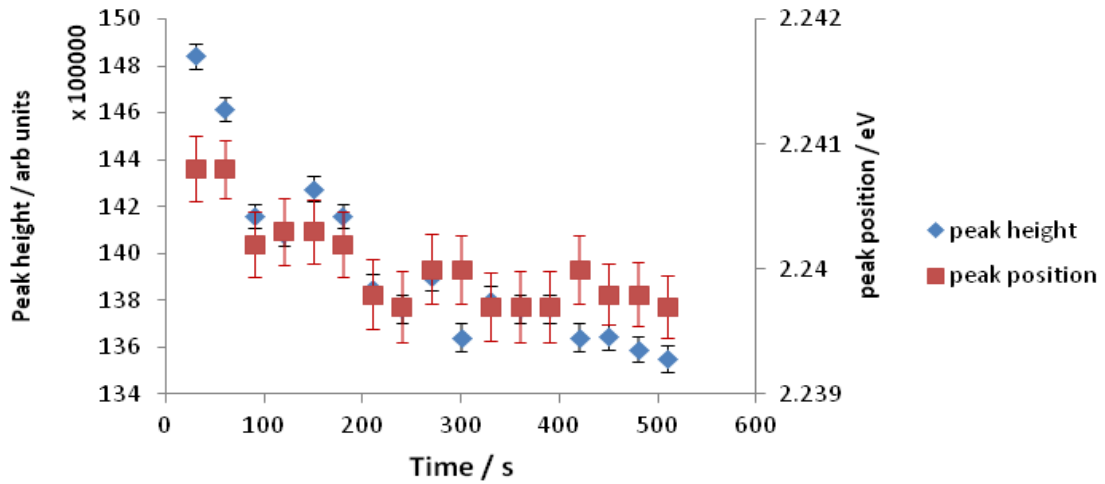


Figure 5-17 - Dose dependence comparative peak height and peak position 564 nm (~2.2 eV) from CLBR at RT. Each integration for 0.5 s centred at 550 nm, 7 keV excitation, 1 mm slits. Peak position in eV in red squares peak height in blue diamond's error bars 2σ .

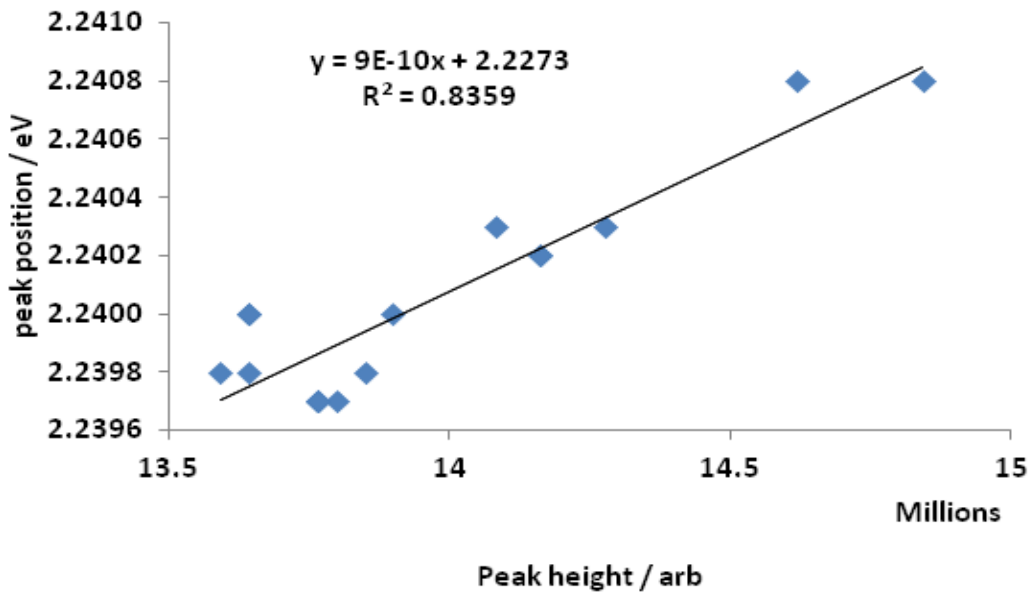


Figure 5-18 - Dose dependence peak height vs peak position collected at ~564nm (~2.2 eV) taken from CLBR spectra

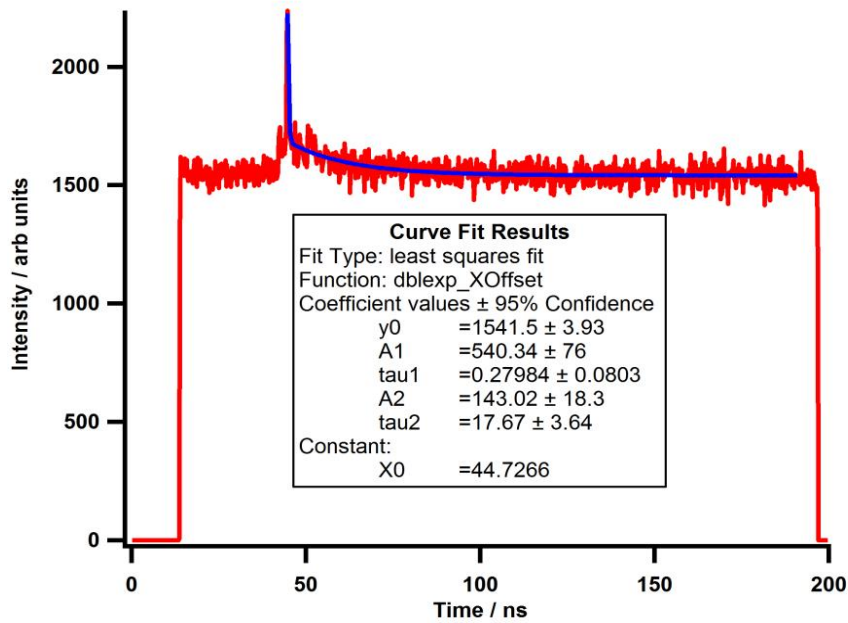


Figure 5-19 - Dose dependence fitted spectra collected after 30 s from CLBR at RT.

Integration for 0.5 s centred at 550 nm (2.25 eV), 7 keV excitation, 1 mm slits.

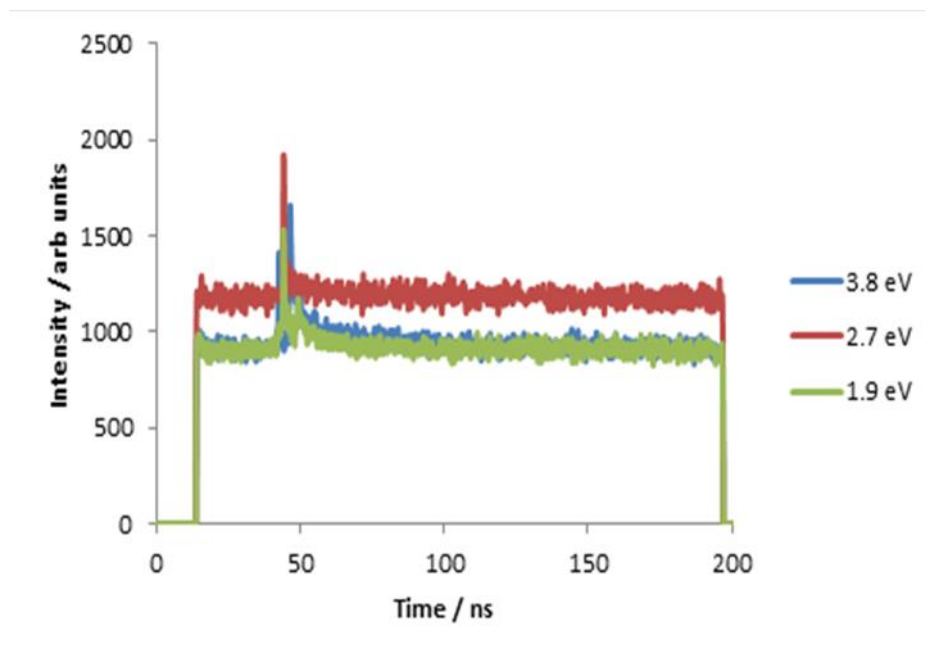


Figure 5-20 TR XEOL from three spectra collected at different emission energies.

Excitation 7 keV LT \sim 91⁰ K 150 line grating blazed at 500nm 0.5nm slits centred at 326, 459, 653 nm (3.8, 2.7, 1.9 eV) 1200 s integrations.

It is noticeable from Figure 5-14 that this portion of the spectrum is fitted with two emissions. The peak centred at ~ 550 nm (2.24 eV) is the majority of the signal; a second peak is centred at 418 nm (2.96 eV). This is consistent with the hypothesis that the 418 nm (2.96 eV) emission correlates to the fast emission in the TR spectra. To test the hypothesis three TR spectra are plotted from the ROI in Figure 5-20 showing both the emission from the centre of the ROI has the highest peak intensity but also the highest QE of the longer life emission. The TR peak from either side diminishes in intensity, consistent with the hypothesis. The data collected at 442 nm (2.8 eV) Figure 5-22 -) display a step change in response in the peak height between ~ 200 -300 s. This behaviour requires further investigation using the correlation of TR peak position and intensity of luminescent emission as a function of dose. There are examples of XEOL dose dependence analysis, for example (Chen et al., 2007) where they concentrate on intensity in isolation. The temporal dimension of a dose dependence experiment probes the process of sample modification that is a new application for this technique.

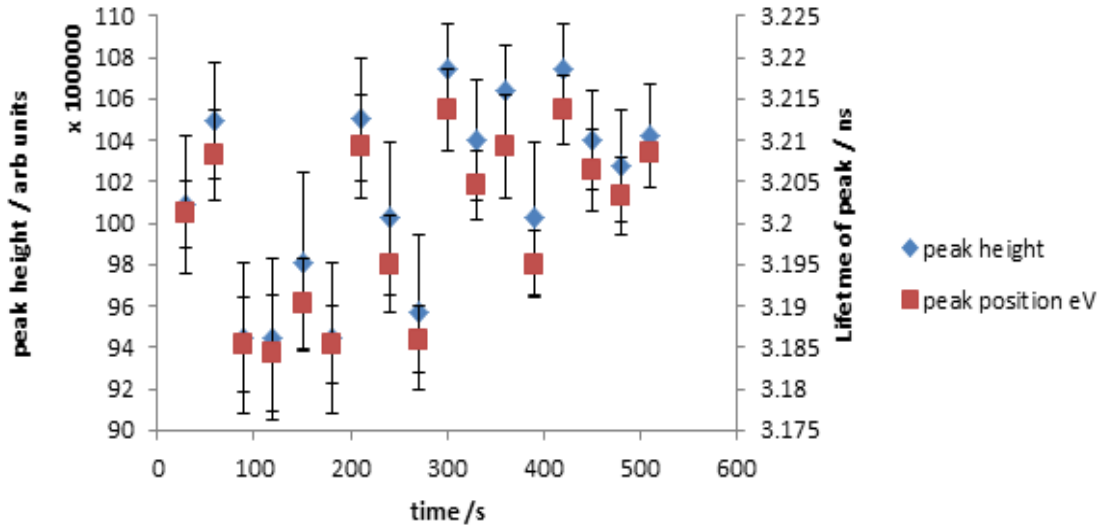


Figure 5-21 - Dose dependence comparative peak height and peak position ~387 nm (~3.2 eV) from CLBR at RT. Each integration for 0.5 s centred at 550 nm (2.25 eV), 7 keV excitation, 1 mm slits. Peak position in eV in red squares peak height in blue diamond's error bars 2σ .

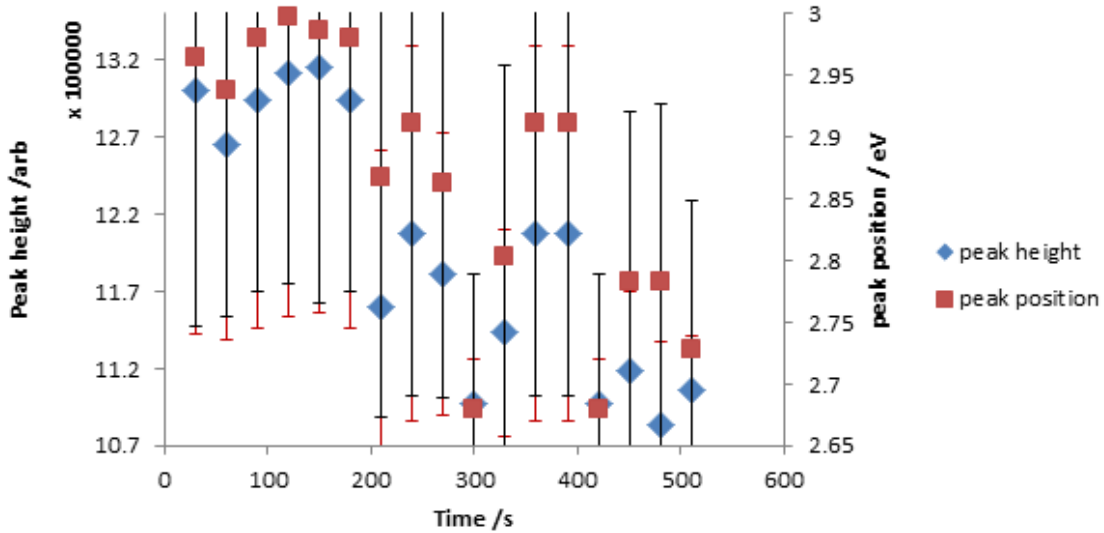


Figure 5-22 - Dose dependence comparative peak height and peak position ~442 nm (~2.8 eV) from CLBR at RT. Each integration for 0.5 s centred at 550 nm (2.25 eV), 7 keV excitation, 1 mm slits. Peak position in eV in red squares peak height in blue diamond's error bars 2σ .

The three higher energy emissions Figure 5-23, Figure 5-24 and Figure 5-25 show no temporal correlation between peak height and peak position.

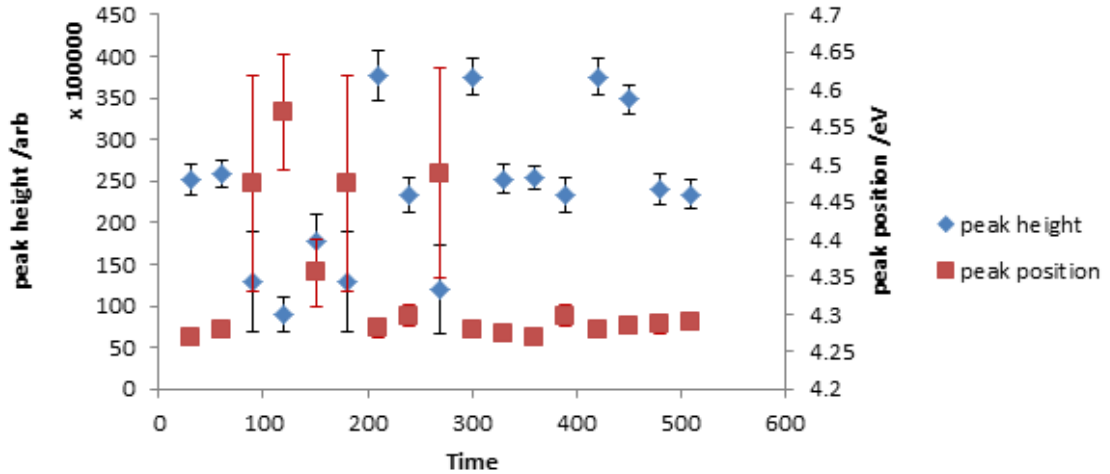


Figure 5-23 - Dose dependence comparative peak height and peak position ~288 nm (~4.3 eV) from CLBR at RT. Each integration for 0.5 s centred at 550 nm (2.25 eV), 7 keV excitation, 1 mm slits. Peak position in eV in red squares peak height in blue diamond's error bars 2σ .

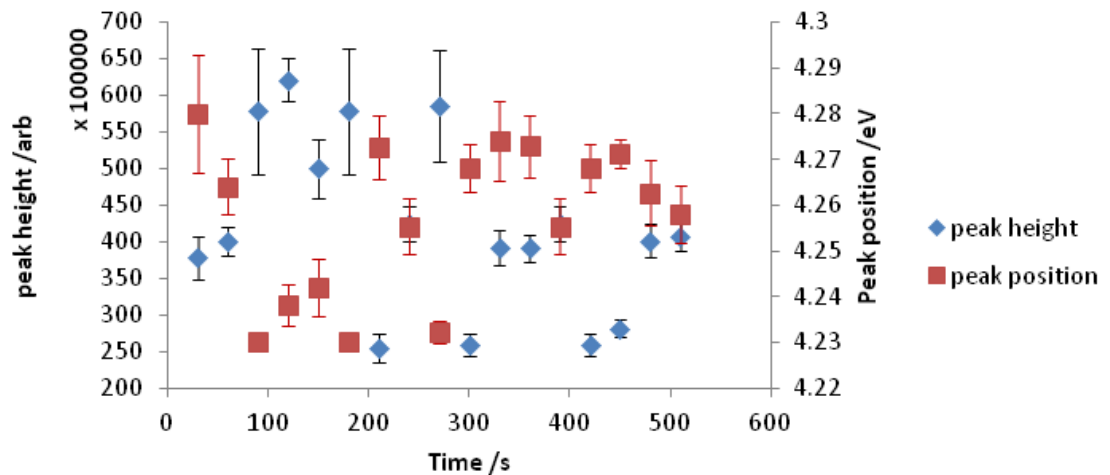


Figure 5-24 - Dose dependence comparative peak height and peak position ~291 nm (~4.25 eV) from CLBR at RT. Each integration for 0.5 s centred at 550 nm (2.25 eV), 7 keV excitation, 1 mm slits. Peak position in eV in red squares peak height in blue diamond's error bars 2σ .

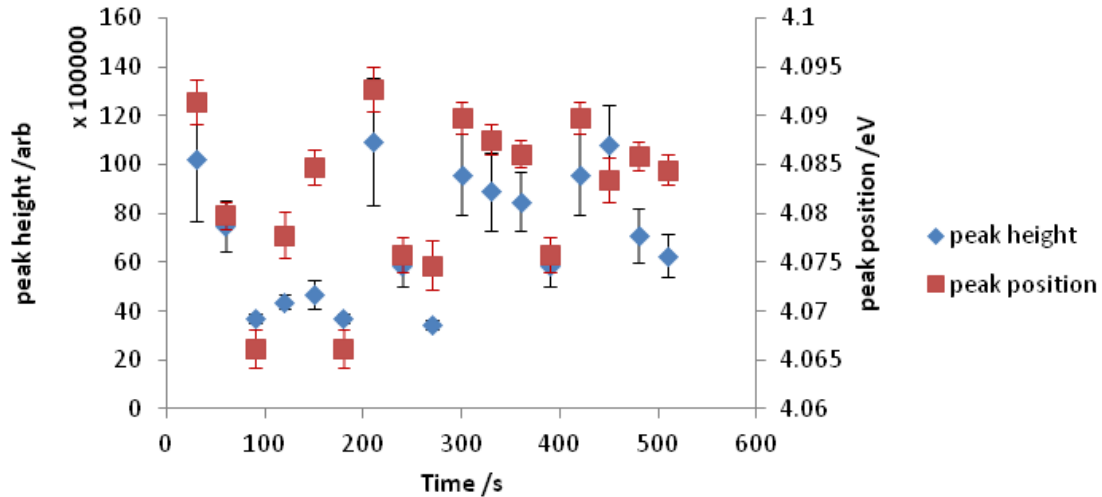


Figure 5-25 - Dose dependence comparative peak height and peak position ~306 nm (~4.05 eV) from CLBR at RT. Each integration for 0.5 s centred at 550 nm (2.25 eV), 7 keV excitation, 1 mm slits. Peak position in eV in red squares peak height in blue diamond's error bars 2 σ .

5.2.2 Dose Rate

Two TR experiments using 7keV excitation and varying the dose rate are completed in the first experiment, the sample was moved between integrations and in the second experiment, the sample remained static, thereby introducing dose effects (Figure 5-26). The data from both experiments are best fitted with two exponential decays, with τ_1 remaining constant within a limited range of ~0.28 -0.4 ns for both experiments illustrating that for these emissions dose rate has no effect on lifetime. The longer lifetime τ_2 shows responses with both the static and moving experiments indicating the effects displayed are not limited to a dose rate component. The variations in the moving τ_2 are most likely explained by sample heterogeneity or possibly preferential absorption or energy transfer mechanisms affecting both experiments in the ranges of 50-100% beam intensity.

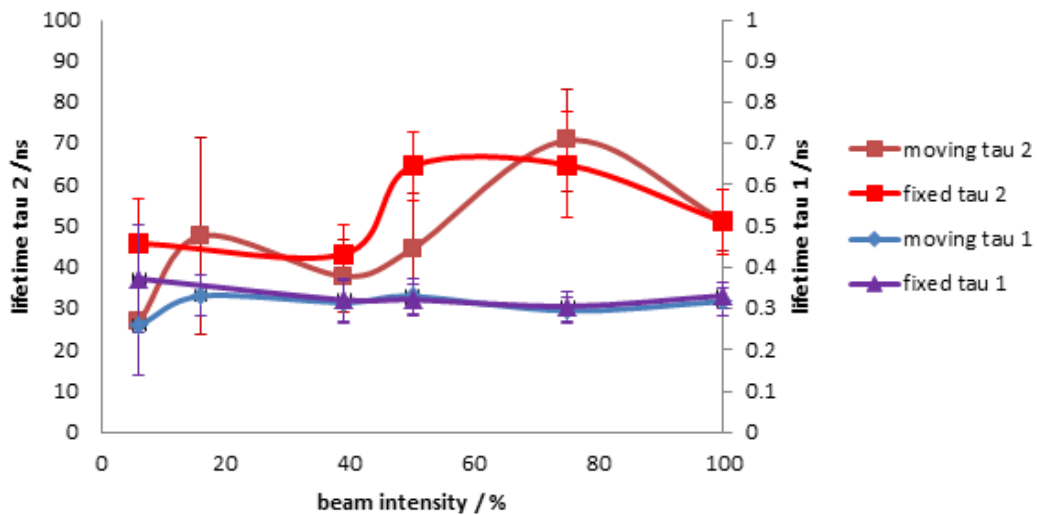


Figure 5-26 - CLBR TR dose rate experiment excited at 7 keV.
Data collected in two consecutive experiments the first experiment results are displayed in blue and brown the sample was moved between each integration. The second experiment results with the sample stationary between integrations, displayed in red and purple. Error bars 2σ .

In Figure 5-27 a comparison of the QE/intensity of both the short and long lifetime intensities are plotted alongside the τ_1 short lifetime emission. This illustrates the concept that the lifetime within error is insensitive to dose rate, in comparison the intensity of both long and short lifetime emissions all show a strong linear correlations to the intensity of excitation. In Figure 5-29 τ_2 is plotted against the QE/intensity of responses, and for beam intensities up to $\sim 75\%$ of all signals including lifetime appear to show a linear correspondence with the excitation. Above this, the behaviour of the lifetime diverges from the linear response. The mechanisms usually used to explain reductions in lifetime are normally accompanied by simultaneous changes in QE/intensity such as saturation, that would be reflected in the intensity, as would sample modification.

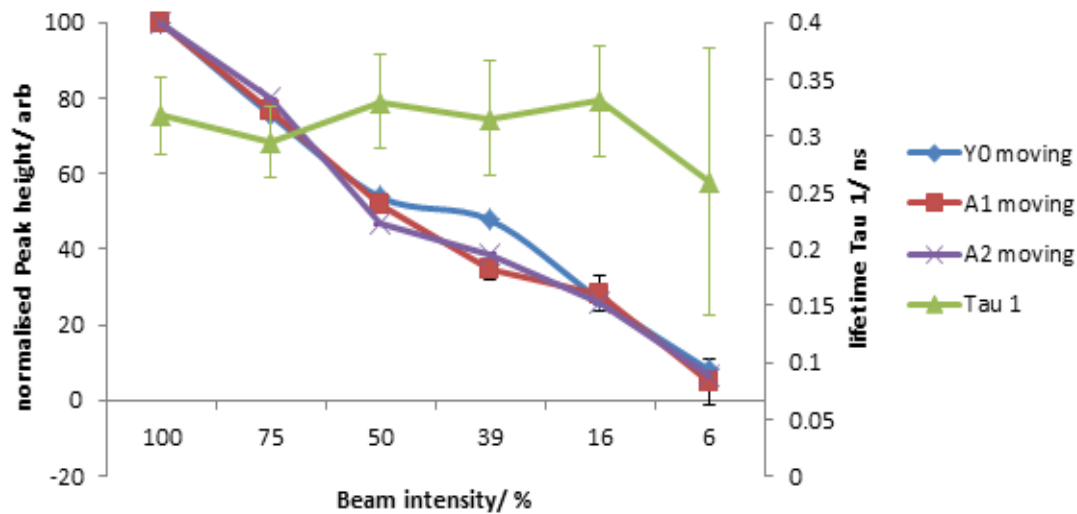


Figure 5-27 - CLBR TR dose rate experiment excited at 7 keV. Displaying intensities of: QE Tau 1 (A1) red, QE Tau 2 (A2) purple, long life emission Y_0 blue and the lifetime of Tau 1 green. The sample is moved between integrations. Error bars 2σ .

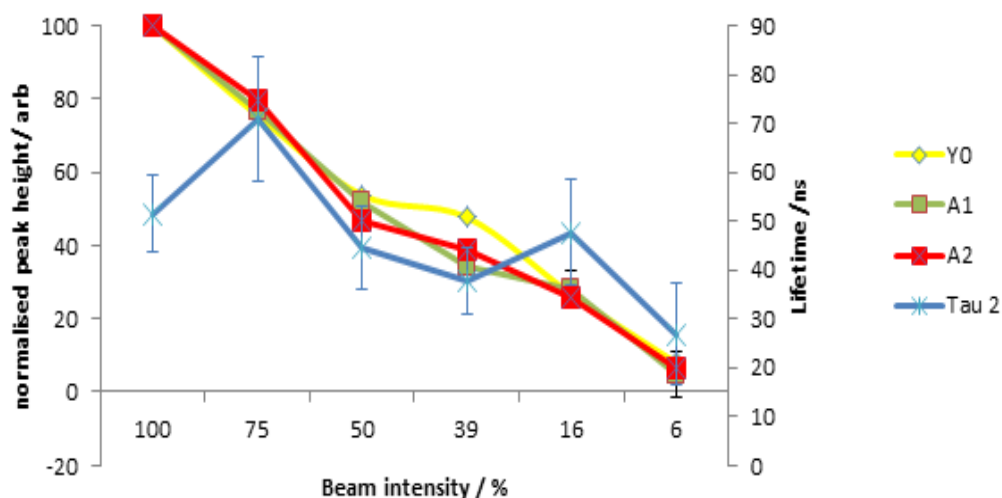


Figure 5-28 - CLBR TR dose rate experiment excited at 7 keV. Displaying intensities of: QE Tau 1 (A1) green, QE Tau 2 (A2) Red, long life emission Y_0 yellow, and the lifetime of Tau 1 blue. The sample is moved between integrations. Error bars 2σ .

These results require further investigation using a higher spectral resolution to explore if more than one emission is involved. It would also be worthwhile to repeat the experiment with longer integration times to reduce the error. If this means that the

lifetime shows a change with no associated effect on the intensity from a single emission mechanism then this requires explanation.

5.3 Moonstone

5.3.1 XEOL

Moonstone, a cryptoperthite, is typically a colourless mineral that typically shows no luminescent response from UV excitation. In comparison to UV responses, moonstone displays a complex XEOL spectrum with emissions in the energy range 1.5 - 5.5 eV (~825 - 225 nm). This behaviour can be explained by the hypothesis that XEOL is primarily a function of the microstructure and interfaces rather than elemental substitution. Since elemental substitutions are frequently excited by UV. If no allowed inter ion transitions exist, then a prerequisite of luminescence is the delocalisation of the excited state electron/exciton that is inherent in X-ray excitation. Table 5-3 compares XEOL emissions to known end-member alkali feldspar emissions and only four of the eight recorded are noted. This is consistent with the hypothesis that many emissions are interface related.

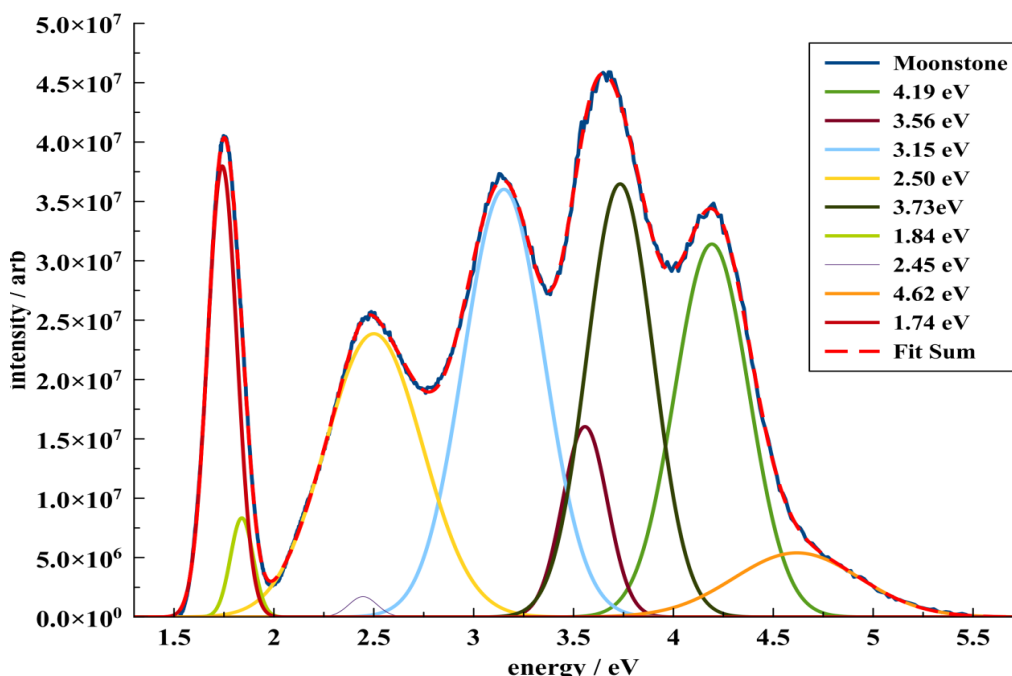


Figure 5-29 - XEOL from RT 83 Moonstone excited at 7 keV. Collected using 150 line grating centred at 550 nm (2.25 eV), system corrected, fitted using Magic Plot Pro 3.2.

<i>Emissions in moonstone nm</i>	<i>eV</i>	<i>Reported Alkali feldspar emissions nm</i>	<i>eV</i>
268	4.62		
295	4.19	290	4.28
332	3.73	340	3.65
348	3.56		
393	3.15	380	3.26
495	2.50		
495	2.48		
673	1.84		
712	1.74	720	1.72

Table 5-3 - Table showing luminescent emissions identified in XEOL collected from moonstone RT83 at 7keV at RT. Collected using 150 line grating centred at 550 nm (2.25 eV) compared to typical luminescent emissions from alkali feldspar (Garcia-Guinea et al., 1996).

5.3.2 Dose Dependence

The results of dose dependence experiments on RT83 are displayed in Figure 5-31 The majority of the spectral features show reducing response as a function of dose, whereas the spectrum at 620 – 635 nm (2.0-1.95 eV)

Figure 5-31 - show an increase. This portion of the spectrum is made up of a convolution of the overlap of the tails of three separate overlapping emissions, as can be seen in Figure 5-32, Figure 5-33, and Figure 5-34. The increase is due primarily to the broadening of individual emissions as well as to a lesser extent the individual emission increases. It should also be noted that in a number of the emissions the fundamental emission intensity is increasing while the gross convoluted response is decreasing, this is explained by the reduction and/or narrowing of overlapping emissions. This illustrates

the importance of de-convolution of the signal into individual emission responses rather than attempting to interpret a convoluted response.

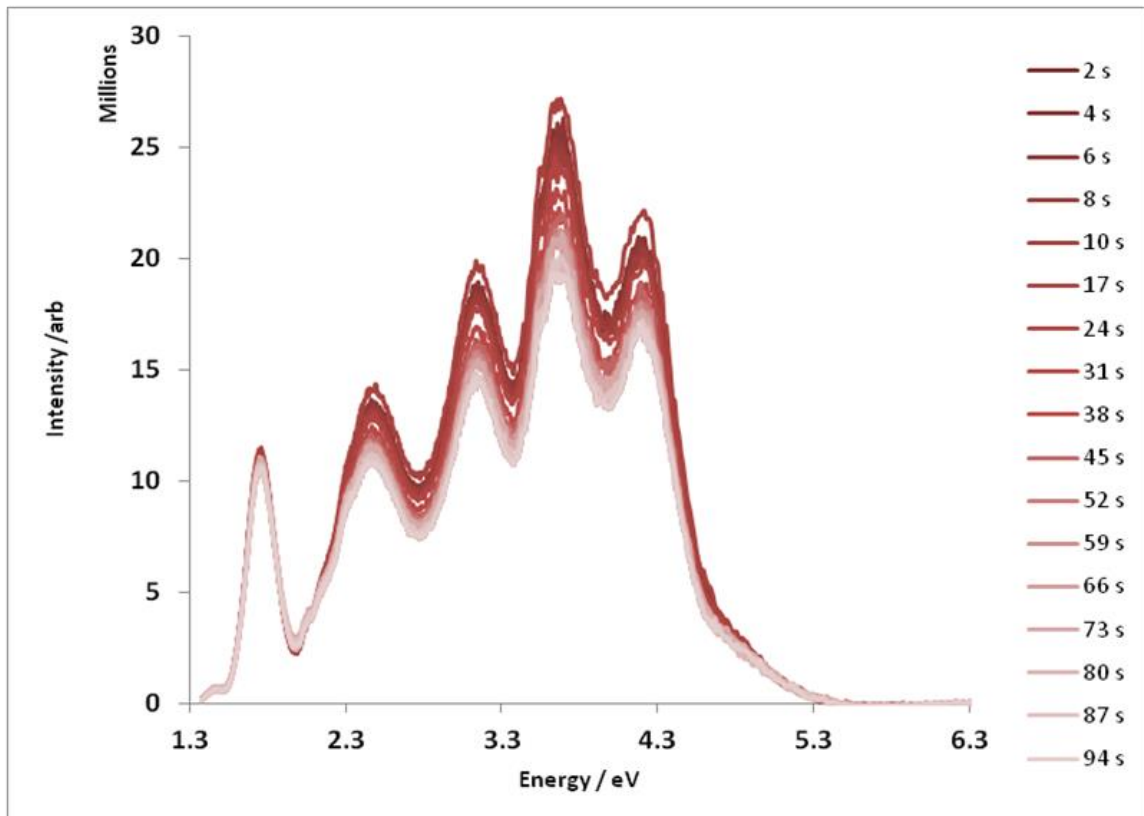


Figure 5-30 - RT83 Moonstone dose dependence spectra.
Collected using 7 keV excitation one hundred 2 s integrations centred at 550 nm (2.25 eV), collected through 1mm entrance slits, data corrected for system response.

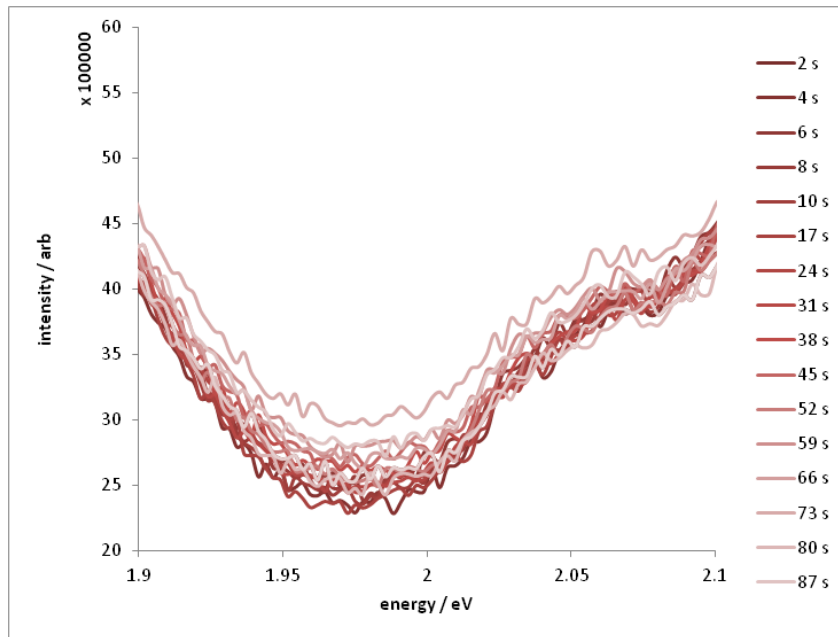


Figure 5-31 - Expanded section of the dose dependence response of RT83 moonstone. (Figure 5-30)

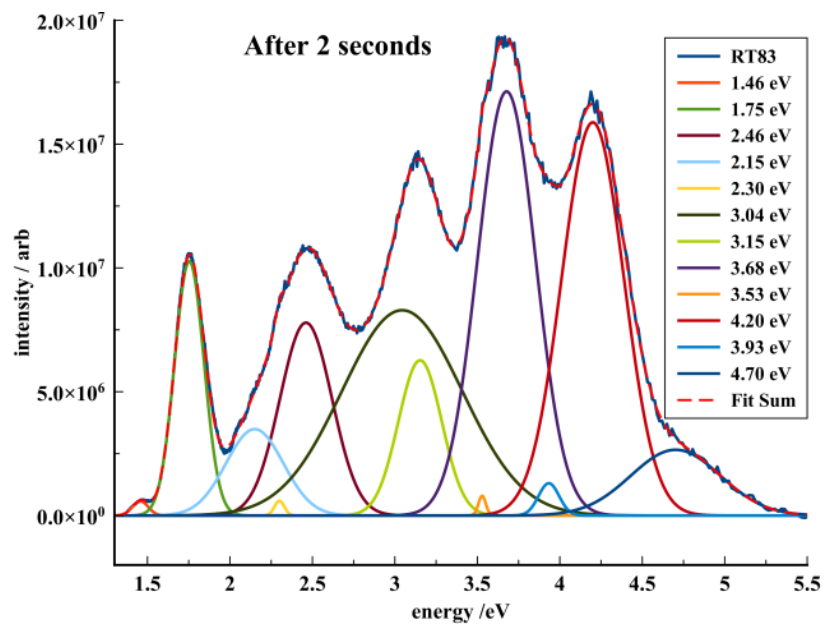


Figure 5-32 - Fitted dose dependence spectra after 2 seconds. Collected using 7 keV, 150 line grating centred at 550 nm (2.25 eV) corrected spectra fitted using Magic Plot Pro 3.2.

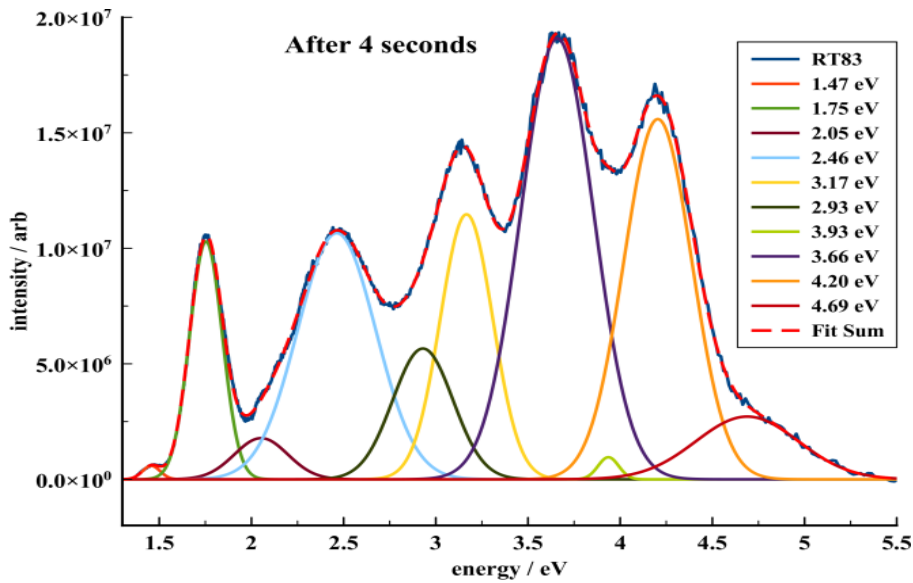


Figure 5-33 - Fitted dose dependence spectra after 4 seconds. Collected using 7 keV, 150 line grating centred at 550 nm (2.25 eV) corrected spectra fitted using Magic Plot Pro 3.2.

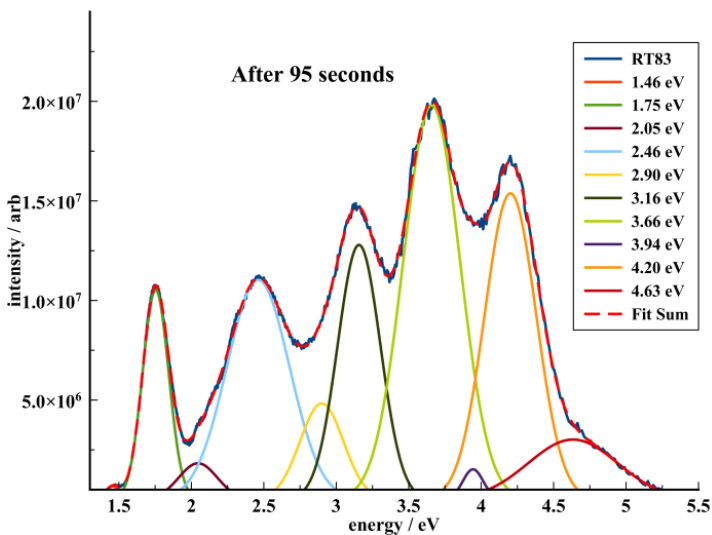
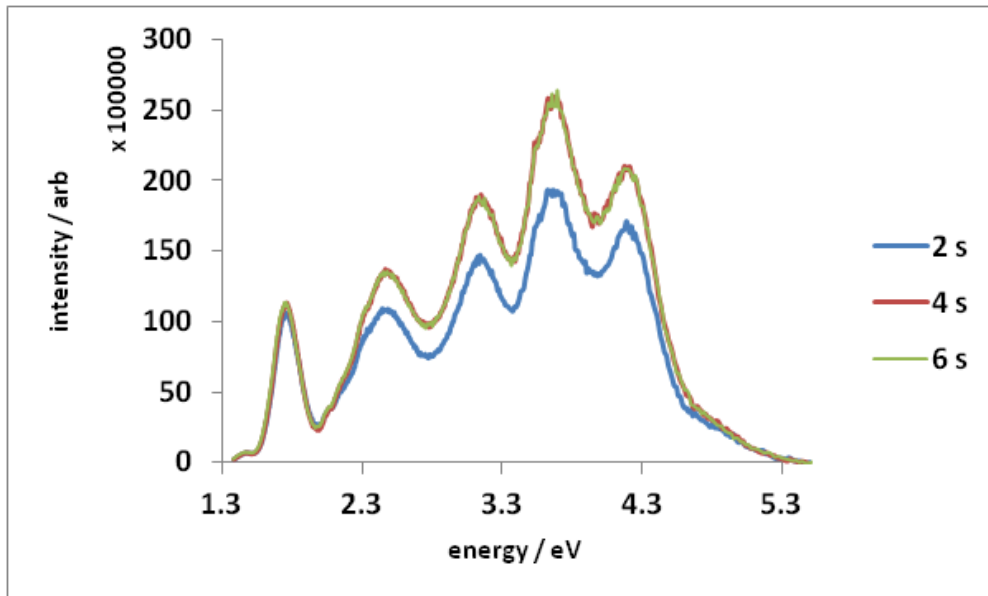


Figure 5-34 - Fitted dose dependence spectra after 95 seconds. Collected using 7 keV using 150 line grating centred at 550 nm (2.25 eV) corrected spectra fitted using Magic Plot Pro 3.2.

From Figure 5-31, it can be seen that the overall trend for intensity of signal can be described as diminishing over time; however, the first measured curve does not have the greatest intensity to explore the nonlinearity the first three spectra in the time series are analysed in Figure 5-35. This shows that for the peaks between 590 and 282 nm (2.1

and 4.4 eV) the intensity of emission increases between the first and second spectra collected; the intensity however remains constant for the peak between 886 -620 nm (1.4 – 2.0 eV). Scrutiny of the deconvoluted individual emissions, as shown in Figure 5-32 and Figure 5-33, shows that this effect is generated from the convolution of two processes, the reduction of both the width and intensity of a broad emission at 408 nm (3.04 eV). Dose effect can be derived primarily from two mechanisms; firstly, the ionisation of the substitutional atom responsible for the emission, and/or secondly, the modification of the local atomic environment of the luminescent defect (Bunker, 2010-220). Broad emissions are normally interpreted as resulting from variations in the defect microenvironment and temperature ie interaction with the host matrix and as such could be described as having a structural component within the emission mechanism (Sharma and Schulman, 1999). The increase in signal seen in the peaks at 393, 504 and 336 nm (3.15, 2.46 and 3.68 eV), occurring in the first two seconds of irradiation, is accompanied by a reduction in the broad peak at 408 nm (3.04 eV) that reduces in both width and intensity over time with an accompanying red shift to 427 nm (2.90 eV). This reduction shows an apparent temporal synchronisation with the increases. If this synchronisation is interpreted as indicating that the mechanisms are linked and the growth of the 393, 504 and 336 nm (3.15, 2.46, and 3.68 eV) peaks are achieved at the expense of the peak at (408 nm) 3.04 eV, the subsequent decrease in the peaks at 393, 504 and 336 nm (3.15, 2.46, and 3.68 eV). Following this initial process, when the conversion is exhausted, a more persistent process becomes dominant generating a slow reduction in the peaks' intensities. Incident radiation is incapable of increasing or decreasing the population of substitutional atoms it can however, affect a luminescent centres through ionisation. If the ionisation model were responsible, it would be unlikely

to affect three separate emissions simultaneously and at the same rate. It can therefore be inferred the modification is structural and affecting the mechanisms involved in both types of emission. This would also be consistent with the hypothesis that the emission spectra are primarily a function of the structure.



**Figure 5-35 - First three spectra from RT83 Moonstone dose dependence spectra
Collected using 7 keV hundred 2 s integrations corrected for system response**

In Figure 5-35 the peak height as a function of time illustrates that behaviour can be separated into two distinct types of response. (Lee et al., 2007b) in a paper exploring CL hyperspectral imaging combined with electron-probe analysis on zoned cryptoperthite alkali feldspars, the authors had a number of unexplained discrepancies between peak intensities and attributed lumiphore concentrations, the red emissions between ~690-725 nm (~1.79 -1.71 eV) showed a good correlation between intensity and Fe concentration. However the intensity of the blue emission ~460nm (~2.7 eV) data displayed a number of irregularities with the concentration of Ti. The attribution of the

lower energy emissions to Fe substitution is described by the authors as having achieved a high degree of consensus. From this current investigation, this is consistent with the uniformity of response of the lower energy emissions. In comparison, the responses of the higher energy emissions are seen to display much more complex responses that if the unconvoluted peak intensity were used would lead to misinterpretation. The technique used by the authors used wavelength range selection rather than deconvolution to estimate individual emission intensities that methodology does not account for emission overlaps. The authors identify the continuing debate over the attribution of responses of the higher energy emissions. The results presented here offer an explanation and methodology to understand these unexplained discrepancies; in addition, these results offer a methodology to resolve outstanding disputed interpretations. These luminescence features have been used to interpret deuteric alteration, which is important in understanding the geological history of minerals. These findings could therefore have useful applications within this area.

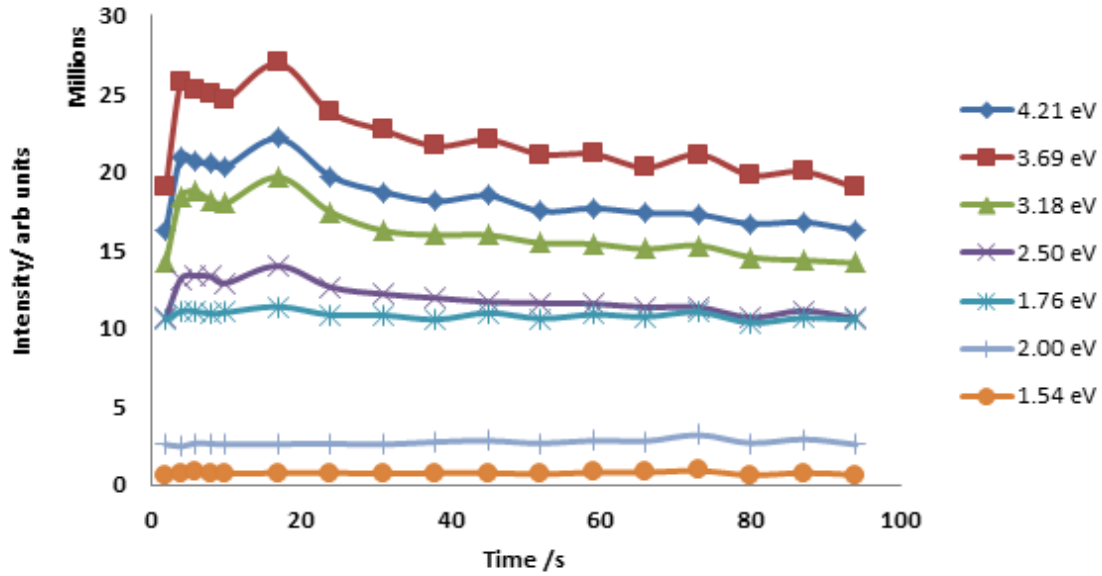


Figure 5-36 - Peak heights taken from figure 5-31 and plotted as a function of time.

5.3.3 Dose rate

In Figure 5-37 and Figure 5-38 the dose rate dependence of the XEOL of moonstone is explored, and the normalised peak heights are plotted against the excitation beam intensity. The 'kink' in the data is within the manufacturer's tolerance for the thickness of the attenuation foils and so cannot be considered as significant as all deviations are within error (error bars are not shown on the graph as they extended beyond the graphs scale). However, the relative variation between the peaks is not significantly affected by the tolerance in the attenuation filters. A variation in the rates of response between peaks has been seen with other samples. Variations in rate changes have been indicative of different emission centres.

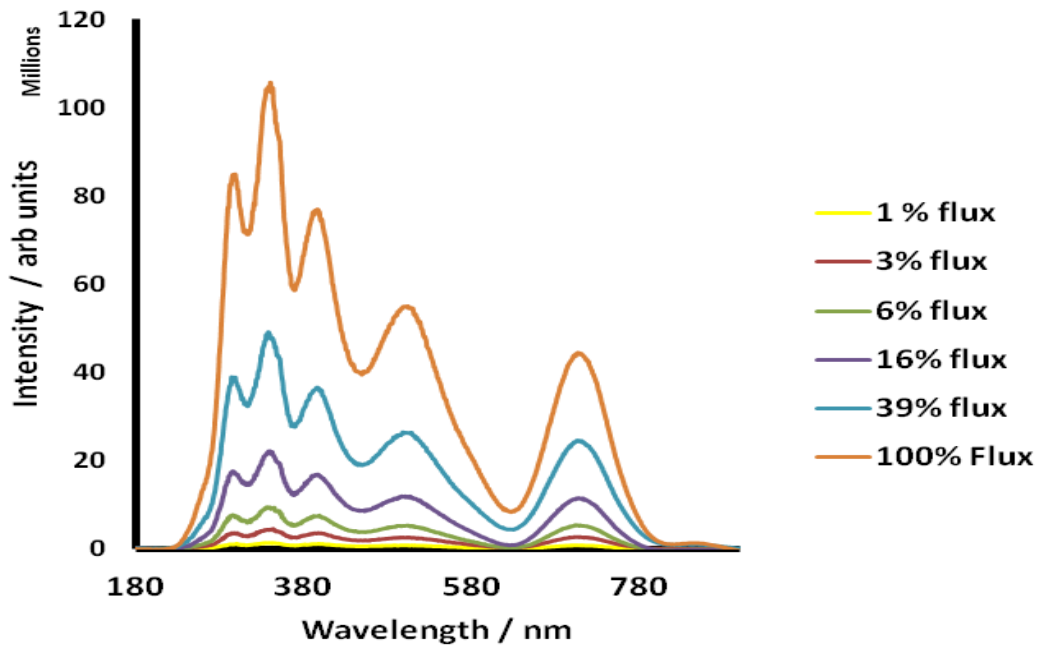


Figure 5-37 - RT moonstone dose dependence using 7keV excitation corrected for system response.

Using 150-line grating centred at 550 nm (2.25 eV) 1mm slits

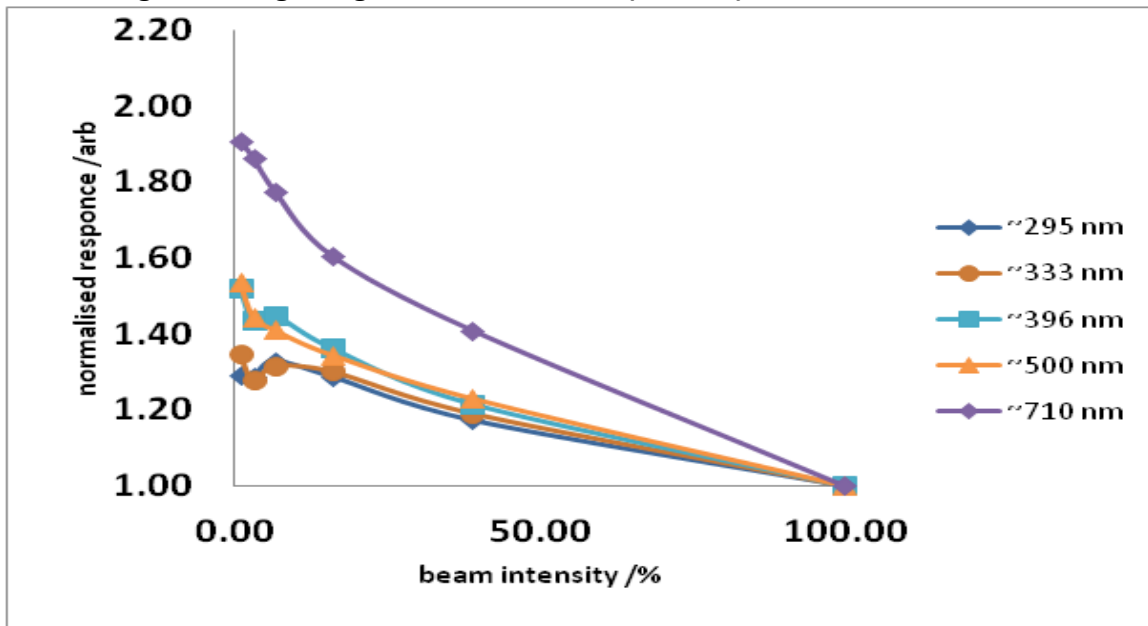


Figure 5-38 - Dose dependence normalised peak height against beam intensity

RT moonstone using 7keV excitation corrected for system response from Figure 5-37

5.4 Copper Bearing Feldspar

The following section illustrates the value of TR XEOL in the role of a complimentary analytical technique. The investigation describes initial applications of conventional techniques and their results. I then show the extent and value of TR XEOL techniques in this on-going investigation. A number of simultaneous investigations have been completed looking at trace element analysis and Ar ratios with varying degrees of success; however, many issues remain in dispute. (Martin et al., 2011, Nasdala et al., 2006, Hirsch and Shankland, 1991).

5.4.1 Characterisation

The first investigations completed on samples of treated and natural material was a combination of EMP, Laser Ablation Inductively Coupled Plasma Mass Spectrometer (LA ICP MS) and (EXAFS), and a summary of the results are provided below. The distribution of copper in natural feldspar (Figure 5-39) is consistent with a link between colour and

the concentration of copper.

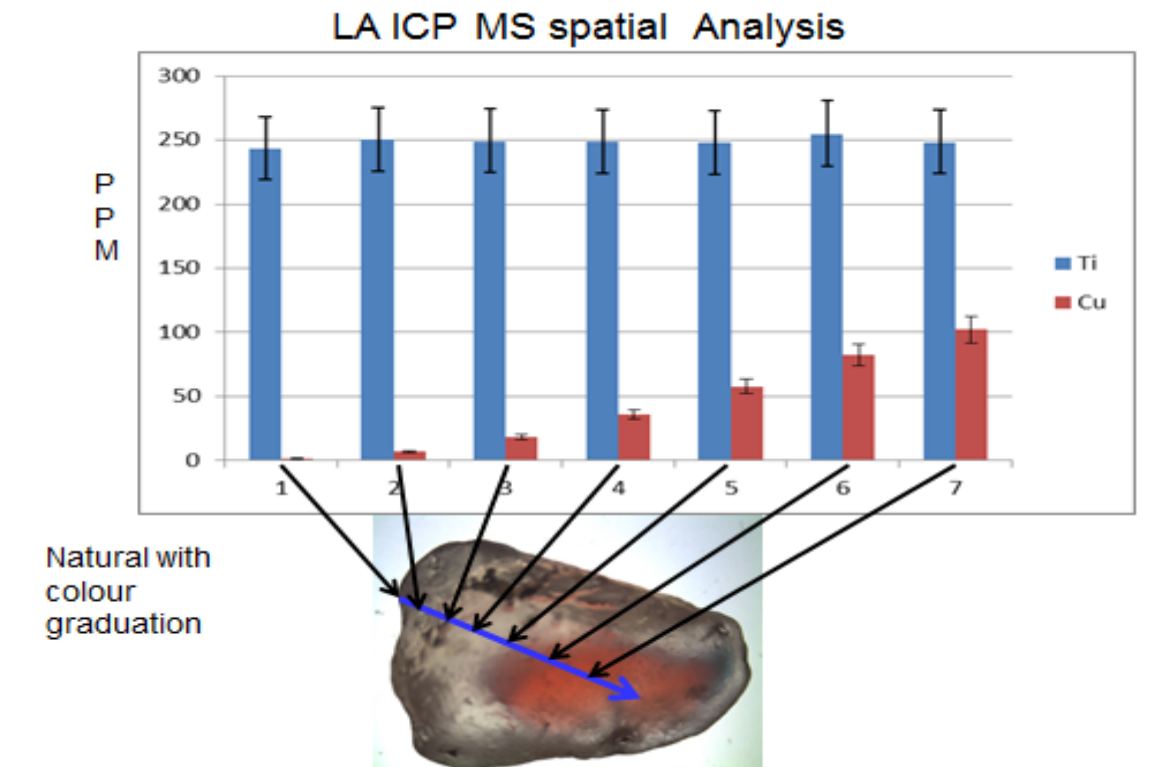
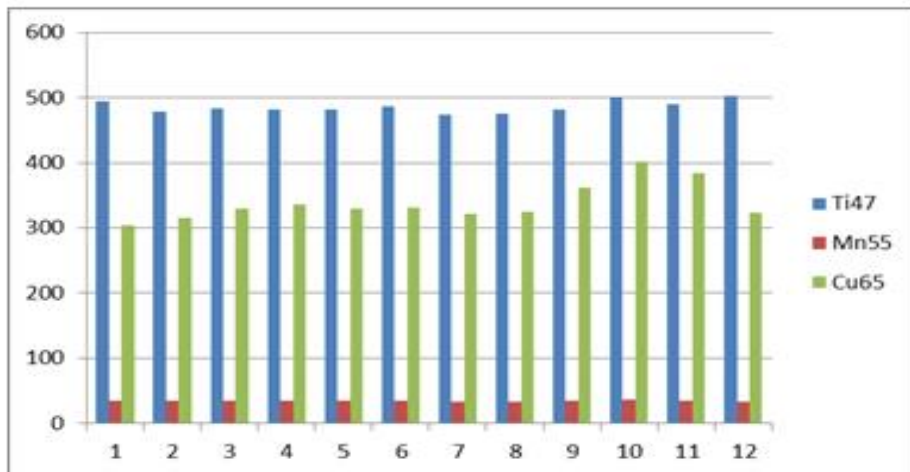


Figure 5-39 - Natural Plush feldspar illustrating the correlation between colour distribution and trace element concentration using LA ICP MS. The copper content within the treated sample is higher, shows less variation, and shows little correlation with the colour distribution



Treated with
Graduation
of colour



Figure 5-40 - Treated feldspar showing the lack of correlation between colour distribution and trace element concentration using LA ICP MS.

The analysis consisting of 12 ablations in single lines starting in LH image at edge of sample in colourless zone, with the third to the ninth ablation lines traversing the red central section of the sample with the last three-ablation lines extending over the colourless portion of the sample top corner of the crystal RH image.

The copper content within heat-treated samples are higher, and shows less variation and little correlation with the colour distribution (Figure 5-40). In contrast, comparable natural samples show a greater variation in concentration and a higher degree of correlation between Cu content and colour concentration. Images of natural and treated feldspar are displayed in Figure 5-41

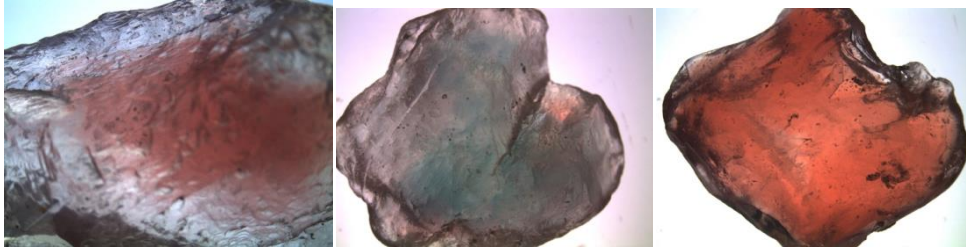


Figure 5-41 - Natural and treated plush feldspar samples.

Samples of natural and treated feldspar were examined using EXAFS on the I18 microfocus beamline at the diamond light source in the UK. Standards for three Oxidation states for Cu were collected for comparison (Figure 5-42). Three standards, copper foil Cu (0) tenorite Cu (ii) and cuprite Cu (i)

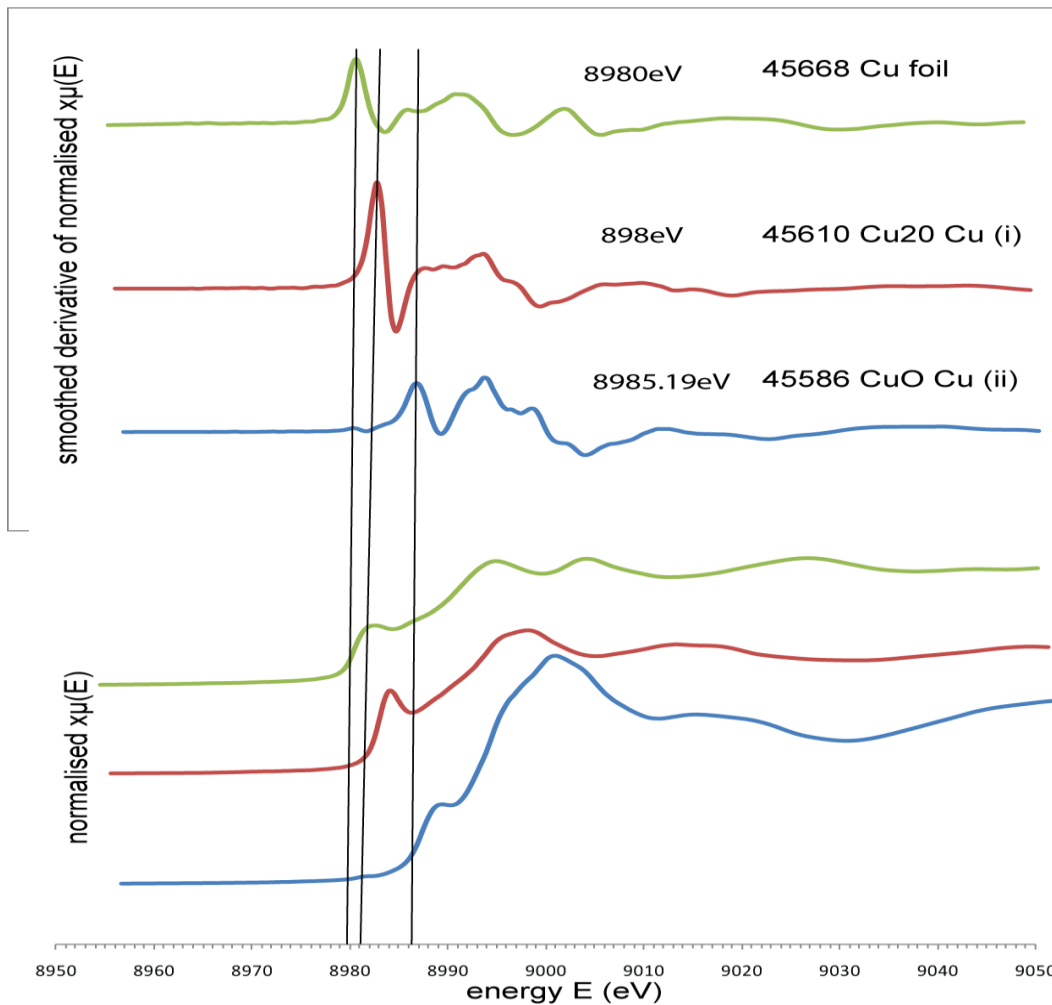


Figure 5-42 - The standards measured for the three copper oxidation states and their first derivative. The graphs illustrate the edge energy shift due to the change in oxidation state

The accepted methodology is to estimate the edge energy from the first inflexion of the first derivative. The edge energy increases as the oxidation state rises. The XANES results for the samples tested are compared to the standards in Figure 5-43, Figure 5-44 and it can be seen that none of the samples show a clear or direct correlation with the edge energies of the Cu standards. This is interpreted as the samples shown contain a mixture of oxidation states.

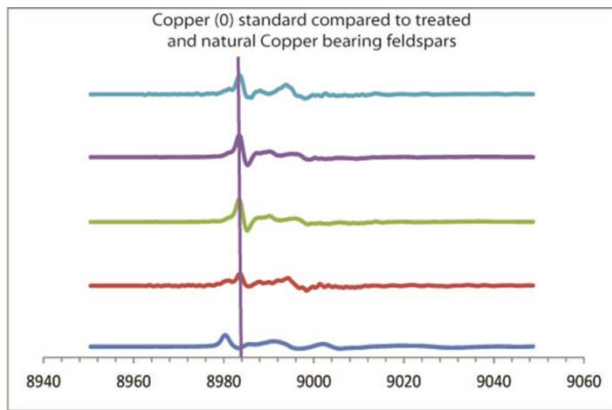


Figure 5-43 – First derivatives of XANES across the Cu K Edge energy of Cu0 (mid blue) compared to natural and treated copper bearing feldspars (Light blue, purple, green red).

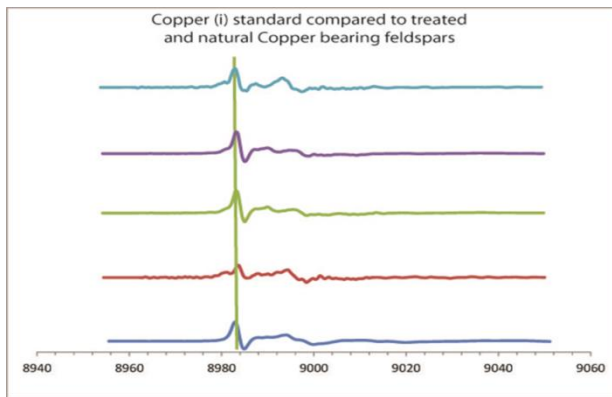


Figure 5-44 - First derivatives of XANES across the Cu K Edge energy of Cu+1 (mid blue) compared to natural and treated copper bearing feldspars (Light blue, purple, green red).

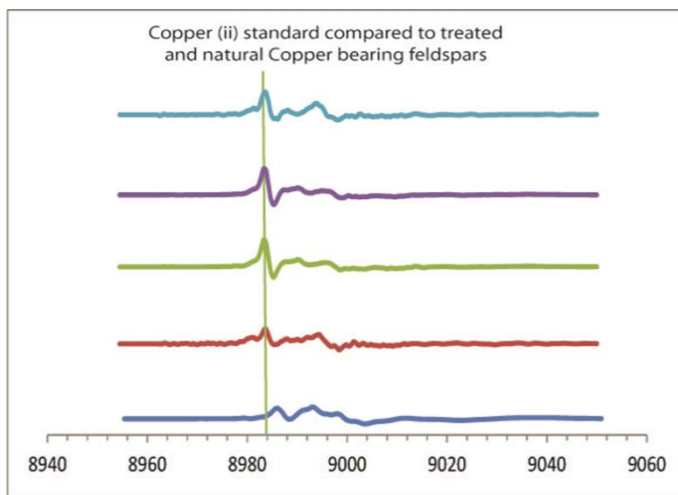


Figure 5-45 - - First derivatives of XANES across the Cu K Edge energy of Cu⁺² (mid blue) compared to natural and treated copper bearing feldspars (Light blue, purple, green red).

eV	treated	natural	treated	natural
8979.9				
8980.3				
8980.8			1	1
8981.3	2	2	2	1
8981.8	2	2		
8982.3				
8982.8				
8983.3	1		12	
8983.8				6

Table 5-4 - Analysis of the measured edge energy of a number of natural and treated samples column 1 is edge energy of absorption edge for sample .

Both the red and green varieties give results consistent with the copper contained within both the natural and treated feldspars is a mixture of oxidation states predominantly Cu^{+1} but with admixtures of Cu^0 and Cu^{+2} . The results also demonstrate that the colour of the feldspar shows no linear dependence upon the oxidation state of copper.

Samples of both natural and treated, green and red, copper bearing feldspar were analysed using EXAFS on the I18 beamline. The results are presented along with those for copper standards in Figure 5-42 to. They show a wide range of edge energies that can only be explained by there being more than one oxidation state present. The samples displaying a lower edge energy are primarily an admixture of Cu^{+1} and Cu^0 the higher edge energies >8983 eV is explained by samples containing a significant percentage of Cu^{+2} . The Cu oxidation state does not show a clear correlation with the

colour of the material nor whether it is natural or treated. The variation in edge energy extends over a range of ~ 4 eV and the distribution shown in Table 5-4, demonstrating that there are two distinct groups of edge energy with a shift of ~ 3 eV between them. The shift in edge energy can be interpreted as a Cu oxidation ratio. This is also consistent with the strong green/red dichroism displayed by the material. (Hofmeister and Rossman, 1985) suggested a mechanism similar to that displayed by copper nano particles in glass described by (Doremus et al., 1992). If the green colouration was obtained from substitutional $\text{Cu}^{+1} / \text{Cu}^{+2}$ this could then explain the lack of correlation between the Cu concentration and nature of the colour seen. The spread of edge energy can only be explained if the Cu is present in all the samples tested in at least two oxidation states, if not all three. The EXAFS portion of the spectrum was modelled to provide information on the local coordination of the absorber, the bond length, and the identity of the surrounding atoms, and the analysis was completed using Excurv 98 (Binsted, 1998). All the analyses showed a good fit in the first coordination shell for a linear coordination with two oxygen atoms and at approximately 1.9 \AA this is consistent with a sp^2 hybridisation coordination typical of $\text{Cu}^{(+1)}$ (Biccari, 2009). This would be consistent with the majority of copper present being Cu^{+1} with the admixtures of Cu^0 and Cu^{2+} .

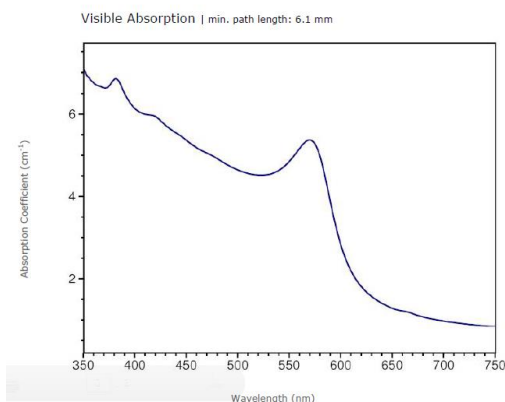


Figure 5-46 -Absorption spectra copper bearing natural 'plush' feldspar. Source: (GIA, 2011)

Photoluminescence | 514.5 nm laser

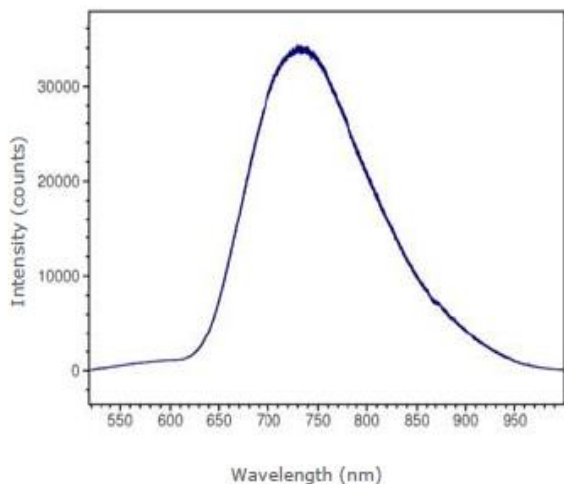


Figure 5-47 - Luminescence spectra copper bearing natural 'plush' feldspar . 514.5 nm (2.41 eV) laser excitation Source: (GIA, 2011)

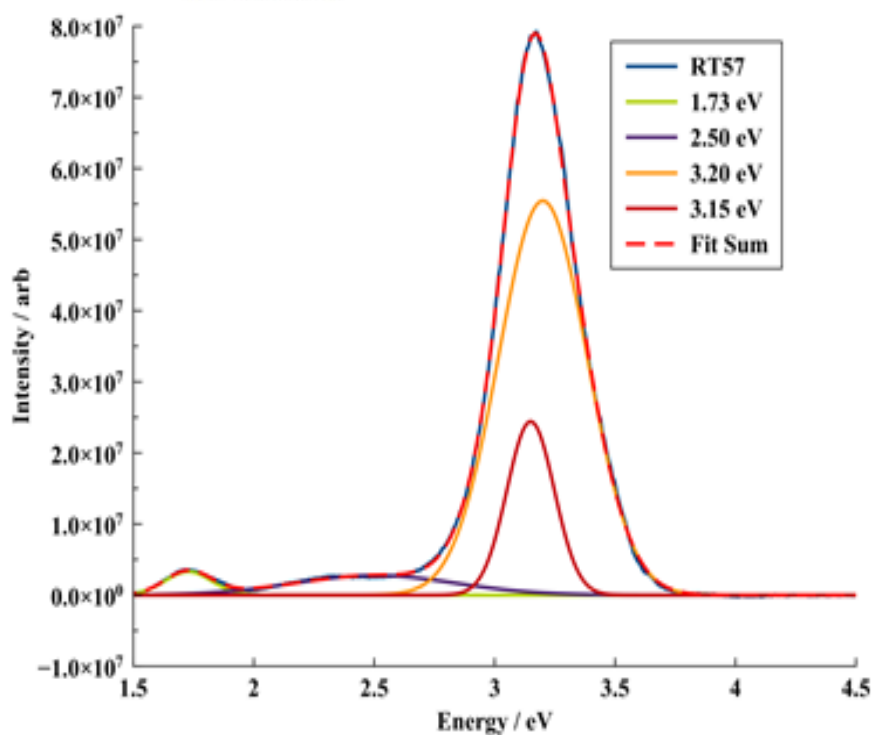


Figure 5-48- CW XEOL RT57 colourless Mongolian Andesine excited 7 keV.collected using 0.5 mm slits, 150 line grating blazed at 500 nm- 2.48 eV centred at 550 nm -2.25 eV from the peak analysis of CW XEOL.

5.4.2 CW XEOL

Spectra collected from samples of treated and natural material are shown in Figure 5-49 to Figure 5-53 is tabulated by peak position in Table 5-5. Figure 5-47 shows a broad emission in the red that could be the energy shifted metallic copper emission seen at 620nm as reported by Boyd et al., and Mooradian (Boyd et al., 1986) Pre-treated material is differentiated by having no luminescent features, with peak wavelengths shorter than 315 nm 3.94 eV. These untreated samples do not contain Cu within the limit of detection (LOD) when tested using a LA ICP MS and I therefore infer that the higher energy emissions in the treated samples are most likely related to the presence of Cu. All samples except RT57 the untreated Mongolian andesine have a common broad feature centred in the range 340-360 nm 3.64- 3.44 eV. A similar feature exists in RT57 but red shifted to a peak wavelength of ~ 393 nm (~3.15 eV. The main peak displayed by RT 57 is different to all the other samples in both peak energy and shape. No distinctive emissions are identified that would allow discrimination

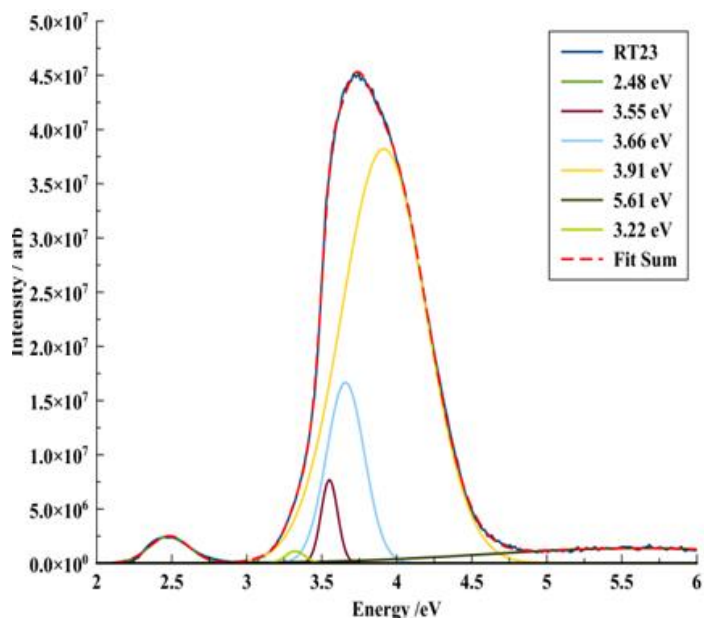


Figure 5-49 - CW XEOL RT23 treated red Andesine excited 7 keV. Collected using 0.5 mm slits, 150 line grating blazed at 500 nm -2.48 eV, centred at 550 nm 2.25 eV

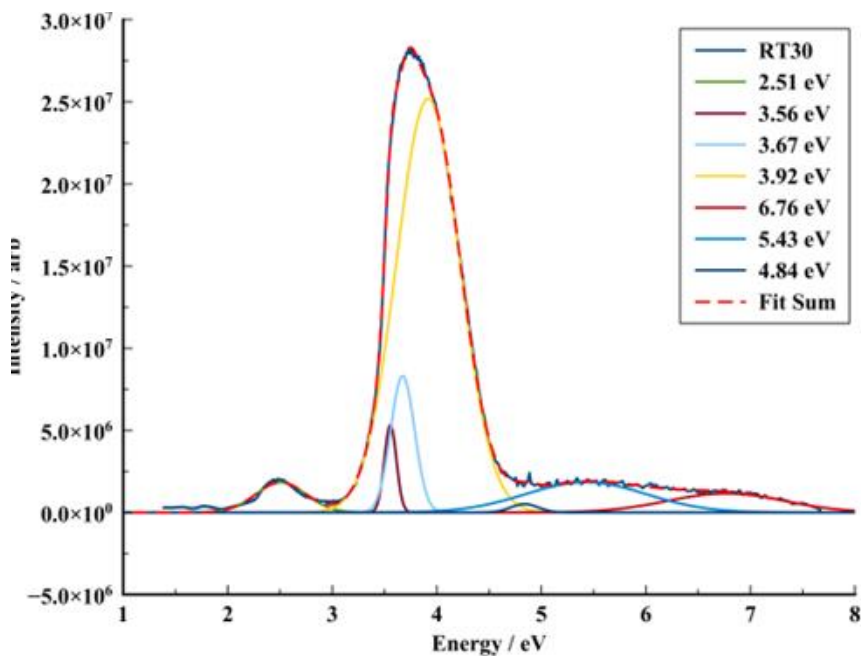


Figure 5-50 - CW XEOL RT30 treated green Andesine excited 7 keV. Collected using 0.5 mm slits, 150 line grating blazed at 500nm -2.48 eV, centred at 550 nm 2.25 eV

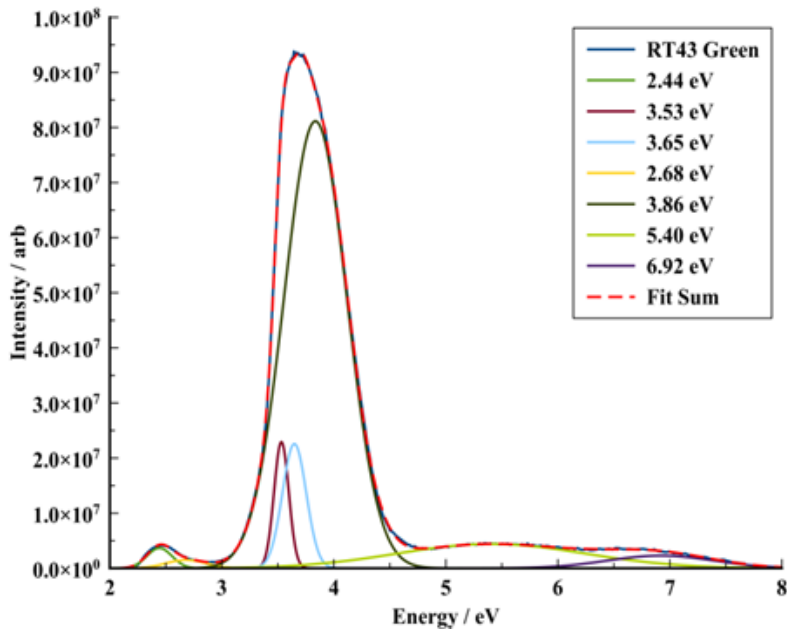


Figure 5-51 CW XEOL RT43 natural green Labradorite excited 7 keV. Collected using 0.5 mm slits, 150 line grating blazed at 500nm -2.48 eV, centred at 550 nm 2.25 eV

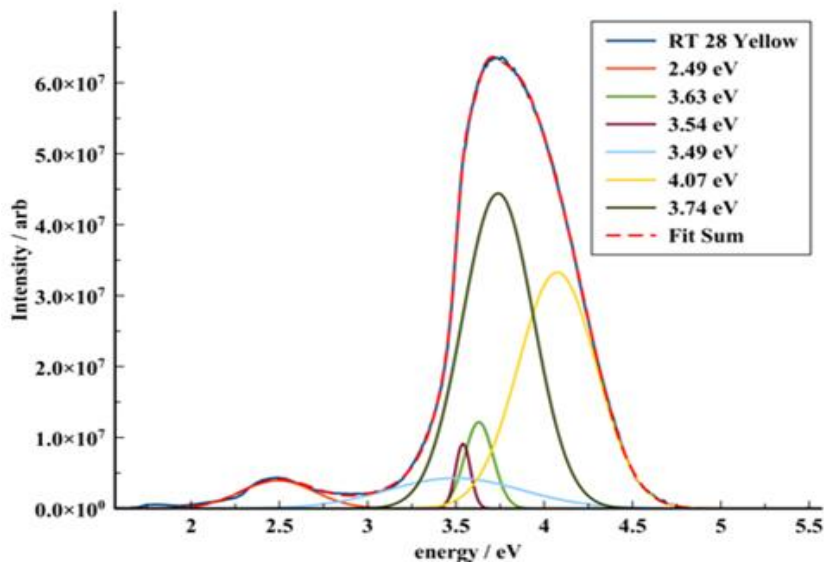


Figure 5-52 CW XEOL RT28 natural colourless Labradorite excited 7 keV. Collected using 0.5 mm slits, 150 line grating blazed at 500 nm -2.48 eV, centred at 550 nm 2.25 eV

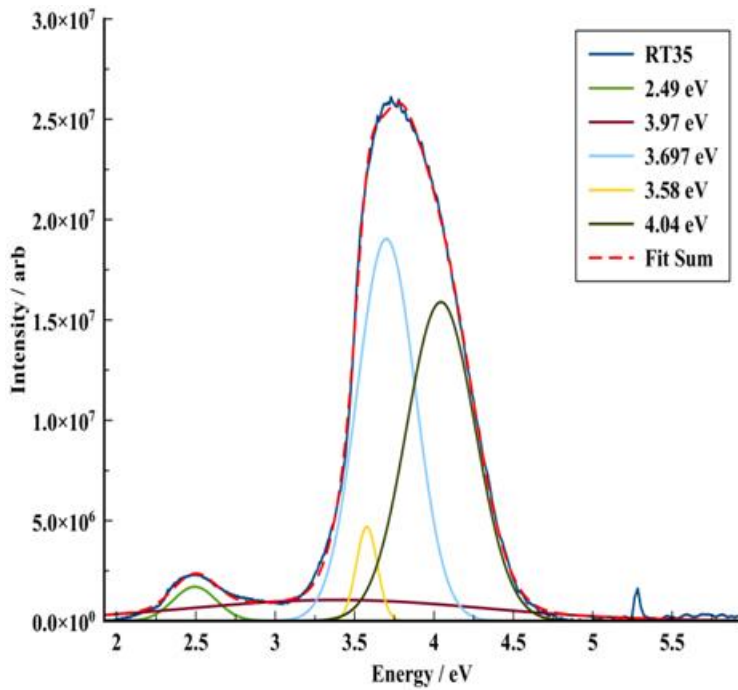


Figure 5-53 CW XEOL RT35 treated andesine excited 6 keV
Collected using 0.5 mm slits, 150 line grating blazed at 500 nm -2.48 eV,
centred at 550 nm 2.25 eV

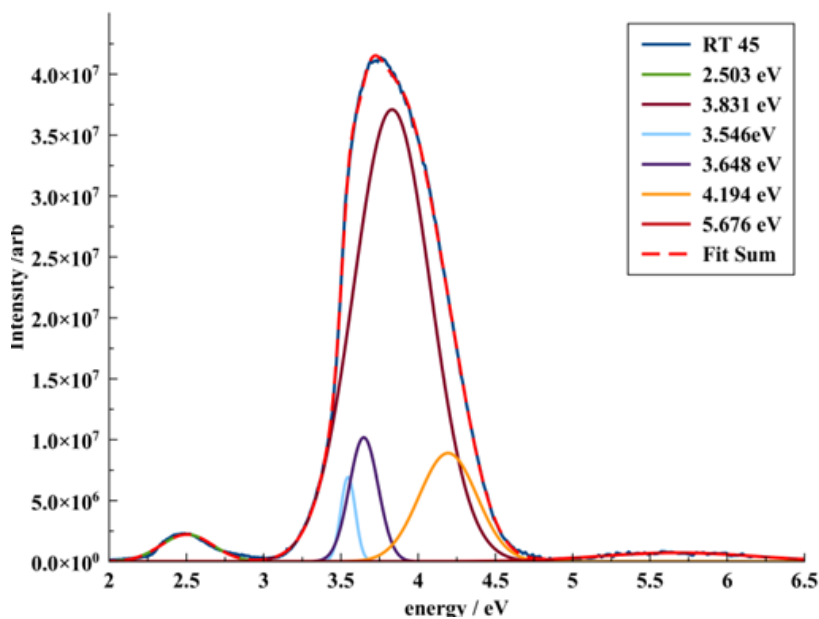


Figure 5-54 CW XEOL RT45 natural red labradorite excited 6 keV
Collected using 0.5 mm slits, 150 line grating blazed at 500 nm -2.48 eV,
centred at 550 nm 2.25 eV

	rt57-N	rt23-T	rt30-1-T	rt30-2-T	RT35-T	rt43-N	rt28-N	rt45-N
peak 1 λ		5.61	5.22	5.43		5.40		5.676
peak 2 λ				4.84	4.04		4.07	4.194
peak 3 λ		3.912	3.97	3.92	3.97	3.86	3.74	3.831
peak 4 λ		3.66	3.67	3.67	3.65	3.65	3.63	3.648
peak 5 λ		3.55	3.56	3.56	3.53	3.53	3.54	3.546
peak 6 λ							3.49	
peak 7 λ	3.20	3.22	3.33					
peak 8 λ	3.15							
peak 9 λ						2.68		
peak 10 λ	2.50	2.48	2.48	2.51	2.49	2.44	2.49	2.503
peak 11 λ	1.73							

Table 5-5 - Peak positions from XEOL collected from samples of treated and untreated labradorite and andesine.

The blue highlighted columns are natural coloured plush labradorite, the colour of figures reflects the colour of the material, and the yellow figures are untreated source material prior to treatment. The final letter in the sample reference indicates if the material is T treated or N natural/untreated

5.4.3 TR XEOL

TR XEOL was collected from untreated feldspar samples that consistently displayed two fitted lifetime emissions, the first > 1 ns, the second ranging between ~10.0 - 40.0 ns. In all heat-treated samples, including blanks (samples heated with no Cu present), only one fitted lifetime was detected with lifetime between 0.9- 2 ns. In the heat-treated samples tested, no short life > 10ns. TRPL was detectable from emissions between 450-900 nm, these spectra were collected on an f900 Edinburgh Instruments laser ns-ms TRPL system using 375 nm laser excitation. Fitting was completed on the proprietary software. These

findings were replicated using TR XEOL where no measurable lifetimes ($\sim < 200$ ns) with an emission wavelength > 500 nm were measured from heat-treated samples.

	τ_1	\pm	A1	τ_2	\pm	Y_0	\pm	Peak height	Treated/ Untreated
RT52a	0.96	0.03	1039	24	3	182	1.4	1323	U
RT51	1.99	0.04	315			18.1	0.3	333	T
RT47	0.96	0.02	699	18.48	3.4	33.86	0.61	764	U
RT48	0.87	0.05	43			0.82	0.07	45	T
RT50c	0.88	0.02	959	20.5	7.3	17.2	0.57	990	U
RT46	0.91	0.12	135			62.1	0.5	194	T
AF1	1	0.02	837	38	12.4	22.49	0.7	849	U
RT53	0.83	0.02	734	11	3.5	28.8	0.5	777	U
DK7	0.9	0.06	277	19.7	4	31.67	0.5	342	U

Table 5-6 TR XEOL representative spectra collected from treated and untreated samples of feldspar detailed in Table 3-3

The results are consistent with heat treatment generating long term alterations to the luminescent signal; the loss of luminescent emissions with lifetimes < 200 ns gives the potential to discriminate heated and thereby treated samples through the absence or presence of lifetime emissions within particular wavelength ranges. The results from repeated heat treatment experiments consistently show high temperature treatment $\sim 1000^{\circ}\text{C}$ reduces significantly or completely removes many luminescent emissions, with the short life luminescent signals (> 200 ns) the most susceptible to being affected (Figure 5-55).

Table 5-6 illustrates differences seen between PL and XEOL spectra in that emissions that cannot be detected using PL Figure 5-55 are still present within X-ray excited spectra however showing significant reductions in signal intensity that identifying sample change. The emissions at 400-600 nm (3.09 – 2.06 eV) are destroyed by the heating process

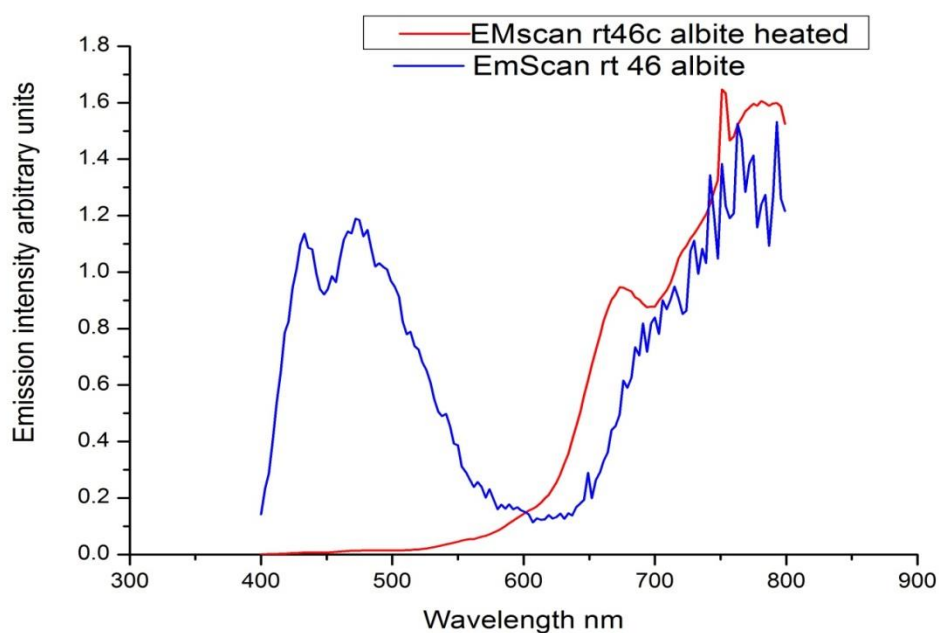


Figure 5-55 RT58 Albite TRPL emission scan showing before and after heat treatment spectra. Collected on Edinburgh instruments F900 TRPL using 375nm pulsed laser excitation

An unusual response from an untreated andesine RT52 was recorded when completing a dose dependence experiment. (Figure 5-56, Figure 5-57) The colourless andesine sample is purported to be an example of the source material from which much of the commercially produced copper treated feldspar is derived. In comparing Figure 5-56 and Figure 5-57 it can be seen at the lower beam intensity there is a high long lifetime

background (Y_0), whereas in the higher beam intensities this 'background' is seen to show significant reductions.

<i>Beam intensity %</i>	<i>Time initial peak / ns</i>	<i>Start exponential decay / ns</i>	<i>Delay in decay start / ns</i>
5	5.66	26.56	20.9
16	5.66	24.21	18.55
39	5.66	23.43	17.77
55	5.66	23.43	17.77
75	5.66	23.43	17.77
100	5.66	23.43	17.77

**Table 5-7 - TR XEOL responses of RT52 colourless Andesine
Collected using 7 keV excitation, 1 mm slits 150 line grating blazed at 500 nm 2.48 eV centred at 410 nm (3.02 eV).**

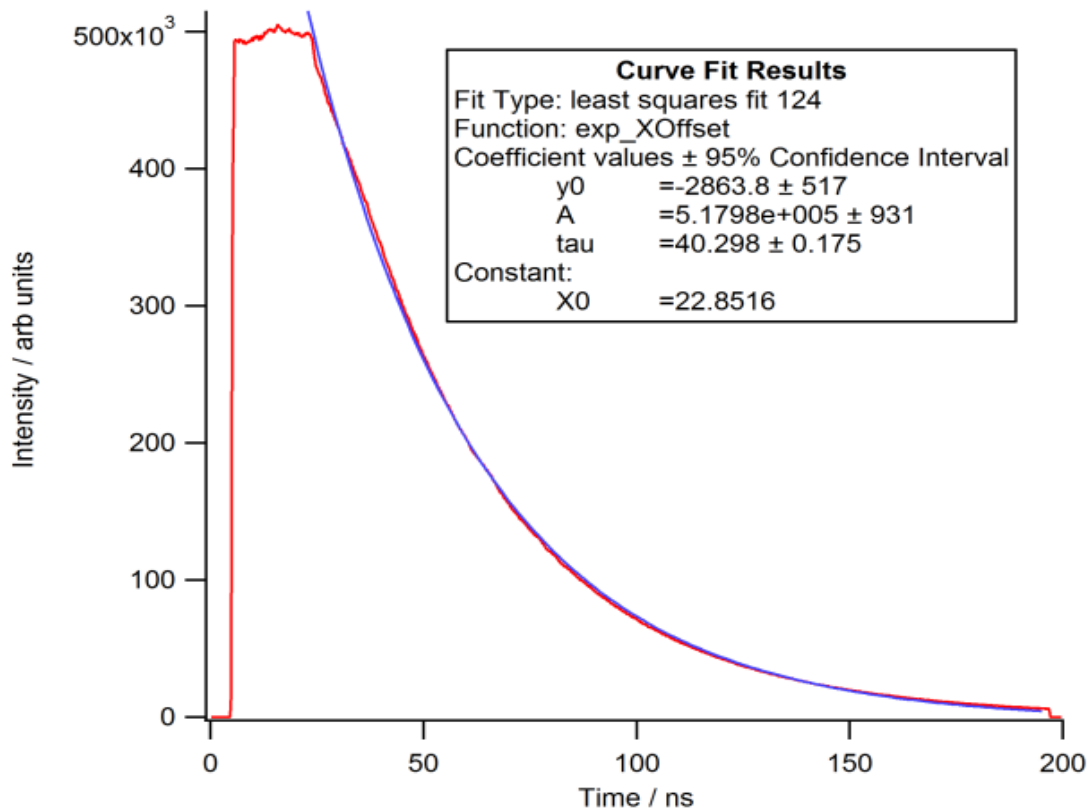
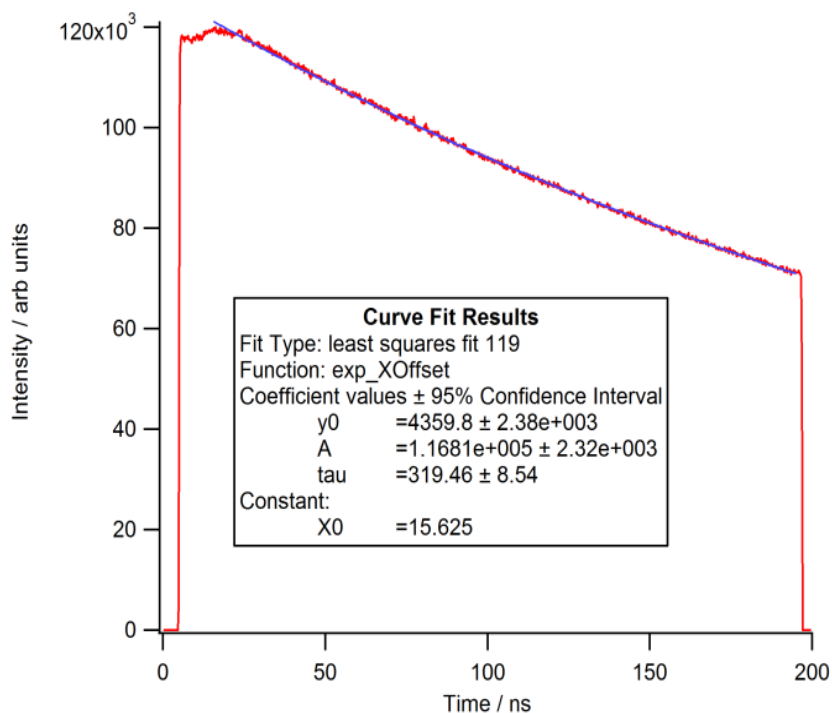


Figure 5-56 - Dose Dependent TR XEOL from RT52
Colourless untreated andesine Excitation 7 keV. Collected using 1 mm slits
150 line grating blazed at 500nm 2.48 eV centred at 460 nm 2.70 eV 100%
beam intensity.



**Figure 5-57 - Dose Dependent TR XEOL from RT52
Colourless andesine excitation 7 keV. Collected using 1 mm slits 150 line
grating blazed at 500nm 2.48 eV centred at 460 nm 2.70 eV 5% beam
intensity.**

From Figure 5-58 the intensity behaviour of A0 and Y0 is seen to show a complex inverse relationship at low beam intensities. This unusual TR behaviour including the exponential decay of the luminescent signal apparent 'delay' between ~17-21 ns, with the longer delay occurring at lower beam intensities. The following discussion will offer an explanation but requires further work to test its validity. The behaviour can be explained by the combination of a number of simultaneous processes.

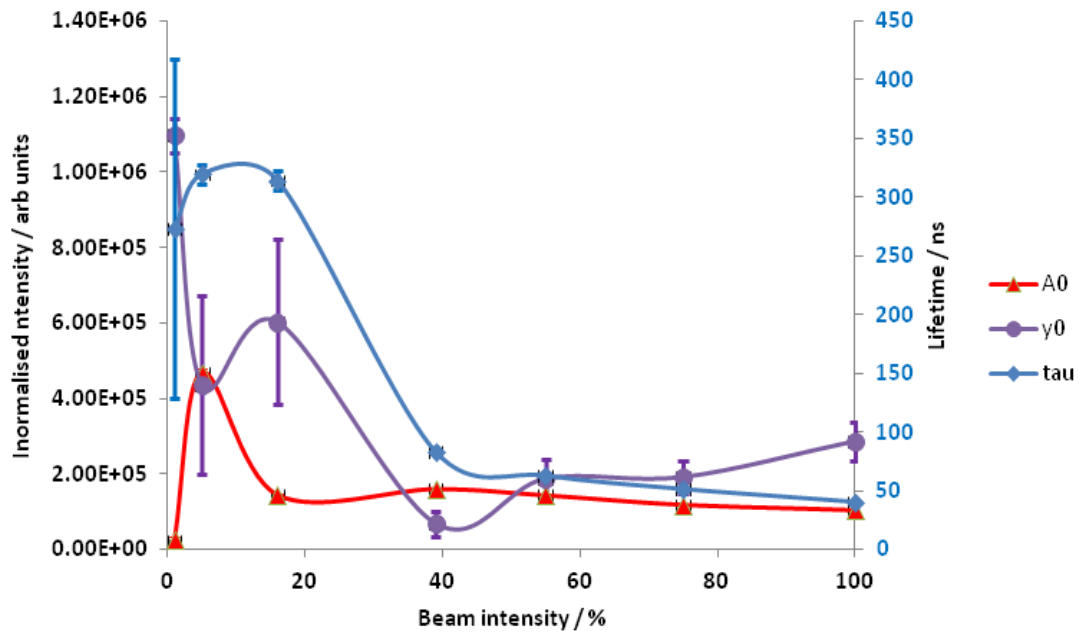


Figure 5-58 - Dose dependence TR XEOL data collected from RT52 Colourless andesine excitation 7keV example data (Figure 5-56) and (Figure 5-57). Red trace is peak intensity of TR peak (A0), Purple intensity of (γ_0) the long lifetime 'background' Blue (τ) lifetime of single exponential luminescent decay.

Firstly, I postulate that the exponential decay is not being delayed it is simply hidden beneath other concurrent effects. The 'delay' I infer to indicate that energy is being transferred into the luminescent site following cessation of the excitation pulse. The process most likely to produce this effect involves a second absorption site that is either metastable or with a long lifetime luminescent emission, this secondary site acts as a donor to the primary, faster lifetime, luminesce site. The mechanism is probably using an energy transfer mechanism as described in section 2.10. The probabilities of transfer (the rate) is a power function of the distance between donor and acceptor and the amount of energy transferred will be a function of the population and absorption cross section of the secondary site and the beam intensity. The mechanism is summarised in Figure 5-59, where the behaviour exhibited is a function of the relative rates of energy transfer to, and direct excitation of, the primary emission site. The energy transfer can

be accomplished with both Förster and Dexter mechanisms and can also be a direct reabsorption if the secondary site is emissive. These alternative mechanisms add the potential for additional rate effects to the energy transfer. The duration of the delay reduces between the 5 and 16% beam intensities and then remains constant for all the higher beam intensities. The limit of the reduction to the delay I would attribute to the saturation of the secondary site.

The reduction of the Y_0 signal at increasing beam intensities I would attribute to the population of the secondary site, and saturation of absorption is reached by ~15% of the beam intensity. Absorption site 'A' has a larger absorption cross section than site 'B', but has a limited population, whereas absorption site 'B' has a smaller absorption cross section relative to site 'A' but a larger population. The apparent reduction in the lifetime of emission of site 'B' is due to the diminishing proportion of energy transfer from site 'A' and this has the effect of lengthening the measured lifetime of 'B.'

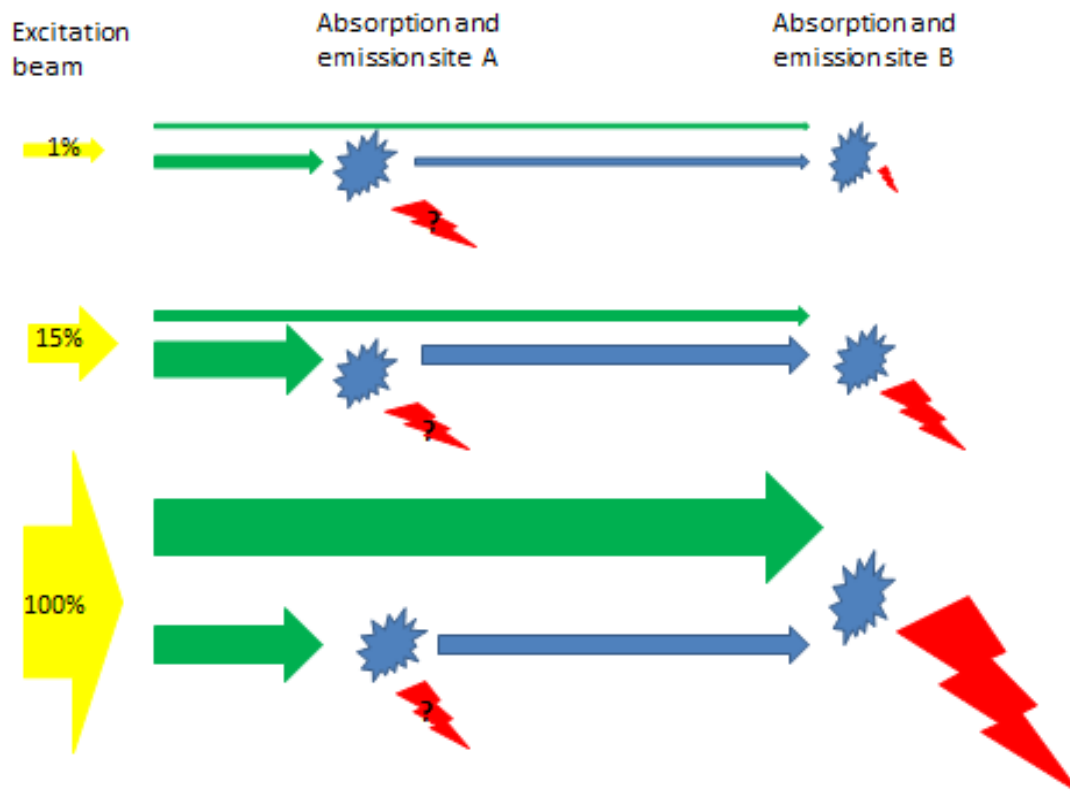


Figure 5-59 - Absorption and energy transfer model to explain TR spectra of RT.

Yellow arrows indicate the excitation beam intensity, green arrows indicate the direct excitation of the centre, blue arrows indicate energy transfer, and red arrows indicate luminescent emission. Thickness/size of arrow is relative to the quanta of mechanism.

The TR dose rate experiment from RT57 Mongolian colourless andesine are presented as the normalised TR Peak height is plotted against the beam intensity in Figure 5-60. The data shows the increasing intensity of response as the dose rate increases up to ~75% beam intensity and the response is then constant up to 100% beam intensity.

Explanations include that the system reaches saturation at the 75% intensity level or that the sample is subject to a dose response and the sample is changing during the experiment or it is a combination of both. This alternative clearly illustrates the importance of completing dose and dose rate experiments in conjunction. However, in

this experiment, the dose rate is obtained from TR data and because the decay is best fit as a single exponential, this is interpreted as representing a single transition and defect centre. As the τ lifetime remains constant for all intensities of beam, this eliminates sample change as the reason for the intensity behaviour.

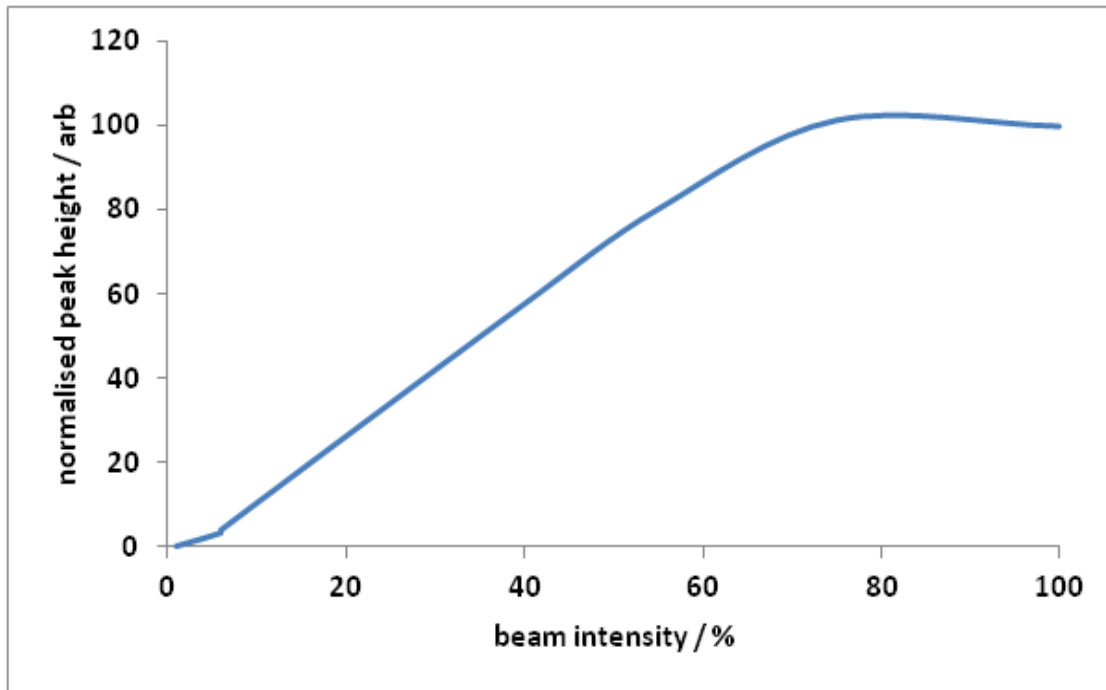


Figure 5-60 -RT57 labradorite Inner Mongolia dose rate TR XEOL. Normalised TR Peak height as a function of beam intensity.

5.5 Chapter summary

Understanding the genesis and history of the feldspar the most common mineral group in the Earth's crust is economically extremely important as its presence almost ubiquitous. Luminescence as a technique to explore minerals has, as previously discussed, the benefit of sensitivity to many of the important diagnostic attributes of feldspar. This includes sensitivity to both the complex trace element substitution typically present in feldspar, and its interrelationship to the local and extended structure

and its defects. This interrelationship goes to the core of interpreting the geological provenance and history of this important mineral group. The work presented in this chapter demonstrates, the technique of considering together the intensity and lifetime of luminescent signals, is particularly useful to understand and interpret feldspar. This in turn leads to better modelling and the potential for quantification of responses.

5.5.1 Suggested further work

The results in this section provide a number of areas worthy of further investigation that are detailed below

Results from 5.1.1 can be further investigated by repeating the experiment, scanning through a range of excitation with smaller energy steps. This probes the relationship between lifetime and intensity of emissions and demonstrates within error there is no discernible correlation between lifetime and intensity.

In section 5.1.1 to test the hypothesis for hot luminescence a repeat experiment using high spectral resolution would determine if a blue shift is measured in the wavelength of emission in response to the increasing excitation energy. Bergstrom et al. (2008) in an experiment comparing the laser induced TR PL with TR XEOL of ZnO nanoparticles, noted variations between the measured τ lifetimes from the alternative excitations, however they could not explain their findings.

In section 5.1.2, two alternative hypotheses for the change in intensity as a function dose were proposed, sample alteration and changes in energy transfer. Further experiments on a suite of similar material containing a range of defect concentrations would enable this issue to be resolved.

In section 5.3.2 I identify that the differentiation of the two groups identified in dose dependence experiments are replicated in the dose rate experiments, with the low energy emissions showing distinctly different responses to the higher energy responses. Investigation of this behaviour could be progressed by characterising a suite of moonstones with varying trace element concentrations and making comparisons to well characterised cryptoperthite alkali feldspars using the same technique, this will enable more direct comparisons of emissions and will allow the assignment of individual emissions to be completed with greater confidence. In addition, by exploring well-characterised perthite and cryptoperthite samples on the microfocus facility using the same techniques the high spatial resolution would facilitate the investigation of structure on luminescence.

6 Additional Results

The results from a wide range of gem quality minerals are presented in this chapter using the same techniques previously described in chapters 4 and 5. Most minerals are anisotropic and of low symmetry, this is of particular importance when considering the QE of a luminescent signal. The effect of orientation is explored using the gem quality biaxial mineral topaz. The results presented are significant and are the justification for a more extensive investigation. The concept of interpreting TR data as a function of crystallographic orientation demonstrates significant potential.

6.1 Zircon

Luminescent emissions including XEOL and PL from zircon are primarily from REE substitutional defects and generally show little vibrational broadening due to the emissions primarily being from 4f orbitals that are shielded from the lattice by mainly 5S and 5P orbitals. However, Friss (2009) documented a number of instances where significant lattice interaction with REE emissions could be determined. Here I analyse ZAF5 a red gem quality zircon.

6.1.1 CW XEOL

The CW spectra (Figure 6-1) as expected has typical REE features, including an emission at $435\text{nm} \pm 1\text{nm}$ that I compare with the attribution made by Gaft (2005) of Tb^{3+} 436nm. the main spectra are most likely derived from Ce^{3+} and Er^{3+}

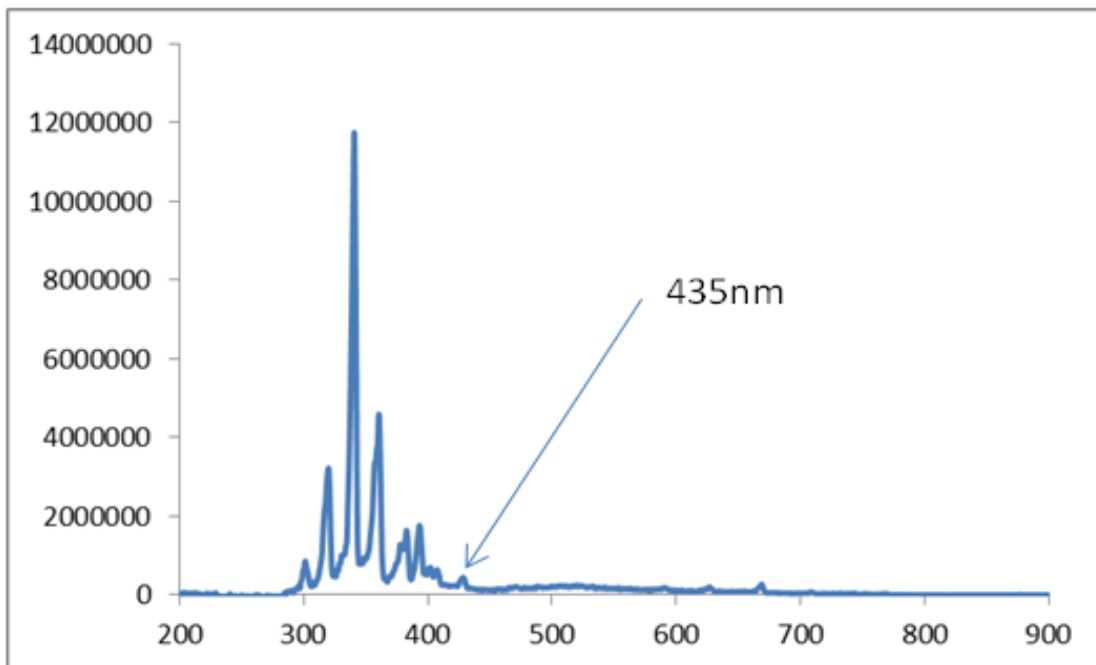


Figure 6-1 - ZAF5 CW XEOL spectrum collected from red zircon. 30 seconds integration using 150 line grating blazed at 500 nm (2.47 eV) centred at 435 nm (2.85 eV) 0.1 mm slits 7 keV excitation.

6.1.2 TR OD XAS

TR OD XAS for samples of zircon with REE lumiphores were attempted; REEs are normally associated with narrow and discreet emission profiles indicating limited interaction between the luminescent defect and the host matrix. An energy scan from 6960-7010 eV collecting TR spectra every 1 eV for 180 s integrations centred at 435 nm (2.85 eV) is collected a sample spectrum is displayed in Figure 6-2, this experiment was performed to test if a structurally isolated emissions carries an OD XAS signals.

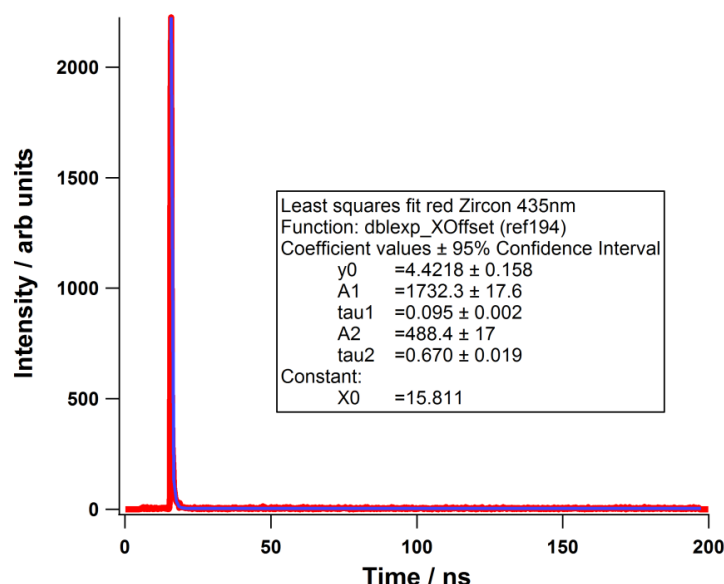
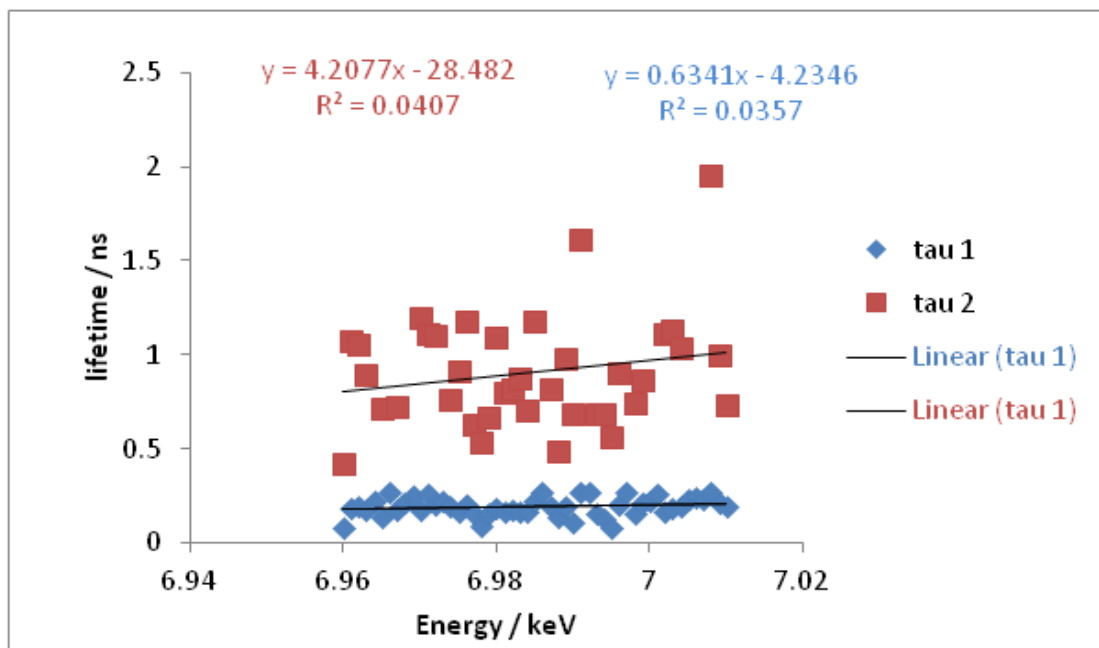


Figure 6-2 - TR XEOL from red zircon (ZAF5) best fitted with a double exponential.

Collected using 7 keV excitation using 150 line grating blazed at 500nm (2.47 eV) centred at 435nm (2.85 eV), 0.5 mm slits

Each data set was individually processed in IGOR 6.22 to fit the exponential lifetime decays. The decay best fitted with two lifetimes in 74 % of cases, and in 26%, the data best fitted with a single lifetime (data table Appendix 5). In Figure 6-3 the summary of the range of lifetimes is displayed, showing that the shorter lifetime has a lower measured range of between ~80 – 270 ps. The range for the longer measured lifetime is

between, 0.71 – 1.95 ns (as the first data point which is irregular is ignored), and if the two outliers are excluded then the range measured reduces to 0.71 -1.1 ns. The trend for the two lifetimes is shown, the trend for the shortest lifetime is a very small increase as a function of energy. The second lifetime shows a stronger response to the energy of excitation. The data does not carry a discernible OD XAS signal.



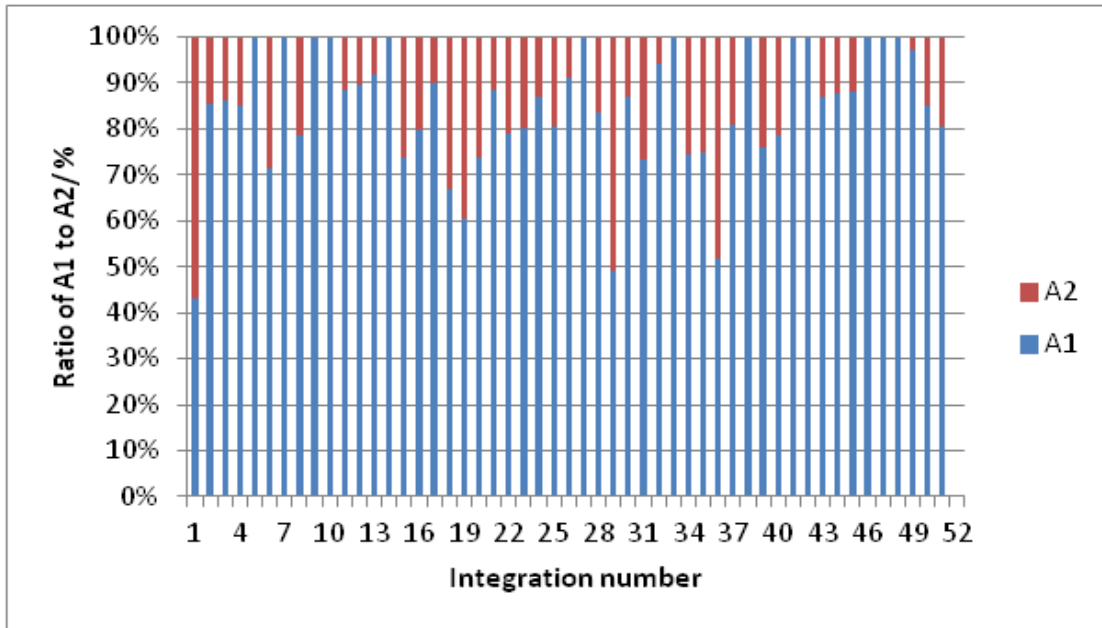


Figure 6-4 - ZAF5 Red Zircon TR XEOL energy scan from 6.95- 7.01 keV. Collected using 150 line grating blazed at 500 nm (2.47 eV) centred at 435nm (2.85 eV) 0.5 mm slits with 50, 180 s integrations Bar chart showing ratio between intensity of short A1 lifetime and Longer lifetime A2.

From Figure 6-4 the ration of intensity between the longer and shorter lifetime emissions displays significant variability that shows no correlation with other measured factors. From these results, it could be inferred that they are not in a linked competitive mechanism.

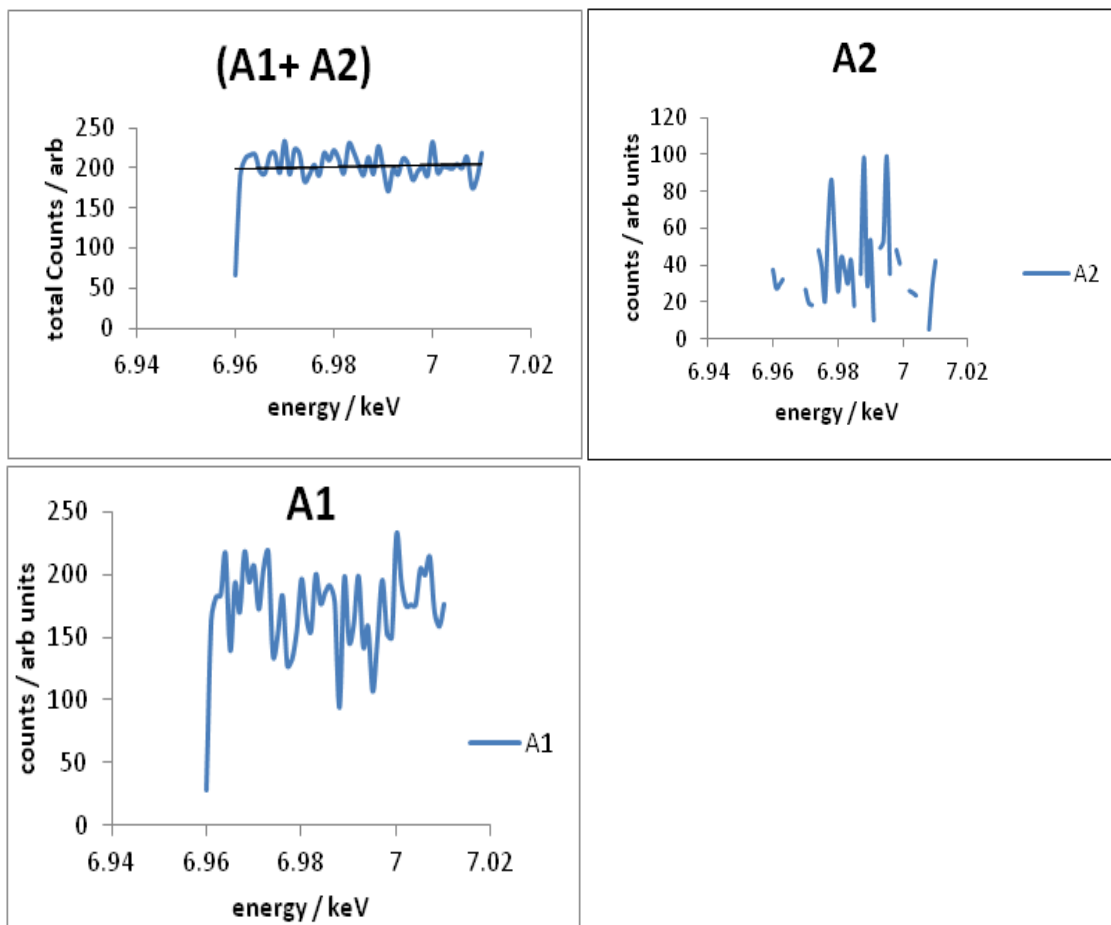


Figure 6-5 - ZAF5 red zircon TR XEOL energy scan from 6.95- 7.01 keV. Collected with grating centred at 435nm (2.85 eV)with 50, 180s integrations chart showing individual energy dependent Intensity responses of short A1 lifetime and longer lifetime A2 and combined response using 150 line grating blazed at 500 nm (2.47 eV)centred at 435nm (2.85 eV) 0.5 mm slits.

The combined intensity response shows a limited response to the energy variation and the separated signals show behaviour that is more erratic. The combined signal shows that the responses have an inverse relationship that is intuitively correct. The amount of noise within the fitted TR signal would indicate that it would be an inappropriate technique to collect EXAFS, as the signal would be lost underneath this level of noise.

6.1.3 TR XEOL as a Function of Incident Energy

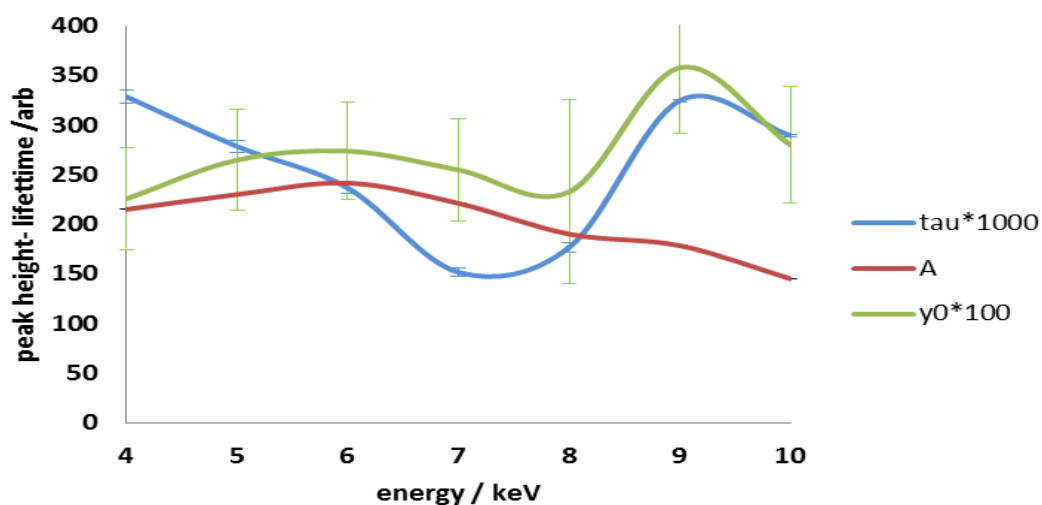


Figure 6-6 - TR XEOL spectra collected from 4 - 10 keV. Showing lifetime and peak height using 150-line grating blazed at 500nm centred at 435 nm 2.85 eV 0.5 mm slits

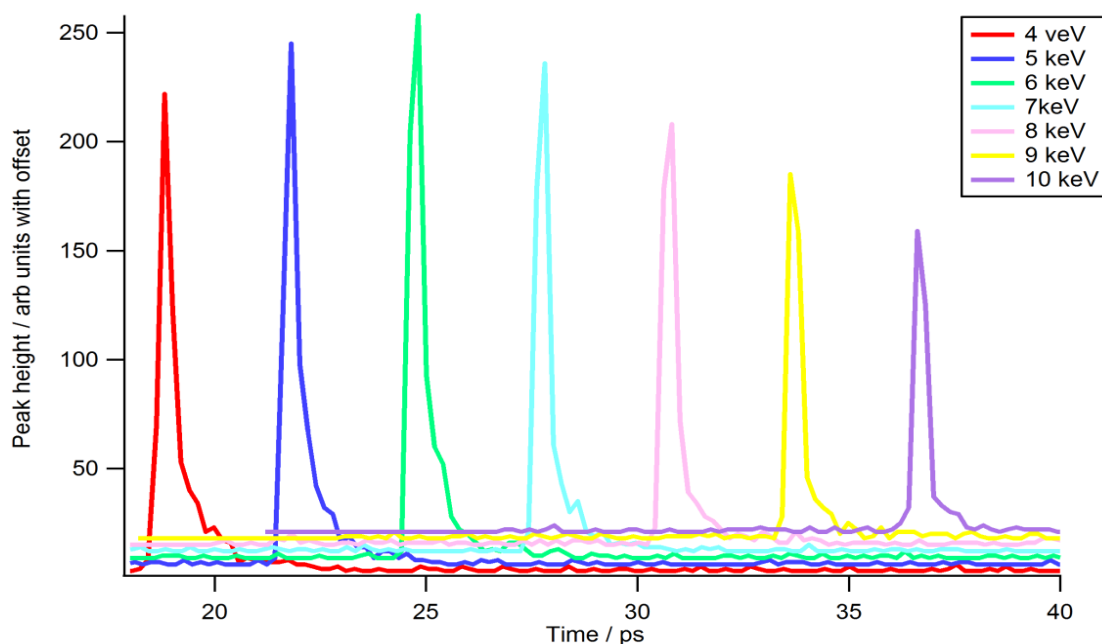


Figure 6-7 - TR XEOL spectra collected from 4 - 10 keV 600 s integrations displayed with offset showing relative peak height. Collected using 150 line grating blazed at 500 nm centred at 435 nm 2.85 eV 0.5 mm slits.

Measuring the energy dependence of a sample over a large energy range is complicated by a number of factors including variations in the efficiency of the insertion device as a

function of energy, and variations in the performance of the optics as a function of energy, thereby creating variations in the incident photon flux during an energy scan. The standard technique to remove these fluctuations is to measure the incident photon flux prior to its incidence on the sample and to use this signal to normalise the collected transmission or fluorescence data. The flux is usually measured using a gas filled ionisation chamber that generates a current and the conditions of the chamber are adjusted so that its output is linear with the incident flux. The difference in signal caused by the changing X-ray cross-section for the ion chamber gases can be ignored over a smaller energy range such as that used in an XAFS experiment (1 keV) but over a large energy range is significant and so normalising the flux over this range is complicated. Additionally, the penetration depth of the X-rays into the sample varies as a function of energy. This affects the amount and depth of absorption that in turn affects the percentage of transmission/ 'self-absorption' of fluorescent photons, and this will also be sample and in many cases orientation sensitive. The X-ray absorption profile will vary as a function of energy that in turn will affect the relaxation pathways.

6.2 Topaz

6.2.1 Orientation

Topaz samples were prepared by mounting oriented samples with polished surfaces cut perpendicular to the three crystallographic axis a, b, c from sections of a single crystal into acrylic blocks. Spectra collected from each of the three orientations are compared and contrasted below.

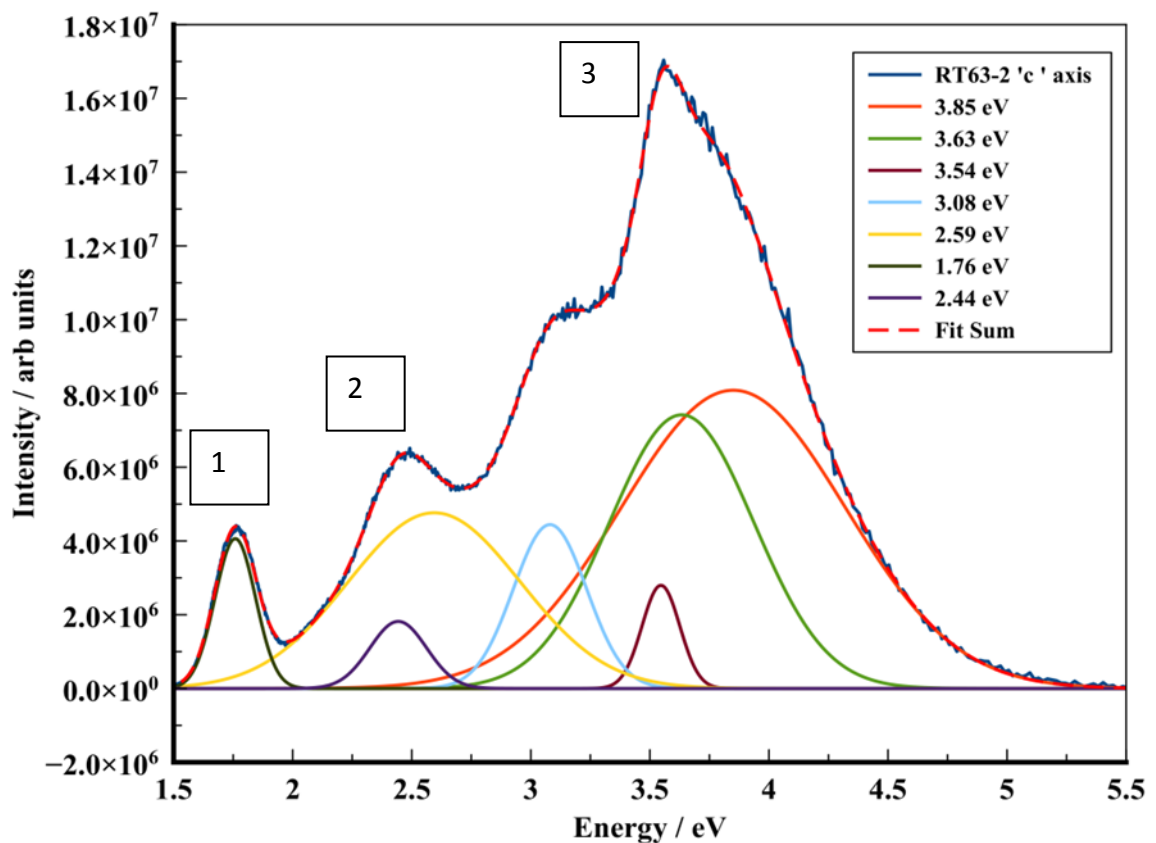


Figure 6-8 - XEOL spectra from topaz RT63 collected
The X-ray beam incident to the face perpendicular to the 'a' axis. Excited at 7 keV 150 grating 550 nm (2.25 eV) centre.

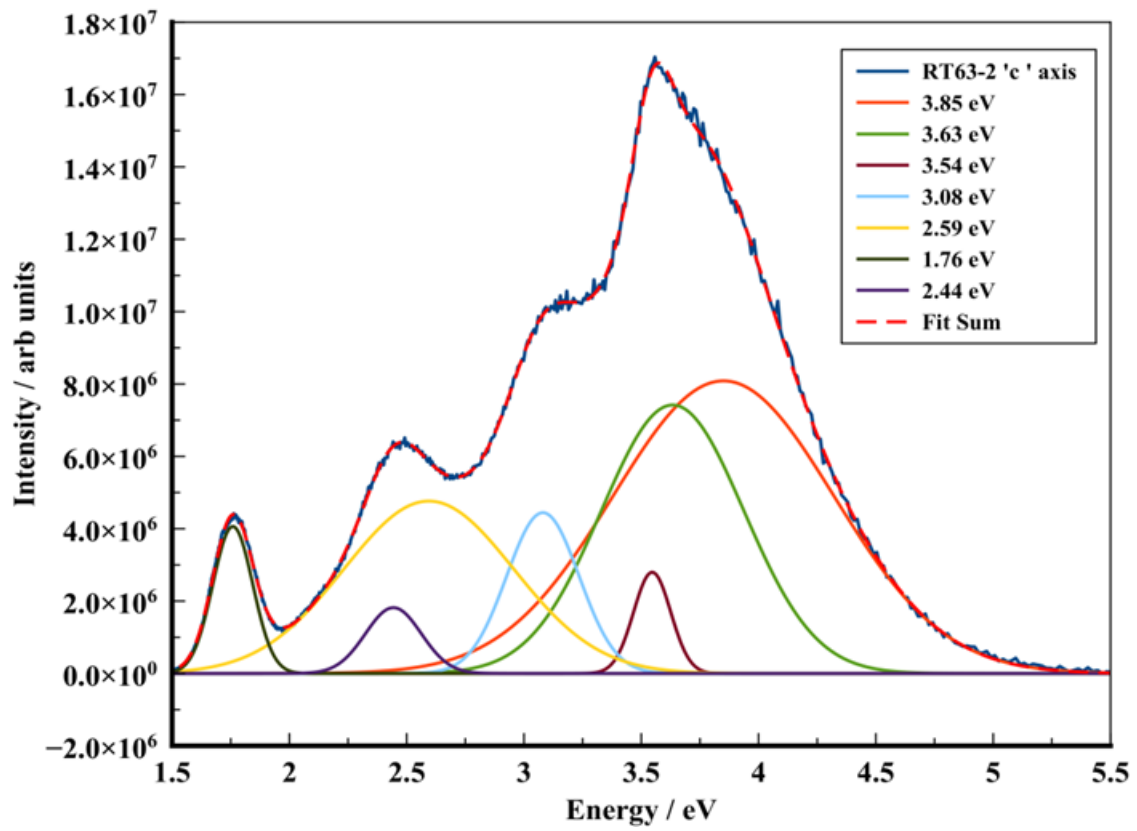


Figure 6-9 - XEOL spectra collected from topaz RT63
 The X-ray beam incident to the face perpendicular to the 'c' axis. Excited at 7 keV 150 grating 550 nm (2.25 eV) centre.

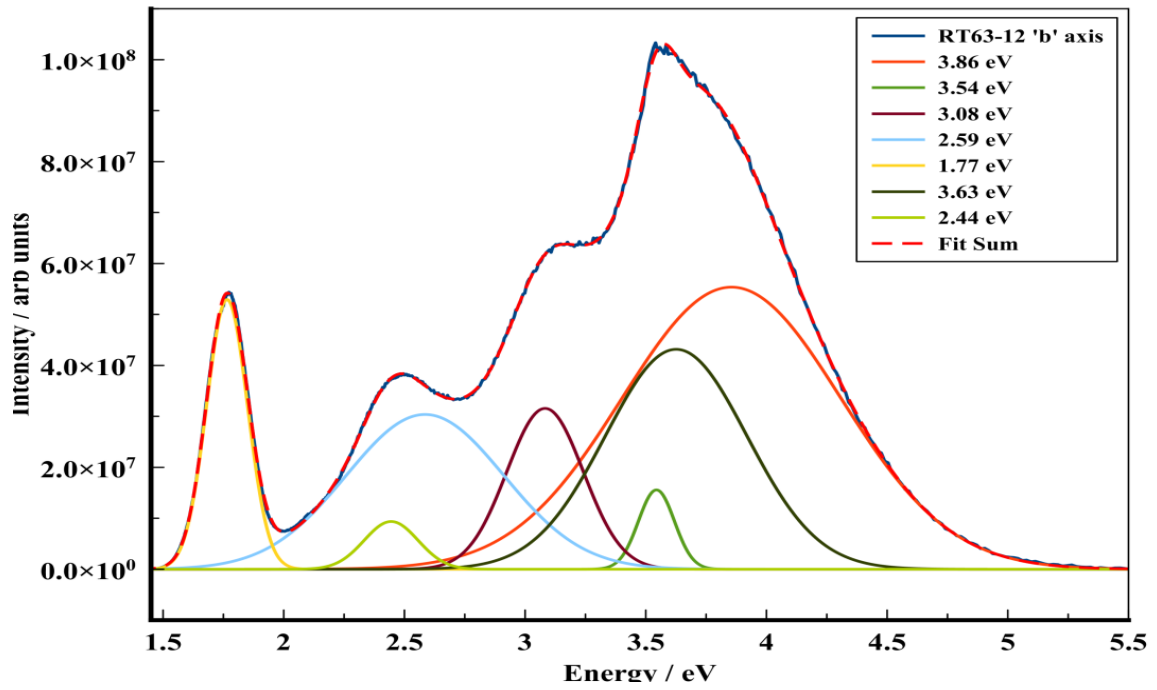
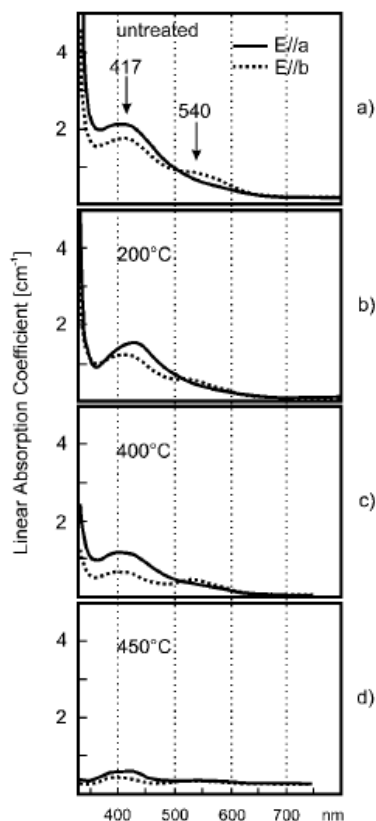


Figure 6-10 -XEO spectra collected from topaz RT63
 The X-ray beam incident to the face perpendicular to the 'b' axis. Excited at 7 keV 150 grating 550 nm (2.25 eV) centre.

<i>'c'</i> Axis	<i>'c'</i> Axis	<i>'b'</i> Axis	<i>'b'</i> Axis	<i>'a'</i> Axis	<i>'a'</i> Axis	<i>Literature</i>	<i>Literature</i>	<i>Attributions</i>	<i>Reference</i>
nm	eV	nm	eV	nm	eV	nm	eV		
		304	4.08						
334	3.71			323	3.84				
354	3.50	363	4.42			356	3.48	Cr3+ 4A2g →4T1g	(Taran et al., 2003)
407	3.05	407	3.05			406	3.05	Mullite Cr3+	
442	2.81	441	2.81	439	2.82	450	2.76	Cr3+ 4A2 →4T2(2G)	
463	2.68	462	2.68			461	2.69	Natural Colourless	(Marques et al., 2000)
489	2.54	480	2.58	485	2.56				
512	2.42								
540	2.30					532	2.33	Cr3+ 4A2 →4T2(2G)	(Taran et al., 2003)
548	2.26					551	2.25	Green Topaz	(Marques et al., 2000)
		584	2.12			583	2.13		(Taran et al., 2003)
596	2.08	595	2.08	596	2.08	590	2.10	Cr3+ 4A2 →4T2(4F)	(Tarashchan et al., 2006) (Taran et al., 2003)
				603	2.06				
621	2.00	619	2.00	619	2.00				
622	1.99	622	1.99	622	1.99				
704	1.76	700	1.77	700	1.77				

Table 6-1 - Summary of CW XEOL spectral features collected from crystallographically orientated topaz RT63. Excited at 7 keV using 150 line grating blazed at 500 nm 2.48 eV centred at 550 nm 2.25 eV 0.5 mm slits.

Much work has been completed on the structure, chemical nature and causes of colour in topaz, including that by (Gatta et al., 2006), (Hoover, 1992), (Taran et al., 2003), (Tarashchan et al., 2006) and (Jasinevicius, 2009). Transition elements Cr, Fe, V and Ti, found in topaz have all been associated with absorption and emission centres, and defect structures have also been implicated, particularly the OH/F substitution. In addition, the role of ordering of the F substitution has been considered. Many issues remain unresolved with a number of conflicting opinions. The features seen in the XEOL spectra (Figure 6-9 and Figure 6-10) do show some similarities with examples from the literature, but all of the higher energy emissions seen, are absent from the literature. A number of authors have used heating experiments and interpreted the transient nature of some of the emissions/absorption centres as in Figure 6-11 to assign them to electron traps. Spectra in, Figure 6-9 and Figure 6-10 show differences not only in the intensity of the emissions but also differences in the relative intensities as a function of



crystallographic orientation. The samples tested are pale in colour and I therefore consider it unlikely that the differences in intensity are a function of pleochroism -variable absorption of light as a function of orientation in a crystal.

Figure 6-11 - Absorption spectra from untreated topaz samples. Annealed to a) unheated ,b) 200⁰ C, c) 400⁰ C, 450⁰ C (Schott et al., 2003a).

6.2.2 Dose Dependent Anisotropy

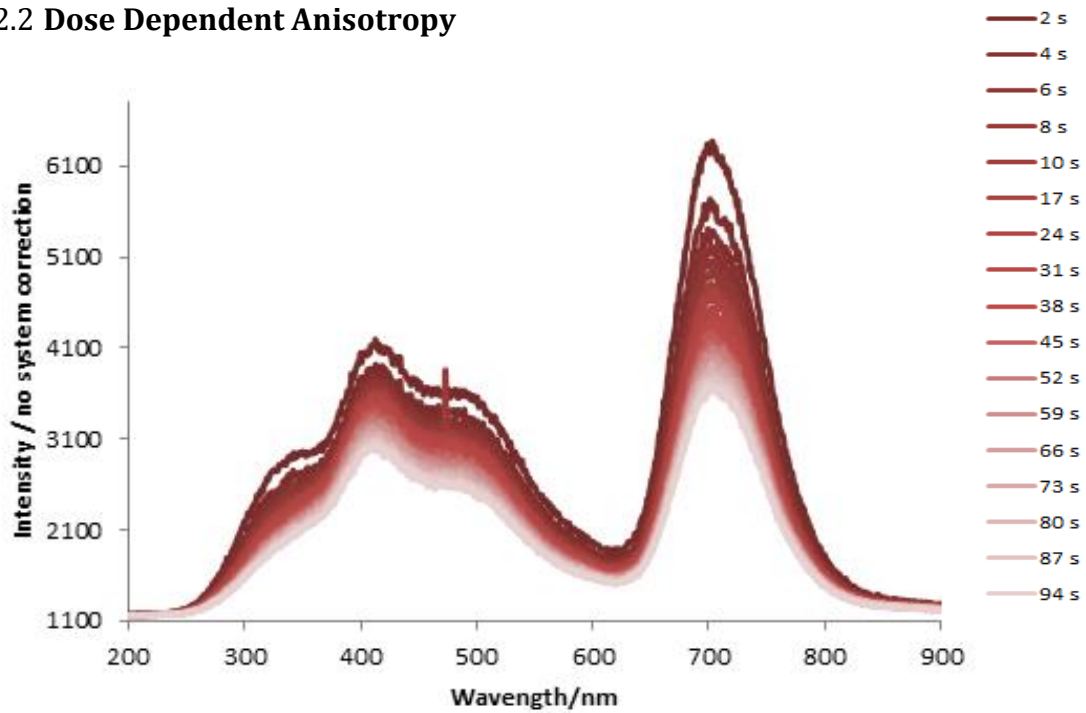


**Figure 6-12 - Topaz RT63-13 'b' first dose dependence spectra shown with no data correction.
Excited 7 keV 100, 1 s integrations collected using 150 line grating blazed at 500 nm centred at 550 nm using 0.5 mm slits.**

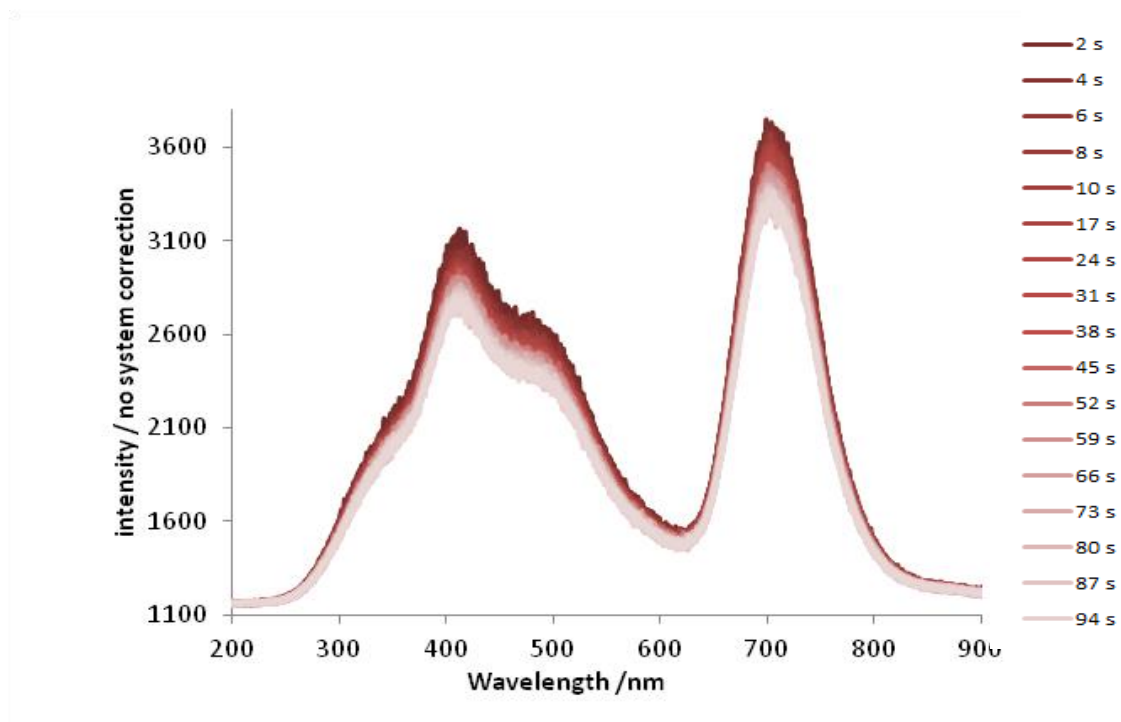


Figure 6-13 - Topaz RT63-13 'b' dose second dependence spectra shown with no data correction. Excited 7 keV 100 1 s integrations collected using 150 line grating blazed at 500 nm centred at 550 nm using 0.5 mm slits, same position as Figure 6-12 collected after 300 s recovery time.

In comparing Figure 6-13 and Figure 6-12 that is two spectra collected consecutively from the same spot with a five minute delay between collections, the peak at ~ 700 nm has a limited recovery from ~ 3400 to ~ 3700 raw counts indicating that the effect that the dose dependence is measuring shows only limited short-term recovery. Interestingly this behaviour is inconsistent with that expected from an electron trap this finding is in contrast with previous interpretations. The three major peaks labelled on figure 6-8 are plotted to compare dose rate effects on the peak heights and they show different intensity responses between the different peaks as a function of the orientation of the incident beam. Figure 6-14 shows the variations in the normalised emission responses as

a function of dose rate for the three crystallographic orientations. From Figure 6-9 the first two peaks are best fitted with at least three components, with the first peak best fitted as a single Gaussian with a small influence from the tail of the broad emission centred at the second peak. Luminescence that displays anisotropic responses can arise from a number of alternative sources; firstly, it has been shown that X-ray absorption can show anisotropy (Korecki et al., 2011), and secondly, anisotropy of the photoelectron 'mean free path' as demonstrated by (Kuzmin, 1994). Fluorescence anisotropy is used extensively in organic and biological research to measure rotational diffusion rate; for example (LiCata and Wowor, 2008) used TR to measure the reduction in the degree of polarisation of the luminescent signal in a time window with the value being described as the rotational lifetime. Finally, following emission, anisotropic materials can affect the signal through selective pleochroic absorption. The technique offers interesting potential as the lifetime and intensity of emission are affected differently as a function of orientation. An application is discriminate between different sources of anisotropy, for example, if the source of the anisotropy is derived from absorption then the intensity will vary, whereas the lifetime will remain unaffected.

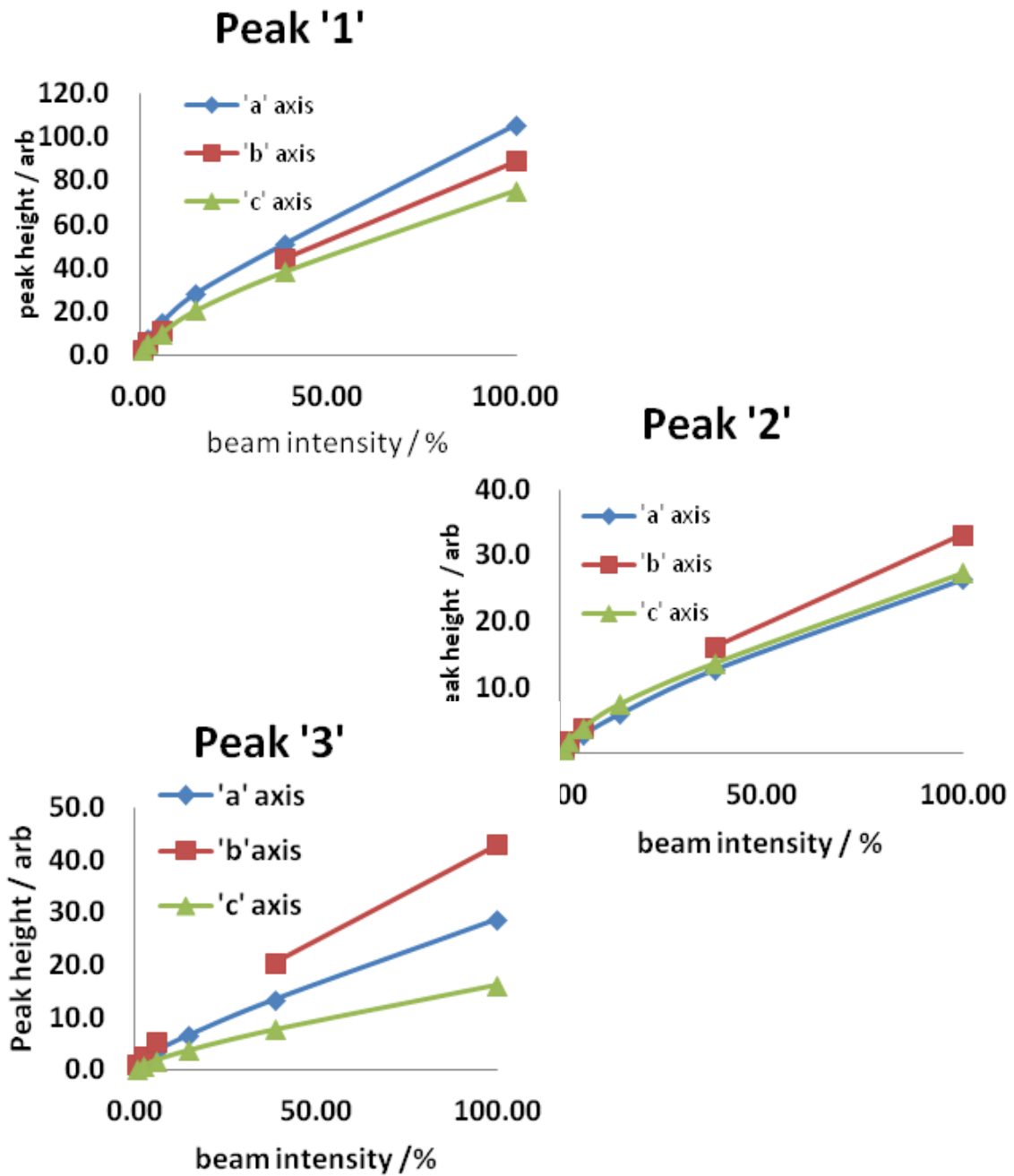


Figure 6-14 - Topaz RT63 dose rate analysed by peak for each crystallographic orientation.

The data collected from the 'b' orientation has one data point omitted due to the incorrect foil being used and so the data points were removed from the data and appear in the graphs as a space. Collected at 7 keV excitation.

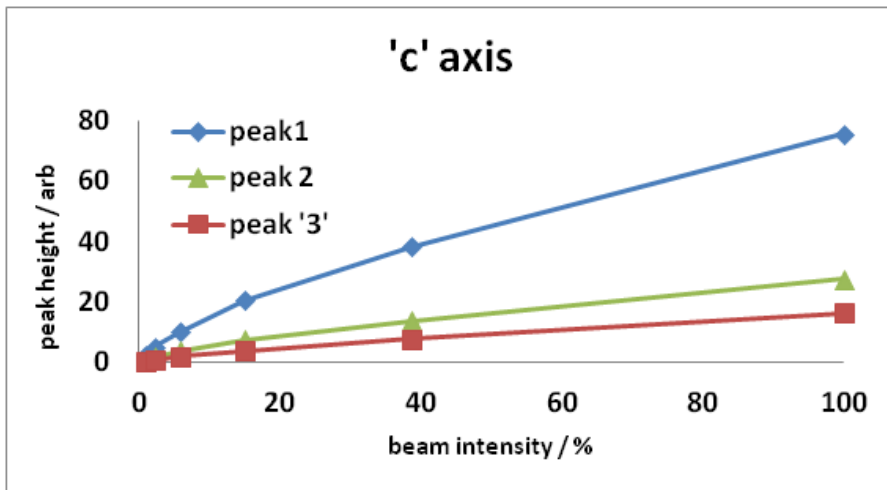
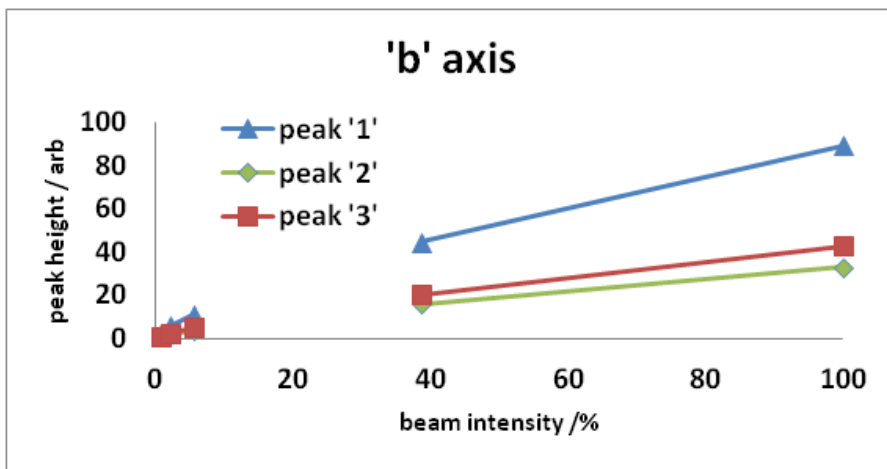
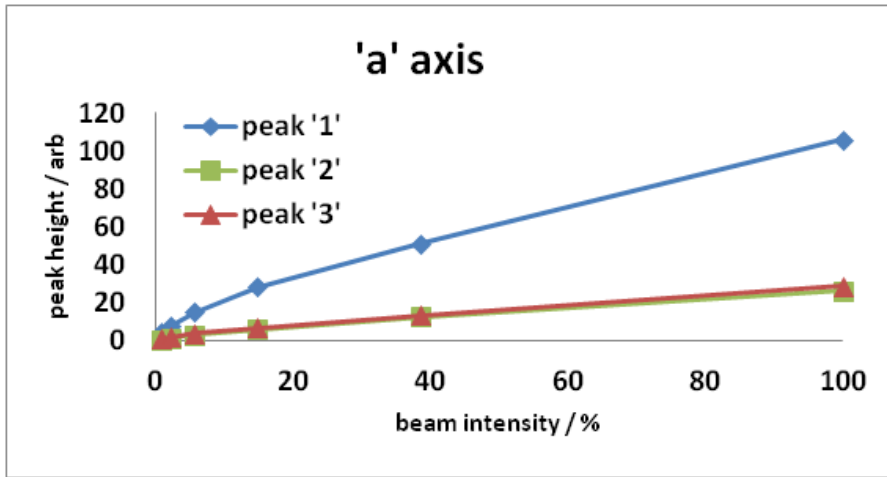


Figure 6-15 - Topaz RT63 dose rate analysed by axis for each peak. The data collected from the 'b' orientation has one data point omitted due to the incorrect foil being used and so was removed from the data Collected at 7 keV excitation.

6.1 Synthetic Ruby RT1-1

Synthetic ruby has been manufactured for over 100 years (Hughes, 1997) and has been well characterised due to its applications in laser technologies. Within the XEOL spectra, (Figure 6-16) collected at 7 keV, I identified a number of previously unreported emissions in the UV, which are detailed in Table 5.8, thus illustrating the potential of the technique to identify previously unseen emissions. Govidina (1976) reported on a number of X-ray induced emissions in the UV but was reporting TL emissions that show no correlation with the emissions recorded here.

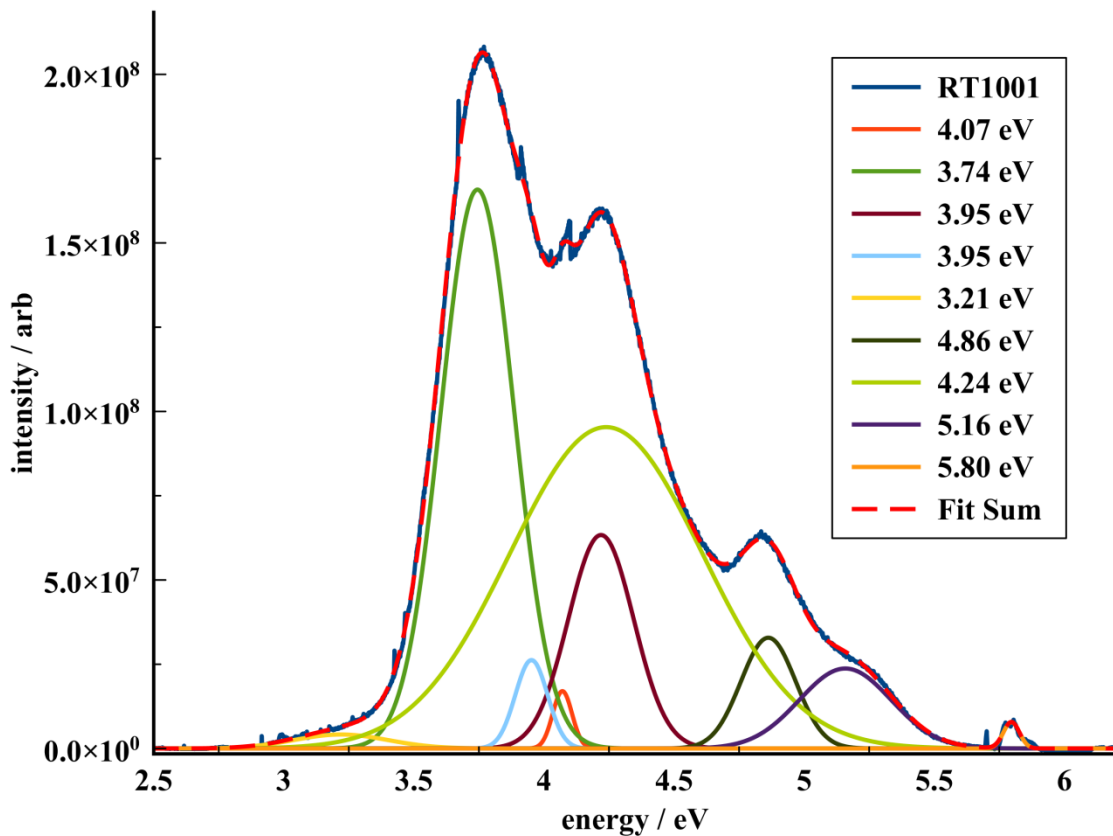


Figure 6-16 - XEOL spectra of RT 1_1 synthetic ruby excited using 7 keV for 60 s. Collected on the 1200 line /500 nm blazed grating for 60 s 0.1 mm entrance slits (corrected data).

<i>Energy /eV</i>	<i>Wavelength /nm</i>
5.80	213
5.16	240.3
4.86	255.1
4.24	292.4
4.21	292.5
4.07	304.6
3.95	313.9
3.74	331.5
3.22	385

Table 6-2 - Summary of XEOL emission peaks for RT 1_1 synthetic ruby excited using 7 keV for 60 s Collected on the 1200 line /500 nm blazed grating 0.1 mm entrance slits taken from (Figure 6-16).

Cr₂O₃ substituting into the Al₂O₃ at approximately 1wt % replaces the Al³⁺ as an isovalent substitution into a trigonally distorted octahedral coordination, thereby converting the colourless mineral corundum into the red gemstone ruby. The substitutional energy levels of the Cr³⁺ ion can be modelled by crystal field theory (Bethe, 1929). If the environment of the substitution was purely octahedral then the e_g and t_{2g} energy levels are split. In ruby the coordination is a trigonally distorted octahedral site that affects the energy levels. ⁴a₂ is the ground state, with three significant spectral energy levels represented as ²e, ⁴t₂ and ⁴t₁, it is transitions between these energy levels that are responsible for both absorption and luminescent emissions. The ²e and ⁴t energy levels are also subject to fine scale splitting due to the distortion from octahedral symmetry. This is significant for the effect on degeneracy in the application of the equation of Strickler and Berg (1962) that is used later.

6.1.1 Strickler and Berg Calculation

A synthetic ruby was selected to test the application of the Strickler and Berg (1962) equation to mineral luminescence. The thickness of the double polished disc sample RT1-1 was measured to be $2.021 \pm .001$ mm, the absorption cross section was measured using a Carey spectrophotometer (Figure 6-17), and the Cr concentration was measured using a mass spectrometer as 834 ± 3 ppm.

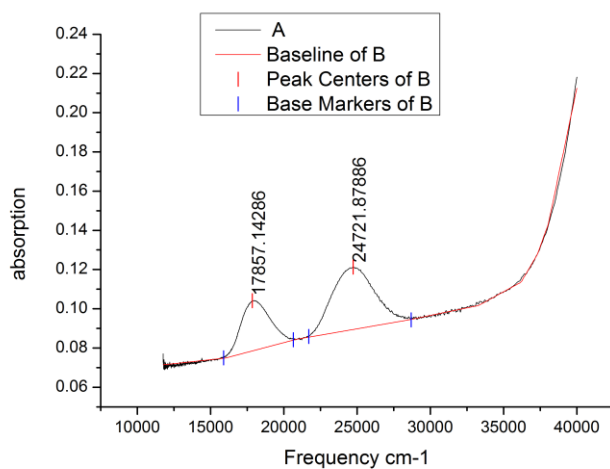


Figure 6-17 - Absorption spectra from RT1-1 synthetic ruby. The area under the curves was calculated using Origin Pro ver. 8.5.1 the results are summarised in Table 6-3.

<i>Index</i>	<i>Area</i>	<i>Area Intg P(%)</i>	<i>Curve Area</i>	<i>Row Index</i>	<i>Beginning X</i>	<i>Ending X</i>	<i>FWHM</i>
1	58.4196	32.55	179.433	580	15898.25	20661.15	2203.30
2	107.227	59.751	179.433	891	21715.52	28694.40	3295.63

Table 6-3 - Results of curve fitting from Origin Pro ver. 8.5.1 of absorption spectra taken from RT1-1 Figure 6-17.

(Strickler and Berg, 1962) $\frac{1}{\tau_0} = 2.880 * 10^{-9} N^2 \langle \tilde{\nu}_f^{-3} \rangle_{av}^{-1} \left(\frac{g_l}{g_u} \right) \int \epsilon d \ln \tilde{\nu}$ *Equation 22*

$\frac{1}{\tau_0}$ is the natural lifetime of the emission.

N is the refractive index of the material, taken as an average of 1.765 (1.76-1.77).

$\langle \tilde{\nu}_f^{-3} \rangle_{av}^{-1}$ is the reciprocal of the mean value of fluorescence and was calculated following the methodology of Strickler and Berg, with two fluorescence spectra curves plotted for each spectrum, one with the corrected intensities and the other $\tilde{\nu}^{-3}$ times this value.

The ratio of the area under the curves gives $\langle \tilde{\nu}_f^{-3} \rangle_{av}^{-1}$ s which was calculated for curve 1 as 2.07 and curve 2 as 4.18.

$\left(\frac{g_l}{g_u} \right)$ is the ratio of degeneracy for the lower and upper states and is taken as 1/1 due to the distortion effects.

ϵ Molar extinction coefficient

$\tilde{\nu}$ the frequency range of absorption cm^{-1}

The equation generates a theoretical natural lifetime for peak 1 as 2.01 ns and peak 2 as 4.04 ns. The transitions investigated are well known red shifted absorption transitions, and they are spin allowed transitions to the $^4T_{1g}$ and $^4T_{2g}$ states. Burns (2005) comments

on the dichroism of the absorption of these two transitions as being significant, but this was not properly accounted for when the spectra were collected. The transitions are not recorded in the literature as emissions, and no measured lifetimes are recorded for comparison.

These theoretical natural lifetime values are plausible, and that is an encouraging result. The sample selection was not ideal, as the emission spectra were more complex than expected; despite this, the application still provides a credible result. Sample preparation and data collection require refinement to ensure that the same crystallographic direction is used for the collection of both the absorption and fluorescence emissions.

The technique requires extensive testing on a number of different materials to determine any limitations in the reliability of the results. This experiment, although limited to the results from a single sample, is a basis and justification for further work to be undertaken. Comparing the calculated natural lifetime with the lifetime data collected from the sample is of limited value due to the complexity of the emission spectra. The software has fitted two longer lifetime decays ~ 7.7 and 186 ns.

Figure 6-19 but does not fit the very short lifetime portion of the decay. It is possible that this very short life component equates to one of the calculated natural lifetimes that has been shortened by competitive energy transfer. Additional high-resolution spectra would be required to answer this question.

3d-levels in octahedral field

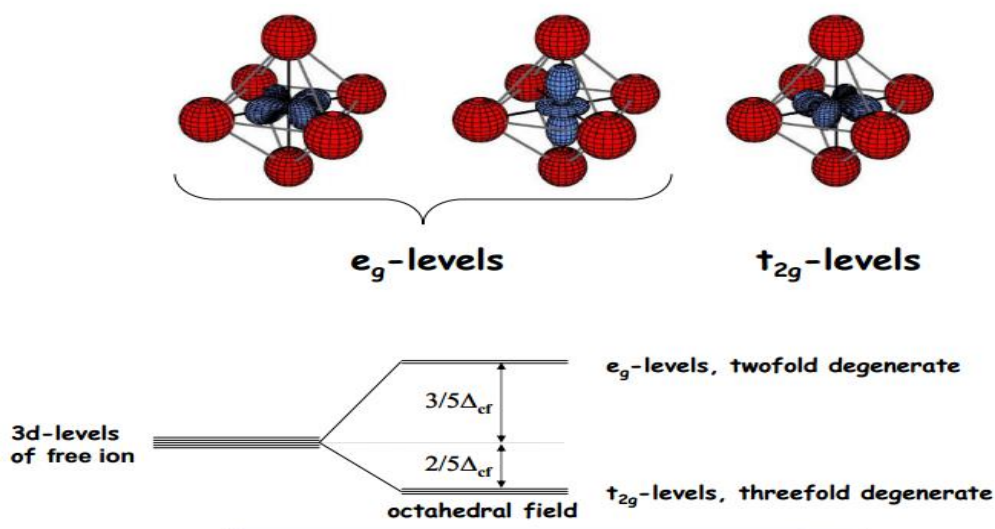


Figure 6-18 - Octahedral coordination and the CF splitting energy levels.
Source: (Nassau, 2001)

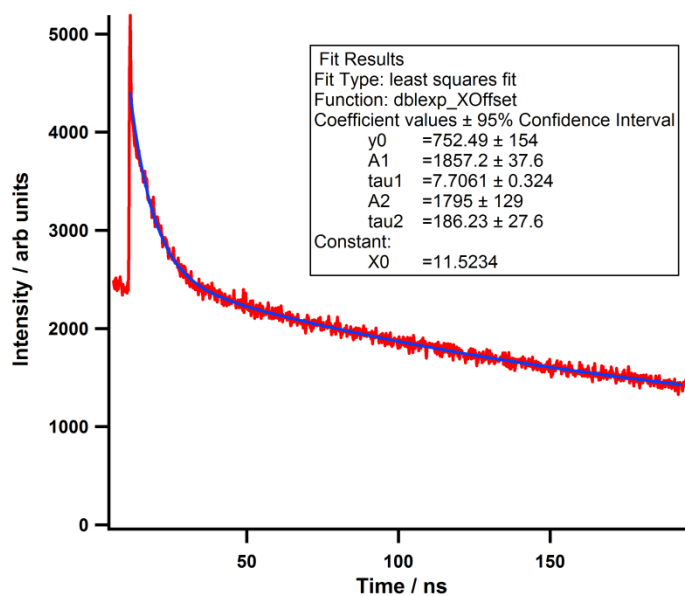


Figure 6-19 - TR XEOL spectra collected from RT1-1 7 keV excitation. Centred at 330 nm (3.76 eV) with 0.1 mm exit slits \sim 90 nm 1.05 eV spectral range. Fitted in Igor 6.22 using least squares fitting.

6.2 Chrome Tourmaline

Chrome tourmaline is a complex borosilicate that belongs to the dravite variety of the tourmaline group. Within the literature, the colour and luminescent emissions have been associated with V and Cr.

6.2.1 CW Dose Dependent XEOL

Figure 6-20 shows the dose dependent response of RT1013 which varies in intensity of response across the spectrum, with the largest changes occurring in the largest peak. This feature consists of a narrow peak centred at 676 nm (1.83 eV) with an overlapping broadband centred at ~713 nm (1.73 eV). This feature is the energy shifted, zero phonon line of Cr and its associated vibrational sideband; this feature reduces to less than 50% of its original intensity within 5 s of the commencement of excitation. In comparison, the second largest feature centred at 516 nm (2.40 eV) shows only a ~30% reduction over the same time interval. These results probe the nature of luminescent centres, testing the relative stability and strength of the surrounding bonds.

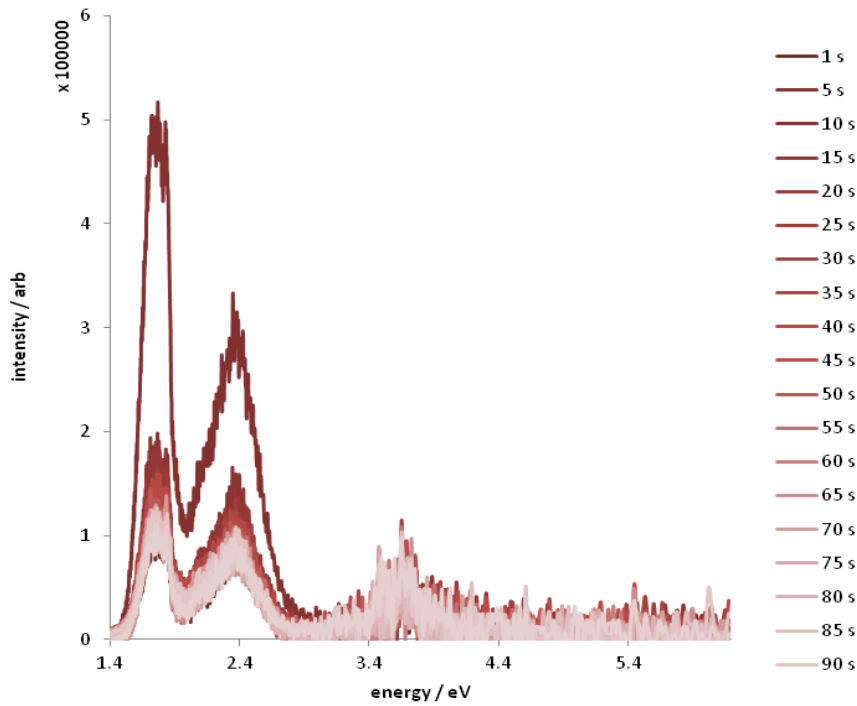


Figure 6-20 - RT1013 chrome tourmaline dose dependence.
 Collected at 7 keV using 150 line grating blazed at 500 nm (2.48 eV) centred at 550 nm (22.25 eV) 0.5 mm slits normalised for system response, 100 1 s integrations sampled first second then every 5 s.

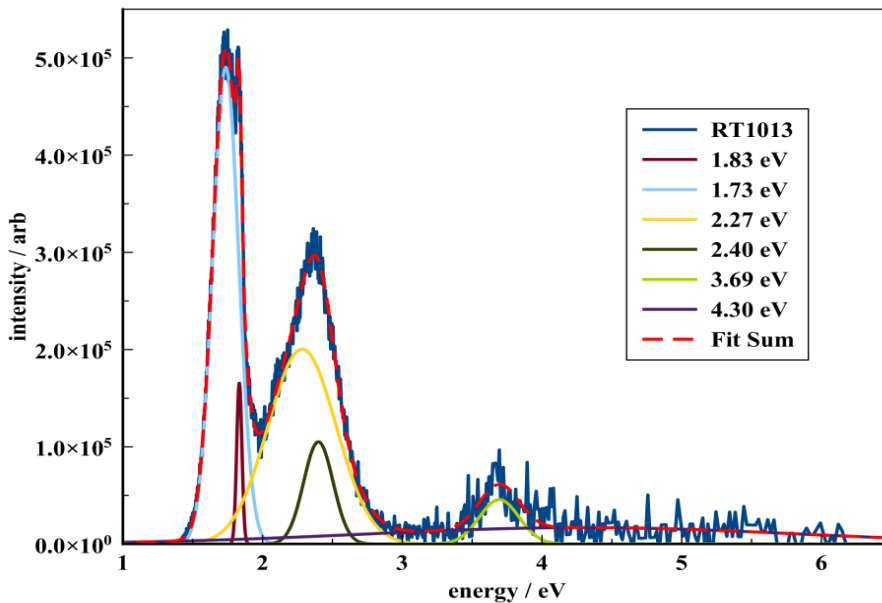


Figure 6-21 - CW XEOL from RT1013 chrome tourmaline.
 Collected using 7 keV excitation using 150 line grating blazed at 500 nm (2.48 eV), centred at 550 nm (2.25 eV) slits 0.5 mm.

The smaller feature in the UV at 336 nm (3.69 eV) shows no dose response displaying no tendency to increased or decreased signal intensity as a function of time. The noise in the data in this portion of the spectrum is due to the low signal and reduced detector sensitivity, in combination with the effects of system correction.

Two of the three main compound peaks, centred at 716 and 516 nm (1.73 and 2.40 eV), are best fitted with two major components. Both components are equally affected by the effects of dose; this is demonstrated by the shape of the spectra remaining constant as a function of the dose. This behaviour is indicative that the separate emissions are derived from the same defect centre or that there is a close correlation between two different centres. The relationship of relative responses to dose dependence is a useful application in the identification of related emissions.

6.2.2 Temperature Dependence of TR XEOL

.Figure 6-22 and Figure 6-23, show that at low temperature the lifetime of the emissions collected at 336 nm (3.69 eV) are best fitted with a single lifetime that reduces from τ_1 4.5 ns to τ_1 3.6 ns respectively between integration times of 180 s and 600 s. Two possibilities exist for this change in lifetime, firstly it could be as a consequence of localised sample heating in the longer collection time, alternatively it could be due to sample modification. This can easily be determined by repeating the experiment. The QE between the shorter and longer integrations increases this is consistent with sample modification increasing the probability of emission. This is not consistent with a temperature increase through localised heating that would be expected to lower the emission probability. In Figure 6-24 the RT spectra was collected at a slightly different centre of wavelength 340nm (3.65 eV) instead of 336 nm (3.69 eV) (The spectral window

used for all experiments exceeds ~ 90 nm, I therefore do not consider this variation significant). The differences seen in the RT spectra are significant both in measured lifetime and in intensity. The RT spectra are best fitted with two exponential decays of much shorter lifetimes τ_1 180 ps, τ_2 2.49 ns and the relative QE as estimated through the TR peak height as a function of time reduces by over $\sim 10\%$ from the shorter LT integration spectra and $\sim 15\%$ of the longer LT integration spectra. The QE of the RT emission is reduced to $0.4 \text{ counts } S^{-1}$ from 0.38 and $0.45 \text{ } S^{-1}$ respectively between the 180 s and the 600 s LT integrations. The shortest lifetime of the RT spectra is significantly shorter than could be expected to have a significant effect upon the QE but the 180 ps emission only represents a small proportion of the total signal measured by the A_0 values this therefore only has a proportionately limited effect on the overall QE of the TR emission. The change in behaviour for the RT spectra is consistent with the effects being a response to temperature change alone, notably the effect on measured lifetimes is significant. The intensity of the 'background signal' is quantified by Y_0 that represents the QE of any long lifetime emissions > 200 ns, at low temperature there is a significant long life emission, Y_0 14.1 and Y_0 44.62 respectively between the 180 s and the 600 s integrations. In contrast, at RT the Y_0 signal is negligible at Y_0 0.9. This demonstrates two concepts firstly, the Y_0 value between the two LT spectra alters with a linear relationship with the integration time in contrast to the short lifetime QE. This is consistent with the long lifetime emissions being unaffected by sample alteration. The long lifetime emission in the RT spectra is almost completely removed from the spectra. This result is consistent with thermal quenching and illustrates that the effect of quenching varies between emissions.

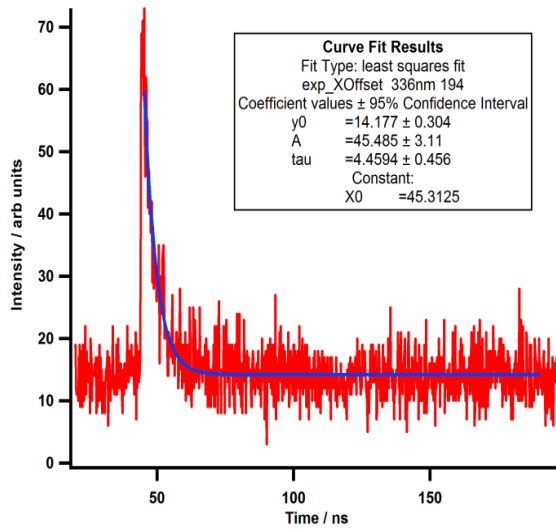


Figure 6-22 - TR XEOL Spectra collected at 336 nm for 180 s at ~91 K excited at 7 keV

Figure 6-23 - TR XEOL Spectra collected at 336 nm for 600 s at ~91 K excited at 7 keV

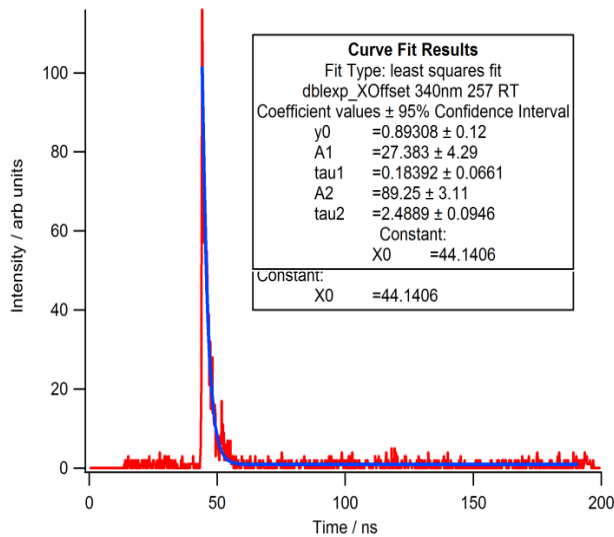
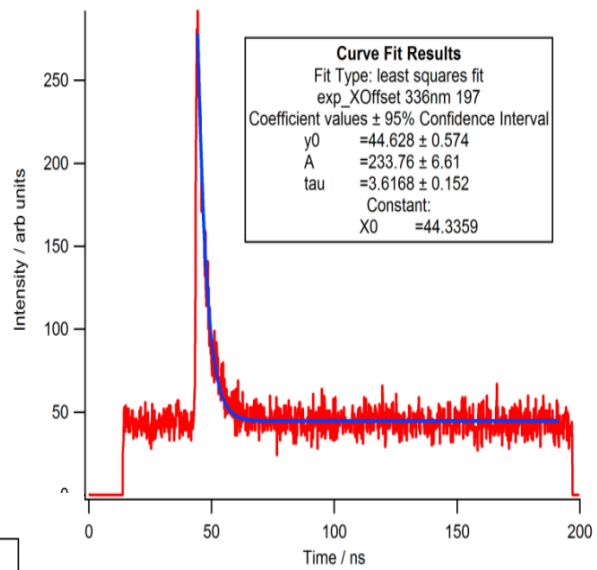


Figure 6-24 - TR XEOL Spectra collected at 340 nm for 300 s at RT excited at 7keV

6.3 Summary of Chapter 6

The results from chapter 6 emphasise the viability of the combined analysis of TR and intensity data as a valuable technique to explore luminescence. Results from the second group of minerals display a broad range of applications for the comparative TR CW intensity technique.

I am unable to locate in the literature any examples where the results from oriented TR XEOL in combination with QE have been used. This also offers an interesting direction for future investigation. By incorporating an adjustable/removable polarising filter into the emission beam to allow the determination of the degree of polarisation of the luminescent signal. This further extends the techniques discrimination as it probes the site-specific symmetry of the luminescent emitter. In section 6.2.2 the oriented dose dependence anisotropy also provided positive results offering interesting potential applications as the lifetime and intensity are affected differently by the different aspects. The application of this can be used to discriminate between the different sources of anisotropy. For example, if the source of the anisotropy is derived from absorption then the intensity will vary, whereas the lifetime will remain unaffected..

The experiment with synthetic ruby applying the Strickler and Berg equation to a mineral application is also positive illustrating the potential for calculating the natural lifetime of an emission. This value can then be used to generate an independent measure of the QE of an emission. The application will be best suited to transitions that are simpler than the one selected.

7 CONCLUSIONS

New perspectives for the understanding of the luminescent behaviour exhibited by minerals can be achieved by incorporating interpretations and techniques from different disciplines. This starting point provided a useful foundation and perspective to interpret the results presented within this thesis. Aspects of luminescence commonly utilised in other disciplines have to date not been fully developed within the Earth sciences. An example is the study of the lifetimes of luminescent emissions.

The selection of X-rays i.e. high-energy photons, for excitation means that results are broadly representative of the bulk since their depth of penetration in minerals is deep $\sim \mu\text{m}$. X-ray energy $>3 \text{ keV}$ is 2-3 orders of magnitude greater than the typical band gap values of $\sim 3\text{-}10 \text{ eV}$ of semi-conductor /insulator minerals. This greater energy removes the influence of resonant valance band absorption intrinsic in PL spectroscopy. This choice of incident energy allows excitation of features in the range of VUV limit $\sim 200 \text{ nm}$ ($\sim 6.2 \text{ eV}$) which is a part of the EM spectrum effectively inaccessible to lower energy techniques.

One of the primary objectives of the present project was to design and build a TR and CW XEOL spectroscopy system to work on the I18 beamline of the Diamond light source, the UK's national synchrotron facility. The achievement of this objective is reported in chapter 4. The system's capabilities for investigating a variety of mineral samples were demonstrated in both CW and TR mode. In CW, I demonstrate the system is capable of collecting high-resolution XEOL spectra from 200-900 nm (6.19 -1.38 eV). In TR mode, the system can collect TR spectra with resolutions in the ps timescale, within a collection

time window of up to 200 ns. Integration with the synchrotron clock signal was achieved allowing the synchronisation of the X-ray pulse with the time card of the system. The application of the TR system was successfully tested using a suite of minerals with the fastest response being 21 ps for a sample of alkali feldspar. This measurement not only illustrated the system's capability to collect data at this temporal resolution, but it also illustrated that unreported very fast emissions exist in minerals. This finding is significant as lifetimes (τ) shorter than a few ns must be a modified natural lifetime, requiring that some form of competitive energy transfer mechanism is affecting the luminescent emission.

The concept of combining the measurement of the lifetime and intensity of an emission is underpinned by the hypothesis that common factors controlling the lifetime and wavelength of emission are different to those controlling the intensity of emission, and lifetime is insensitive to many factors that affect the intensity of a luminescent emission. This inter-relationship has a number of profound implications, for example in measuring the intensity of a luminescent emission to test the correlation with the concentration of a trace element lumiphore, the lifetime can be used to quantify the efficiency of the emission and can validate comparisons made between experiments, to establish if competitive energy transfer has entered as an additional factor.

Typically, within the Earth sciences luminescence intensity is considered to vary as a function of the intensity and nature of excitation, the concentration of lumiphore, and the overall QE of the mechanism. Variations in the measured lifetime of an emission are due to variations in the probability of emission i.e. a change of the QE of the mechanism, or a variation in the magnitude of competitive relaxation. Therefore, when making

comparisons of luminescence intensity, either between samples or between experimental setup, it could be expected that standard practice would be to measure the lifetime of the emissions; this however at present is rarely the case. I would propose one of the most significant findings of this thesis is that the measurement of lifetimes should become an intrinsic aspect of both quantitative and qualitative mineral luminescence spectroscopy. The ability of the measured lifetime of an emission both to detect and quantify these effects is demonstrated within the thesis and of great significance. The importance of competitive energy transfer upon luminescence is observed in this thesis in a variety of minerals.

Another objective of the project was to explore the collection of OD XAS of trace elements in mineral systems through either CW or TR XEOL. The advantages of OD XAS over traditional absorption or fluorescence methodologies is that OD XAS potentially provides additional site selectivity derived from the inherent site specific nature of luminescent emissions in minerals. At an early stage in the project, I demonstrated that the technique is not viable for the detection of OD XAS of trace element concentrations in minerals. However, the system was used successfully to collect OD XAS from some major element systems. The system will be useful in this way for certain applications, such as (Sapelkin et al., 2012) who used the system to collect OD XAS from nano rods of ZnO allowing differentiation of the ZnO signal from that of a Zn rich substrate.

The explicit application of XEOL and TR XEOL spectroscopy to minerals is at the heart of this thesis. The underlying objectives identified are the development of new techniques for analysing luminescence, the development of techniques to allow the quantification of luminescence and the application of techniques from alternative disciplines.

Luminescence in minerals is invariably a complex convoluted signal and so any technique that allows the isolation and identification of a particular component is of particular importance in mineral luminescence. This thesis demonstrates a number of useful XEOL techniques that isolate and identify interesting and previously unexplored aspects of mineral luminescence. XEOL and TR XEOL also demonstrate the potential to explore energy transfer mechanisms within samples, a currently poorly constrained aspect of XEOL.

The results I report from TR experiments frequently record luminescent lifetimes for minerals at >100 ps; interestingly the majority of luminescent minerals tested exhibited at least one emission with a $< ns$ lifetime, with many minerals exhibiting lifetimes orders of magnitudes shorter than lifetimes previously reported within the literature, where typically the shortest are $\sim ns$. This finding illustrates the extent to which energy transfer effects are present within mineral luminescence, influencing not only the measured lifetime, but also more importantly the intensity of emission. The concept of exploring luminescence within the ps and fs domains opens a new and significant avenue within which to investigate minerals and their defects. This has the potential to expand our ability to interpret luminescent defects within minerals and gain a better understanding of their geological history.

In Chapter 5 the luminescence of the feldspar group is probed in more detail, for this discussion I consider luminescence as three consecutive processes, absorption, energy transfer, and emission. The relationship of a substitutional atom and its local and extended environment is a fundamental aspect of mineral luminescence. This relationship extends from the level of local atomic coordination as described for

example by CFT (Bethe, 1929), to defect planes and grain boundaries extending into the macro environment. The interaction between an atom's electronic structure and its environment has profound effects on the luminescent process and represents an important aspect of interest of this chapter.

A dose rate experiment (section 5:1) completed on a Fe rich alkali feldspar (MISI) demonstrates the intensity of emission of the TR peak is linear with the dose rate. This finding is important as it allows us to interpret variations in intensity. I also postulate that TR intensity will be linear with lumiphore concentration whilst the centre is dilute and effectively isolated. In contrast, the TR peak intensity is shown to be non-linear as a function of excitation energy. This experiment also identifies variations in response between the long and short lifetime emissions. These observations are consistent with variations in energy transfer or hot luminescence. The significance of this finding is that it introduces the identification and interpretation of both hot luminescence and variations in energy transfer processes occurring in mineral luminescence. Significantly, these concepts have previously not been discussed as mechanisms affecting luminescence in the Earth sciences literature. This finding is also significant in respect to the objective of collecting TR OD XAS; this lack of linearity will complicate the interpretation of any signal collected.

The TR dose response of (MISI) is explored through two consecutive TR experiments collected from the same sample position; the effects of sample alteration are seen by comparing the results from the first and second experiment. This technique demonstrates that information regarding alternative mechanisms of alteration can be explored. This is significant, as naturally occurring radiation and the way it modifies

minerals are an important process over geological time. Understanding and interpreting the mechanisms of alteration are a prerequisite for using radiation effects to interpret the geological history of a mineral. Techniques that probe the mechanisms of modification are an important tool in understanding and modelling the modification processes. The facility to explore sample modification can have a wide range of applications for example Nasdala et al.; (2006) demonstrated radiation modification is an important aspect in the interpretation of BSE images that is rarely considered, the understanding of radiation effects are important in both TL and OSL dating in relation to defect creation and trap filling processes.

Trap defects as described within the TL and OSL communities are by nature somewhat poorly constrained, in that the standard spectroscopic techniques to detect and explore them are unavailable as to be defined as a trap the site local transition is disallowed . Their presence in a mineral is usually inferred through stimulated emissions. In section 5:13 exploring dose responses the alteration and the behaviour and inter-relationships of related emissions are explored. The potential to identify and probe trap defects through triplet-triplet annihilation is considered. This methodology if it can be applied more widely to other mineral systems will find applications within luminescence dating and dosimetry. The temporal accuracy of the system is tested by measuring the fibre optic transit time as a function of emission wavelength in section 5:14. The results show a good correlation between the measured and calculated times thus increasing confidence in the temporal accuracy of the system.

Low temperature XEOL responses are explored with experiments on cleavelandite (CLBR) an albite variety, in Section 5:21 using the comparison of LT and RT CW XEOL. The

low temperature spectra predictably show more fine structure with the main features appearing narrower. This finding confirms that responses of XEOL at LT are consistent with LT responses in PL. In Section 5:22 the dose dependence spectra collected at both RT and LT are compared, although the compound spectra appear consistent variations between the contributory peaks between the LT and RT spectra are found. This finding underlines one of the conclusions of this thesis that the deconvolution of compound spectra is essential for the correct interpretation of dose and dose rate responses. In addition, unreported emissions are identified from the sample using the technique. A linear relationship between peak height and peak position (energy) as a function of excitation energy is determined, this is consistent with sample alteration and can therefore be considered as a useful technique to monitor and model sample modification.

The TR dose rate responses of (CLBR) are reported in section 5:23 the results from two sequential experiments, one incorporating sample moves between integrations to limit sample alteration through dose effects and in comparison a second experiment where all experiments are collected consecutively from the same position on the sample introducing the potential for sample modification. The technique allows the differentiation between variations in spectra due sample heterogeneity and sample modification and as such can be considered a useful technique.

. I explored a hypothesis that the delayed peak was a harmonic of a higher energy emission; this was confirmed with the use of a UV filter that blocked the emission and removed the feature. The delay was a consequence of the 'path lengthening effect' of fibre optic cables to shorter wavelength transmissions.

Moonstone cryptoperthite alkali feldspar is investigated (section 5:3) using CW XEOL the spectra identified numerous unpublished emissions. The sample was investigated to determine the extent to which interfaces play in the generation of these emissions. The temporal analysis of dose dependence experiments were explored that identified significant changes in behaviour during the first few seconds of excitation with a number of the compound features of the spectra responding collectively. Interestingly the concept of sample modification, although considered within mineral luminescence, has resulted in little work on the temporal nature of the process involved, identifying either linked or sequential processes. The behaviour exhibited is consistent with the features being closely related or they are linked to the same structural defect. Other work discussed has identified inconsistencies of intensity of luminescent responses to trace element concentrations. These results offer a methodology to investigate and explain inconsistencies through the deconvolution of trace element and structural emissions.

Copper bearing feldspar 'Plush Feldspar' was investigated in Section 5:4 using a combination of standard analytical techniques including XANES, EXAFS, LA ICP MS, EMP and UV Vis spectroscopy in combination with XEOL and TR XEOL to illustrate the potential of the system as part of a timely investigation into a modern mineralogical conundrum. The techniques identified unpublished emissions and emissions that were sensitive to heat treatment, and are potentially diagnostic of heat treatment. The experimental data were also useful in further characterising the material. In section 5:43 the investigation of an unusual delayed TR emission profile is reported. In the discussion, I postulate a mechanism that would explain the results. The explanation involves a temporal evolution within the collection of the TR signal and the convolution of more

than one emission defect. This again emphasises the importance of deconvolution of emissions, which cannot simply be achieved by simply looking at a limited portion of a spectrum, as at any position within a spectrum the gross intensity measured can be the accumulation of two or more overlapping emissions. These results and methods again demonstrate the importance of differentiation and deconvolution as a recurring theme.

In chapter 6 the potential for the collection of OD XAS is revisited using a suite of minerals with common absorption and emission centres. The hypothesis being tested is that where the absorption and emission are localised and emission does not require significant interaction with the bulk lattice, the potential for the retention of an XAS signal is maximised. The results looked for OD XAS from known absorption/emission trace element defects within the samples. No positive identification of OD XAS was made although two samples provided spectra that warrant further investigation as potentially showing inverse responses. The technique was shown either not to work or be so limited in application as not to be a viable general analytical technique.

Luminescence in zircon is explored in section 6:2. The luminescent signal in zircon is primarily derived from REE's that are described as exhibiting responses consistent with electrons that are isolated from the lattice. They typically display discreet narrow emissions with little vibrational broadening. The CW XEOL spectra collected are consistent with REE spectra recorded using PL. Spectra are also analysed as a function of energy to determine if 'isolation' facilitates the retention of XAS signal, the results again were negative.

TR XEOL collected as a function of incident energy display a variable inverse relationship between lifetime and intensity of emission as a function of incident energy. This finding is significant as it affects the interpretation of luminescence within zircon. Zircon is an important mineral in rock dating, which routinely uses CL imaging is an important aspect in sample selection. The TR XEOL of zircon as a function of incident energy was measured displaying non-linear responses. The data are difficult to interpret due to issues with normalisation of the incident excitation. This aspect would be ideally explored with new Free Electron Laser (FEL) facilities being developed.

Anisotropy is an important aspect that I explored; its effects upon the lifetime/intensity relationship are investigated. The results identified areas worthy of further investigation.

An occasionally overlooked aspect of luminescence is the nature and behaviour of light; its behaviour both as the mechanism of excitation and the resultant propagation of the emission. Exploring the dichroism and anisotropy of absorption and emission signals provides important insights into the nature of both absorption and emission sites.

Luminescence is fundamentally a polarised phenomenon in absorption, and in the propagation of the emission; this is shown to have profound implications for the interpretation of luminescence. The polarised nature of the luminescent process can often be obscured by sample heterogeneity and the inherent complex nature of the systems investigated; however, I demonstrate its implications should not be ignored.

Section 6:31 explores the effect of orientation in the low symmetry mineral topaz. Dose dependant anisotropy is demonstrated to have significant impacts upon CW emission peak intensity. These results highlight the importance of orientation; anisotropy is known to affect both absorption and the propagation of luminescent emissions. In

addition, the potential of directionally preferential energy transfer mechanisms between the absorption and emission sites. The technique of combining the measurement of intensity and lifetime as a function of orientation and polarisation is demonstrated as being well suited to explore these aspects. These results and their application have great potential to expand our understanding and interpretation of contentious luminescent signals. Understanding anisotropy is particularly important in mineralogy, where the vast majority of major rock-forming minerals are low symmetry solids.

Section 6:4 the results from CW XEOL dose and TR dose experiments on a chrome tourmaline the spectra demonstrates interesting variations between individual deconvolved responses, again reinforcing the importance of deconvolution.

Section 6:5 describes the application of the Stickler and Berg (1962) equation to a mineral luminescence system. The results are very encouraging and represent a strong justification for a continuation and extension of this aspect of my research. This concept would have important and far-reaching applications. It has the potential to identify, explain and quantify discrepancies arising from the comparison of intensity of luminescent signal to lumiphore concentration.

To summarise the system when used in stand-alone mode displays the potential for a wide variety of applications within solid-state science. XEOL can be used to probe the nature of defects in solids, and by dose and dose rate experiments gain insights into the interaction of X-rays with matter. In a few select systems, studying XEOL as a function of X-ray energy may provide OD-XAS, but the success of such experiments to explore the local coordination of elements in luminescent phases has proven limited.

The system can be combined with existing detection on a beamline to provide simultaneous collection of XEOL with EXAFS and XRF-based XAS. The potential for simultaneous analysis in a high spatial resolution system has similar benefits to OD XAS, with the ability to infer site selectivity to XAS through the XEOL responses. Although this aspect is compromised by variations in the sample volumes probed between techniques.

7.1 Further Development

The system is capable of further development to allow TR XEOL mapping and this would be a technique comparable to laser FLIM, which has proven to be powerful within the life sciences.

The majority of findings in this thesis emanate from aspects of the lifetime of luminescence. This is shown to be a useful and versatile aspect of the luminescence. I identify numerous circumstances better characterised with TR analysis. The thesis clearly demonstrates many applications would benefit from use or incorporation of TR spectroscopy. One valuable objective for future work would be to determine the natural lifetime for the most important luminescent signals from minerals. These data would then allow quantification of experiments in a wide variety of situations to be completed using the relationship between measured and natural lifetime to calculate the QE of the emission mechanism. Such insights have the potential to underpin far more fully the luminescence of minerals and therefore to understand more rigorously the geological information encoded within the emissions.

8 Appendix

Appendix 1. Hamamatsu MCP PMT R3809U-50



PHOTON IS OUR BUSINESS

MICROCHANNEL PLATE-
PHOTOMULTIPLIER TUBE (MCP-PMTs)

R3809U-50 SERIES

**Compact MCP-PMT Series Featuring
Variety of Spectral Response with Fast Time Response**

FEATURES

- **High Speed**
Rise Time: 150 ps
T.T.S. (Transit Time Spread)[®]: ≤25 ps (FWHM)
- **Low Noise**
- **Compact Profile**
Useful Photocathode: 11 mm diameter
(Overall length: 70.2 mm Outer diameter: 45.0 mm)

APPLICATIONS

- **Molecular Science**
Analysis of Molecular Structure
- **Medical Science**
Optical Computer Tomography
- **Biochemistry**
Fast Gene Sequencing
- **Material Engineering**
Semiconductor Analysis
Crystal Research



Figure 2: Transit Time Spread

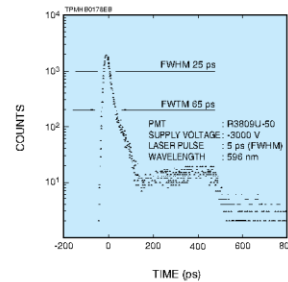


Figure 1: Spectral Response Characteristics

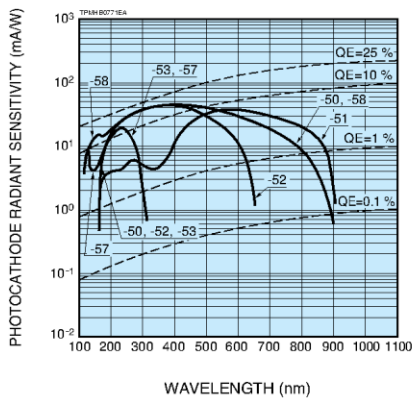
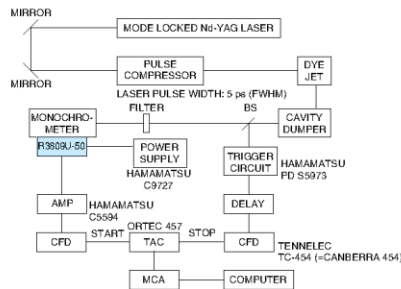


Figure 3: Block Diagram of T.T.S. Measuring System



Subject to local technical requirements and regulations, availability of products included in this promotional material may vary. Please consult with our sales office. Information furnished by HAMAMATSU is believed to be reliable. However, no responsibility is assumed for possible inaccuracies or omissions. Specifications are subject to change without notice. No patent rights are granted to any of the circuits described herein. ©2011 Hamamatsu Photonics K.K.

MCP-PMTs R3809U-50 SERIES

SPECIFICATIONS

PHOTOCATHODE SELECTION GUIDE

Suffix Number	Spectral Response (nm)		Photocathode Material	Window Material
	Range	Peak Wavelength		
50	160 to 850	430	Multialkali	Synthetic Silica
51	160 to 910	600	Extended Red Multialkali	Synthetic Silica
52	160 to 650	400	Bialkali	Synthetic Silica
53	160 to 320	230 to 250	Cs-Te	Synthetic Silica
57	115 to 320	230	Cs-Te	MgF ₂
58	115 to 850	430	Multialkali	MgF ₂

GENERAL

Parameter	Description / Value	Unit
Photocathode Useful Area in Diameter	11	mm
MCP Channel Diameter	6	μm
Dynode Structure [®]	2-Stage Filmed MCP	—
Capacitance Between Anode and MCP out	3	pF
Weight	98	g
Operating Ambient Temperature [Ⓒ]	-50 to +50	°C
Storage Temperature	-50 to +50	°C

MAXIMUM RATINGS (Absolute Maximum Values)

Parameter	Value	Unit
Supply Voltage	-3400	V
Average Anode Current	100	nA
Pulsed Peak Current [Ⓓ]	350	mA

ELECTRICAL CHARACTERISTICS (R3809U-50) at 25 °C[Ⓔ]

Parameter	Min.	Typ.	Max.	Unit
Cathode Sensitivity	Luminouse [Ⓔ]	100	150	—
	Radiant at 430 nm	—	70	—
Gain at -3000 V	1 × 10 ⁵	2 × 10 ⁵	—	—
Anode Dark Counts at -3000 V	—	—	2000	—
Voltage Divider Current at -3000 V	—	—	75	μA
Time Response	Rise Time [Ⓔ]	—	150	ps
	Fall Time [Ⓔ]	—	360	ps
	I.R.F. (FWHM) [Ⓔ]	—	45 [Ⓔ]	—
	T.T.S. (FWHM)	—	—	25 [Ⓔ]

NOTES

- Ⓐ Transit-time spread (T.T.S.) is the fluctuation in transit time between individual pulse and specified as an FWHM (full width at half maximum) with the incident light having a single photoelectron state.
- Ⓑ Two microchannel plates (MCP) are incorporated as a standard but we can provide it with either one or three MCPs as an option depending upon your request.
- Ⓒ We recommend use R3809U-51 with thermoelectric cooling unit to reduce dark counts (Refer to Figure 5)
- Ⓓ This is specified under the operating conditions that the repetition rate of light input is 100 Hz or below and its pulse width is 70 ps.
- Ⓔ This data is based on R3809U-50. All other types (suffix number 51 through 58) have different characteristics on cathode sensitivity and anode dark counts.
- Ⓕ The light source used to measure the luminous sensitivity is a tungsten filament lamp operated at a distribution temperature of 2856 K. The incident light intensity is 10⁻⁴ lumen and 100 V is applied between the photocathode and all other electrodes connected as an anode.
- Ⓖ This is the mean time difference between the 10 % and 90 % amplitude points on the output waveform for full cathode illumination.
- Ⓗ This is the mean time difference between the 90 % and 10 % amplitude points on the trailing edge of the output waveform for full cathode illumination.
- Ⓘ I.R.F. stands for Instrument Response Function which is a convolution of the δ pulse function (H(t)) of the measuring system and the excitation function (E(t)) of a laser. The I.R.F. is given by the following formula:

$$I.R.F. = H(t) \times E(t)$$
- Ⓛ We specify the I.R.F. as an FWHM of the time distribution taken by using the measuring system in Figure 13 that is Hamamatsu standard I.R.F. measurement. It can be temporary estimated by the following equation:

$$(I.R.F. (FWHM))^2 = (T.T.S.)^2 + (Tw)^2 + (Tj)^2$$
 where Tw is the pulse width of the laser used and Tj is the time jitter of all equipments used. An I.R.F. data is provided with the tube purchased as a standard.
- Ⓜ T.T.S. stands for Transit Time Spread (seeⒺ above). Assuming that a laser pulse width (Tw) and time jitter of all equipments (Tj) used in Figure 3 are negligible, I.R.F. can be estimated as equal to T.T.S. (seeⒺ) above. Therefore, T.T.S. can be estimated to be 25 picoseconds or less.

TECHNICAL REFERENCE DATA

Figure 4: Typical Gain

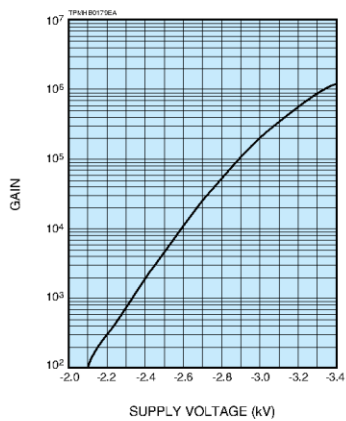


Figure 5: Variation of Dark Counts Depending on Ambient Temperature

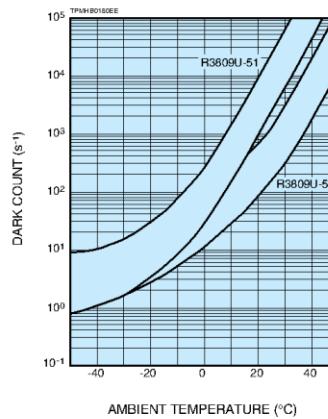


Figure 6: Typical Output Deviation as a Function of Anode DC Current

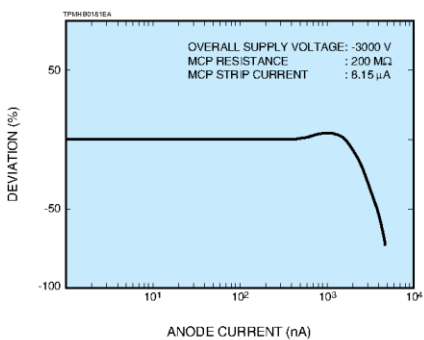
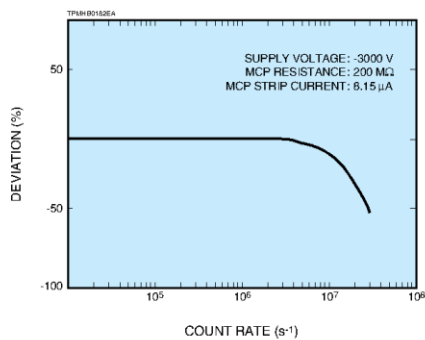


Figure 7: Typical Output Deviation as a Function of Anode Count Rate



MCP-PMTs R3809U-50 SERIES

Figure 8: Typical Output Waveform

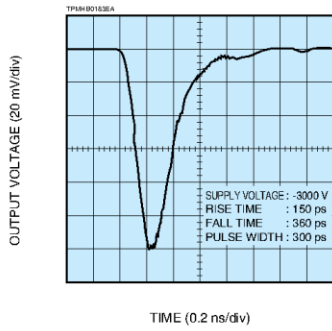


Figure 9: Block Diagram of Output Waveform Measuring System

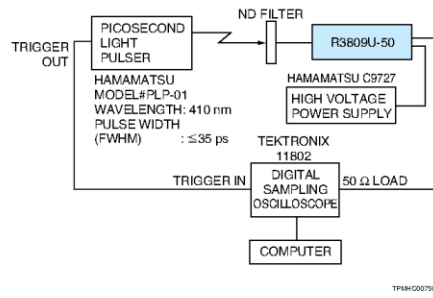


Figure 10: Typical Pulse Height Distribution (PHD)

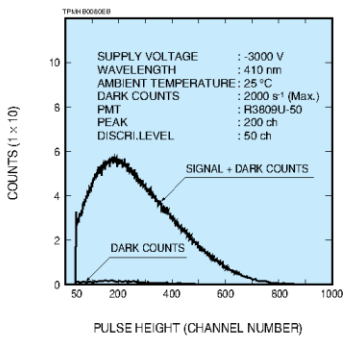
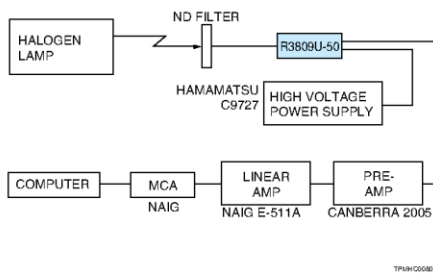


Figure 11: Block Diagram of PHD Measuring System



MCP-PMTs R3809U-50 SERIES

PRECAUTIONS FOR PROPER OPERATION

Handling on set-up

- 1) The photomultiplier tube (PMT) is a glass product under high vacuum. EXCESSIVE PRESSURE, VIBRATIONS OR SHOCKS TO THE TUBE FROM THE SURROUNDING COULD CAUSE A PERMANENT DAMAGE. Please pay special attention on insuring proper handling.
- 2) DO NOT PLACE ANY OBJECTS OF GROUND POTENTIAL CLOSER THAN 5mm TO THE PHOTOCATHODE WINDOW when negative high voltage is applied to the photocathode. It could generate extra noise and damage the photocathode permanently.
- 3) DO NOT EXPOSE THE PHOTOCATHODE TO SUNLIGHT DIRECTLY and any light stronger than the room light even during of no operation.
- 4) NEVER TOUCH THE INPUT WINDOW WITH YOUR BARE HANDS. In case the window contaminated by dust or grease, wipe it off using alcohol and a soft cloth or dust free tissue.
- 5) DO NOT OPERATE OR STORE IN A PLACE OF UNSPECIFIED TEMPERATURE AND HUMIDITY.

Supplying high voltage

- 1) DO NOT SUPPLY ANY VOLTAGE HIGHER THAN SPECIFIED. Also make sure the output current does NOT EXCEED THE MAXIMUM CURRENT specified.
- 2) This device is very sensitive even with weak light input. When applying high voltage to the tube, GRADUALLY (IDEALLY 100 Vdc STEP BUT 500 Vdc STEP IS OK) AND CAREFULLY INCREASE THE VOLTAGE while monitoring the output using an ammeter or oscilloscope. Also make sure before use that the polarity of the applied voltage is correct.
- 3) DO NOT REMOVE OR CONNECT ANY INPUT OR OUTPUT CABLES WHILE HIGH VOLTAGE IS APPLIED. If a high voltage is applied when its output is opened, DO NOT CONNECT ANY READOUT CIRCUIT TO THE TUBE IMMEDIATELY after turning the high voltage off. Ground the anode of the tube before connecting in order to avoid possible damage to the readout circuit due to an excessive electron charge flowing from its anode.
- 4) IT IS RECOMMENDED TO TURN HIGH VOLTAGE OFF WHILE NOT BEING USED FOR MEASUREMENTS. This is to avoid shortening its period of life time as well as a risk of damage due to an exposure of excessive incident light.

Incident light amount

- 1) KEEP THE INCIDENT LIGHT AMOUNT AS LOWS AS POSSIBLE to extend its period of life time.
- 2) In a case of photon counting application, it is recommended to KEEP THE SIGNAL COUNT RATE LESS THAN 20 ks⁻¹.
- 3) ILLUMINATE PHOTOCATHODE EFFECTIVE AREA AS LARGE AS POSSIBLE to keep better linearity characteristics and avoid an excessive stress in partial area, which may result in a reduction of sensitivity partially.

Usage in vacuum

- 1) DO NOT USE A PMT AS AN INTERFACE BETWEEN VACUUM AND ENVIRONMENTAL PRESSURE.
Standard MCP-PMT is not designed for vacuum-tight construction.
- 2) KEEP THE TUBE CLEAN. Unless otherwise, it would cause outgassing in a vacuum.
- 3) DO NOT SUPPLY HIGH VOLTAGE UNLESS THE VACUUM LEVEL REACHES 1×10^{-3} Pa OR HIGHER.
- 4) DO NOT PROCEED BAKING VACUUM INSTRUMENTS WHILE THE TUBE IS PLACED INSIDE.

OTHERS

- 1) If the tube won't be used with a cooler, it is recommended to LEAVE THE TUBE IN DARKNESS (YOUR INSTRUMENT WITHOUT ANY INPUT LIGHT) FOR 30 MINUTES OR SO before start any measurements because it occasionally takes a little while until its dark noise settles down.

WARRANTY

The detectors indicated in this data sheet are warranted to the original purchaser for a period of 12 MONTHS following the date of shipment. The warranty is limited to repair or replacement of any defective material due to defects in workmanship or materials used in manufacture.

- 1) Any claim for damage of shipment must be made directly to the delivering carrier within five days.
- 2) Customer must inspect and test all detectors within 30 days after shipment. Failure to accomplish said incoming inspection shall limit all claims to 75% of invoice value.
- 3) No credit will be issued for broken detector unless in the opinion of Hamamatsu the damage is due to a manufacturing defect.
- 4) No credit will be issued for any detector which in the judgement of Hamamatsu has been damaged, abused, modified or whose serial number or type number have been obliterated or defaced.
- 5) No detector will be accepted for return unless permission has been obtained from Hamamatsu in writing, the shipment has been returned repaired and insured, the detector is packed in their original box and accompanied by the original data sheet furnished to the customer with the tube, and a full written explanation of the reason for rejection of detector.

ACCESSORIES

THERMOELECTRIC COOLING UNIT C10373



Left: Power Supply Right: Cooled PMT Housing

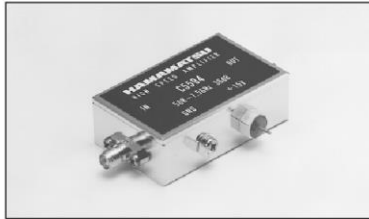
HOLDER E3059-500



Parameter	Description / Value
Cooling Methode	Thermoelectric cooling using peltier module
Heat Exchange Medium	Water
Amount of Cooling Water	1 L/min to 3 L/min (water pressure: below 0.3 MPa)
Cooling Temperature (with cooling water at +20 °C)	Approx. -30 °C
Temperature Controllable Range (with cooling water at +20 °C)	-30 °C to 0 °C (continuously adjustable)
Cooling Time	Approx. 120 min
Optical Window Material	Evacuated double-pane synthetic silica window with heater (185 nm to 2200 nm)
Operating Ambient Temperature [Ⓐ]	+5 °C to +40 °C / Below 75 %
Storage Temperature [Ⓐ]	-15 °C to +50 °C / Below 80 %
Weight	5.5 kg

NOTE: [Ⓐ]No condensation

HIGH SPEED AMPLIFIER C5594 Series



Suffix numbers and input / output connectors

Input Connectors	Output Connectors	
	SMA Jack	BNC Jack
SMA Plug (male)	C5594-12	C5594-14
SMA Receptacle (female)	C5594-22	C5594-24
BNC Plug (male)	C5594-32	C5594-34
BNC Receptacle (female)	C5594-42	C5594-44

Specifications

Parameters	Description / Value
Frequency Response Range	50 kHz to 1.5 GHz
Gain	Typ. 36 dB
Input / Output Impedance	50 Ω
Noise Figure (NF)	Typ. 5 dB
Recommend Input Voltage	+12 V to 16 V
Supply Current	Typ. 95 mA
Absolute	Supply Voltage +17 V
Maximum Ratings	Input Power +10 mW

BENCH-TOP HIGH VOLTAGE POWER SUPPLY C9727 Series



Specifications

Parameter	Description / Value
Output Voltage	0 V to ±3500 V
Maximum Output Current	2 mA
Line Regulation Against ±10 % Line Voltage Change ^{ⒶⒷ}	Max. ±0.005 %
Load Regulation Against 0 % to 100 % Load Change [Ⓐ]	Max. ±0.03 %
Ripple / Noise (p-p) ^{ⒶⒷ}	Max. 0.003 %
Drift (after 30 min Warm-up) ^{ⒶⒷ}	Max. ±0.05 % / h
Temperature Coefficient ^{ⒶⒷ}	Max. ±0.01 % / °C
AC Input	C9727 / C9727-50 120 V (±10 %) (50 / 60 Hz)
Voltage	C9727-01 / C9727-51 230 V (±10 %) (50 / 60 Hz)
Power Consumption ^{ⒶⒷ}	Approx. 40 V-A
Operating Ambient Temperature / Humidity [Ⓒ]	0 °C to +40 °C / below 85 %
Storage Temperature / Humidity [Ⓒ]	-20 °C to +50 °C / below 90 %

NOTE: [Ⓐ]At maximum output voltage [Ⓑ]At maximum output current
[Ⓒ]No condensation

MCP-PMTs R3809U-50 SERIES

HAMAMATSU PHOTONICS K.K. www.hamamatsu.com

HAMAMATSU PHOTONICS K.K., Electron Tube Division

314-5, Shimokanzo, Iwata City, Shizuoka Pref., 439-0193, Japan, Telephone: (81)539/62-5248, Fax: (81)539/62-2205

U.S.A.: Hamamatsu Corporation, 380 Foothill Road, P. O. Box 2910, Bridgewater, NJ 08807-0910, U.S.A., Telephone: (1)609-221-0660, Fax: (1)609-221-1219, E-mail: usa@hamamatsu.com

Germany: Hamamatsu Photonics Deutschland GmbH, Arzbogenstr. 10, D-82211 Herrsching am Ammersee, Germany, Telephone: (49)8152-375-0, Fax: (49)8152-2659, E-mail: info@hamamatsu.de

France: Hamamatsu Photonics France S.A.R.L., 19, Rue du Saule Traipu, Parc du Moulin de Massy, 91882 Massy Cedex, France, Telephone: (33)1 69 53 71 00, Fax: (33)1 69 53 71 10, E-mail: info@hamamatsu.fr

United Kingdom: Hamamatsu Photonics UK Limited, 2 Howard Court, 10 Town Road, Welwyn Garden City, Hertfordshire AL7 1BW, United Kingdom, Telephone: 44(0)1707-294999, Fax: 44(0)1707-267777, E-mail: info@hamamatsu.co.uk

North Europe: Hamamatsu Photonics Norden AB, Smidesvågen 12, SE-171-41 SOLNA, Sweden, Telephone: (46)8-509-031-00, Fax: (46)8-509-031-01, E-mail: info@hamamatsu.se

Italy: Hamamatsu Photonics Italia S.P.A., Strada della Moia, 1/E, 20020 Aressè, (Milano), Italy, Telephone: (39)02-935 81 733, Fax: (39)02-935 81 741, E-mail: info@hamamatsu.it

IPMH1067E09
JAN.2011. IP

Appendix 2. Specification sheet time card

CTRL		Doc No: IDI-CTRL-TI-SPEC-BL-001 Issue: 1 Date: 15 Jan 2008 Page: 3 of 5
-------------	---	--

Table 1: Parameters of signals for VME-EVR in Top-up mode

Name of Signal	Reference event	Delay range	Width range	Comments
SHORT GATE	TOP-UP-ON	0 – 100ms	8ns - < 200ms	User defined pulse delay/width. Pulse starts before injection, their width should overlap injection time.
LONG GATE	TOP-UP-ON and TOP-UP-OFF	= 0	200ms x (N-1) + 110ms	Fixed position of the signal, defined on system level

Fig 1 and Table 1 define the decoded top signals with respect to a single injection cycle and the top up super cycle. Control of the gate signals is through the EVR and will allow setting and storing of configuration specific to each beamline.

As sample interface is shown to control timing signals in Fig. 2. This defines the type of timing information produced by each channel, required reference events for delayed pulses, their delay and width and also enable-disable functions for each channel.

VME-EVR Control Panel				
	Pulse / Gate / Data	Event Type of Data	Delay / Width (us)	Enable - Disable
CHANNEL 0	PULSE	TOP-UP-ON	80000 / 30000	Enable Disable
CHANNEL 1	GATE	TOP-UP-ON TOP-UP-OFF	0 / 0	Enable Disable
CHANNEL 2	DATA	SR-CLK	0 / 0	Enable Disable
CHANNEL 3	PULSE	TOP-UP-ON	xxxxxx / xxxxxx	Enable Disable
CHANNEL 4	GATE	TOP-UP-ON TOP-UP-OFF	0 / 0	Enable Disable
CHANNEL 5	DATA	SR-CLK	0 / 0	Enable Disable
CHANNEL 6	PULSE	TOP-UP-ON	xxxxxx / xxxxxx	Enable Disable

Fig.2: EVR Control Panel for Beamlines

3. SR RF AND ORBIT CLOCKS

The storage ring RF clock is available as a PECL signal and the SR Orbit clock is decoded (from the timing distributed bus) and is available as TTL signal.

Name of Signal	Source	Period	Stability (RMS Jitter)	Comments
SR CLK	Distributed Bus	1.872 us	< 8 ps	By default, this is taken from VME-EVR port #2
RF CLK	Restored RF	2.0 ns	< 5 ps	This is taken from VME-EVR RF OUT port.

Table 2: Parameters of signals for SR RF and Orbit Clocks

4. USER CONFIGURABLE CHANNELS

There are four user configurable channels. They can be used to decode the same or other events and referenced to them delay/width modulated pulses. Their applications bespoke to the end user requirements.

5. ELECTRICAL INTERFACE PANEL FOR BEAMLINES

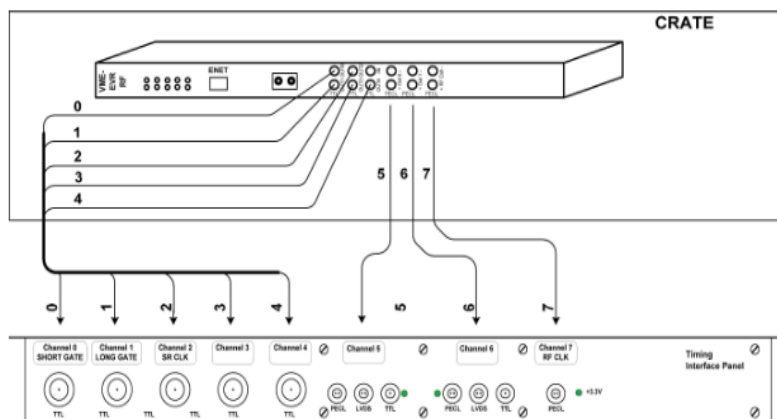


Fig 3: Timing Interface panel for Beamlines with VME-EVR

A 1U high interface panel brings out and conditions signals from the EVR.

Name of Signal	Channel	TTL Connector	PECL Connector	LVDS Connector	Comments
SHORT GATE	0	BNC			Direct connection to EVR output 0
LONG GATE	1	BNC			Direct connection to EVR output 1
SR CLK	2	BNC			Direct connection to EVR output 2
User defined 1	3	BNC			Direct connection to EVR output 3
User defined 2	4	BNC			Direct connection to EVR output 4
User defined 3	5	Coax LEMO	2-pin LEMO	2-pin LEMO	Translation PECL to TTL, LVDS and PECL
User defined 4	6	Coax LEMO	2-pin LEMO	2-pin LEMO	Translation PECL to TTL, LVDS and PECL
RF CLK			2-pin LEMO		Direct connection to EVR RF output

Table 3: Electrical parameters for decoded signals

Components for signal level translations and AC-DC converter are mounted on the rear side of the interface panel.

Appendix 3. Ortec 9327

ORTEC[®]

9327
1-GHz Amplifier and
Timing Discriminator



- For picosecond timing with mV signals from
 - Microchannel Plate Detectors
 - Microchannel Plate PMTs
 - Fast Photodiodes
 - Fast Photomultiplier Tubes
- 1-GHz Amplifier and Timing Discriminator are internally matched for minimum walk and timing jitter
- Walk typically $<\pm 40$ ps over the top 90% of full scale
- Jitter < 20 ps FWHM at 50% of full scale
- Optimized for pulse widths from 250 ps to 1 ns; accepts pulse widths up to 5 ns
- Selectable input pulse height range: 0 to -30 mV, or 0 to -150 mV full scale
- 2:1 Fine Gain control
- Over-Range LED for precise gain adjustment without an oscilloscope

The Model 9327 1-GHz Amplifier and Timing Discriminator combines into one compact preamplifier sized package the two functions normally needed for picosecond timing with ultra-fast detectors. It is ideal for Fluorescence/Phosphorescence Lifetime Spectrometry (Fig. 1), Time-of-Flight Mass Spectrometry (Fig. 2) and LIDAR applications. The Model 9327 is optimized for use with the millivolt signals produced by microchannel plate detectors, microchannel plate photomultiplier tubes, fast photodiodes, and fast, discrete-dynode photomultiplier tubes. The compact package avoids degradation of the sub-nanosecond signals from these detectors by enabling an exceptionally short cable connection between the detector and the amplifier. The timing discriminator output logic pulse can be transmitted over much longer cables to the rest of the time spectrometer without compromising the picosecond time resolution.

The amplifier provides a 1-GHz bandwidth to minimize the noise and rise time contributions to timing jitter on detector pulses having widths as narrow as 250 ps. The 50- Ω amplifier input includes diode clamps to protect against overload pulses. A PC-board-mounted jumper controls the coarse gain to yield two ranges for full-scale input pulse amplitudes: 0 to -30 mV and 0 to -150 mV. A fine gain control permits varying the gain over nominally a 2:1 range. An oscilloscope is not needed to adjust the gain, because an over-range LED indicates when pulse amplitudes have exceeded the full-scale limit of the amplifier. Detector and/or amplifier gain can be increased until the over-range LED turns on, and then decreased until the LED just turns off. This ensures that the pulses utilize all of the amplifier's linear range.

The timing discriminator employs a zero-crossing technique that processes pulse widths from 250 ps to 5 ns without the need to adjust pulse-shaping cables. The zero-crossing technique results in minimal timing jitter and walk as a function of pulse amplitude. It is optimized for sub-nanosecond pulse widths, but will accommodate pulses up to 5 ns wide. The shift in the timing output (walk) as a function of pulse amplitude is typically less than ± 40 ps over the top 90% of full scale when employing a 300-ps input pulse width (Fig. 3). The typical contribution of the 9327 to timing jitter is illustrated in Figure 4. With such a small contribution from the 9327, the detector normally becomes the dominant source of timing jitter. The Model 9327 includes a noise discriminator adjustable over a major fraction of full scale. With the source of

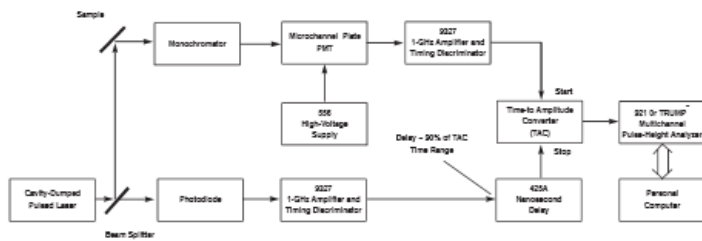


Fig. 1. Typical Block Diagram for a Fluorescence Lifetime Spectrometer (with reversed start/stop assignments).

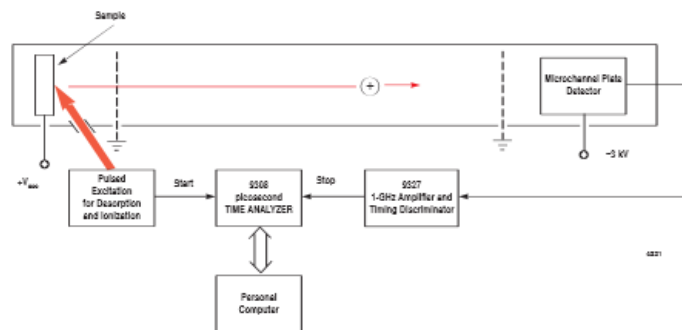


Fig. 2. The Model 9327 In a Simplified Illustration of a Time-of-Flight Mass Spectrometer. The Model 9308 picosecond TIME ANALYZER functions as a multiple-stop time spectrometer.

detector events turned off, the discriminator threshold can be adjusted until the associated LED is turned on by triggering on noise. Subsequently, the threshold is adjusted until the LED just turns off, thus ensuring that the discriminator will not trigger on noise.

The Model 9327 provides two fast-negative NIM logic signals suitable for operating other timing instruments with picosecond time resolution. A 100-ns wide TTL output is also provided for counting applications. In addition to excelling in high-resolution time spectrometry, the Model 9327 can be used for single-photon and single-ion counting applications.

A 3-meter long captive power cord terminated in a 9-pin, D connector supplies power to the unit. Power can be derived from the mating connectors on a 9308 picosecond TIME ANALYZER, a 4002P Portable Power Supply, a 4003 Preamp Power Output Module, or any ORTEC spectroscopy amplifier. Alternatively, a dc power source in the range of +12 to +15 V at 350 mA can be connected to the designated pins on the power connector.

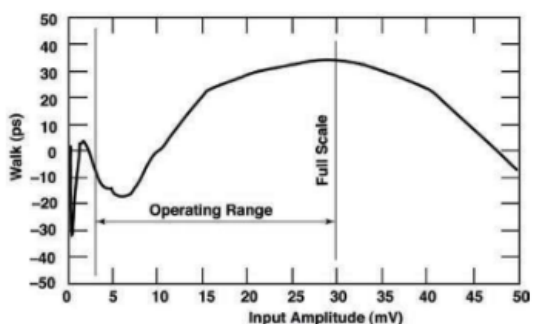


Fig. 3. Typical Walk vs. Pulse Amplitude. Full scale is denoted by the Over Range LED turning on. Measured with a pulse width of 300 ps FWHM.

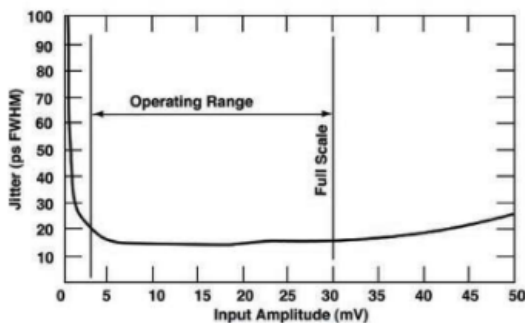


Fig. 4. Timing Jitter vs. Pulse Amplitude. Measured with the system in Fig. 1 by replacing the detectors with a pulser having a pulse width of 300 ps FWHM. Full scale is denoted by the Over Range LED turning on.

9327

1-GHz Amplifier and Timing Discriminator

Specifications

PERFORMANCE

Performance is measured on the 0 to -30 mV input range unless specified otherwise.

INPUT RANGE 0 to -30 mV (full scale) or 0 to -150 mV (full scale), selectable via a circuit board jumper.

EQUIVALENT INPUT NOISE <100 μ V rms on the 0 to -30 mV range.

TIME SLEWING (Walk) Typically < \pm 40 ps shift in the timing output as a function of pulse amplitude over the top 90% of full scale. Includes the contribution of both the amplifier and the timing discriminator. Measured with an input pulse width of 300 ps FWHM.

TIMING JITTER <20 ps FWHM for a pulse amplitude at 50% of full scale. Measured with the same pulse shape listed under TIME SLEWING.

PULSE-PAIR RESOLUTION <10 ns at the fast negative NIM outputs.

OPERATING TEMPERATURE RANGE 0 to 50°C.

TRANSMISSION DELAY TEMPERATURE SENSITIVITY <10 ps/°C from 0 to 50°C. Measured at 50% of full scale with the pulse shape listed under TIME SLEWING.

INPUTS AND OUTPUTS

INPUT (Amplifier) Rear-panel SMA connector for negative input pulses. Accepts pulse widths from 250 ps to 5 ns FWHM. Optimized for sub-nanosecond pulse widths. Input range is jumper selectable for 0 to -30 mV or 0 to -150 mV. Input impedance: 50 Ω ac, <1000 Ω dc to ground. Diode clamps provide protection against overload to \pm 2 V dc, or \pm 10 V for a 50 ns-wide pulse at a duty cycle <1%.

AMP OUT Rear-panel SMA test point suitable for oscilloscope monitoring via a 50- Ω coaxial cable terminated in 50 Ω . Test point output impedance: 1000 Ω . The amplifier drives the timing discriminator input in parallel with the output monitor via an internal connection.

NIM OUT Front- and rear-panel BNC connectors provide two independent, fast-negative NIM output logic pulses. Output amplitude is nominally -800 mV into a 50- Ω load. Pulse width is nominally 4 ns.

TTL OUT Rear-panel BNC connector provides a positive TTL pulse, triggered by the fast-negative NIM output. The 100-ns width of the TTL pulse is non-updating. Output impedance: <50 Ω , short-circuit protected.

THRESH Front-panel test-point jack near the THRESH control permits monitoring of the threshold setting with a voltmeter for resetability. Output impedance is 1000 Ω . Nominal output range is -10 mV to -1 V.

WALK Front-panel test-point jack near the WALK adjustment for monitoring the walk (time slewing) adjustment. See WALK under Controls and Indicators.

GND Front-panel test-point jack for connecting the ground lead of a voltmeter.

CONTROLS AND INDICATORS

INPUT RANGE (Coarse Gain) Circuit board jumper near the amplifier INPUT permits input range selection for 0 to -30 mV or 0 to -150 mV.

FINE GAIN Front-panel, 15-turn screwdriver adjustment to calibrate the full-scale sensitivity. Can be used as a fine gain control with approximately a 2:1 range of gain adjustment.

THRESH Front-panel, 15-turn screwdriver adjustment to set the input discriminator threshold. Adjustable from <2% to >50% of full scale. THRESH test-point jack permits monitoring the setting with a voltmeter.

WALK Front-panel, 15-turn, screwdriver fine tuning to minimize time slewing as a function of input pulse amplitude. Adjustable over a range of approximately \pm 150 mV. A WALK test jack permits monitoring the actual voltage setting through an output impedance <100 Ω .

OUTPUT LED Front-panel, LED flashes on each output pulse to indicate active triggering. Used to set the threshold beyond the noise level.

OVER RANGE LED Front-panel, LED flashes on each preamplifier pulse that has an amplitude exceeding full scale. Used during detector gain adjustment to avoid overloads while maximizing pulse amplitudes.

PWR LED Front-panel LED indicates when power is being supplied to the unit.

ELECTRICAL AND MECHANICAL

POWER REQUIRED The Model 9327 derives its power through a 3-meter long (9-ft.) captive power cable terminated with a 9-pin D, preamplifier power connector. This connector is compatible with the preamplifier power connectors on ORTEC Models 9308, 4003, 4002P, or most ORTEC spectroscopy amplifiers. Power required is +12 to +15 V at 350 mA (Pin 4) and ground (Pins 1 and 2).

WEIGHT

Net 0.48 kg (1.1 lb).

Shipping 1.1 kg (2.5 lb).

DIMENSIONS Approximately 3.3 cm x 12.5 cm x 13.5 cm (1.3 in. x 4.9 in. x 5.3 in.).

MISCELLANEOUS Meets EEC standards (CE) for emissions, susceptibility, and power.

9327

1-GHz Amplifier and Timing Discriminator

Ordering Information

To order, specify:

Model	Description
9327	1-GHz Amplifier and Timing Discriminator

Suggested Cable Accessories:

SMA58-0.15	RG-58A/U (50-Ω) Coaxial Cable with SMA connectors, 0.15-m length
SMA/BNC	SMA to BNC Adapter with male SMA and female BNC
BNC/SMA	BNC to SMA Adapter with male BNC and female SMA
C-25-12	RG-58A/U (50-Ω) Coaxial Cable with BNC connectors, 3.7-m (12-ft) length

Specifications subject to change
092507

ORTEC[®]

www.ortec-online.com

Tel. (865) 482-4411 • Fax (865) 483-0396 • ortec.info@ametek.com
801 South Illinois Ave., Oak Ridge, TN 37831-0895 U.S.A.
For International Office Locations, Visit Our Website

AMETEK[®]
ADVANCED MEASUREMENT
TECHNOLOGY

Appendix 4. ORTEC 566

ORTEC[®]

566

Time-to-Amplitude Converter

- For time spectroscopy in the range from 10 ns to 2 ms
- Valid Start and Valid Conversion outputs
- Selectable output delay and width
- Output synchronized with a stop or external strobe signal
- Provision to reject unwanted start input signals
- Positive or negative input signals



The ORTEC Model 566 Time-to-Amplitude Converter (TAC) measures the time interval between pulses to its start and stop inputs and generates an analog output pulse proportional to the measured time. Timing experiments requiring time ranges from 10 ns to 2 ms may be performed, giving the experimenter flexibility in analyzing random nuclear events that occur within a selected time range. Time ranges from 50 ns to 2 ms are provided via the front-panel controls.

The Model 566's start input can be inhibited by a pulse or a dc level at the rear-panel Gate Input connector.

Valid Start and Valid Conversion outputs are provided for each accepted start and stop input, respectively. The duration of the Valid Start output indicates the interval from the accepted start until the end of reset. The Valid Conversion output occurs from the end of the internal delay after stop to the end of reset.

The selectable TAC output width and variable delay, which are easily adjusted, further serve to make the Model 566 a flexible instrument, easily adapted into many time spectroscopy systems. The output of the TAC may be synchronized with the stop signal or an external strobe signal to further enhance its versatility.

The Model 566 is dc-coupled and gated so that input count rates will not paralyze or otherwise hinder normal operation. The TAC output should be connected to the dc-coupled input of a multichannel analyzer for optimum high-count-rate performance.

Specifications

PERFORMANCE

TIME RESOLUTION FWHM $\leq 0.01\%$ of full scale plus 5 ps for all ranges.

TEMPERATURE INSTABILITY $\leq \pm 0.01\%/^{\circ}\text{C}$ (± 100 ppm/ $^{\circ}\text{C}$) of full scale or ± 10 ps/ $^{\circ}\text{C}$ (whichever is greater), 0 to 50 $^{\circ}\text{C}$.

DIFFERENTIAL NONLINEARITY Typically, $< 1\%$ from 10 ns or 2% of full scale (whichever is greater) to 100% of full scale.

INTEGRAL NONLINEARITY $\leq \pm 0.1\%$ from 10 ns or 2% of full scale (whichever is greater) to 100% of full scale.

RESET CYCLE Fixed 1.0 μs for X1 and X10 Multipliers, fixed 5 μs for X100 Multiplier, and fixed 50 μs for X1K, and X10K Multipliers. Occurs after Over Range, Strobe cycle, or Ext Strobe Reset cycle.

START-to-STOP CONVERSION TIME Minimum ≤ 5 ns.

INPUT COUNT RATE > 30 MHz.

CONTROLS (Front Panel)

RANGE (ns) Three-position rotary switch selects full scale time interval of 50, 100, or 200 ns between accepted Start and Stop input signals.

MULTIPLIER Five-position rotary switch extends time range by a multiplying factor of 1, 10, 100, 1K, or 10K.

DELAY (μs) 20-turn screwdriver-adjustable potentiometer varies the delay of the TAC output from 0.5 μs to 10.5 μs , relative to an accepted Stop input signal; operable in the Int Strobe mode only.

STROBE MODE Two-position locking toggle switch selects either Internal or External source for initiating the strobe cycle to strobe valid information from the TAC output.

CONTROLS (Rear Panel)

GATE MODE Two-position locking toggle switch selects Coincidence or Anticoincidence mode of operation for the Start circuitry. Start circuitry is enabled in the Coinc position or inhibited in the Anti position during the interval of a Gate input signal.

LOG CURR Two-position locking toggle switch selects the use of ± 6 V or ± 12 V bin lines to provide current for the internal logic circuitry.

In the ± 6 V position, the Model 566 is within the current allotment for a single NIM width when using a NIM Standard Class V power supply. In the ± 12 V position, the Model 566 exceeds the current allotment for a single NIM width on the +12 V and -12 V bin lines.

566

Time-to-Amplitude Converter

However, this position allows the Model 566 to be used with power supplies not providing +6 V and -6 V.

INPUTS

All four inputs listed below are dc-coupled, edge triggered, and printed wiring board (PWB) jumper selectable to accept either negative or positive NIM standard signals. Input impedance is 50 Ω in the negative position and >1 k Ω in the positive position. The threshold is nominally -400 mV in the negative position and +2 V in the positive position.

STROBE Front-panel BNC connector provides an external means to strobe a valid output signal from the TAC in the Ext Strobe mode. The input signal, exceeding threshold within the Ext Strobe reset interval after the Stop input, initiates the read cycle for the linear gate to the TAC output. Factory-set in the positive input position. Ext Strobe reset interval has a minimum value of -0.5 μ s and a maximum value of nominally 10 μ s.

START Front-panel BNC connector initiates time conversion when Start input signal exceeds threshold. Factory-set in the negative input position.

STOP Front-panel BNC connector terminates time conversion when Stop input signal exceeds threshold. Factory-set in the negative input position.

GATE Rear-panel BNC connector provides an external means of gating the Start circuitry in either Coincidence or Anticoincidence with the Start input signal. Gate input signal must cross threshold \geq 10 ns prior to the Start input signal and must overlap the trigger edge of the Start input signal. Factory-set in the positive input position.

OUTPUTS

TAC OUTPUT Front-panel BNC connector provides unipolar pulse.

Amplitude 0 V to +10 V proportional to Start/Stop input time difference.

Time End of delay period in Int Strobe mode; prompt with Strobe input in Ext Strobe mode.

Width Adjustable by PWB potentiometer from \leq 1 μ s to \geq 3 μ s.

Impedance $Z_o < 1 \Omega$.

Rise Time -250 ns.

Fall Time -250 ns.

VAL ST Rear-panel BNC connector provides NIM-standard slow positive logic level signal.

Amplitude Nominally +5 V. Complement signal selectable by PWB jumper.

Time and Width From accepted Start input to end of reset.

Impedance $Z_o < 10 \Omega$.

Rise Time \leq 50 ns.

Fall Time \leq 50 ns.

VALID CONV Rear-panel connector provides NIM-standard slow positive logic level signal to indicate a Valid Conversion.

Amplitude Nominally +5 V. Complement signal selectable by PWB jumper.

Time and Width From end of internal delay after Stop to end of reset.

Impedance $Z_o < 10 \Omega$.

Rise Time \leq 50 ns.

Fall Time \leq 50 ns.

ELECTRICAL AND MECHANICAL

POWER REQUIRED

Logic Current Switch

\pm 6 V

+24 V, 45 mA; +12 V, 95 mA; +6 V, 140 mA;
-24 V, 50 mA; -12 V, 140 mA; -6 V,
300 mA.

\pm 12 V

+24 V, 45 mA; +12 V, 210 mA; -24 V,
50 mA; -12 V, 405 mA.

WEIGHT

Net 1.5 kg (3.3 lb).

Shipping 3.0 kg (7 lb).

DIMENSIONS NIM-standard single-width module 3.43 X 22.13 cm (1.35 X 8.714 in.) per DOE/ER-0457T.



Ordering Information

To order, specify:

Model	Description
566	Time-to-Amplitude Converter

Specifications subject to change
011008

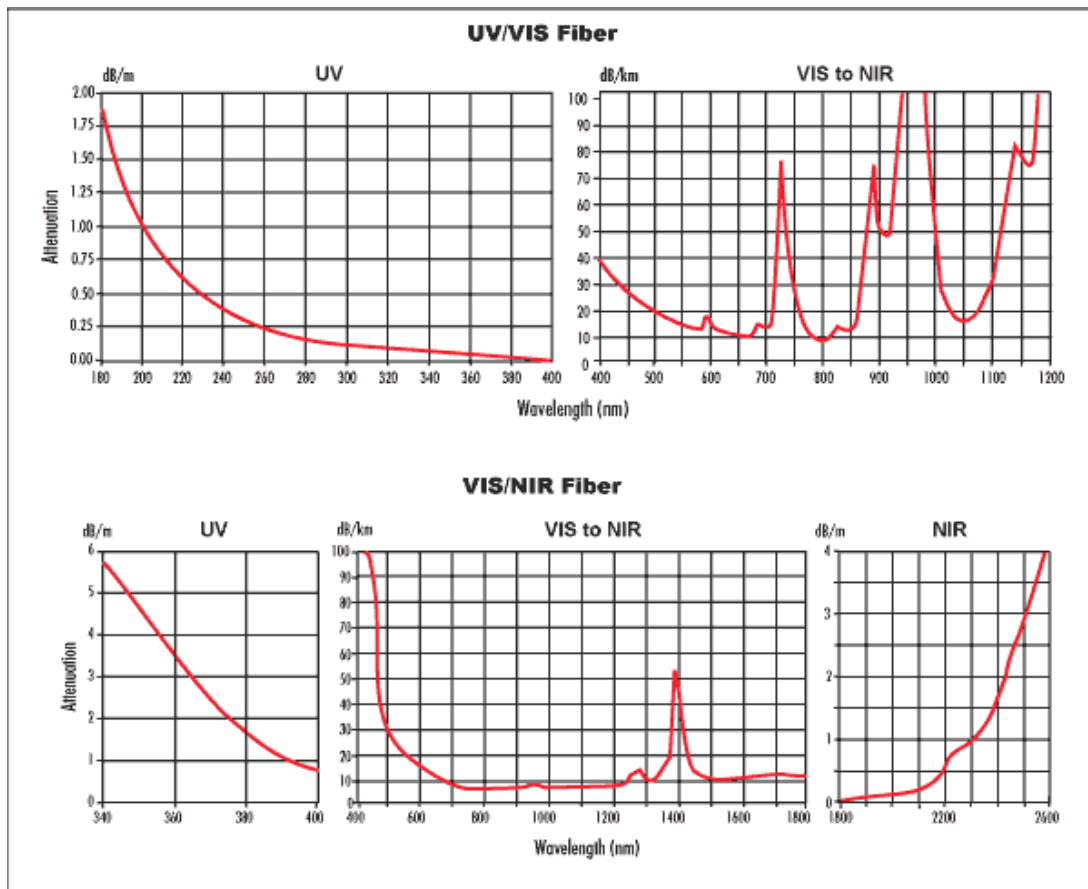
ORTEC[®]

www.ortec-online.com

Tel. (865) 482-4411 • Fax (865) 483-0396 • ortec.info@ametek.com
801 South Illinois Ave., Oak Ridge, TN 37831-0895 U.S.A.
For International Office Locations, Visit Our Website

AMETEK[®]
ADVANCED MEASUREMENT
TECHNOLOGY

Appendix 5. Transmission curves optic fibres



Appendix 6. Fitting results from ZAF5 red zircon

TR XEOL energy scan from 6.95- 7.01 keV using 150 line grating blazed at 500nm (2.47 eV) centred at 435 nm (2.85 eV) 0.5 mm slits with 50, 180 s integrations.

nm	tau 1	(±)	A1	(±)	tau 2	(±)	A2	(±)	
232	0.0776	0.0776	0.0362	28.323	6.64	0.4181	0.0489	37.474	0.0489
233	0.1874	0.1874	0.0069	163.65	3.98	1.0722	0.117	27.6	3.88
234	0.1966	0.1966	0.0072	182.13	4.66	1.0524	0.123	29.437	4.58
235	0.1787	0.1787	0.0064	183.96	4.91	0.8975	0.097	32.229	4.85
236	0.2257	0.2257	0.0041	216.79	1.87				
237	0.1398	0.1398	0.0077	139.59	5.59	0.7105	0.0489	56.119	5.42
238	0.2748	0.2748	0.0052	193.39	1.88				
239	0.1803	0.1803	0.0093	170.31	8.18	0.7206	0.0787	46.318	8.17
240	0.2181	0.2181	0.0038	218.18	1.81				
241	0.2524	0.2524	0.0052	194.25	2.01				
242	0.1764	0.1764	0.0041	207.12	2.78	1.1959	0.0997	26.753	2.63
243	0.2573	0.2573	0.0102	172.52	5.87	1.1127	0.22	19.638	5.9
244	0.2032	0.2032	0.0051	204.93	3.6	1.1025	0.16	18.375	3.53
245	0.2261	0.2261	0.0044	217.97	2.04				
246	0.1962	0.1962	0.0145	135.61	9.7	0.7621	0.094	48.025	9.72
247	0.1646	0.1646	0.0075	152.47	4.74	0.9098	0.0822	38.788	4.63
248	0.2041	0.2041	0.0082	183.17	4.84	1.1791	0.21	20.657	4.71
249	0.1529	0.1529	0.0099	127.6	7.37	0.6299	0.046	63.135	7.35
250	0.087	0.087	0.0083	132.53	6.2	0.5315	0.0277	86.221	6.09
251	0.1524	0.1524	0.0082	155.08	6.94	0.6714	0.0554	54.845	6.9
252	0.183	0.183	0.0055	196.43	3.76	1.0956	0.123	25.744	3.64
253	0.1652	0.1652	0.0108	166.5	8.31	0.7986	0.104	44.157	8.23
254	0.1774	0.1774	0.0099	155.04	6.92	0.82	0.1	38.342	6.88
255	0.1708	0.1708	0.0053	200.15	4.5	0.8736	0.0935	30.041	4.44
256	0.164	0.164	0.007	177.11	6.51	0.7067	0.0695	42.827	6.49
257	0.22	0.22	0.0075	185.99	4.42	1.1793	0.214	17.969	4.35
258	0.2694	0.2694	0.0045	191.19	1.63				
259	0.1952	0.1952	0.0095	178.2	7.7	0.8208	0.115	35.228	7.69
260	0.1334	0.1334	0.0184	94.294	12.9	0.489	0.0363	98.344	12.8
261	0.1925	0.1925	0.0055	197.72	4.12	0.9799	0.0981	29.526	4.07
262	0.1112	0.1112	0.0064	0.6904	0.0459	0.6904	0.0459	53.512	4.57
263	0.272	0.272	0.0121	160.83	4.57	1.6111	0.558	10.172	4.44
264	0.2698	0.2698	0.0046	198.74	1.73				
265	0.1562	0.1562	0.0096	142.59	7.37	0.6816	0.0661	49.361	7.33
266	0.1278	0.1278	0.0069	158.61	5.67	0.6903	0.0529	53.21	5.57
267	0.0851	0.0851	0.0122	106.95	6.92	0.5633	0.0308	98.894	6.76
268	0.2034	0.2034	0.0115	149.99	7.14	0.9006	0.121	35.267	7.12
269	0.2725	0.2725	0.0044	195.72	1.59				

270	0.1571	0.1571	0.0092	152.98	7.02	0.7396	0.0732	48.194	6.96
271	0.2142	0.2142	0.0147	149.98	9.5	0.864	0.127	40.832	9.53
272	0.2233	0.2233	0.0042	232.64	2.1				
273	0.2634	0.2634	0.0043	194.43	1.6				
274	0.1699	0.1699	0.006	175.25	3.67	1.1088	0.123	26.106	3.5
275	0.1893	0.1893	0.0055	176	3.28	1.1317	0.114	25.066	3.17
276	0.1992	0.1992	0.0075	175.82	4.8	1.0322	0.152	23.607	4.73
277	0.2278	0.2278	0.0044	204.57	1.88				
278	0.2446	0.2446	0.0051	199.88	2.05				
279	0.2293	0.2293	0.0044	213.9	1.98				
280	0.2699	0.2699	0.0067	170.21	2.35	1.9542	0.714	5.2	0.714
281	0.217	0.217	0.01	158.99	5.9	0.9963	0.143	28.028	5.89
282	0.1898	0.1898	0.0085	176.43	7.63	0.7327	0.0803	42.28	7.64

9 References

- ADLER, F., GEIGER, M., BAUKNECHT, A., HAASE, D., ERNST, P., DORNEN, A., SCHOLZ, F. & SCHWEIZER, H. 1998. Self-assembled InAs/GaAs quantum dots under resonant excitation. *Journal of Applied Physics*, 83, 1631-1636.
- AITKENS, I. 1931. feldspar Gems. *US Bureau of Mines Information circular*, 6553.
- AKIZUKI, M. & SUGAWARA, H. 1970. The lamellar structure in moonstone and anorthoclase from Korea. *Contributions to Mineralogy and Petrology*, 29, 28-32.
- ANGEL, R. J., CARPENTER, M. A. & FINGER, L. W. 1990. Structural variation associated with compositional variation and order-disorder behavior in anorthite-rich feldspars. *American Mineralogist*, 75, 150-162.
- AWSCHALOM, D. 2012. *Awschalom Group* [Online]. University of California. [Accessed 15/03/2012 2012].
- BACHINSKI, S. W. & MÜLLER, G. 1971. Experimental Determinations of the Microcline—Low Albite Solvus. *Journal of Petrology*, 12, 329-356.
- BANGERT, U., BARNES, R., GASS, M. H., BLELOCH, A. L. & GODFREY, I. S. 2009. Vacancy clusters, dislocations and brown colouration in diamond. *Journal of Physics: Condensed Matter*, 21, 364208.
- BARBIN, V. & SCHVOERER, M. 1997. Cathodoluminescence géosciences. *Comptes Rendus de l'Académie des Sciences - Series IIA - Earth and Planetary Science*, 325, 157-169.
- BECKER, W. (ed.) 2005. *Advanced Time-Correlated Single Photon Counting Techniques*, Berlin: Springer.
- BECKER, W. 2008. *The bh TCSPC Handbook*, Berlin, Becker & Hickel GMBH.
- BECKER, W., BERGMANN, A. & BISKUP, C. 2007. Multi spectral fluorescence lifetime imaging microscopy. *Microsc. Res. Tech.*, 70, 403-409.
- BECKER, W., BERGMANN, A., HINK, M. A., KÖNIG, K., BENNDORF, K. & BISKUP, C. 2004. Fluorescence Lifetime imaging by time correlated single-photon counting. *Microsc. Res. Tech.*, 63, 58-66.
- BECKER, W., BERGMANN, A., MASTER, B. R. & SO, P. (eds.) 2008. *Handbook of Biomedical Nonlinear Optical Microscopy*: Oxford University Press.
- BEER, A. 1852. Determination of the absorption of red light in coloured liquids. *Annalen der Physik und chemie*, 86, 78-88.
- BERAN, A. & LIBOWITZKY, E. 2004. *Spectroscopic methods in mineralogy : University textbook*, Budapest, Eotvos University Press.
- BERGIN, F. J., DONEGAN, J. F., GLYNN, T. J. & G.F., I. 1985. Luminescence and fluorescence line narrowing studies of chromium doped glass. *Journal De Physique, Colloque C7*, 337.
- BERGSTROM, J., BLYTH, R., BRUNET, S., CHEN, W., DALLIN, L., DEJONG, M., HOFFMEYER, R., KWAN, B., MALEY, J., REIGIER, T., SHAM, T. K., J., V. & SAMMYNAIKEN, R. 2008. Comparison of TRXEOL and Laser TCSPC of Zinc Oxide Nanoparticles: A merit for TRXEOL. *Canadian light source 2008 activity report*. Saskatoon: Canadian Light Source.
- BETHE, H. 1929. Splitting of terms in crystals. *Ann Phys*, 3, 133-206.

- BIANCONI, A. & JACKSON, D. 1977. Intrinsic luminescence excitation spectrum and extended X-ray absorption fine structure above the k edge in CaF₂. *Physical Review B*, 17, 2021-2023.
- BICCARI, F. 2009. *Defects and doping in Cu₂O*. PhD, Sapienza university of Rome.
- BINSTED, N. 1998. Excurv98. In: CCLRC (ed.) <http://srs.dl.ac.uk/xrs/computing/Programs/excurv97/intro.html> ed.: Daresbury laboratory
- BLOCH, F. 1929. Über die Quantenmechanik der Elektronen in Kristallgittern. *Zeitschrift für Physik*, 52, 555-600.
- BOLLMANN, W. & NISSEN, H.-U. 1968. A study of optimal phase boundaries: the case of exsolved alkali feldspars. *Acta Crystallographica Section A*, 24, 546-557.
- BOSI, F., LUCCHESI, S. & REZNITSKII, L. Z. 2004. Crystal chemistry of the dravite-chromdravite series. *European Journal of Mineralogy*, 16, 345-352.
- BOYD, G. T., YU, Z. H. & SHEN, Y. R. 1986. Photoinduced luminescence from the noble metals and its enhancement on roughened surfaces. *Physical Review B*, 33, 7923-7936.
- BROWN, B. E. & BAILEY, Y. W. 1964. The structure of maximum microcline. *Acta Crystallographica*, 17, 1391-1400.
- BUBB, F. W. 1924. Direction of Ejection of Photo-Electrons by Polarized X-rays. *Physical Review*, 23, 137-143.
- BUNKER, G. (ed.) 2010. *Introduction to XAFS, A Practical Guide to X-ray Absorption Fine Structure Spectroscopy*, Cambridge: Cambridge Press.
- BURGESS, S. A., RATNER, D., CHEN, B. R. & HILLMAN, E. M. C. 2010. Fiber-optic and articulating arm implementations of laminar optical tomography for clinical applications. *Biomed. Opt. Express*, 1, 780-790.
- BURNS, R. G. 2005. *Mineralogical Applications of Crystal Field Theory*, Cambridge, Cambridge Press.
- CALLISTER, W. D. J. 2005. *Fundamentals of materials science and engineering*, Danvers MA, John Wiley and Sons.
- CANZZANELLI, M., VINEGONI, C. & PAVESI, L. 1999. temperature dependance of the photoluminescence of all porous-silicon optical microcavities. *Journal of Applied Physics*, 85, 1760-1765.
- CHEN, R. & LEUNG, P. L. 2001. Dose dependence and dose-rate dependence of the optically stimulated luminescence signal. *Journal of Applied Physics*, 89, 259-263.
- CHEN, R. & PAGONIS, V. 2011. Analytical and Approximate Expressions of Dose Dependence of TL and OSL. *Thermally and Optically Stimulated Luminescence*. John Wiley & Sons, Ltd.
- CHEN, W., WESTCOTT, S. L. & ZHANG, J. 2007. Dose dependence of x-ray luminescence from CaF₂:Eu²⁺, Mn²⁺ phosphors. *Applied Physics Letters*, 91, 211103-3.
- CHENG, Y. Y., KHOURY, T., CLADY, R. G., TAYEBJEE, M. J., N.J., E.-D., M.J., C. & T.W., S. 2010. On the efficiency limit of triplet-triplet annihilation for Photochemical upconversion. *Phys Chem Phys*, 7, 66-71.
- CLEAVE, V. 1999. *Organic semiconductors and devices*. 2012.
- COCHRANE, K., BAILEY, J. E., LAKE, P. & CARLSON, A. 2001. Wavelength-Dependent Measurements of Optical-Fiber Transit Time, Material Dispersion, and Attenuation. *Appl. Opt.*, 40, 150-156.

- CONDON, E. 1926. A Theory of Intensity Distribution in Band Systems. *Physical Review*, 28, 1182-1201.
- CORRECHER, V., GARCIA-GUINEA, J., ROBREDO, L. M. & SANCHEZ-MUÑOZ, L. 2007a. Spectra luminescence characterization of metamictization in a Brazilian zircon megacryst. *Radiation Measurements*, 43, 401-405.
- CORRECHER, V., SANCHEZ-MUÑOZ, L., GARCIA-GUINEA, J., BENAVENTE, D. & DELGADO, A. 2007b. Comparison of UV-IR radioluminescence and cathodoluminescence spectra of a potassium feldspar. *Radiation Measurements*, 42, 780-783.
- DALBY, K. N., ANDERSON, A. J., MARIANO, A. N., GORDON, R. A., MAYANOVIC, R. A. & WIRTH, R. 2009. An investigation of cathodoluminescence in albite from the A-type Georgeville granite, Nova Scotia. *Lithos*, 114, 86-94.
- DALDOSSO, N., ROCCA, F., DALBA, G., FORNASINI, P. & GRISENTI, R. 2000. New EXAFS Measurements by XEOL and TEY on Porous Silicon. *Journal of Porous Materials*, 7, 169-172.
- DEXTER, D. L. 1953. Energy transfer. *J. Chem Phys*, 21, 836-50.
- DOREMUS, R., KAO, S., C., & GARCIA, R. 1992. Optical absorption of small copper particles and the optical properties of copper. *Applied Optics*, 31, 5773-5778.
- EINSTEIN, A. 1916. The emission and absorption of radiation in quantum theory. *Verhandlungen der Deutschen physikalischen Gesellschaft*, 8, 318-323.
- EINSTEIN, A. 1917. Zur Quantentheorie der Strahlung. *Physik. Z.*, 18, 121-128.
- ELTON, R. C. 1990. *X-Ray lasers*, Boston, Academic Press.
- EMMETT, J., DOUTHIT, T. 2009. Copper diffusion of plagioclase *News from research* [Online], August 21. Available: www.gia.edu/research-resources/newsfrom-research/Cu-diffusion-emmett.pdf,Aug.21 [Accessed 11/12].
- EMURA, S., MORIGA, T., TAKIZAWA, J., NOMURA, M., BAUCHSPIESS, K. R., MURATA, T., HARADA, K. & MAEDA, H. 1993. Optical-luminescence yield spectra produced by x-ray excitation. *Physical Review B*, 47, 6918.
- ESPOSTI, C. D. & BIZZOCCHI, L. 2007. Absorption and Emission Spectroscopy of a Lasing Material: Ruby. *Journal of Chemical Education*, 84, 1316.
- EVANS, J. B. & GROVE, T. 2004. *MIT opencourse ware* [Online]. Massachusetts: MIT. Available: ocw.mit.edu/NR/rdonlyres/Earth--Atmospheric.../0/lecture9.pdf [Accessed 07/01/2010 2010].
- FINCH, A. 1999. Luminescence phenomena in minerals: Thematic set. *Mineralogical Magazine*, 63, 147-147.
- FINCH, A. A., HOLE, D. E. & TOWNSEND, P. D. 2003. Orientation dependence of luminescence in plagioclase. *Physics and Chemistry of Minerals*, 30, 373-381.
- FINCH, A. A. & KLEIN, J. 1999. The causes and petrological significance of cathodoluminescence emissions from alkali feldspars. *Contributions to Mineralogy and Petrology*, 135, 234-243.
- FLEET, S. G. & RIBBE, P. H. 1963. An electron-microscope investigation of a moonstone. *Philosophical Magazine*, 8, 1179-1187.
- FÖRSTER, T. 1948. Zwischenmolekulare Energiewanderung und Fluoreszenz. *Ann. Phys.*, 437, 55.
- FÖRSTER, T. & HOFFMANN, G. 1971. Die Viskositätsabhängigkeit der Fluoreszenzquantenausbeuten einiger Farbstoffsysteme (effect of viscosity on the fluorescence quantum yield of some dye systems). *Z. Phys. Chem.*, 75, 63-76.
- FOX, M. 2006. *Quantum Optics an introduction*, Oxford, Oxford University Press.

- FRENKEL, J. 1931. On the Transformation of light into Heat in Solids. I. *Physical Review*, 37, 17-44.
- FRIIS, H. 2009. *Luminescence Spectroscopy of Natural and Synthetic REE-bearing Minerals*. PhD, The university of St Andrews 128-132.
- FRIIS, H., FINCH, A. & WILLIAMS, C. 2011. Multiple luminescent spectroscopic methods applied to the two related minerals, leucophanite and meliphanite. *Physics and Chemistry of Minerals*, 38, 45-57.
- FULLER, R. E. 1917. The geomorphology and volcanic sequence of Steens mountain in south eastern Oregon. *Washington University Geological publications* 3, 130.
- GAFT, M., REISFELD, R. & PANCZER, G. 2005. *Luminescence spectroscopy of minerals and materials*, Berlin, Springer.
- GARCIA-GUINEA, J., FINCH, A., CAN, N., HOLE, D. & TOWNSEND, P. 2007a. Orientation dependence of the ion beam and cathodoluminescence of albite. *Physica Status Solidi (c)*, 4, 910-913.
- GARCIA-GUINEA, J., RENDELL, H. M. & SANCHEZ-MUÑOZ, L. 1996. Luminescence Spectra of Alkali Feldspars: Some Relationships Between Structural Features and Luminescence Emission. *Radiation Protection Dosimetry*, 66, 395-398.
- GARCIA-GUINEA, J., SANCHEZ-MUNOZ, L. & CORRECHER, V. 2007b. A new Classification of feldspars by luminescence spectral techniques. *Granitic pegmatites: the State of the Art - International Symposium*. Porto.
- GARCIA-GUINEA, J., TOWNSEND, P. D., SANCHEZ-MUÑOZ, L. & ROJO, J. M. 1999. Ultraviolet-blue ionic luminescence of alkali feldspars from bulk and interfaces. *Physics and Chemistry of Minerals*, 26, 658-667.
- GATTA, G. D., NESTOLA, F., BROMILEY, G. D. & LOOSE, A. 2006. New insight into crystal chemistry of topaz: a multi-methodological study. *American Mineralogist*, 91, 1839-1846.
- GEAKE, J. E., G. WALKER, D.J. TELFER, A.A. MILLS 1977. The cause and significance of luminescence in lunar feldspar. *Philosophical Transactions Royal Society London*, A245, 403-408.
- GERRITSEN, H., VAN DE HEUVEL, D. & AGRONSKKAIA, A. High speed fluorescence lifetime imaging. In: PERIASAMY, A., SO, P., ed. *Multiphoton Microscopy in the Biomedical Sciences IV*, 2004 Bellingham. SPEI, 77-87.
- GIA 2011. *Gia gem database* Edward J Gubelin. GIA.
- GIL, M. A., SIMON, J. M. & FANTINO, A. N. 1988. Czerny-Turner spectrograph with a wide spectral range. *Appl. Opt.*, 27, 4069-4072.
- GOLUBOV, A. A., HOUWMAN, E. P., GIJSBERTSEN, J. G., KRASNOV, V. M., FLOKSTRA, J., ROGALLA, H. & KUPRIYANOV, M. Y. 1995. Proximity effect in superconductor-insulator-superconductor Josephson tunnel junctions: Theory and experiment. *Physical Review B*, 51, 1073-1089.
- GOROBETS, B. S. & ROGOJINE, A. A. 2002. *Luminescent Spectra of Minerals*, Moscow, VIMS.
- GÖTZE, J. K., ULF 2009. *Physical Principles of Cathodoluminescence (CL) and its Applications in Geosciences*.
- GOULON, J., TOLA, P., LEMONNIER, M. & DEXPERT-GHYS, J. 1983. On a site-selective exafs experiment using optical emission. *Chemical Physics*, 78, 347-356.

- GOVINDA, S. 1976. Coloration and luminescence in pure and chromium-doped Al₂O₃ single crystals irradiated with X-rays at room temperature. *Physica Status Solidi (a)*, 37, 109-117.
- GRIBKOVSKII, V., P. 1975. *Theory of light absorption and emission in semiconductors*, Minsk, Nauka i Technica.
- HARRISON, T. N., PARSONS, I. & BROWN, P. E. 1990. Mineralogical evolution of fayalite-bearing rapakivi granites from the Prins Christians Sund pluton, South Greenland. *Mineral Mag*, 54, 66.
- HARVEY, E., NEWTON, 1957. *A history of luminescence*, Philadelphia, F H Furst.
- HAYAKAWA, S., HIROSE, T., YAN, L., MORISHITA, M., KUWANO, H. & GOHSHI, Y. 1999. Synchrotron radiation x-ray excited optical luminescence for chemical state selective analysis. *X-Ray Spectrometry*, 28, 515-518.
- HELD, G. 2009. Introduction to light emitting diode technology and applications. *Introduction to light emitting diode technology and applications*. Fl: Taylor and Francis.
- HIRSCH, L. M. & SHANKLAND, T. J. 1991. Determination of defect equilibria in minerals. *Journal of Geophysical Research: Solid Earth*, 96, 377-384.
- HOFMEISTER, A. M. & ROSSMAN, G. R. 1985. Exsolution of metallic copper from Lake County labradorite. *Geology*, 13, 644-647.
- HOOGENSTRAATEN, W. 1958. Electron traps in zinc rich sulphide phosphors. *Philips Res. Rep.*, 13, 515.
- HOOVER, D. B. 1992. *Topaz*, Oxford, Butterworth Heinemann.
- HUGHES, R. W. 1997. *Ruby and Sapphire*, Boulder Co, RWH Publishing.
- HUGHES, R. W. 2010. Andesine _Timeline of a controversy. *Ruby and Sapphire .com* [Online]. [Accessed nov 2011].
- JAANIMAGI, P. A. Breaking the 100-fs barrier with a streak camera. In: TATCHYN, R. O., CHANG, Z., KIEFFER, J.-C. & HASTINGS, J. B., eds., 2004 San Diego, CA, USA. SPIE, 171-182.
- JAHN, H. & TELLER, E. 1937. Stability of polyatomic molecules in degenerate electronic states : orbital degeneracy. *Proceedings of the Royal Society A*, 220-235.
- JASINEVICIUS, R. 2009. *CHARACTERIZATION OF VIBRATIONAL AND ELECTRONIC FEATURES IN THE RAMAN SPECTRA OF GEM MINERALS*. Masters, THE UNIVERSITY OF ARIZONA.
- JOHNSON, I. 2012. *Jablonski energy diagram* [Online]. Florida: Olympus america inc. Available: <http://www.olympusmicro.com/primer/java/jablonski/jabintro/index.html>. [Accessed 10/03/2012 2012].
- KAPPERS M.J. 2011. *RE: GaN thin film*. Type to TAYLOR, R.
- KAYAMA, M., NAKANO, S. & NISHIDO, H. 2010. Characteristics of emission centers in alkali feldspar: A new approach by using cathodoluminescence spectral deconvolution. *American Mineralogist*, 95, 1783-1795.
- KING, G. E., FINCH, A. A., ROBINSON, R. A. J. & HOLE, D. E. 2011a. The problem of dating quartz 1: Spectroscopic ionoluminescence of dose dependence. *Radiation Measurements*, 46, 1-9.
- KING, G. E., FINCH, A. A., ROBINSON, R. A. J., TAYLOR, R. P. & MOSSELMANS, J. F. W. 2011b. The problem of dating quartz 2: Synchrotron generated X-ray excited

- optical luminescence (XEOL) from quartz. *Radiation Measurements*, 46, 1082-1089.
- KLEIN, C. & DUTROW, B. 2008. *The manual of mineral Science*, New Jersey, Wiley and Sons.
- KONINGSBERGER, D. C. *X-Ray Absorption Principles, Applications, Techniques of EXAFS, SEXAFS and XANES*, Berlin, John Wiley and sons
- KORECKI, P., TOLKIEHN, M., DABROWSKI, K. M. & NOVIKOV, D. V. 2011. Fluorescence detection of white-beam X-ray absorption anisotropy: towards element-sensitive projections of local atomic structure. *Journal of Synchrotron Radiation*, 18, 851-861.
- KUZMIN, A. 1994. Anisotropy of the photoelectron mean free path and its influence on the EXAFS amplitude. *J Phys.: Condens. Matter*, 6, 5761-5770.
- LAGOIS, J. & FISCHER, B. 1976. Experimental Observation of Surface Exciton Polaritons. *Physical Review Letters*, 36, 680-683.
- LAKOWICZ, J. R. (ed.) 1999. *Principles of Fluorescence Spectroscopy*: Springer.
- LAKOWICZ, J. R. 2006. *Principles of Fluorescence Spectroscopy*.
- LANKINEN, A., SVENSK, O., MATTILA, M., TUOMI, T. O., LIPANEN, H., MCNALLY, P. J., O'REILLY, L. & PAULMANN, C. 2008. X-ray excited optical luminescence of Mg-doped GaN. *Journal of X-Ray Science and Technology*, 16, 215-220.
- LARCHERI, S., ROCCA, F., JANDARD, F., PAILHAREY, D., GRAZIOLA, R., KUZMIN, A. & PURANS, J. 2008. X-ray excited optical luminescence detection by scanning near-field optical microscope: A new tool for nanoscience. *Review of Scientific Instruments*, 79, 1-9.
- LEE, M. R., BROWN, D. J., SMITH, C. L., HODSON, M. E., MACKENZIE, M. & HELLMANN, R. 2007a. Characterization of mineral surfaces using FIB and TEM: A case study of naturally weathered alkali feldspars. *American Mineralogist*, 92, 1383-1394.
- LEE, M. R., PARSONS, I., EDWARDS, P. R. & MARTIN, R. W. 2007b. Identification of cathodoluminescence activators in zoned alkali feldspars by hyperspectral imaging and electron-probe microanalysis. *American Mineralogist*, 92, 243-253.
- LEVERENZ, H., W., 1968. An introduction to the luminescence of solids. New York: Dover publications.
- LI, B. & LI, S.-H. 2011. Luminescence dating of K-feldspar from sediments: A protocol without anomalous fading correction. *Quaternary Geochronology*, 6, 468-479.
- LICATA, V. J. & WOWOR, A. J. 2008. Applications of fluorescence anisotropy to the study of protein-DNA interactions. *Methods Cell Biol*, 84, 243-62.
- LUCAREZ, F. 2003. *Silicon nanocrystals in erbium-doped silica for optical amplifiers*. MSc, UCL.
- LYTLE, F. W., SAYERS, D. E. & STERN, E. A. 1975. Extended x-ray-absorption fine-structure technique. II. Experimental practice and selected results. *Physical Review B*, 11, 4825-4835.
- MACRAE, C. M. & WILSON, N. C. 2008. Luminescence database : Minerals and materials. *Microscopy and Microanalysis*, 14, 184-204.
- MANNING, P. G. 1969. Optical absorption spectra of chromium-bearing tourmaline, black tourmaline and buergerite. *The Canadian Mineralogist*, 10, 57-70.
- MARFUNIN, A. S. 1979. *Spectroscopy Luminescence and Radiation Centers in Minerals*, New York, Springer

- MARQUARDT, D. 1963. An Algorithm for Least-Squares Estimation of Nonlinear Parameters. *Journal of the Society for Industrial and Applied Mathematics*, 11, 431-441.
- MARQUES, C., SANTOS, L., FALCÃO, A. N., SILVA, R. C. & ALVES, E. 2000. Luminescence studies in colour centres produced in natural topaz. *Journal of Luminescence*, 87-89, 583-585.
- MARTIN, I. P. S., REHM, G., THOMAS, C. & BARTOLINI, R. 2011. Experience with low-alpha lattices at the Diamond Light Source. *Physical Review Special Topics - Accelerators and Beams*, 14, 040705-16.
- MARTINEZ-CRIADO, G., STEINMANN, R., ALEN, B., LABRADOR, A., FUSTER, D., RIPALDA, J. M., HOMES, A., LABOURE, S. & SUSINI, J. 2007. New cryogenic environment for beamline ID22 at the European Synchrotron Radiation Facility. *Rev Sci Instrum*, 78, 025106.
- MASON, R., CLOUTER, M. & GOULDING, R. 2005. The luminescence decay-time of Mn²⁺ activated calcite. *Physics and Chemistry of Minerals*, 32, 451-459.
- MCKEEVER, S. W. S. 1985. *Thermoluminescence of solids*, Cambridge [Cambridgeshire] ; New York, Cambridge University Press.
- MCKEEVER, S. W. S., MOSCOVITCH, M. & TOWNSEND, P. D. 1995. *Thermoluminescence Dosimetry Materials: Properties and Uses*, Ashford, Nuclear Technology Publishing.
- MOSELMANS, F. The edge to X-ray absorption. The diamond Synchrotron Summer School, 2009 2009 Diamond Light Source Ltd. Diamond Light source Ltd.
- MOSELMANS, J. F. W., QUINN, P. D., DENT, A. J., CAVILL, S. A., MORENO, S. D., PEACH, A., LEICESTER, P. J., KEYLOCK, S. J., GREGORY, S. R., ATKINSON, K. D. & ROSELL, J. R. 2009. I18 - the microfocuss spectroscopy beamline at the Diamond Light Source. *Journal of Synchrotron Radiation*, 16, 818-824.
- MUHLHAUSEN, C. & GORDON, R. G. 1981. Electron-gas theory of ionic crystals, including many-body effects. *Physical Review B*, 23, 900-923.
- MURPHY, M., ZHOU, X. T., HEIGL, F., REGIER, T. & SHAM, T. K. 2007. An X-ray excited optical luminescence (XEOL) analysis of Mn²⁺ doped ZnS nanostructures. In: HEDMAN, B. & PAINETTA, P. (eds.) *X-Ray Absorption Fine Structure-XAFS13*. Melville: Amer Inst Physics.
- NASDALA, L., KRONZ, A., HANCHAR, J. M., TICHOMIROVA, M., DAVIS, D. W. & HOFMEISTER, W. 2006. Effects of natural radiation damage on back-scattered electron images of single crystals of minerals. *American Mineralogist*, 91, 1739-1746.
- NASSAU, K. 2001. *The Physics and chemistry of colour*, New York, Wiley inter science.
- OETZEL, M. & HEGER, G. 1999. Laboratory X-ray powder diffraction: a comparison of different geometries with special attention to the usage of the CuKalpha doublet. *Journal of Applied Crystallography*, 32, 799-807.
- PAHAJU, O., P., 2005. *Solid state Physics*, Dehli, Laxmi publications.
- PANKOVE, J., I., 1971. *Optical processes in semiconductors*, Dover publicatipons.
- PARSONS, I., STEELE, D. A., LEE, M. R. & MAGEE, C. W. 2008. Titanium as a cathodoluminescence activator in alkali feldspars. *American Mineralogist*, 93, 875-879.

- PARTOVI-AZAR, P. & NAMIRANIAN, A. 2010. The effect of the orientation of the Stone–Wales defects on the bands structure of carbon nanotubes. *Journal of Physics: Conference Series*, 248, 012010- 23
- PERNA, G., CAPOZZI, V., AMBRICO, M. & SMALDONE, D. 1998. Temperature dependence of the red shift and broadening of the exciton line in CdSe/GaAs laser ablated heterostructures. *Journal of Luminescence*, 76–77, 534-539.
- PETERSON, N. V. 1972. Oregon Sunstones. *Ore Bin*, 34, 197-215.
- PHOTONICS., H. 2012. Picosecond fluorescence lifetime measurementsystem C11200. *Hamamatsu Photomics*. Hamamatsu city Japan.
- POOLTON, N. R. J., PANTOS, E., HAMILTON, B., DENBY, P. M. & JOHNSEN, O. 2004. Application of wavelength-resolved optically-detected XAS methods to phase-segregated silicates. *physica status solidi (b)*, 241, 3656-3663.
- POOLTON, N. R. J., TOWLSON, B. M., HAMILTON, B. & EVANS, D. A. 2006. New instrumentation for micro-imaging X-ray absorption spectroscopy using optical detection methods. *Nuclear Instruments and Methods in Physics Research Section B: Beam Interactions with Materials and Atoms*, 246, 445-451.
- POOLTON, N. R. J., TOWLSON, B. M., HAMILTON, B., WALLINGA, J. & LANG, A. 2007. Micro imaging synchrotron -laser interactions in wide band gap luminescent materials. *Journal of Physics D-Applied Physics*, 40, 3557-3562.
- RAVEL, B. & NEWVILLE, M. 2005. ATHENA, ARTEMIS, HEPHAESTUS: data analysis for X-ray absorption spectroscopy using IFEFFIT. *J. Synchrotron rad*, 12, 537--541.
- READ, P. G. 1999. *Gemology*, Oxford, [England] ; Boston, Butterworth-Heinemann.
- REBANE, K., L., SAARI, P.,M. 1976. Hot Luminescence and relaxation processes in the centres of luminescence. *J Luminescence*, 12/13, 23-31.
- RENNINGER, M. 1937. Multiple diffraction in crystals *Phys*, 106, 175-179.
- RETHFELD, B., KAISER, A., VICANEK, M. & SIMON, G. 2002. Ultrafast dynamics of nonequilibrium electrons in metals under femtosecond laser irradiation. *Physical Review B*, 65, 214303.
- RIBBE, P. H., MEGAW, H. D., TAYLOR, W. H., FERGUSON, R. B. & TRAILL, R. J. 1969. Anisotropy of the sodium atom in low albite. *Acta Crystallographica B*, 25, 1503-1518.
- RIEGER, T. Z., VOGT, J. M., SAMMYNAIKEN, R. & SHAM, T. K. 2010. Advances in Time Resolved X-ray Excited Optical Luminescence Instrumentation at the Canadian Light Source. *AIP Conference Proceedings*, 1234, 838-841.
- RIOS, S., MALCHEREK, T., SALJE, E. K. H. & DOMENEGHETTI, M. C. 2000. Localized defects in radiation-damaged zircon. *Acta Crystallographica B*, 56, 947-952.
- ROSENBERG, R. A., ZOHAR, S., KEAVNEY, D., DIVAN, R., ROSENMAN, D., MASCARENHAS, A. & STEINER, M. A. 2012. Elemental and magnetic sensitive imaging using x-ray excited luminescence microscopy. *Review of Scientific Instruments*, 83, 073701-6.
- SAPELKIN, A. V., BOLMATOV, D., LITTLE, W., KARATUTLU, A., TRACHENKO, K., DENT, A., F., M., CIBIN, G., R.P., T. & 2012. Origin of photoluminescence in Ge Quantum Dots *Nature Nanotechnology*, 1.
- SCHLAFER, H. L. & GLIEMANN, G. 1969. Basic principles of ligand field theory. *Journal of molecular structure*, 11, 162-163.

- SCHOTT, S., RAGER, H., SCH, UUML, RMANN, K. & TARAN, M. 2003a. Spectroscopic study of natural gem quality "Imperial"-Topazes from Ouro Preto, Brazil. *European Journal of Mineralogy*, 15, 701-706.
- SCHOTT, S., RAGER, H., SCHÜRMAN, K. & TARAN, M. 2003b. Spectroscopic study of natural gem quality "Imperial"-Topazes from Ouro Preto, Brazil. *European Journal of Mineralogy*, 15, 701-706.
- SHAM, T.-K. & ROSENBERG, R. A. 2007. Time-Resolved Synchrotron Radiation Excited Optical Luminescence: Light-Emission Properties of Silicon-Based Nanostructures. *ChemPhysChem*, 8, 2557-2567.
- SHAM, T. K. & GORDON, R. A. 2010. RIXS, XEOL and XEOL Imaging of Rare-earth Phosphors at the L_{3,2}-edges. *AIP Conference Proceedings*, 1234, 133-136.
- SHAM, T. K., KIM, P.-S. G., LAM, S., ZHOU, X. T., ROSENBURGR, A., SHENOY, G. K., HEIGL, F., JURGENSEN, A., REIGER, T., COULTARD, I. & ZUINL, H. Y.-F. 2006. Materials analysis using photon in photon out spectroscopy. *SRMS -5 conference*. Chicago: SRMS.
- SHARMA, A. & SCHULMAN, S. G. 1999. *Introduction to fluorescence spectroscopy*, New York, A.Wiley.
- SMITH, J. V. & BROWN, W. L. 1987. *Feldspar minerals*, Berlin ; New York, Springer-Verlag.
- SODERHOLM, L., LIU, G. K., ANTONIO, M. R. & LYTLE, F. W. 1998. X-ray excited optical luminescence (XEOL) detection of x-ray absorption fine structure (XAFS). *The Journal of Chemical Physics*, 109, 6745-6752.
- SPOONER, N. A. 1994. The anomalous fading of infrared-stimulated luminescence from feldspars. *Radiation Measurements*, 23, 625-632.
- STAROSKE, W., PFEIFFER, M., LEO, K. & HOFFMANN, M. 2007. Single-Step Triplet-Triplet Annihilation: An Intrinsic Limit for the High Brightness Efficiency of Phosphorescent Organic Light Emitting Diodes. *Physical Review Letters* [Online], 98. Available: <http://link.aps.org/doi/10.1103/PhysRevLett.98.197402>.
- STEPANOV, B., I. 1961. *Foundations of the spectroscopy of negative light flows*, Minsk, BGU.
- STERN, E. A. 1974. Theory of the extended x-ray-absorption fine structure. *Physical Review B*, 10, 3027-3037.
- STERN, E. A., SAYERS, D. E. & LYTLE, F. W. 1975. Extended x-ray-absorption fine-structure technique. III. Determination of physical parameters. *Physical Review B*, 11, 4836-4846.
- STOKES, G. G. 1850. On the Change of Refrangibility of Light. *Abstracts of the Papers Communicated to the Royal Society of London*, 6, 195-200.
- STRICKLER, S. J. & BERG, R. A. 1962. Relationship between absorption intensity and fluorescence lifetime of molecules. *J. Chem Phys*, 37, 814-822.
- STRUTT, J. 1899. On the Transmission of light through an atmosphere containing small particles in suspension, and on the origin of the blue of the sky. *Philosophical Magazine*, 47, 375-394.
- TARAN, M. N., TARASHCHAN, A. N., RAGER, H., SCHOTT, S., SCHÜRMAN, K. & IWANUCH, W. 2003. Optical spectroscopy study of variously colored gem-quality topazes from Ouro Preto, Minas Gerais, Brazil. *Physics and Chemistry of Minerals*, 30, 546-555.

- TARASHCHAN, A. N., TARAN, M. N., RAGER, H. & IWANUCH, W. 2006. Luminescence spectroscopic study of Cr³⁺ in Brazilian topazes from Ouro Preto. *Phys Chem Min*, 32, 679-690.
- TAYLOR, R. P., FINCH, A. A., MOSSELMANS, J. F. W. & QUINN, P. D. 2013. The development of a XEOL and TR XEOL detection system for the I18 microfocuss beamline Diamond light source. *Journal of Luminescence*, 134, 49-58.
- TENDERHOLT, A., B. H. & HODGSON, K. 2007. Pyspline: A modern, cross-Platform Program for the processing of raw Averaged XAS and EXAFS Data. *AIP Proceedings* Stanford University: IOP INSTITUTE OF PHYSICS PUBLISHING LTD.
- TERSOFF, J. & HAMANN, D. R. 1985. Theory of the scanning tunneling microscope. *Physical Review B*, 31, 805-813.
- THOMAS, A. V., BEREZOVSKA, O., HYMAN, B. T. & VON ARNIM, C. A. 2008. *Methods*, 44, 299.
- THOMAS, C. A., REHM, G., OWEN, H. L., WYLES, N. G., BOTCHWAY, S. W., SCHLOTT, V. & WAHL, M. 2006. Bunch purity measurement for Diamond. *Nuclear Instruments and Methods in Physics Research Section A: Accelerators, Spectrometers, Detectors and Associated Equipment*, 566, 762-766.
- THOMSEN, J. K., MURRAY, A., JAIN, M., BUYLAERT, J. 2012. re luminescence dating of kfeldspar from sediments a protocol without anomalous fading correction by bo li and shenghua li. *quaternary geochronology*, 8, 46-48.
- VAN DEN EECKHOUT, K., SMET, P. F. & POELMAN, D. 2010. Persistent Luminescence in Eu²⁺-Doped Compounds: A Review. *Materials*, 3, 2536-2566.
- VIJ, D. R. (ed.) 1998. *Luminescence of solids*, New York ; London: New York ; London : Plenum Press, c1998.
- WALKER, R. P. Joint accelerator conference. In: (FERMILAB), M. A., (TRIUMF), M. C., (ANL), C. E., (CLS), C. F., (GSI), K. H., (ORNL), C. H., (MSL), L. L., (DESY), M. M., (CERN), C. P.-J. G., (INFN/LNS), L. P., (CERN), J. P., (INFN/LNL), P. P., (GSI), V. S. & (KEK), A. S., eds. PAC09, 2009 Vancouver. CERN, 3169-3171.
- WALL, W. A., KARPICK, J. T. & BARTOLO, B. D. 1971. Temperature dependence of the vibronic spectrum and fluorescence lifetime of YAG:Cr³⁺. *Journal of Physics C: Solid State Physics*, 4, 3258.
- WANNIER, G. H. 1937. The Structure of Electronic Excitation Levels in Insulating Crystals. *Physical Review*, 52, 191-197.
- WEBER, J. R., KOEHL, W. F., VARLEY, J. B., JANOTTI, A., BUCKLEY, B. B., VAN DE WALLE, C. G. & AWSCHALOM, D. D. 2010. Quantum computing with defects. *Proceedings of the National Academy of Sciences*, 107, 8513-8518.
- WEBSTER, R. & ANDERSON, B. W. 1983. *Gems : their sources, description and identification*, London ; Boston, Butterworths.
- WIEDEMANN, E. & SCHMIDT, G. C. 1896. *Ann. Phys.*, 58, 103.
- WIEN, I. V. W. 1919. Uber Messungen der Leuchtdauer der atome und der Dämpfung der Spektrallinien *Annalen der Physik*, 23.
- WILDE, S. A., PECK W.H., GRAHAM, C.M., 2001. Evidence from detrital zircons for the existence of continental crust and oceans on the Earth 4.4 Gyr ago. *Nature Geoscience*, 409, 175-178.
- WUNDER, B., RUBIE, D. C., ROSS II, C. R., MEDENBACH, O., SEIFERT, F. & SCHREYER, W. 1993. Synthesis, stability, and properties of Al₂SiO₄(OH)₂: a fully hydrated analogue of topaz *Am Min*, 78, 285-297.

- YEN, W., SHIONOYA, S. & YAMAMOTO, H. (eds.) 2007. *Fundamentals of Phosphors*, Boca Raton FL: Taylor and Francis group.
- ZHAO, J., JI, S. & GUO, H. 2011. Triplet-triplet annihilation based upconversion: from triplet sensitizers and triplet acceptors to upconversion quantum yields. *RSC Advances*, 1, 937-950.